

# TECHNISCHE UNIVERSITÄT MÜNCHEN

Lehrstuhl für Numerische Mechanik

## Simulation of Self-assembly and Mechanics of Transiently Crosslinked, Semiflexible Biopolymer Networks

Kei Wieland Müller

Vollständiger Abdruck der von der Fakultät für Maschinenwesen der Technischen Universität München zur Erlangung des akademischen Grades eines

Doktor-Ingenieurs (Dr.-Ing.)

genehmigten Dissertation.

Vorsitzender: Univ.-Prof. Dr. rer. nat. Oliver Lieleg

Prüfer der Dissertation: 1. Univ.-Prof. Dr.-Ing. Wolfgang A. Wall  
2. Univ.-Prof. Dr. rer. nat. Andreas Bausch

Die Dissertation wurde am 07. Mai 2014 bei der Technischen Universität München eingereicht und durch die Fakultät für Maschinenwesen am 27. Juni 2014 angenommen.



Ehern wahrt,  
Was stoisch reift,  
Doch stetig gart.  
Die Zeit verkehrt  
Muhe in Freud' .  
Sie zeugt den Wert.



## Danksagung

Die Ahnung, dass dieses Buch das einzig dauerhafte Zeugnis sein könnte, über das ich so gänzlich und unmittelbar verfüge, und die Gewissheit, dass dessen Inhalt, nicht aber meine Dankbarkeit, an Belang verlieren kann, verleiten mich zu einer etwas längeren Form.

Der Vater ist dem Sohn ein Vorbild in fortwährendem Wandel, an dessen Anfang verdichtet Anreiz und Versprechen stehen: „gesetzt, Du willst, sei ich Dir Maß und Ansporn.“. Fortan gibt der Vater Halt und Richtung, aber auch die nötige Freiheit und vergibt die notwendigen und andere Irrungen in einem Gefüge aus Vertrauen, Mühe und deren Anerkennung, bis er den Zögling ziehen lässt. In großem Einklang mit dieser Beschreibung darf ich stolz und in aufrichtiger Dankbarkeit Prof. Wolfgang Wall meinen Doktorvater und mich den jüngsten Spross der Familie nennen.

Die Überführung meines zunächst vagen Vorhabens in die vorliegende definierte Form wurde in besagtem Anfang durch helfende Hände geleitet. Herr Prof. Michael Gee förderte und führte mich ganz maßgeblich in der ersten Zeit. Seine zielgerichtete Kompromisslosigkeit und seine Fairness gaben mir die Überzeugung, am richtigen Ort zu sein. Herrn Dr. Andreas Maier nehme ich als denjenigen wahr, der mir die anfänglichen Zweifel nahm und mich zum tatsächlich allerersten Schritt ermutigte. Als stets optimistischer, umtriebiger Freigeist und Freund ist er mir ein großer persönlicher Gewinn.

Über das im allgemeinen empfundene Glück hinaus, Teil eines menschlich so feinen wie vielfältigen, fachlich so exzellenten Kollegenkreises zu sein, möchte ich einzelne im besonderen hervorheben. Es war mir eine große Freude, mit meinem Bürokipfel Jonas Biehler Raum ( $\sim 0.2 \text{ m}^3$ , neuen Expeditionen zufolge eventuell mehr) und Zeit auf Konferenzen und alpinen Gipfeln zu teilen. Christoph Meier hat mit enormem fachlichem Tiefgang und großer Sorgfalt in ganz besonderem Maße zum Erfolg der vorliegenden Schrift beigetragen. Ihm gebührt über den Dank hinaus meine ehrliche Bewunderung. In nicht minder tiefgründiger und sorgfältiger Auseinandersetzung entstand in jahrelanger Arbeit die gemeinsame praktische Abhandlung *Zur Erkundung und Vermessung der Urmass (in der) Bar jeder Vernunft*. Ausdrücklich hoffe ich, dass meine Freundschaft zu Dr. Mahmoud Ismail und Matthias Mayr erhalten bleibt und sie uns noch manch gemeinsame Freude bereitet. Ich danke ihnen für all die kleinen und großen Hilfen im Laufe der vergangenen Jahre. Ganz herzlich danke ich Frau Dr. Lena Wiechert für die spannende Zeit, in welche die Gestaltung der Lehrveranstaltung zur *Biomechanik* fiel. Svenja Schoeder danke ich für die Lektüre und Korrektur meiner Arbeit. Sudhakar möchte ich als Freund und für seine Verwegenheit würdigen, die ihn zum Bedürftigen Erster Hilfe und alpiner Bergrettung werden ließ. Zuletzt danke ich Dr. Christian Cyron (*«On ne voit bien qu'avec le cœur.»*) für die thematische Heranführung und die intensive Zusammenarbeit der ersten Zeit.

Als einem der geistigen Väter des Projekts möchte ich Herrn Prof. Andreas Bausch ein ausdrückliches Dankeschön widmen. Seine Ideen umrissen das thematische Feld, auf welchem ich mich austoben durfte. Die äußerst direkten, aber stets zielführenden Gespräche habe ich kennen und auch schätzen gelernt. Sie haben merklich zum Erfolg meines Promotionsvorhabens beigetragen und mich auch in außerfachlicher Hinsicht vorangebracht. Ich danke ihm zudem in seiner

Funktion als zweiter Prüfer.

Nicht nur in seiner Funktion als Vorsitzender der Prüfungskommission hatte Herr Prof. Oliver Lieleg großen Einfluss auf meine Arbeit. In der Anfangsphase meiner Promotion dienten seine Experimente als Referenz für meine Forschung, in ihrer Endphase trug er fachlich in erheblichem Maße zu deren erfolgreichen Abschluss bei. Ich bedanke mich hiermit für seine wertvolle Unterstützung.

Dank Prof. Bausch entstand eine äußerst fruchtbare Zusammenarbeit mit Prof. Robijn Bruinsma und Prof. Alexander Levine von der University of California, Los Angeles. Gemeinsame Anstrengungen ermöglichten es mir, meine Arbeit auf ein Niveau zu heben, welches ich allein nicht einmal ansatzweise erreicht hätte. Ich bedanke mich bei beiden für das große Vergnügen, welches sie mir mit ihrer fachlich, persönlich und nicht zuletzt durch ihren großartigen Humor bereitet haben. Ein Dankesgruß geht darüber hinaus an Devin Kachan, mit dem es sich trefflich über fachliches und nicht so fachliches diskutieren und lachen ließ.

Meinen Studenten Julian Riba, Christian Roth, Anna Birzle, Max Grill, Anja Bestler, Evelyn Flesch, Max von Danwitz, Philipp Johné, Weiwei Wang, Christoph Kocher und Rebecca Kächele gilt mein Dank für Ihre großartige Mitarbeit im Rahmen von Arbeiten und Projekten.

Der *International Graduate School of Science and Engineering* (IGSSE) der Technischen Universität München danke ich für das Promotionsstipendium und dem *Institute for Advanced Study* (TUM-IAS) für die finanzielle Förderung meiner beiden USA-Aufenthalte in den Jahren 2011 und 2013.

Der am wenigsten greifbare, da komplexeste und umfassendste Einfluss ist der der Familie. Ein Versuch, ihn zumindest zu skizzieren: vor meiner Mutter Yoshiko Abé-Müller verneige ich mich zum Dank für alles Musische und Feine, unzählige für meinen Leistungssport zurückgelegte Kilometer und die Gnade der zweiten Muttersprache. Meinem Vater Günter Müller verdanke ich meinen Zugang zu Literatur und Geschichte, das mitunter Brachiale, die gleichsam fokussierten und erlebnisreichen Jahre im Ausland und die gezielte Infragestellung gültiger und angeblicher Regeln, auch wenn er mich dafür als Kind über unzählige rote Fußgängerampeln schleifen musste. Meiner Schwester Emika Müller danke ich für wunderschöne gemeinsame Erlebnisse und an dieser Stelle besonders für die große Freude, die sie mir im Anschluss an meine Verteidigung mit ihrem Geigenspiel bereitet hat. Das Wirkgeflecht dieser Einflüsse ermöglicht es mir, in genau dieser Form als der, der ich sein darf, den Schlusspunkt der Danksagung zu setzen.

München, im Juli 2014

Kei Wieland Müller

## Abstract

Eukaryotic cells are the base units of all multi-celled organisms. Despite their large morphological variety, nearly all cells share the same fundamental intracellular organization and functions. Among the cellular constituents, the cytoskeleton stands out. It is a highly dynamic fibrous network consisting of different fiber species and carrying out a variety of essential intracellular tasks. It orchestrates cell division and provides means for cell migration. It also serves as the cell's sensory organ.

One of the cytoskeletal filament species, actin, is of particular scientific interest. It creates highly variable network structures, which adjust their shape and mechanical properties in accordance to current requirements. Its morphological variety is provided by a multitude of small *crosslinking proteins*, which tie actin filaments together. Research on actin fiber networks is a fruitful endeavor as it entails a better understanding of fundamental intracellular mechanisms and, as a consequence, can advance pharmacology or the knowledge on causes and therapies of diseases on the subcellular level.

The main focus of this work lies on the simulation-based investigation of network self-assembly and mechanics. Owing to the microscopic scale of the problem, gaining experimental insight below a certain spatial and temporal resolution is often unfeasible, hampering subsequent theoretical modeling as well. Simulations seek to remove this scientific bottleneck by enhancing experimental observations, thereby significantly contributing to modeling and the theoretical understanding of biopolymer networks.

The goal of this thesis is the development and application of an approach to the simulation of crosslinked biopolymer networks, which provides answers to fundamental questions concerning network self-assembly and the complex mechanical behavior of these networks. Therefore, in a first step, a highly efficient simulation framework is set up, which describes single filaments and crosslinks as micromechanical continua subject to Brownian motion. The fundamental computational method is enriched by recovered information on the discrete molecular microstructure, which has been lost previously due to choosing a continuum description. In conjunction, molecular motor activity is introduced and validated. These modeling steps allow for the investigation of tantalizing biophysical problems such as the mechanisms behind bundle assembly, the formation and motor-induced stiffening of stress fibers, or the cooperativity between different motor species.

Based on this strong methodic fundament, a variety of biophysical problems can be studied successfully. Two closely related research topics are discussed here. First, the linker-mediated emergence of various distinct thermodynamically equilibrated network morphologies is examined. Essential conclusions are drawn about dynamics and the thermodynamic causes of network self-assembly. Having obtained detailed knowledge on network evolution, one can generate tailor-made in silico network geometries by using specific crosslinking proteins. Bundle networks, for example, are a biologically most relevant network structure. Such networks serve various purposes such as cell adhesion and mechanosensing and are generically in a state of thermal non-equilibrium. For the first time, the proposed computational approach enables the micromechanical simulation of biopolymer networks on biologically relevant time scales up to several thousands of seconds and length scales of up to 10 microns. In this thesis, the approach reveals previously unknown mechanical properties of bundle networks and thus enables modeling and the derivation of a physical theory on bundle network rheology.



## Zusammenfassung

Eukaryotische Zellen sind die Grundbausteine vielzelliger Lebewesen. Trotz ihrer großen morphologischen Diversität folgen die Grundzüge intrazellulärer Organisation und Arbeitsteilung einem allgemeinen Schema. In diesem Schema ist dem Zellskelett, einem dynamischen Netzwerk verschiedenartiger Proteinfasern, eine exponierte Rolle zugeordnet. Es koordiniert unter anderem die Zellteilung sowie die Zellmigration und dient zudem als sensorisches Organ der Zelle.

Dem Zytoskelettbestandteil Aktin, welcher variable Fasernetzwerkstrukturen ausbildet, gilt besonderes Interesse. Aktinfasernetzwerke passen sich in Form und mechanischen Eigenschaften der ihnen zugeordneten Aufgabe an. Dies wird durch kleine, die Aktinfasern verknüpfende Proteine ermöglicht, sogenannte Quervernetzer.

Die Erforschung von Aktinnetzwerken ist besonders lohnend, da neben dem grundsätzlichen Verständnis intrazellulärer Vorgänge auch weiterführende Erkenntnisse locken, etwa bezüglich der Auswirkung pharmakologischer Wirkstoffe oder auch krankhafter Veränderungen der Zelle, was wiederum die Entwicklung von Therapien vorantreibt.

In dieser Arbeit liegt das Hauptaugenmerk auf der simulationsbasierten Erforschung der Netzwerkentstehung und -mechanik. Der Erkenntnisgewinn durch Experimente ist aufgrund der mikroskopischen Skala oftmals unmöglich, wodurch auch die weiterführende Modellbildung behindert wird. An diesem Engpass setzen Simulationen an und erweitern oder erzeugen Beobachtungen, die die Modellierung und das Verständnis der Netzwerke entscheidend prägen.

Ziel dieser Arbeit ist die Entwicklung und Anwendung einer Simulationsmethode, welche grundsätzliche Fragen zur Selbstorganisation und zu den Ursachen für das komplexe mechanische Verhalten quervernetzter Biopolymernetzwerke beantwortet. Hierfür wird zunächst ein leistungsfähiges Simulationsgerüst aufgebaut, welches auf einem mikromechanischen Kontinuumsansatz für Einzelfasern und Quervernetzer unter Berücksichtigung der Brownschen Dynamik beruht. Die zugrunde liegende Simulationsmethode wird durch diese Arbeit erweitert, sodass zum einen Details der diskreten molekularen Geometrie, welche durch den Kontinuumsansatz verlorengegangen sind, wiedergewonnen werden. Zum anderen wird ein Modell für enzymatische Motoraktivität vorgestellt und erprobt. Diese Entwicklungen ermöglichen die Beantwortung hochaktueller biophysikalischer Fragen, etwa nach den Mechanismen der Faserbündelbildung durch Quervernetzer, der Versteifung durch molekulare Motoren oder nach dem kooperativen Verhalten verschiedener Motorproteine.

Im weiteren Verlauf der Arbeit werden erfolgreich zwei große biophysikalische Themenkomplexe bearbeitet. Zunächst gilt das Interesse thermischen Gleichgewichtsstrukturen, welche durch das ordnende Wirken von Quervernetzern entstehen. Die Untersuchung des Faser-Quervernetzer-Systems führt zu einem neuen, umfassenden Verständnis der Dynamik der Netzwerkbildung sowie deren Ursachen. Dieses Wissen ermöglicht die gezielte Erzeugung von Netzwerken mit bestimmten Eigenschaften durch die Gabe bestimmter Quervernetzer. Eine biologisch besonders relevante Morphologie ist die des Bündelnetzwerks. Faserbündelnetzwerke dienen unter anderem der mechanischen Verankerung der Zelle sowie der Zellsensorik und befinden sich allgemein in einem Zustand thermischen Ungleichgewichts. Die vorgestellte Methode ermöglicht erstmals die Simulation biologischer Zeiträume von mehreren tausend Sekunden und großer räumlicher Ausdehnungen bis  $1000 \mu\text{m}^3$ . Mit ihrer Hilfe werden grundlegend neue physikalische Netzwerkeigenschaften entdeckt, welche im Rahmen der Arbeit zu einer umfassenden rheologischen Modellbildung und Theorie zusammengeführt werden.



# Contents

<b>1</b>	<b>Introduction</b>	<b>1</b>
1.1	From cell to simulation . . . . .	2
1.1.1	The eukaryotic cell . . . . .	2
1.1.2	The cytoskeleton and its filaments . . . . .	4
1.1.3	Reduced model systems . . . . .	7
1.2	Simulations on biologically relevant time scales . . . . .	7
1.3	Objectives and achievements . . . . .	9
1.4	Organization of the thesis . . . . .	10
<b>2</b>	<b>Micromechanical finite element simulation of biopolymer networks</b>	<b>13</b>
2.1	General modeling requirements . . . . .	13
2.2	Simulation of biopolymers in literature . . . . .	14
2.3	Micromechanical continuum model for biopolymer networks . . . . .	15
2.3.1	General modeling strategy . . . . .	15
2.4	Mechanical model of a semiflexible filament . . . . .	18
2.4.1	Balance of linear and angular momentum . . . . .	18
2.4.2	Forces and Moments . . . . .	19
2.5	Discretization . . . . .	24
2.5.1	Weak form . . . . .	24
2.5.2	General remarks on discretization in space and time . . . . .	25
2.5.3	Discretized forces and moments . . . . .	27
2.6	Mechanical and chemical model of a linker molecule . . . . .	29
2.6.1	Chemical states of a linker . . . . .	29
2.6.2	Free linkers in solution . . . . .	30
2.6.3	Singly bound linkers . . . . .	31
2.6.4	Doubly bound linkers: crosslinks . . . . .	33
2.7	Periodic boundary conditions . . . . .	33
2.8	Concluding remarks . . . . .	34
<b>3</b>	<b>Extended micromechanical approach – the reintroduction of sub-continuum microstructure</b>	<b>35</b>
3.1	Decoupling chemical and mechanical resolution . . . . .	35
3.2	Extended filament model . . . . .	37
3.2.1	Parametrization of the monomeric structure of F-actin . . . . .	37
3.2.2	Binding events and modified reaction volumes . . . . .	39
3.2.3	Structural polarity of filaments . . . . .	40

3.3	Extended linker model . . . . .	40
3.3.1	Design concept . . . . .	40
3.3.2	Geometrical and mechanical interpolation and constraint formulation for a two-noded beam element . . . . .	40
3.3.3	Linearized system of equations for a tied two-noded Reissner beam el- ement . . . . .	41
3.3.4	Constraint formulations . . . . .	43
3.3.5	Linearized system of equations of the constrained problem . . . . .	47
3.3.6	A preview on constraint enforcement by Lagrange multipliers . . . . .	47
3.4	Numerical examples . . . . .	49
3.4.1	Validation of constraint enforcement . . . . .	49
3.4.2	Network morphologies in crosslinked semiflexible networks . . . . .	50
3.4.3	Linear rheology of semiflexible bundle networks . . . . .	55
3.4.4	Linear rheology of homogeneous isotropic networks . . . . .	56
3.5	Conclusions and outlook . . . . .	57
<b>4</b>	<b>A beam-element based model of a molecular motor</b>	<b>61</b>
4.1	Molecular machines . . . . .	61
4.1.1	Actin motors . . . . .	63
4.1.2	Microtubule motors . . . . .	65
4.2	Numerical model of a non-processive molecular motor . . . . .	65
4.2.1	Modeling strategy . . . . .	66
4.2.2	Force-dependent model of chemical bonds . . . . .	67
4.2.3	Cyclic motor activity and motor-filament interaction . . . . .	69
4.2.4	Modeling of conformational change . . . . .	71
4.2.5	Comprehensive incorporation of all modeling aspects into the existing finite element framework . . . . .	74
4.3	Numerical examples . . . . .	74
4.3.1	Motility assays in experiments . . . . .	75
4.3.2	Transport velocity of filaments in one-dimensional in silico motility assays	76
4.3.3	Simulation of a two-dimensional motility assay . . . . .	78
4.3.4	Conclusions . . . . .	83
4.4	Outlook . . . . .	83
4.4.1	Future model refinements . . . . .	83
4.4.2	Towards modeling myosin thick filaments . . . . .	84
4.4.3	Simulation of contractile bundles and active networks of bundles . . . .	85
<b>5</b>	<b>Equilibrium morphologies of semiflexible, transiently crosslinked biopoly- mer networks</b>	<b>87</b>
5.1	Simulation of Network Evolution . . . . .	89
5.2	The fundamental network morphologies of crosslinked semiflexible filament networks . . . . .	90
5.2.1	Preliminary remarks on nomenclature . . . . .	90
5.2.2	Network morphologies . . . . .	91
5.2.3	Parameter dependence of network morphologies . . . . .	93

5.3	Equilibrium phase diagram of semiflexible filament networks with transient linkers	95
5.3.1	Establishment of the phase diagram	95
5.3.2	Discussion	95
5.3.3	Impact of linker entropy on network morphology	97
5.3.4	Experimental support of in silico results	98
5.4	Structural analysis of network morphologies and their phase transitions	99
5.4.1	On the order of phase transitions	99
5.4.2	Analytical tools for the structural and mechanical analysis of crosslinked networks	99
5.5	Fundamental phase transitions	102
5.5.1	The bundle transition	102
5.5.2	The cluster transitions	104
5.5.3	The lamella transition	107
5.5.4	The cluster-lamella transitions	109
5.5.5	Energy conservation during network evolution	113
5.6	The effect of chirality on the formation of semiflexible network structures	114
5.6.1	Effects on the equilibrium phase diagram	115
5.7	Conclusions	117
<b>6</b>	<b>Rheology of semiflexible biopolymer bundle networks</b>	<b>119</b>
6.1	General remarks on rheology	120
6.2	Micromechanical simulation of network rheology	120
6.2.1	Parametrization	120
6.2.2	Sample preparation and application of shear strain	122
6.3	Linear rheology of semiflexible bundle networks	124
6.3.1	Temporal stress response and its Fourier transform	125
6.3.2	The frequency regimes of linear bundle network rheology	125
6.3.3	Comparison of simulation and experiments	134
6.4	Aspects of nonlinear viscoelasticity of semiflexible bundle networks	136
6.4.1	Generic description of the nonlinear elastic response	136
6.4.2	Linker-specific nonlinear elastic response	137
6.4.3	Simulation of nonlinear network viscoelasticity	137
6.4.4	Effect of strain rate variation	138
6.4.5	Effect of the dissociation rate constant	141
6.4.6	Remark on computational aspects in the nonlinear deformation regime	142
6.5	Conclusions	143
<b>7</b>	<b>Conclusions and outlook</b>	<b>145</b>
7.1	Conclusions	145
7.1.1	Methods	145
7.1.2	Biophysical applications	146
7.2	Outlook	147
7.2.1	Methods	147
7.2.2	Biophysical applications	148
7.2.3	Engineering applications	149

<b>A</b>	<b>Linearized stiffness matrix of the extended linker element</b>	<b>151</b>
<b>B</b>	<b>Methods</b>	<b>155</b>
B.1	Mechanical contact of beams . . . . .	155
B.2	Search Algorithms . . . . .	156
B.3	Sampling of a uniform distribution of spherical coordinates . . . . .	158
<b>C</b>	<b>High-frequency bundle rheology</b>	<b>159</b>
<b>D</b>	<b>Simulation parameters</b>	<b>161</b>

# Nomenclature

## Notation of scalars, vectors, and matrices

$c, C$	Scalar values
$\mathbf{v}$	Vector
$\mathbf{M}$	Matrix
$c, C$	scalar of the (discrete) BD/FE model
$\mathbf{v}$	vector of the (discrete) BD/FE model
$\mathbf{M}$	matrix of the (discrete) BD/FE model

## Operators and symbols

$(\cdot)^T$	Transpose of a matrix
$(\cdot)^{-1}$	Inverse of a matrix
$\dot{(\cdot)}$	Time derivative
$(\cdot)'$	Derivative with respect to line parameter $s$
$\tilde{(\cdot)}$	Modified quantity
$\overset{\circ}{(\cdot)}$	Spin matrix
$\langle \cdot \rangle$	Mean value
$\times$	Vector product
$\otimes$	Dyadic product
$\delta(\cdot)$	Variation
$\delta_{ab}$	Dirac-Delta function with argument $(a - b)$
$\ln(\cdot)$	Natural logarithm
$\exp(\cdot)$	Natural exponential function
$\det$	Determinant
$\text{Lin}$	Linearization
$\Delta(\cdot)$	(i) Increment of $(\cdot)$ , (ii) tolerance of $(\cdot)$
$\mathcal{W}$	Multi-dimensional Wiener process
$\Omega_{(\cdot)}$	Mathematical set
$\mathbf{1}$	Identity matrix
$\mathbf{e}_i$	$i^{\text{th}}$ Cartesian base vector
$\tilde{\mathcal{J}}$	Jacobian

### Superscripts and subscripts

$(\cdot)^i, (\cdot)_i$	Quantity at time $t_i$ or the $i^{\text{th}}$ time step
$(\cdot)^{\{j\}}$	Quantity at the $j^{\text{th}}$ iteration step
$(\cdot)^{[k]}$	Quantity of the $k^{\text{th}}$ finite element node
$(\cdot)_{xyz}$	Index related to continuous quantities
$(\cdot)_{xyz}$	Index related to quantities of the (discrete) BD/FE model
$(\cdot)_{xyz}$	Index related to the chemical model
$(\cdot)_s, (\cdot)_s$	Section quantity
$(\cdot)_{visc}, (\cdot)_{visc}$	Viscous quantity
$(\cdot)_{stoch}, (\cdot)_{stoch}$	Stochastic quantity
$(\cdot)_{ext}, (\cdot)_{ext}$	External quantity
$(\cdot)_t, (\cdot)_t$	Translational quantity
$(\cdot)_r, (\cdot)_r$	Rotational quantity
$(\cdot)_{loc}$	Local quantity
$(\cdot)_f, (\cdot)_f$	Filament quantity
$(\cdot)_l, (\cdot)_l$	Linker quantity
$(\cdot)_{\mathcal{E}}$	Quantity of element $\mathcal{E}$ , Chapter 3)
$(\cdot)_{\mathfrak{r}}$	Quantity of a <i>real</i> node (Chapter 3)
$(\cdot)_{\mathfrak{v}}$	Quantity of a <i>virtual</i> node (Chapter 3)
$(\cdot)_{\mathfrak{b}}$	Quantity of a binding site
$(\cdot)_{\mathfrak{m}}$	Quantity of a motor

### One-dimensional continua

$s$	Line parameter
$L$	Curve length of the continuum
$t$	Time
$T$	Upper bound of the time interval
$\mathbf{x}(s, t)$	Position vector of the continuum
$\boldsymbol{\theta}(s, t)$	Cross section orientation of the continuum
$\gamma$	Material strain measure
$\kappa$	Material curvature
$\nu$	Poisson ratio
$A$	Cross section
$A_i$	Cross section, shear correction with respect to the $i^{\text{th}}$ principal axis
$E$	Young's modulus
$G$	Shear modulus

$I_r$	Polar moment of inertia of area
$I_i, I_i$	Moment of inertia of area with respect to the $i^{\text{th}}$ principal axis
$\mathbf{C}_f, \mathbf{C}_m$	Constitutive matrices
$\mathbf{f}'_s, \mathbf{f}'_s$	Derivative of the section force with respect to $s$
$\mathbf{f}_{stoch}, \mathbf{f}_{stoch}$	Stochastic force per unit length
$\mathbf{f}_{visc}, \mathbf{f}_{visc}$	Viscous force per unit length
$\mathbf{f}_{ext}, \mathbf{f}_{ext}$	Deterministic external force per unit length
$\mathbf{f}_\Gamma, \mathbf{f}_\Gamma$	Boundary force
$\mathbf{m}'_s, \mathbf{m}'_s$	Derivative of the section moment with respect to $s$
$\mathbf{m}_{stoch}, \mathbf{m}_{stoch}$	Stochastic moment per unit length
$\mathbf{m}_{visc}, \mathbf{m}_{visc}$	Viscous moment per unit length
$\mathbf{m}_{ext}, \mathbf{m}_{ext}$	Deterministic external moment per unit length
$\mathbf{m}_\Gamma, \mathbf{m}_\Gamma$	Boundary moment

### Finite Rotations in $\mathbb{R}^3$

$SO(3)$	Special orthogonal group in three dimensions
$\boldsymbol{\theta}$	Rotational pseudo-vector
$\boldsymbol{\psi}_l$	Local rotational pseudo-vector
$\boldsymbol{\Lambda}(\boldsymbol{\theta})$	Rotation matrix
$\boldsymbol{\vartheta}$	Spin variable
$\Delta\boldsymbol{\theta}$	Additive rotation increment
$\Delta\boldsymbol{\vartheta}$	Multiplicative rotation increment
$\mathbf{T}(\boldsymbol{\theta})$	Transfer matrix

### Friction model and diffusion

$\gamma_\perp, \gamma_\parallel, \gamma_a$	Damping coefficients per unit length
$\zeta_\perp, \zeta_\parallel, \zeta_a$	Damping coefficients with respect to a rod of length $L$
$\eta$	Dynamic viscosity of the fluid phase
$\mathcal{D}$	Diffusion coefficient
$k_B$	Boltzmann constant
$T$	Absolute temperature
$\mathbf{D}_t, \mathbf{D}_r$	Damping matrices of translational and rotational motion
$\mathbf{S}_t, \mathbf{S}_r$	Decomposed damping matrices of translation and rotation
$\mathbf{v}$	Translational background fluid velocity field
$\mathbf{w}$	Rotational background fluid velocity field
$\dot{\mathbf{x}}_{rel}, \dot{\boldsymbol{\theta}}_{rel}$	Relative velocities between fluid and rod

### Chemical interaction between filaments and linkers

$N_A$	Avogadro constant
$[\cdot]$	Molar concentration
$c_f, c_l$	Molar concentration of filaments and linkers
$c_{l,c}$	Crosslink concentration
$R$	Molar ratio
F, L	Chemical species (filaments and linkers)
$\mathbf{x}_A, \mathbf{x}_B$	Binding site locations on filaments
$\mathbf{x}_l$	Location of the linker centroid
$\Delta_l$	Distance between binding site and linker centroid
$R_l$	Radius of the reaction volume of the linker
$\Delta R_l$	Tolerance of the reaction volume
$V_{\text{react}}$	Reaction volume of the binding sites
$\mathbf{v}_{\Delta b}$	Orientation of a binding site in a helical binding site topology
$\varphi_b$	Opening angle of a conoidal reaction volume of a helical topology
$\phi$	Preferred binding angle of a linker
$\Delta\phi$	Binding angle tolerance
$k_+$	Experimentally measured chemical association rate constant
$k_{\text{on}}$	Simulated chemical association rate constant
$k_-$	Experimentally measured chemical dissociation rate constant
$k_{\text{off}}$	Simulated chemical dissociation rate constant
$k_{\text{bell}}$	Chemical dissociation rate constant according to Bell's model
$k_{\text{eff}}$	Effective, reduced association rate constant under shear
$p_{\text{on}}$	Probability of bond establishment
$p_{\text{off}}$	Probability of bond rupture
$p_{\text{bell}}$	Probability of bond rupture according to Bell's model
$p_{\text{eff}}$	Effective, reduced probability of bond establishment under shear
$G$	Free energy
$\Delta G$	Binding energy
$\Delta x$	Bell parameter

### Extended models, beam tying, and rotation interpolation

$\alpha$	Rotation per monomer
$d_g$	Translational rise per monomer along the helical filament
$d_b$	Distance between two modeled binding sites
$D$	Periodic repeat

$\theta_{\Delta b}$	Binding site rotation angle
$\Lambda_b$	Rotation triad associated with a binding site
$\mathbf{u}_b, \mathbf{v}_b, \mathbf{w}_b$	Principal axes of $\Lambda_b$
$\mathbf{r}_{\mathcal{E}}^{[k]}$	$k^{\text{th}}$ <i>real</i> node of element $\mathcal{E}$
$\mathbf{v}^{[k]}$	$k^{\text{th}}$ <i>virtual</i> node
$\Lambda_{R\mathcal{E}}$	Reference triad of elements $\mathcal{E} = \{A, B\}$
$\tilde{\xi}, \tilde{s}$	Interpolated tying positions along beam elements
$\mathbf{x}_{\mathcal{E}}^{[k]}$	Position of the $k^{\text{th}}$ nodes of elements $\mathcal{E}$
$\mathbf{x}_{\mathcal{E}}(\tilde{\xi}_{\mathcal{E}})$	Interpolated tying positions on elements $\mathcal{E}$
$\Lambda_{vA}, \Lambda_{vB}$	Triads of the <i>virtual</i> nodes of element $C$
$\Lambda_{\mathcal{E}}^{[k]}$	Triad of the $k^{\text{th}}$ node of elements $\mathcal{E}$
$\Lambda_{\mathcal{E}}(\tilde{\xi}_{\mathcal{E}})$	Interpolated tying positions on elements $\mathcal{E}$
$\mathbf{x}_{vA}, \mathbf{x}_{vB}$	Positions of the <i>virtual</i> nodes of element $C$
$\mathbf{H}_t, \mathbf{H}_r$	Translational and rotational constraints
$\tilde{\mathbf{I}}_t, \tilde{\mathbf{I}}_r$	Tying matrices
$\lambda$	Discrete nodal Lagrange multipliers
$N_d$	Number of dimensions of a problem
$N_c$	Number of constrained dimensions

### Molecular motors

A, M, ATP, ADP, P	Chemical species: Actin, Myosin, ATP, ADP, Phosphate
l, s	chemical states of the motor: <i>long</i> , <i>short</i>
$\delta_w$	Working distance of the motor
$\delta_p$	Path distance of the motor
$\delta_{\text{ATP}}$	Distance per ATP
$\delta_+$	Power stroke distance of the motor
$\delta_-$	Drag stroke distance of the motor
$\tau_c$	Duration of the enzymatic cycle
$\tau_{\text{on}}$	Duration of motor attachment to filament
$\tau_{\text{off}}$	Duration that motor is detached from filament
$r$	Duty ratio of the motor
$\mathbf{F}_l, F_l$	Vector and magnitude of the force exerted by the motor
$p_{ls}, p_{sl}$	Probabilities for chemical transitions
$k_{ls}, k_{sl}$	Reaction rate constant for chemical transitions
$\mathbf{x}_b$	Filament binding site position
$\mathbf{t}_b$	Binding site tangent
$\mathbf{x}_m$	Motor position

$L_m$	Motor size
$\Delta L_m$	Motor size tolerance
$\mathbf{d}_{mb}, \mathbf{d}_{mb}$	Distance vector and distance between motor and binding site
$\mathbf{d}_{mb,\perp}, \mathbf{d}_{mb,\parallel}$	Orthogonal and parallel projection of $\mathbf{d}_{mb}$
$\mu$	Polarity measure
$\lambda$	Longitudinal contraction factor
$[\varphi_\delta^-; \varphi_\delta^+]$	Binding angle interval
$\varphi_{mb}$	Rotation angle of a motor
$\boldsymbol{\theta}_{ls}$	Power stroke rotation pseudo vector
$\Delta \boldsymbol{\theta}_{ls}$	Rotation pseudo vector increment of the power stroke
$\boldsymbol{\Lambda}_{ls}$	Difference rotation of the power stroke motion
$\boldsymbol{\Lambda}_{m,l}, \boldsymbol{\Lambda}_{m,s}$	Triad of the motor in the chemical states $l$ and $s$
$\boldsymbol{\Lambda}_{b,l}, \boldsymbol{\Lambda}_{b,s}$	Triad of the binding site in the chemical states $l$ and $s$
$\rho_f$	Filament surface density in a motility assay
$\rho_m$	Motor surface density in a motility assay
$\rho_f^*$	Filament threshold density
$\rho_m^*$	Motor threshold surface density
$v_f$	Absolute filament transport velocity

### Semi-flexible filaments and networks

$L_p$	Thermal persistence length
$L_{e2e}$	End-to-end distance
$\xi$	Network mesh size
$\rho$	Filament length density

### Structural analysis of networks

$\varphi, \psi$	Azimuth and polar angle of filaments
$\rho(\varphi), \rho(\psi)$	Distributions of azimuth and polar angles of filaments
$O$	Orientation correlation function
$S$	Nematic order parameter
$E_{int}$	Network strain energy
$C_i(d)$	Two-point density-density correlation function for coordinate $i$
$I_i(q_i)$	Structure function for coordinate $i$
$n_l$	Ratio of crosslink number and the number of available binding sites

### Linear rheology of bundle networks

$\bar{R}$	Simulated molar ratio
$G^*(\omega)$	Complex modulus
$\alpha(\omega)$	Compliance function
$\gamma(t)$	Time-dependent shear displacement pattern
$\hat{\gamma}$	Shear amplitude
$G'(\omega)$	Storage modulus
$G''(\omega)$	Loss modulus
$\bar{G}$	Plateau modulus
$G_0$	Modulus scale
$\omega_1$	Cross-over frequency
$\mathcal{N}$	Number of filaments in a bundle
$\mathcal{D}$	Bundle diameter
$q_n$	$n^{\text{th}}$ transverse mode
$\kappa_n$	Bending stiffness of the $n^{\text{th}}$ transverse mode of a bundle
$\bar{\omega}(n)$	mode-dependent relaxation rate
$b$	Bundle diameter
$k_{\times}$	Spring constant of the linker
$\Delta$	Bundling parameter
$\phi(t)$	Orientation of one principal axis of the inertia tensor
$\phi(\omega)$	Spectrum of the orientations of one of the inertia tensor's axes
$S(\omega)$	Spectrum of stress fluctuations

### Nonlinear viscoelasticity of bundle networks

$K$	Differential modulus
$K_{lin}$	Linear modulus
$\gamma_m$	Strain at the peak value of $K$
$\gamma_c$	Critical strain, the onset of the nonlinear deformation regime
$\dot{\gamma}$	shear rate

### Discretization, Numerics & Simulation

$\mathbf{W}_t$	Translational weighting functions
$\mathbf{W}_r$	Rotational weighting functions
$\mathbf{l}_t$	Interpolation function of translational DOFs

$\mathbf{l}_r$	Nodal interpolation function of rotational DOFs
$\xi$	Local FE line parameter
$s$	Global FE line parameter
$\mathbf{X}$	Positions of nodes
$\Theta$	Rotations of nodes
$\mathbf{u}$	Translational nodal displacements
$\theta$	Nodal rotational pseudo vector
$\vartheta$	Nodal multiplicative spin variable
$\mathbf{d}$	Nodal displacement vector
$\mathcal{K}$	Stiffness matrix
$\mathcal{D}$	Damping matrix
$\mathcal{S}$	Stochastic contribution to $\mathbf{K}$
$\mathbf{K}$	Tangential stiffness matrix
$\mathbf{r}$	residual force vector
$\Lambda$	Nodal triad
$h$	Discretization length in space
$L$	Discretized curve length
$L_e$	Finite element length
$\Delta t$	Discrete time step size
$T_{\text{sim}}$	Simulated time
$i$	Time step index
$l$	Maximal time step
$j$	Index of Newton iteration
$J$	Maximal number of Newton iterations
$k$	Nodal index
$K$	Maximal nodal number
$N_e$	Number of elements per filament
$w_{\text{IP}}$	Weight of quadrature point
$p$	Polynomial order of the interpolation function
$N_f, N_l, N_m$	Number of discretized filaments, linkers, and motors
$L_f, 2R_l, L_m$	Filament length, linker size, and motor size
$E_f, E_l, E_m$	Young's moduli
$A_f, A_l, A_m$	Cross sections
$H$	Edge length of the simulation box
$\mathcal{Z}(\mu, \sigma)$	Vector of Gaussian random numbers with mean $\mu$ and variance $\sigma$

**Abbreviations**

ABP	Actin binding protein
ADP	Adenosine diphosphate
ATP	Adenosine triphosphate
BD	Brownian dynamics
BD/FE	Brownian dynamics finite element
BFE	Beam finite element
COBB	Cylindrical, oriented bounding box
DNA	Deoxyribonucleic acid
DDCF	Density-density correlation function
F-actin	Filamentous actin
FDT	Fluctuation-dissipation theorem
FE	Finite element
FEM	Finite element method
G-actin	Globular actin
GMRES	Generalized minimal residual
HMM	Heavy meromyosin
ILU	Incomplete lower upper triangular matrix
IP	Integration point
KKT	Karush-Kuhn-Tucker
LMM	Light meromyosin
MD	Molecular dynamics
MD	Microtubule organizing center
OCF	Orientation correlation function
PTC	Pseudo-transient continuation
RNA	Ribonucleic acid
SPDE	Stochastic partial differential equation



# 1 Introduction

Biological cells are the base unit of life. All life on earth is composed of at least one cell. A first distinction has to be made between procaryotes and eukaryotes. Procaryotes are organisms that do *not* have a nucleus and are single-celled, whereas eukaryotes *do* have a nucleus and can be multi-celled. The latter type of organism is going to be in the spotlight. Complex eukaryotic organisms consist of a myriad of cells, that take on different shapes and carry out diverse tasks in order to maintain the organism's vital functions. Although cellular morphologies and functionalities differ, their organizational blueprint is generic as recurring structures can be found in all cells. One of the most important intracellular structures is the cytoskeleton, a complex biopolymer network consisting of different species of protein filaments. This network provides for a multitude of crucial cellular functions and, as a consequence, has received considerable scientific appreciation over the past decades. The cytoskeleton enables cells to crawl and to establish adhesive connections to the extracellular matrix. It orchestrates the process of cell division and determines the temporal and spatial organization of the organelles within the cell. Apart from a variety of metabolic activities, the cytoskeleton also serves as the cell's sensory organ. If the cytoskeleton is struck by disease, the organism is likely to perish. Beyond doubt, the cytoskeleton is essential to eukaryotic life in all aspects and is therefore worth every painful inch of scientific progress. Despite having been studied intensely by researchers from different disciplinary backgrounds, the cytoskeleton still remains only partially understood and attracts the scientific attention of biologists, biochemists, biophysicists, and biologically or biomedically oriented engineers.

The motivations for the scientific investigation of the cytoskeleton are as diverse as the involved scientific disciplines. In fact, it is close to impossible to draw clear lines that distinguish purely mono-disciplinary interests as the cytoskeleton represents a scientific playground, on which the efforts of the various disciplines are as convoluted and intertwined as the cytoskeleton's filaments. Research on the cytoskeleton can be loosely assigned to one of three kinds: the first kind is *observational*, the second seeks for *causal connections*, and the third *applies* existing knowledge.

The first kind examines the cytoskeleton to unveil previously unknown constituents or processes. The research questions revolve around first observations of a certain biological component, a chemical species, a process or a part of a process within the cytoskeleton. Prominent examples are the experimental confirmation of the lipid double-layer of the cell membrane (cf. [44]), the discovery of the myosin cross-bridge [96], or the direct observation of the myosin recovery stroke, a subprocess of the enzymatic cycle of myosin [198]. The main finding *is* the observation, i.e., the discovery.

The second kind of research often succeeds the first (not always since theoretical predictions sometimes predate the observation). If a scientific discovery is made, modeling, theory, and analysis ensue, all of which aim to *explain* this discovery and to point out the underlying causal connections. Prototypical works of this kind are, e.g., models of stress fiber formation [223]

or the well-established rheological model for entangled actin solutions [59]. Here, simulations *without* an engineering background and often limited numerical performance (e.g. [114]) are readily applied to support modeling.

Finally, the third kind makes use of the knowledge gathered by fundamental research in order to create applications, e.g., in biomedical technology or the design of bio-inspired materials. Cell culture technology and tissue engineering are further popular practical fields of application. In this context, computational methods often provide predictive numerical models for single cells or agglomerates of cells (e.g., [182]). On larger length scales, entire tissues and organs are modeled using continuum descriptions with fitted material laws [84].

These three levels of research may be loosely attributed to disciplines. While first observations concerning the cytoskeleton are commonly made by biologists or biochemists, the in-depth analysis in search for causal relations mostly falls to either biologists, biochemists, or physicists depending on the problem. To a large extent, applications can be attributed to the engineering sciences.

This work aims to provide an *engineering solution* to the simulation of transient biopolymer networks, which is *not* restricted to applications in the engineering context. It enables the study of networks on length scales and time scales that no other comparable computational approach is able to access to date. This capability permits the support or even the initiation of fundamental research in biophysics as will be demonstrated in the chapters on the self-assembly and the rheology of semiflexible biopolymer networks.

## 1.1 From cell to simulation

Science's fundamental interest in the eukaryotic cell and its cytoskeleton has been pointed out and is readily understandable. However, having the entire cell in mind, a considerable mental leap is required to appreciate the scientific benefit of an abstracted computational model. Therefore, the following introduction will offer guidance by gradually motivating the most important steps leading from the initial *in vivo* to the *in vitro* and eventually to the *in silico* problem. To this end, the eukaryotic cell and its architecture are introduced in the beginning in order to convey a basic idea of the cytoskeleton's location and its purpose in the cellular context (Section 1.1.1). Subsequently, the cytoskeleton is discussed in more detail, emphasizing its three main components, their structure, and their main functions (Section 1.1.2). The scope of this thesis is then limited further to the part of the cytoskeleton, which consists of the protein *actin*, and the study of reduced actin model systems (Section 1.1.3). At this point, one arrives at the level of abstraction of the proposed computational framework, which models the components of this reduced model. After a few general words on the motivation behind scientific simulations, the introduction is concluded by a brief description of the structure of this thesis (Section 1.4).

### 1.1.1 The eukaryotic cell

Eukaryotic cells in multi-celled organisms are often highly differentiated. They develop into different shapes and carry out different specialized tasks within the organism. They synthesize and degrade bones (osteoblasts and osteoclasts), enable macroscopic motion (myocytes), or provide sensory abilities (e.g. retinal cells, hair cells). Despite their great morphological and

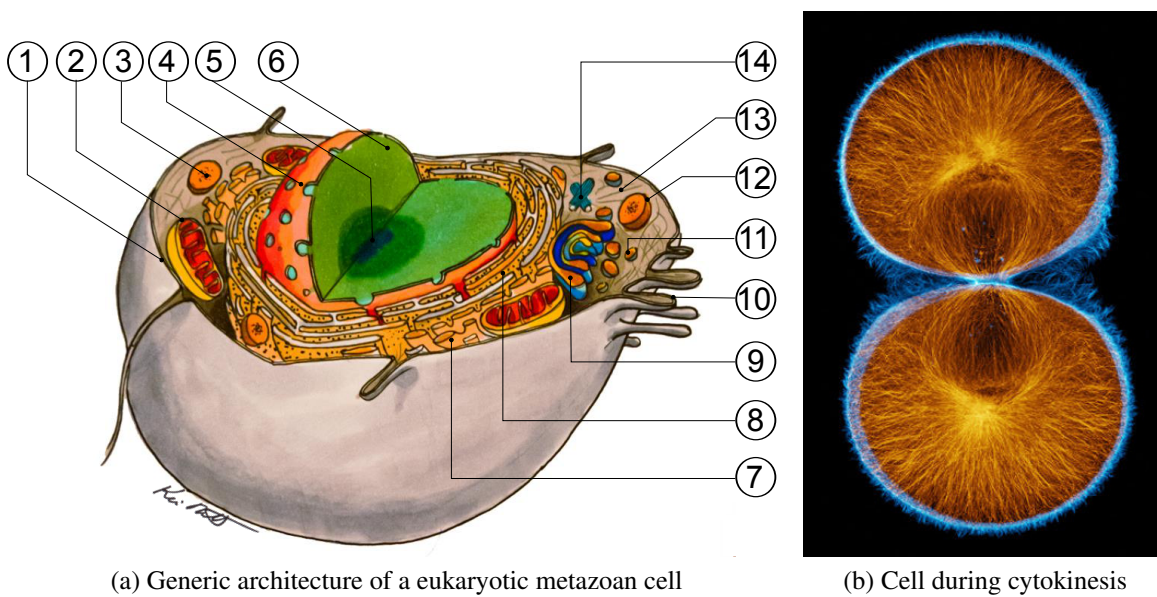


**Figure 1.1** (a) Sketch of the spatial organization of organelles within an animal cell. The individual numbers indicate (1) plasma membran, (2) mitochondrion, (3) lysosome, (4) nuclear envelope, (5) nucleolus, (6) nucleus (filled with chromatin), (7) smooth endoplasmatic reticulum, (8) rough endoplasmatic reticulum, (9) Golgi apparatus, (10) microvilli, (11) vesicles, (12) peroxysomes, (13) cytoskeletal filaments, (14) centrosome. (b) A sea urchin zygote during cell division. Actin filaments (blue) and microtubules (orange) of the cytoskeleton are shown. The image in Figure 1.1b has been provided by G. von Dassow [3].

functional variety, the cellular architecture can be generalized (with very few exceptions). Such a generalized cell is shown in Figure 1.1a, which makes clear that the cell is a crowded place. The cellular components shown in this figure as well as their primary functions will be briefly introduced. In case that more detailed information is required, the reader is referred to comprehensive textbooks [4, 145]. The majority of the following information on cellular constituents is drawn from [4] if not indicated otherwise.

The central component of the cell is its *nucleus*, keeper of the organism's entire set of genetic information in the form of *deoxyribonucleic acids* (DNAs). The *nucleolus* resides within the nucleus. It is tasked with ribosome production and the transcription of *ribonucleic acids* (RNAs). The interior of the nucleus is separated from the intracellular environment by a lipid bilayer, the *nuclear envelope*. This barrier is temporarily lifted during cell division. In most cases, cells have *one* nucleus with the exception of a few multinucleate cells, e.g., in muscle, as well as cells without a nucleus such as *red blood cells*. Leaving the nucleus towards the periphery of the cell, one enters the *cytoplasm*. The cytoplasm consists of the *cytosol* and the cell's *organelles*. The cytosol accounts for about 70% of the cell's volume and consists of water, proteins, and ions. Proteins suspended in the cytosol account for approximately 20 - 30% of the cytosol's total weight. Among these proteins, the proteins that constitute the cytoskeleton can be found.

The organelles of a cell perform specialized tasks in order to maintain the cell's global operativeness. They are suspended in the cytosol and can be displaced by the cytoskeleton if required. The most important organelles will be briefly introduced. *Mitochondria* are the *power plants* of the cell. Here, the bulk of *adenosine triphosphate* (ATP) is produced, the main storage for chemical energy. Mitochondria carry their own set of DNA and self-replicate like procaryotes.

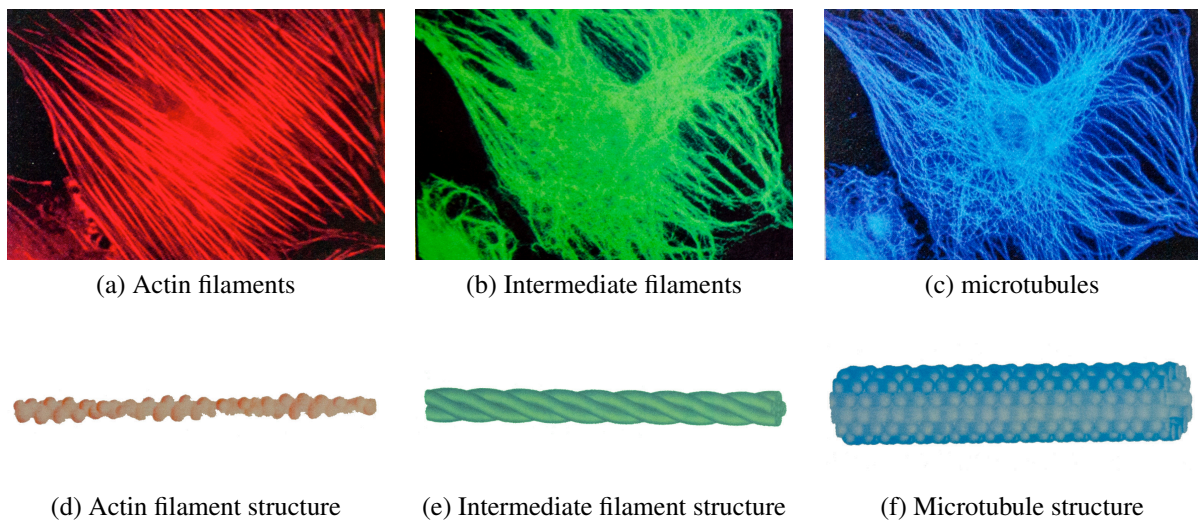


**Figure 1.2** The three main filament species of the eukaryotic cytoskeleton. *Top row:* (a) Actin filaments in bundles, (b) intermediate filaments, and (c) microtubules of one and the same cell. The coloration stems from fluorescent dye. *Bottom row:* Cartoons of the structures of (d) an actin filament, (e) an intermediate filament, and (f) a microtubule. All images are taken and modified from Lodish et al. [145].

The ATP produced by the mitochondria is metabolized, for example, during protein synthesis, noticeable fraction of which takes place in the *endoplasmic reticulum* (ER), the largest single organelle. The ER consists of flattened, lobe- or sac-like compartments delimited by membranes. Beside proteins, which are built in the *rough* ER, lipids and fatty acids are synthesized by the *smooth* ER. Proteins leave the ER by means of vesicles budding from the ER membrane. The vesicles approach the *Golgi apparatus*, another membrane-bounded organelle, at one of its two ends. Inside the Golgi apparatus, the proteins are modified, wrapped into vesicles again at the other end, and sent to their destinations either within or outside of the cell.

Cells do not only synthesize macromolecules, they also need to digest and degrade components that are not required anymore. In animal cells, this task is carried out by *lysosomes*, which contain a large set of degradative enzymes. *Peroxisomes* degrades toxic peroxides. Both lysosomes and peroxisomes contain enzymes that would have a destructive effect on the cell if they were to be released. In plant cells, a similar functionality is believed to be provided by the *vacuole*.

With all principal organelles of the cytoplasm introduced, the focus is once again shifted back to the cytosol as it contains the cytoskeleton, which is in the focus of this thesis. The cytoskeleton shall be introduced separately and in more detail in the following section.

### 1.1.2 The cytoskeleton and its filaments

The eukaryotic cytoskeleton is a complex network of filamentous proteins, which provides with a large variety of cellular functions. Its structure is highly dynamic as filaments are constantly polymerized and depolymerized again. The cytosol serves as a reservoir of the subunits which constitute the filaments. Three filament species constitute the cytoskeleton: *actin filaments*, *intermediate filaments*, and *microtubules*. All three filament types constitute network structures (see Figure 1.2). The subsequent compact introduction of the three species of cytoskeletal fila-

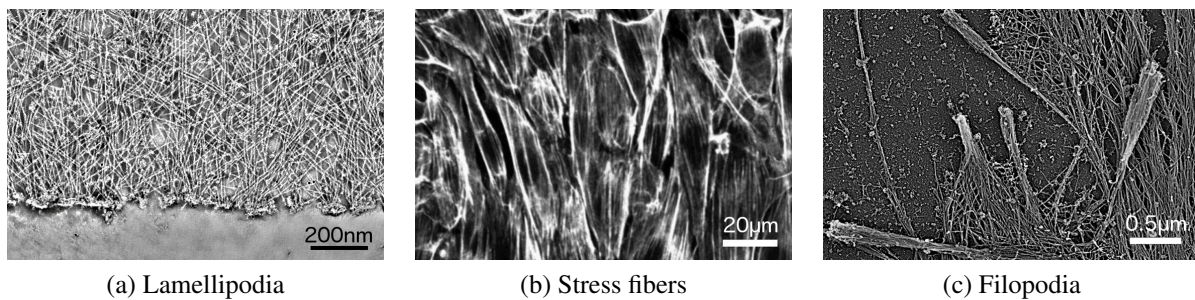


**Figure 1.3** Three F-Actin network structures which are often encountered in cells. (a) Lamellipodia (image kindly provided by M. Vinzenz and J. V. Small [1]), (b) actin stress fibers [92], and (c) filopodia emerging from lamellipodia meshwork [229].

ments comprises a description of their molecular structure, their main functions, and the network structures they establish.

**Actin filaments** Actin filaments (F-actin) are the most abundant among the cytoskeletal filaments and can be found throughout the cell but predominantly in the actin cortex close to the plasma membrane, where filament growth is initiated. F-actin belongs to the group of semiflexible polymers, which means that their length is close to their *persistence length*. The persistence length is the length, beyond which the thermally excited filament curves noticeably [88] (more details follow in Chapter 2; see also [107, Figure 1]). The persistence length of F-actin is 10 - 18  $\mu\text{m}$ . F-actin aggregates take on different morphologies depending on the *actin binding protein* (ABP), which crosslinks the filaments among each other. For example, Figure 1.2a depicts aligned actin bundles in a fibroblast cell.

As shown in Figure 1.2d, an actin filament consists of *globular monomer subunits*, which are referred to as *G-actin*. The filament is a *single-stranded, levorotary helix* (also termed *one-start, left-handed helix* [88]) with 26 monomer subunits per period and a periodic repeat of 72 nm. The rise per actin monomer along the helical path is 2.77 nm. The helix makes twelve full turns before returning to its initial orientation, which means that the rotation per monomer is  $166^\circ$ . The size of G-actin is given as 5.5 nm [88]. F-actin has a diameter of five to nine nanometers. The polymerization of F-actin from G-actin subunits does not occur spontaneously but requires regulatory complexes. The length of a single actin filament is in the range of  $10^1 \mu\text{m}$  and is regulated by certain growth factors. F-actin is a structurally polar filament since its G-actin subunits are polar and equally oriented. As a consequence, F-actin has two dissimilar ends, a (+)-end and a (-)-end. F-actin determines the shape of the cell and acts as a tensile fiber in bundles and networks. In *lamellipodia*, which are the locomotive units of cells and enables them to crawl, F-actin is found in a dense, crosslinked meshwork (Figure 1.3a). This mesh pushes the plasma membrane in the direction of motion and by doing so constantly reshapes the cell.

In the stress fibers depicted in Figure 1.3b, F-actin is localized in densely packed bundles that allow for the transduction of forces. Stress fibers often emerge in conjunction with *filopodia* protruding from the lamellipodia (Figure 1.3c). Filopodia have sensory functions but also create focal adhesion points and support wound healing [154]. Simple unicellular organisms such as amoeba do not have filopodia but create *pseudopodia*, which contain actin gel, i.e., entangled or only sparsely crosslinked actin networks, which also serve the purpose of migration. Aside

from these transient states, F-actin also constitutes permanent structures as in the case of the stereocilia of the inner ear, which enable hearing.

F-actin can be employed to exert forces not only in muscle but also within other cells. The incorporation of myosin-based motors into filament aggregates allows for the constitution of actively contracting structures such as apolar bundles [205]. An alternative way of generating movement is by *treadmilling*, which propels F-actin through the cytosol and which originates from differing polymerization rates at the ends of the filament [88]. Polymerization at the (+)-end is five to ten times faster than at the (−)-end [24]. In summary, actin is not only an integral part of macroscopic muscle but can also be considered the *muscle* of the cell.

**Intermediate filaments** Intermediate filaments are rope-like fibers with a diameter of ten nanometers and are structurally more diverse than actin or microtubules. They are only expressed in certain animals (including humans). They establish fiber networks that span the entire cell as Figure 1.2b shows. Their subunits are different polypeptides of the keratin family, different lamins, and others [88], which constitute hair and nails but are also found in neurons. These subunits form coiled-coil structures, that align and intertwine to establish tetrameric structures, which in turn accumulate with other tetramers to establish filamentous structures. The principal structure is given in Figure 1.2e. Intermediate filaments are globally *apolar* because of the axisymmetric arrangement of their subunits. The persistence length of intermediate filaments is approximately 0.5  $\mu\text{m}$ , which makes this filament species about 30 times more flexible than F-actin and about  $10^4$  times more flexible than microtubules. The axial stiffness of an intermediate filament is very high compared to its bending stiffness. Networks of crosslinked intermediate filaments deform easily but fail only under high mechanical loads, making intermediate filaments the *tendons* of the cell.

In order to fulfill their primary function as mechanical stabilizers, intermediate filaments can establish bonds to the membrane, to microtubules, as well as to actin filaments. Intermediate filament networks are highly dynamic with their filaments polymerizing and depolymerizing within minutes. The chemical mechanisms behind the build up and the decomposition of intermediate filaments are only vaguely understood.

**Microtubules** The third filament species of the cytoskeleton is the so-called microtubule. Microtubules are hollow cylindrical filaments with a diameter of about 25 nm, which are made of helically arranged tubulin dimers. The polymerization of a microtubule filament from dimers is driven by a polymerization agent called  $\gamma$ -tubulin. Microtubules are the stiffest among the cytoskeletal filaments. Their persistence length is 5 mm, and if tubulin subunits were homogeneous and isotropic, the hypothetical Young's modulus would be 1.2 GPa, which is close to plexiglas [60]. As the average length of a microtubule in vivo is 25  $\mu\text{m}$ , it can be seen as a straight, rigid, and hollow rod. The structure of microtubules is *polar* and they therefore have two distinct ends called (+)-end and (−)-end. Polymerization and depolymerization at the (+)-end are faster than at the (−)-end. Microtubules of animal cells emerge from a *microtubule organizing center* (MTOC), the *centrosome*. From this location, the microtubules spread out radially with their (+)-ends pointing away from the centrosome.

Microtubules carry out important transport-related tasks within the cell. During mitosis, microtubules constitute the mitotic spindle, which separates pairs of chromosomes. Furthermore,

motor proteins of the kinesin and the dynein family use microtubules as tracks, along which these motors transport vesicles. Finally, cilia and flagella consist of microtubule arrangements and serve the purpose of cell locomotion. They either propel the cell itself as in the case of flagellates or transport particles as in the human trachea, where they remove dirt and mucus.

Due to its high stiffness and brittleness, the microtubule can be considered the microscopic analog to *bone*.

### 1.1.3 Reduced model systems

Sections 1.1.1 and 1.1.2 convey only a faint idea of the actual complexity of a cell and its cytoskeleton but they make clear that intracellular space is a highly multicausal environment. Any observation made in this environment surely is the product of a multitude of correlated influences. Drawing unambiguous conclusions is difficult. A reduction of the system complexity presents a remedy to this problem, be it in experiments or in simulations.

The complexity of the cytoskeleton can be reduced, e.g., by limiting the model system to one filament species. In this thesis, the *one* filament is the semiflexible F-actin (i.e., its in silico representation). Having only F-actin in principle already enables research on entangled solutions. If the formation of networks or the mechanics of certain network morphologies are examined, in most cases, a *single species* of crosslinking protein is added, which will be generally referred to as *linker* from here on. Experimental F-actin model systems have led to a better understanding of the mechanics of entangled actin filaments (e.g., [58, 118]) and the various shapes and mechanics of crosslinked actin networks (cf. [135]). If, in addition, the examined network exhibits motor activity, specialized but straight-forward to interpret model systems, e.g., motility assays (e.g., [183, 189]) or single-filament/motor set-ups (cf. [88]), are used. In few cases, more than one motor protein is employed to elucidate cooperative effects (e.g., [199]).

Theoretical work on actin networks by nature relies on abstraction and reduction of complexity, be it for single filaments (e.g., [59, 160]), crosslinked networks (e.g., [14]), or active networks (e.g., [105, 132]).

This thesis focuses on simulated networks of semiflexible biopolymers, that have properties very similar to in vitro actin networks. Simulations and experiments have the same two fundamental components, filaments and linkers, which are suspended in a viscous fluid. The simulation does not only model a reduced system, it relies on a reduction of model complexity itself: a Brownian dynamics approach in conjunction with a continuum description of the network constituents. Like experimental networks, the computational approach profits by design from the same advantage: reduced causal complexity, which facilitates the interpretation of an observation.

In the following section, the general suitability of this computational approach and its potential in view of advancing the understanding of biopolymer networks will be discussed.

## 1.2 Simulations on biologically relevant time scales

Traditionally, the scientific process begins with the observation of nature, from which the observer deduces a model that is able to reproduce certain aspects of the observed. Modern physics

has inverted this causality in some cases but the majority of scientific research still works according to this principle.

A deliberate observation aiming to test a hypothesis is called an experiment. If a hypothesis is corroborated by the outcome of an experiment, it can give rise to a model and be condensed into a theory. This direct transition from an observation to a model represents the ideal case. Oftentimes, however, this causal chain is interrupted for one of two reasons, the first being a lack of data, the second being the inability to *directly* translate an observation into a model. In both scenarios, computer simulations provide technological extensions that lead to additional insight into experiments or support and sometimes even enable theoretical modeling. Simulations create repeatable *artificial observations*, which allow for data acquisition and the prediction of the behavior of the observed system.

Of course, a simulation is based upon a model as well. As such, it relies on assumptions made at its axiomatic level. Below this threshold, everything is a product of these assumptions. Above it, only a certain part is. If this part is known, quantifiable, and controllable, a simulation can be scientifically useful. In a nutshell, the simulation's base scale needs to be smaller than the characteristic scale on which the observation is made with respect to both time and space. Chapter 2 will detail this argument with respect to its practical application to the simulation of biopolymer networks.

Having mentioned scales, it is worthwhile touching the topic of the regularly mentioned, but seldom sharply defined *biologically relevant time scales*. The term suggests general validity but in fact depends strongly on the characteristic time scale of the observation. In molecular dynamics (MD) simulations of pharmaceutically relevant molecules, for example, the term *biologically relevant* refers to times longer than a microsecond [236]. A microsecond is more than seven orders of magnitude too short if one is interested in biopolymer network assembly and mechanics. Characteristic biological processes on this length scale are, e.g., the formation of actin stress fibers and filopodia during cell migration or the polymerization of microtubules during cell division. The time intervals, on which these processes take place, depend on the cell type but usually span tens of minutes up to a few hours. Some examples are given to provide bounds for what is considered biologically relevant in this thesis: filopodia form and reform within minutes, mitosis in mammalian cells takes approximately an hour, and cell migration takes place on the scale of hundreds of minutes [4]. MD simulations on time and length scales such as these are technologically infeasible. There exist various computational approaches modeling single filaments (cf. [31]). The overwhelming majority is numerically inefficient and a rigorous quantification of the numerical error is often impossible such that their application in long-term simulations is limited. Brownian dynamics finite element (BD/FE) simulations, however, perform exceptionally well as will be shown in the upcoming chapters.

Biologically relevant *length scales* in the context of semiflexible biopolymer networks are less difficult to grasp. Since one is interested in phenomena that occur on the scale of network structures, one should in principle be able to cover system sizes on the subcellular level, i.e., of the order  $10^{-1}$  -  $10^1$   $\mu\text{m}$ . The upper bound approaches the size of small cells like the human red blood cell, which measures approximately 10  $\mu\text{m}$  in the direction of its largest expansion.

## 1.3 Objectives and achievements

Two major research objectives can be formulated for this thesis: the development of methods unmatched in terms of computational performance and their application to biophysical problems that previously have been out of scientific reach.

**Development of methods** The thesis aspires to develop methods that enable the simulation of large biopolymer networks on previously unfeasible time and length scales. To this end, the already highly efficient single-filament model of [33, 38] will be employed to simulate crosslinked network structures at filament and linker concentration close to physiological values. By an efficient parallelization of the simulation framework, filament concentrations up to an experimental equivalent of  $8\ \mu\text{M}$  can be simulated over time intervals spanning several thousands of seconds, thereby enabling the study of phenomena on aforementioned biologically relevant time scales. To the author's knowledge, no other comparable simulation approach is even remotely capable of reaching the level of computational efficiency displayed here.

In order to boost the method's computational performance even further without losing numerical accuracy, extended models of filaments and linkers will be introduced. The advantages of the new models are manifold. The extended filament model provides linker binding sites along its entire geometry instead of only at its nodes, which remedies the modeling predicament of coinciding mechanical and chemical resolution. Furthermore, by taking advantage of the underlying mechanical description, it is possible to mimic the molecular topology of the filament without a refinement of the discretization. Helical geometries such as in the case of F-actin or more complex geometries as in the case of microtubules are easily parameterized by the new model. The complementary linker model requires the capability of binding to these arbitrary positions along the filament. This is achieved by a novel beam tying method, which connects positions and orientations of binding sites and linker beam elements. Binding site spacings down to the level of single monomers can be realized, which has been virtually impossible up to this point. The use of this enhanced approach enables the simulation of systems as large as  $10\ \mu\text{m}$  in each spatial dimension at high filament and linker concentrations. The size of the simulated domain in fact approaches cellular dimensions.

Being able to resolve such small chemical length scales without suffering from a significant loss of performance, the next logical step is the introduction of motor activity. Molecular motors accomplish astounding feats in cells and the scientific urge is great to understand how these small enzymes cooperatively give rise to large-scale motion. Therefore, a model of a molecular motor is developed, which adequately reproduces the enzymatic activity of the non-processive motor myosin II. The approach is developed and validated to the point of application in large-scale network simulations.

**Biophysical applications** A creation without an application is called *art* on rare occasions, and *useless* in most other cases. Therefore, the major part of the available methods is applied to explore the self-assembly processes of semiflexible filament networks and their mechanical properties.

The linker-mediated evolution of biopolymer networks into different morphologies represents a computationally challenging problem, which is why it has not been attempted so far. In this thesis, vast studies on emerging network morphologies and the phase transitions between them

will be presented. Network evolution has been studied on time scales up to 10000 s in a few cases. Thus, it is a showcase of the capabilities of the BD/FE approach on the one hand and allows for scientific insights on the other hand as previously unknown mechanisms driving the aggregation of networks have been determined.

Knowing the possible paths of network evolution allows for the mechanical testing of in principle any of the found network architectures. The perhaps most interesting among these networks is a homogeneous network of bundles, a generic structure found not only in cells but also elsewhere in nature. Numerical experiments probing the linear rheology of bundle networks are the centerpiece of this last part of the thesis. Rheological simulations reach shear frequencies as low as 0.003 Hz, which corresponds to time scales close to three orders of magnitude larger than what has been previously reported [114, 116]. By sweeping a broad frequency band  $[0.003; 10^5]$  Hz, a comprehensive novel understanding of the rheology of bundle networks is provided. For very low and very high frequencies, universal rheological properties are found and explained theoretically.

### 1.4 Organization of the thesis

On its most abstract level, the thesis can be understood as the complementary effort of two major parts. The first part of this thesis is of methodic nature and introduces the reader to the fundamental techniques of the finite-element-based simulation of subcellular filamentous microstructures as well as networks, which are composed of these microstructures. The second part revolves around the application of the first part's achievements in order to advance the physical understanding of network mechanics, the process of network self-assembly, and the rheology of this biologically most relevant material. The first part comprises Chapters 2 to 4, the second part consists of Chapters 5 and 6.

The fundamental properties of BD/FE simulations of slender microstructures are reprised in Chapter 2. It recapitulates the foundations laid by [33, 38] on the simulation of rod-like micromechanical continua and introduces the computational model for the simulation of biopolymer networks, which has been elaborated by [33, 34]. The computational models of filaments and linkers, the basic components of the network, are discussed in detail. Due to the continuum assumption, information on the (molecular) microstructure of the filaments is lost. Chapter 3 enriches both the filament and the linker model such that this information can be partially retrieved. Building up on the two preceding chapters, the model of a molecular motor will be introduced and discussed in Chapter 4. This chapter represents the first step towards the modeling of more complex biological motor units such as myosin thick filaments. The methodic part is concluded at this point. Subsequently, Chapter 5 documents the first major application, which explores the linker-mediated aggregation of filaments into thermodynamically equilibrated network structures. The chapter is based on [35, 163]. It grants novel insights into the mechanisms of network self-assembly and provides parameters that enable the precise evocation of a certain type of network. In the subsequent Chapter 6, this knowledge enables the *controlled* self-assembly of complex bundle networks, which represent a ubiquitous and basic mechanical module in biological systems. These networks are thoroughly examined resulting in a comprehensive and novel description of their linear rheology. In addition, some aspects of the nonlinear viscoelasticity of these networks will be studied. This chapter is based on [164]. Finally, the outlook in Chapter 7

will conclude this thesis by pointing out ongoing projects as well as avenues of future research and development.

The individual chapters of the thesis aim to provide a certain degree of self-contained readability by means of compact introductions to the immediate problem and a concluding numerical validation in case of the methodic Chapters 3 and 4. There are two reading approaches to this thesis, either in a sequential way or a chapter-wise, non-sequential fashion, both of which work equally well.



## 2 Micromechanical finite element simulation of biopolymer networks

This is the first of three chapters that introduce the reader to the basic building blocks of *mesoscale* simulations of semiflexible (bio-)polymer networks, i.e., on the scale of microns. A finite element (FE) discretization resolves the network down to single filaments. The chapter is divided into three parts. The first part motivates the application of beam finite elements (BFEs) to discretize the slender polymers which constitute biopolymer networks like the cytoskeleton (Sections 2.1 and 2.3). Furthermore, it elaborates on fundamental modeling assumptions, e.g., concerning the fluid phase or the application of thermal forces, by considering and weighing different options available in literature. In the second part, the mechanical and the numerical model for filaments (and linkers) are introduced, pointing out selected important aspects (Sections 2.4 and 2.5). Both filament and linker molecules share the same discretization technique, namely a FE discretization using three-dimensional, geometrically exact, nonlinear beam elements. The last part of the chapter deals with linkers and their chemical and mechanical interactions with the filaments (Section 2.6)

A more detailed reading of what will be compactly presented here is offered by [33]. The original BD/FE approach was developed by C. J. CYRON, who gradually introduced the application of stochastic and viscous forces and moments combined with an implicit time integration scheme [36], increasingly complex drag laws [37], and the transition from two-dimensional, planar to three-dimensional space [38]. The computational framework set up for the simulation of biopolymer networks has been introduced in [34].

### 2.1 General modeling requirements

Having detailed the physical interest in the introduction to this thesis, attention is now directed towards the choice and design of an appropriate numerical technique for the problems at hand. The bluntly direct question of how to best simulate biopolymer networks within biological cells may be countered by three slightly more directed, basic modeling questions:

- (1) Which is the required spatial resolution?
- (2) Which is the smallest required time scale?
- (3) What is the largest length scale of the system?

The economic principle demands an optimal proportionality of detail and efficiency with respect to the chosen model. Since the aim is to determine the most appropriate computational model, the questions above may be reformulated into rather methodic *requirements*.

- (1) The modeling length scale has to be smaller than, yet as close as possible to the smallest phenomenological length scale.
- (2) Given (1), the smallest (discrete) time scale involved in the (numerical) model needs to be smaller than, yet as close as possible to the smallest time scale in need of observation.
- (3) Given (1) and (2), a sufficiently high computational efficiency must be guaranteed on the system scale.

## 2.2 Simulation of biopolymers in literature

Based on these modeling guidelines, the appropriate computational method can be chosen. The resolution of subatomic scales or the length scales of small molecules by means of quantum mechanics simulations or MD simulations are infeasible as the size of the numerical problem in terms of the number of simulated degrees of freedom (DOFs) very quickly exceeds the limits of current computer hardware before even remotely reaching length and time scales of interest.

A review of literature on cellular and subcellular simulations thus restricts technically feasible approaches in a first step to *macromechanical* or *micromechanical* (continuum) models. Macromechanical approaches such as [170, 212] assume biopolymer networks or whole cells to be continua. They are best suited for supercellular length scales and thus for the simulation of tissues or even whole organs. These approaches usually incorporate the microstructure implicitly by appropriate nonlinear constitutive laws, which are formulated based on assumptions concerning filament orientation and entanglement length. For this reason, they fail to meet requirement (1) and are thus discarded from application.

Micromechanical approaches comprise a large variety of simulation techniques used to discretize single filaments. They range from simple Metropolis-Monte-Carlo simulations [12] to bead-spring [91, 113, 116], bead-rod-models [159], rods-on-string-models [19], worm-like chain models [93], and Finite element approaches, e.g., [142, 217, 218]. A comprehensive overview on bead-rod-string models as the state-of-the-art approach is given in [31]. They occupy the gap between atomistic and molecular simulation models on the one hand, and macroscopic models on the other hand. In the context of mesoscale simulations, the former provide an unnecessarily high spatial detail combined with the inability to efficiently cover relevant time scales and system sizes. The latter lack the spatial resolution necessary to resolve processes on the mesoscale, which are of scientific interest to biologists, chemists, and biophysicists. Micromechanical models such as the ones mentioned resolve polymer networks down to the level of single filaments, which are typically of the size of several microns in length. All presented approaches have in common that none of them so far offers the computational performance required to simulate on the scale of hundreds of seconds, which is most important to biological processes on this length scale. Apart from this major issue, they suffer from shortcomings such as, e.g., an incorrect modeling or even the complete neglect of torsion and anisotropic bending [113, 116], unnatural (but sometimes useful) inextensibility constraints [159], or the absence of thermal excitations in models using Euler-Bernoulli [7, 167, 232] or Timoshenko beam theory [21]. Eventually, although fulfilling requirement (1), they fail to meet requirements (2) and (3). Only very recently, other micromechanical approaches based on a FE approach have been presented, that account

for thermal excitations (e.g., [142]). In summary, the modeling requirements listed above are in favor of a mechanically coarse-grained approach, which is best realized by a FE discretization.

## 2.3 Micromechanical continuum model for biopolymer networks

*Bottom-up* modeling of a biopolymer network requires models of its constituents. In view of the tremendous degree of heterogeneity and, consequently, the vast mechanical complexity of *in vivo* biopolymer networks like the cytoskeleton, simplifications are necessary, which leads to modeling only the mechanically most important constituents. First, there are long slender polymers serving as the matrix and providing the mechanical backbone of the network. The most important representatives are semiflexible actin *filaments* ( $L_p \approx 15\mu\text{m}$ ), intermediate filaments ( $L_p \leq 1\mu\text{m}$ ), and microtubules ( $L_p > 1\mu\text{m}$ ) [162]. The second family of molecules are the linkers, which establish connections between separate filaments. Finally, there is a fluid, in which both filaments and linkers are immersed. In a cell, this fluid phase would correspond to the cytoplasm.

### 2.3.1 General modeling strategy

As elaborated above, the most suitable solution is the application of a mechanical coarse-graining up to the scale of single filaments, which represents the largest possible length scale to consistently model mechanical properties on the network scale. On this length scale, the application of continuum models is legitimate judging from experiments with single f-actin filaments as will be argued later on. Linkers are modeled as continua as well, although they are considerably smaller than filaments. The decision to do so will be elaborated below.

**Fluid phase** To a large extent, the interior of eukaryotic cells is occupied by a fluid phase, which is characterized by small Reynolds numbers due to the microscopic scale, low flow velocities and a high viscosity (cf. PURCELL's *Life at low Reynolds number* [175]). It is considered incompressible. In both experimental studies as well as theoretical analyses, in order to understand the causes for observed phenomena, the model system should feature a certain degree of simplicity. Thus most biopolymer networks studied in literature tend to have filaments and linkers immersed into fluids with very simple flow states: in most cases, the fluid velocity field is assumed to be zero or corresponding to a simple shear flow. Given these circumstances, complex hydrodynamic models such as [20, 40, 70] may be replaced by a much simpler approach, that accounts for the influence of the fluid only in terms of effective anisotropic drag forces on any solid structure suspended in it. Literature offers a large number of ways to calculate effective friction coefficients for such fluid drag models (e.g., [19, 69, 88, 168]). Such simplified models of the fluid's influence on structures do not include the interaction of different structures among another via the fluid. However, slightly more sophisticated approaches that incorporate the cross-influence among different solid objects [47, 181] could be employed in the future. In light of the implications of this modeling decision, the fluid – as an explicitly simulated entity – is neglected. Its effective contribution to the dynamics of structural components will be presented in Section 2.4.

**Filaments** In biological fiber networks, filamentous proteins can be found in abundant numbers. They are polymers, which are long, slender and have a comparatively high bending stiffness  $EI$ , which results in persistence lengths  $L_p \sim 16\mu\text{m}$  (F-actin, [130]) up to  $L_p \sim 5\text{mm}$  (microtubules, [88]). The persistence length represents one of the most important quantities in the description of slender polymers, which is why it will be discussed in a slightly more detailed fashion. The intuitive understanding is that the persistence length marks the distance beyond which the bending of a filament becomes noticeable. The persistence length of a filament confined to two spatial dimensions is defined as

$$\langle \cos(\gamma(s) - \gamma(0)) \rangle = \exp\left(-\frac{s}{2L_p}\right), \quad (2.1)$$

where  $\langle \cdot \rangle$  is the time average,  $\gamma(s)$  denotes the angle enclosed between the tangent of the filament at position  $s$  along the filament and an arbitrarily chosen reference direction [88]. Derived from the *Principle of Equipartition of Energy* (cf. [126]), a more convenient relation from the point of view of modeling filaments in simulations is given by

$$L_p = \frac{EI}{k_B T} \quad (2.2)$$

with Boltzmann constant  $k_B$  and absolute temperature  $T$ . With this relation,  $L_p$  can be set by means of appropriate material and global model parameters. While Equation (2.1) can be exploited experimentally to measure the persistence length of stiff polymers like microtubules, another measure is the end-to-end distance

$$\langle L_{ee}^2 \rangle = 2L_p^2 \left[ \exp\left(-\frac{L}{L_p}\right) - 1 + \frac{L}{L_p} \right], \quad (2.3)$$

with curve length  $L$ , which is commonly used to find the persistence length of semiflexible polymers, which lie in the focus of this thesis. The term *semiflexible* refers to polymers with  $L_p \sim L$ . Equations (2.2) and (2.3) are also useful for consistency checks and the evaluation of a numerical implementation [36].

Filaments represent the backbone of a biopolymer network, accounting for a major part of the mechanical response to forces exerted on the network. Biological filaments are polymeric macromolecules consisting of a large number of molecular subunits (e.g., globular actin or tubulins, cf. Figure 2.1a). The question arises, whether one has to explicitly account for the molecular structure or if a coarse-grained modeling approach can be motivated in order to describe their dynamics. At  $T > 0\text{K}$ , thermally induced oscillation of atoms around their rest position entail interatomic and intermolecular (elastic) collisions. Now consider a filament set amongst fluid molecules. The fluid molecules gain translational and rotational momentum and transfer them to other fluid molecules or the filament. The molecules' trajectories are random causing the filament to take on randomly bent shapes, which can be observed with a light-optical microscope. From optical data and the knowledge of experimental conditions such as temperature or solvent viscosity, mechanical properties of the filament can be deduced. Experiments strongly suggest (e.g., [209, 225]) that approaches modeling single filaments as mechanical continua are valid, if one is interested in studying physics on the filament length scale and above [88]. Many

modeling approaches exist, which vary in complexity and mathematical rigor. They may be divided into basically two kinds: both simple and intuitive bead-spring, bead-rod, or even simpler inextensible chain models on the one side, and on the other side more intricate models employing, e.g., one of the many beam formulations, among which some fully account for extension, bending, torsion, and shear in a consistent, nonlinear fashion. The former kind mainly enjoys popularity among natural scientists, while the latter is usually applied to engineering problems. The tendency towards more rigorous models has become evident in recent years as the introductory excerpt on topical literature implies (cf. Section 2.1). In engineering, reduced models such as the *Euler-Bernoulli* beam theory or the *Timoshenko* beam theory have long been applied to problems in structural mechanics, that deal with long slender geometries. The term *reduced* refers to the number of explicitly modeled spatial dimensions, which in a beam's case is its curved shape in the longitudinal dimension. First ideas date back as far as the 18<sup>th</sup> century.

Filaments in biological cells have length-to-thickness ratios, which easily exceed 50. Semi-flexible filaments usually feature even higher ratios, e.g., F-actin with values of  $r = l/d \geq 500$ . At such ratios, beam theory becomes applicable (cf. [29, 193]). Modeling slender structures in cellular environments as beams can thus be motivated both theoretically and computationally. Theoretically, beam models are fully capable of an accurate description of filament dynamics. In terms of computational efficiency, spatial discretizations based on BFE formulations combined with an implicit time integration scheme are unmatched. As a result of overall positive mechanical and numerical properties, filaments are modeled and discretized with three-dimensional, geometrically exact, nonlinear BFEs, which are path-independent and strain-invariant, and based on the work of [29, 30, 103].

**Linkers** The last among the modeled constituents of biopolymer networks are the so-called *actin binding proteins* (ABPs), crosslinkers, or simply linkers. The most general term *linker* will be applied from here on. Linkers undergo chemical reactions with binding domains on filaments and are able to establish mechanical connections between filaments. In most cases, biologically relevant linkers are macromolecules with a mass of about 50 – 200 kDa, e.g.,  $\alpha$ -actinin [43, 153] and filamin [224], which can be found in muscle cells. Covalent bonds and ions like  $Ca^{2+}$  can also act as linkers [11], but are not of specific relevance in this thesis.

Linkers are considerably smaller than filaments, often measuring only a few nanometers in size as in the case of *scruin* or *fascin*. Arguably it might be insufficient to model these linkers as continua as well due to their convoluted molecular structure or their complex kinematics in case of active proteins such as *myosin* [15, 27]. However, as long as the focus lies on mesoscale mechanics rather than the accurate portrayal of the (molecular) dynamics of single linkers, this simplified model of a linker is still applicable. As a consequence, detached, solute linkers are modeled as point-like particles, which do not affect the mechanical properties of the network. Linkers, that actually connect two separate filaments, can be described as short, stiff rods and thus be represented by beams as well. Chemical interactions between linkers and filaments are modeled according to [34].

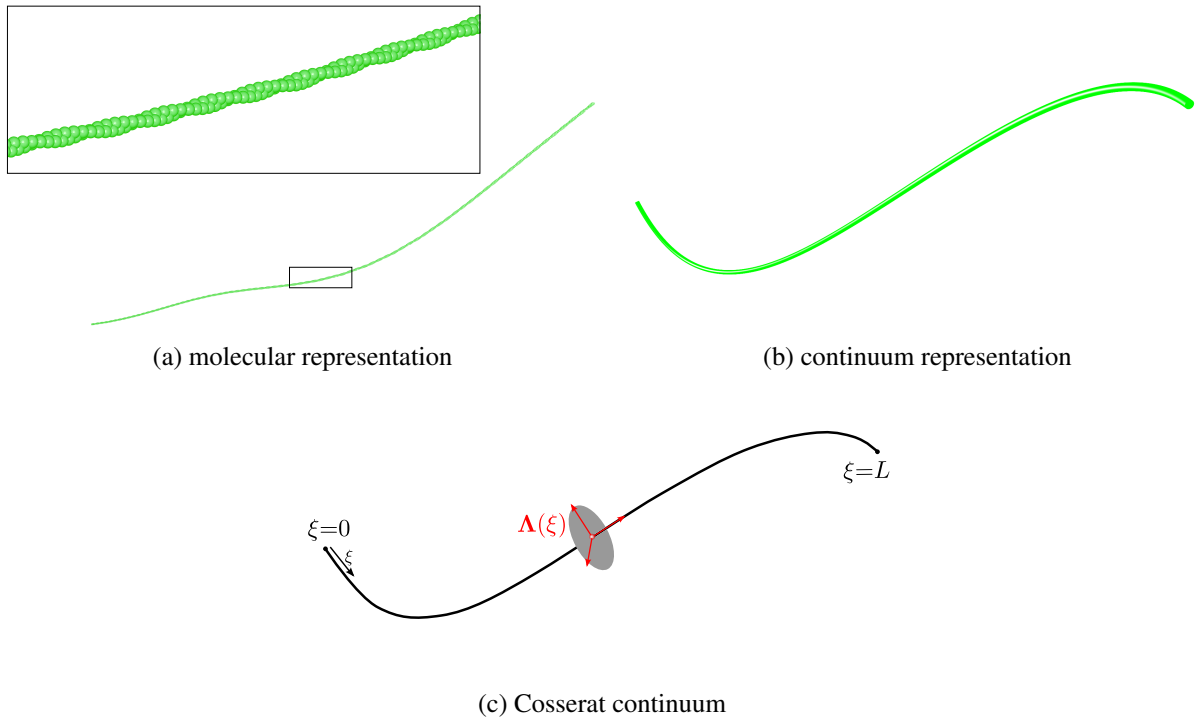


**Figure 2.1** (a) An actin filament consists of a large number of actin monomers, which take the quaternary structure of a left-handed, 1-start helix. It is surrounded by myriads of fluid molecules (not shown). At finite temperature, their random trajectories cause intermolecular collisions, which make the filament take on some contorted shape. (b) Coarse graining the molecular structure, one arrives at a continuum description of the filament, which is affected by forces and moments representing the effect of thermal excitation and drag due to the surrounding fluid. (c) Dimensional reduction leads to *Cosserat continuum* description: the filament's center line and the orientation of its cross sections are described by an enhanced one-dimensional continuum.

## 2.4 Mechanical model of a semiflexible filament

The filament model used in this thesis was introduced by [38] and will be presented in a compact manner, laying the technical foundations for modeling extensions and numerical examples to come. Full details can be found in C. J. CYRON's doctoral thesis on a *Micromechanical continuum approach for the analysis of biopolymer networks* [33].

### 2.4.1 Balance of linear and angular momentum

Modeling filaments, or in fact any slender structure shaped like a rod, is most elegantly done by a description as a one-dimensional *Cosserat continuum*. The term *slender* refers to the basic modeling assumption that one dimension of the geometry is significantly larger than the other two ( $L \gg (4A/\pi)^{-1/2}$  in case of a circular cross section). In  $\mathbb{R}^3$ , such extended continua feature an additional set of 3 rotational DOFs, which describe the orientation of the cross sections. In other words, the two lateral dimensions are accounted for by rigid orthonormal triads, whose origins coincide with the centroids of the cross sections. The set of all centroids is the center line of the continuum. In general, any geometrical configuration of a rod-like microstructure of curve length  $L$  on a time interval  $[0; T]$  can be described by a pair of functions, that determine

the spatial positions of the material points and the orientations of the cross sections at these points. All cross sections remain planar, have a circular shape, and are assumed rigid. The curve parameter  $s \in [0; L]$  represents the scalar argument of the vector-valued function definitions

$$\mathbf{x} : [0; L] \times [0; T] \rightarrow \mathbb{R}^3, (s, t) \mapsto \mathbf{x}(s, t), \quad (2.4a)$$

$$\boldsymbol{\theta} : [0; L] \times [0; T] \rightarrow \mathbb{R}^3, (s, t) \mapsto \boldsymbol{\theta}(s, t). \quad (2.4b)$$

where  $\mathbf{x}(s, t)$  maps  $s$  to its time-dependent position in  $\mathbb{R}^3$  and  $\boldsymbol{\theta}(s, t)$  does the same for the orientation of the respective cross section. Rotations are expressed in terms of so-called *pseudo vectors* [28] of the form

$$\boldsymbol{\theta} = [\theta_1, \theta_2, \theta_3]^T, \quad \theta = \sqrt{\boldsymbol{\theta}^T \boldsymbol{\theta}}. \quad (2.5)$$

The correct mathematical treatment is a non-trivial matter and represents one of the main challenges in the formulation of geometrically exact beam models [29]. Pseudo-vectors parametrize a group of three-dimensional rotations, which represents a nonlinear manifold and thus is in contrast to a *vector space* with defining properties such as additivity, commutativity, etc.. In other words, the prefix ‘‘pseudo’’ implies non-additivity in  $\mathbb{R}^3$ . A pseudo vector unites two pieces of information: the unit vector of  $\boldsymbol{\theta}/\theta$  defines the axis of rotation, while its  $L^2$ -norm determines the rotation angle  $\theta$ . With (physically sensible) initial configurations  $\mathbf{x}_0 = \mathbf{x}(s, t=0)$  and  $\boldsymbol{\theta}_0 = \boldsymbol{\theta}(s, t=0)$  and boundary values for  $s = \{0, L\}$ , Equations (2.4a) and (2.4b) fully describe the space/time evolution of the geometrical configuration of a filament. Solutions of  $(\mathbf{x}, \boldsymbol{\theta})$  can be found solving the beam’s equations of motion, i.e. the conservation equations of linear and angular momentum, which read

$$\mathbf{f}'_s(\mathbf{x}, \boldsymbol{\theta}, s, t) = \mathbf{f}_{stoch}(\mathbf{x}, \boldsymbol{\theta}, s, t) + \mathbf{f}_{visc}(\mathbf{x}, \boldsymbol{\theta}, s, t) + \mathbf{f}_{ext}(\mathbf{x}, s, t), \quad (2.6a)$$

$$\begin{aligned} \mathbf{m}'_s(\mathbf{x}, \boldsymbol{\theta}, s, t) &= \mathbf{m}_{stoch}(\mathbf{x}, \boldsymbol{\theta}, s, t) + \mathbf{m}_{visc}(\mathbf{x}, \boldsymbol{\theta}, s, t) + \mathbf{m}_{ext}(\mathbf{x}, s, t) + \\ &+ \mathbf{x}'(s, t) \times \mathbf{f}_s(\mathbf{x}, \boldsymbol{\theta}, s, t). \end{aligned} \quad (2.6b)$$

Equation (2.6) is a so-called *stochastic partial differential equation* (SPDE). Quantities  $(\cdot)_{el}$  denote elastic,  $(\cdot)_{stoch}$  stochastic,  $(\cdot)_{visc}$  viscous, and  $(\cdot)_{ext}$  other external contributions, all of which represent line loads in the context of one-dimensional continua. The elastic section force  $\mathbf{f}_s(\mathbf{x}, \boldsymbol{\theta}, s, t)$  and the section moment  $\mathbf{m}_s$  are defined as the integral of the internal stresses and their resulting moment, respectively. The prime-operator denotes  $(\cdot)' = \partial(\cdot)/\partial s$ . For the sake of visual clarity, from here on, the bracketed list of arguments of functions will be omitted in unambiguous cases, e.g.,  $\mathbf{f}_{visc}(\mathbf{x}, \boldsymbol{\theta}, s, t)$  simply becomes  $\mathbf{f}_{visc}$ .

## 2.4.2 Forces and Moments

**Elastic forces and moments** Dimensionally reduced mechanical representations of beams describe their geometrical configuration by means of orientations. Various ways for the parametrization of orientations exist, one of which is the description by means of orthonormal rotation matrices  $\boldsymbol{\Lambda} \in \mathbb{R}^{3 \times 3}$  of the special orthogonal group

$$SO(3) := \{\boldsymbol{\Lambda} : \mathbb{R}^3 \rightarrow \mathbb{R}^3 \text{ linear} \mid \boldsymbol{\Lambda}^T \boldsymbol{\Lambda} = \mathbf{1}, \det \boldsymbol{\Lambda} = 1\}, \quad (2.7)$$

which incorporates all rotations in three-dimensional Euclidean space (cf. [193]). Geometry and elastic response are crucially related since any geometrical configuration can be understood

as the result of acting and reacting forces. The calculation of rotation matrices  $\Lambda$  by means of pseudo-vectors  $\theta$  is performed introducing a spin matrix, which is a skew-symmetric representation of an arbitrary vector  $v \in \mathbb{R}^{3 \times 1}$  given by

$$\mathring{v} = \begin{bmatrix} 0 & -v_3 & v_2 \\ v_3 & 0 & -v_1 \\ -v_2 & v_1 & 0 \end{bmatrix}. \quad (2.8)$$

It parametrizes a vector product operation and will be henceforth denoted with an overset “ $\circ$ ”. The mathematical relation between rotation matrices and rotation pseudo-vectors is described by an exponential map, which according to [193] reads

$$\Lambda(\mathring{\theta}) = \exp(\mathring{\theta}) = \mathbf{1} + \frac{\sin \|\theta\|}{\|\theta\|} \mathring{\theta} + \frac{1 - \cos \|\theta\|}{\|\theta\|^2} \mathring{\theta}^2. \quad (2.9)$$

The infinite series  $\exp(\mathring{\theta})$  is compactly expressed by what is commonly known as *Rodrigues’ formula* (cf. [193]). The columns of  $\Lambda$  represent the base vectors of the triad, which are associated to the principal directions of the corresponding cross section. In the following,  $\Lambda(\theta)$  is abbreviated as  $\Lambda$  unless stated otherwise. Further details can be found in [30, 103], and the appendices of [38]. Using orientations  $\Lambda$ , Young’s modulus  $E$ , and shear modulus  $G$ , elastic section forces and moments of the employed beam model can be written as

$$\mathbf{f}_s = \Lambda \mathbf{C}_f \gamma, \quad (2.10a)$$

$$\mathbf{m}_s = \Lambda \mathbf{C}_m [\boldsymbol{\kappa} - \boldsymbol{\kappa}_0] \quad (2.10b)$$

with the material strain measure  $\gamma = \Lambda^T \mathbf{x}' - [1 \ 0 \ 0]^T$  and reference orientation  $\Lambda_0 = \Lambda(\theta_0)$ , as well as current and initial curvature vectors  $\boldsymbol{\kappa}$  and  $\boldsymbol{\kappa}_0$ , which are only given implicitly by their triad representations

$$\Lambda' = \mathring{\boldsymbol{\kappa}} \Lambda, \quad \Lambda'_0 = \mathring{\boldsymbol{\kappa}}_0 \Lambda_0 \quad (2.11)$$

in the current and the reference configuration, respectively. The constitutive matrices are

$$\mathbf{C}_f = \begin{bmatrix} EA & 0 & 0 \\ 0 & GA_2 & 0 \\ 0 & 0 & GA_3 \end{bmatrix}, \quad \mathbf{C}_m = \begin{bmatrix} GI_r & 0 & 0 \\ 0 & EI_2 & 0 \\ 0 & 0 & EI_3 \end{bmatrix}, \quad (2.12)$$

where  $A$  is the cross section area and  $A_2 = A_3$  denotes the cross section area with a shear correction factor for circular cross sections.  $I_r = I_2 + I_3$  represents the polar moment of inertia, i.e., in the direction perpendicular to the planar cross section, and  $I_2 = I_3$  are the area moments of inertia with respect to the in-plane principal axes.

**Viscous forces and moments** The surrounding fluid damps the motion of a filament. Strictly speaking, formulae for drag components introduced in [33] only account for the damping of straight rigid rods. However, as single segments of a filament, on which these forces act, are nearly straight in the case of semiflexible filaments, the formulae may be applied in good approximation of the exact values. As already elaborated in Section 2.3.1, the present model

refrains from a complex description of the interaction between the fluid phase and the filament. Rather, simple velocity-dependent drag laws

$$\mathbf{f}_{visc} = \mathbf{D}_t (\dot{\mathbf{x}} - \mathbf{v}(\mathbf{x})) = \mathbf{D}_t \dot{\mathbf{x}}_{rel}, \quad (2.13a)$$

$$\mathbf{m}_{visc} = \mathbf{D}_r (\dot{\boldsymbol{\theta}} - \mathbf{w}(\mathbf{x})) = \mathbf{D}_r \dot{\boldsymbol{\theta}}_{rel} \quad (2.13b)$$

are employed with  $\mathbf{v}(\mathbf{x})$  and  $\mathbf{w}(\mathbf{x})$  as translational and angular velocities of the fluid, respectively. Consequently,  $\dot{\mathbf{x}}_{rel}$  and  $\dot{\boldsymbol{\theta}}_{rel}$  are the relative velocities. In many cases,  $\mathbf{v}(\mathbf{x}) = \mathbf{w}(\mathbf{x}) = \mathbf{0}$  as the fluid is assumed to be at rest. However, flow patterns such as simple oscillatory shear occurring in rheological studies may be easily incorporated this way. In order to calculate the anisotropic drag forces acting on a segment, appropriate damping matrices have to be set up. Therefore, as a first step, damping constants per unit length

$$\gamma_{\perp} = 4\pi\eta, \quad \gamma_{\parallel} = 2\pi\eta, \quad \gamma_a = 4\pi\eta r^2 \quad (2.14)$$

are defined with rod radius  $r$  and the fluid's dynamic viscosity  $\eta$ , which characterize the damping behavior perpendicular and parallel to the segment's axis as well as for the segment's rotation around its axis. These damping constants are calculated from global damping constants

$$\zeta_{\perp} = \gamma_{\perp} L, \quad \zeta_{\parallel} = \gamma_{\parallel} L, \quad \zeta_a = \gamma_a L, \quad (2.15)$$

which are given with respect to the total length of the filament. Values for  $\zeta$  can be drawn from textbooks (e.g., [88, Table 6.2]) or experimentally determined. The topical outline in Section 2.3.1 already hints at the complexity of modeling hydrodynamic interaction. The decision to employ this set of simplified damping constants can be motivated due to sensible numerical results already found appropriate for semiflexible filaments [37, 69]. More elaborate damping constants presented in [168] have been tried [38], yet perceptible differences were not observed on the network scale. Translational and rotational damping matrices with respect to a segment's principal axes take the form

$$\mathbf{D}_{t,loc} = \begin{bmatrix} \gamma_{\parallel} & 0 & 0 \\ 0 & \gamma_{\perp} & 0 \\ 0 & 0 & \gamma_{\perp} \end{bmatrix}, \quad \mathbf{D}_{r,loc} = \begin{bmatrix} \gamma_a & 0 & 0 \\ 0 & 0 & 0 \\ 0 & 0 & 0 \end{bmatrix}. \quad (2.16)$$

From here on, subscripts  $\{t, \mathbf{t}\}$  mark translational quantities and  $\{r, \mathbf{r}\}$  refer to rotational quantities. Finally, accounting for the orientation of a segment in  $\mathbb{R}^3$ , its damping matrices read

$$\mathbf{D}_t = \boldsymbol{\Lambda} \mathbf{D}_{t,loc} \boldsymbol{\Lambda}^{\top} \quad (2.17a)$$

$$\mathbf{D}_r = \boldsymbol{\Lambda} \mathbf{D}_{r,loc} \boldsymbol{\Lambda}^{\top} \quad (2.17b)$$

Alternatively, Equation (2.17a) can be expressed as

$$\mathbf{D}_t = \gamma_{\perp} \mathbf{1} + (\gamma_{\parallel} - \gamma_{\perp}) \|\mathbf{X}'(s)\|^{-2} \mathbf{x}' \otimes \mathbf{x}' \quad (2.18)$$

with identity tensor  $\mathbf{1} \in \mathbb{R}^{3 \times 3}$  and Jacobian  $\|\mathbf{X}'(s)\|$ , which norms the tangential vector to unit length. The  $\otimes$ -operator represents the tensor product. According to [33], this formulation can be applied in a more straight-forward manner than Equation (2.17a).

**Stochastic Forces and Moments** At finite temperature, molecules have kinetic energy causing them to move around, bounce off each other and exchange their energy through elastic collisions. In such thermal environments, collisions are undirected and random, which causes a microscopic particle to change its trajectory randomly due to forces and moments acting on it. Assuming a sealed-off environment without heat fluxes across its boundaries as well as a spatially invariant temperature, these forces and moments can be described as random variables of stochastic processes. Assuming both forces and moments to be Gaussian, one can define the stochastic processes by their first and second moments, i.e. their means and covariance matrices. The Principle of Equipartition of Energy determines how much energy each DOF receives on average, which is  $k_B T/2$  for a point-like particles [88]. Appendix 4.1 in [88] offers the derivation of this fundamental thermodynamic theorem. With respect to beam models, this statement translates to each of a beam's eigenmodes having this amount of energy, which directly relates to the amplitude of these modes. By understanding that thermal fluctuations and viscous drag are two effects stemming from a common origin [45], one realizes that the response of a mechanical system to a spontaneous (random) excitation has to equal its response to a small applied force. What is sloppily expressed in words, can be mathematically derived and culminates in the so-called *fluctuation-dissipation theorem* (FDT) [127]. Condensed into formulae, it states that forces and moments  $\mathbf{f}_{stoch}, \mathbf{m}_{stoch} \in \mathbb{R}^{3 \times 1}$  of a thermodynamically equilibrated system with space/time-invariant temperature  $T$  of obey

$$\langle \mathbf{f}_{stoch}(s, t) \rangle = \mathbf{0}, \quad (2.19a)$$

$$\langle \mathbf{f}_{stoch}(s, t) \otimes \mathbf{f}_{stoch}(s^*, t^*) \rangle = 2k_B T \delta_{ss^*} \delta_{tt^*} \mathbf{D}_t, \quad (2.19b)$$

$$\langle \mathbf{m}_{stoch}(s, t) \rangle = \mathbf{0}, \quad (2.19c)$$

$$\langle \mathbf{m}_{stoch}(s, t) \otimes \mathbf{m}_{stoch}(s^*, t^*) \rangle = 2k_B T \delta_{ss^*} \delta_{tt^*} \mathbf{D}_r, \quad (2.19d)$$

where  $\langle . \rangle$  denotes mean values,  $\delta$  is the *Dirac* function written in a slightly abbreviated manner  $\delta_{ss^*} := \delta(s-s^*)$  and  $\delta_{tt^*} := \delta(t-t^*)$ . Equations (2.19a) - (2.19d) state that the realizations of the stochastic processes are spatially and temporally uncorrelated [37]. Therefore, a constant power spectral density is observed in Fourier space, which is a defining characteristic of *White noise*. Altogether, the properties of the kind of stochastic process described above allow for the formulation of stochastic forces and moments in terms of their respective generalized derivatives of standard vector-valued *Wiener processes*  $\mathcal{W}_t(s, t)$  and  $\mathcal{W}_r(s, t)$  in three spatial dimensions. The mathematical nature of generalized derivatives will not be elucidated further than stating that they represent an extension of the concept of a derivative to non-smooth functions as any detailed discussion would definitely extend well beyond the scope of this thesis. The inclined reader is referred to mathematical textbooks such as [90]. A scalar Wiener process  $\mathcal{W}(t)$  is characterized by

(I)  $\mathcal{W}(t=0) = 0$

(II)  $\mathcal{W}(t)$  is almost surely continuous in  $t$

(III)  $\mathcal{W}(t)$  has stationary, independent increments

(IV)  $\mathcal{W}(t) - \mathcal{W}(t_0) \sim \mathcal{N}(0, t - t_0)$  for  $0 \leq t_0 \leq t$  and normal distribution  $\mathcal{N}(\mu, \sigma^2)$ .

The extension to a vector-valued Wiener process is straight-forward as the spatial components are independent of each other. Based on the considerations presented above and having ensured consistency with stochastic theory [38], the discrete stochastic forces and moments are given by

$$\mathbf{f}_{stoch} = \sqrt{2k_B T} \mathbf{S}_t \frac{\partial^2 \mathcal{W}_t(s, t)}{\partial s \partial t}, \quad (2.20a)$$

$$\mathbf{m}_{stoch} = \sqrt{2k_B T} \mathbf{S}_r \frac{\partial^2 \mathcal{W}_r(s, t)}{\partial s \partial t} \quad (2.20b)$$

with damping matrices satisfying  $\mathbf{D}_t = \mathbf{S}_t \mathbf{S}_t^\top$  and  $\mathbf{D}_r = \mathbf{S}_r \mathbf{S}_r^\top$  as one requires here the value of the standard deviation.

**External forces and moments** Deterministic external forces and moments may be applied to filaments of biopolymer networks, e.g., mechanically, in order to study creeping phenomena. Their incorporation utilizes standard procedures amply described in standard textbooks, e.g., in the form of *Neumann* boundary conditions (cf. [235]), and will thus not be further discussed. Such boundary conditions can be utilized, e.g., to conduct simulations of the creeping behavior of networks.

Other kinds of external forces and moments may arise from interactions between filaments due to mechanical contact or intermolecular forces. Contact interactions are commonly referred to as *steric interactions* in physical literature, where atoms are assumed to occupy a certain volume, which allows intrusions only when associated with an energetic cost. Finite element literature with a focus on contact interactions offers solutions that can adequately model steric interactions by means of contact potentials. Such potentials usually contain simple expressions equivalent to the potential of linear-elastic springs [129, 228]. In Chapter 5, an Augmented-Lagrange regularization of the contact between two beams ensures a minimization of the volume overlap. A short outline of the method is given in Appendix B.1. There are several approaches to the detection and evaluation of mechanical contact between beams (e.g., [41, 42, 228]).

Electrostatic interactions depend on a molecule's structure and the electric charge patterns created by the molecule's constituents. In fact, all intermolecular forces originate from electrostatic interactions and may be (theoretically) calculated solving *Schrödinger's* Equation [51, 73]. However, finding exact solutions even for such simple problems as the interaction between two hydrogen atoms is virtually impossible, which is why one resorts to a classification of intermolecular interaction forces by categories such as strength or range [101], e.g., by means of Van-der-Waals forces, hydrogen bonds, or dipole-dipole forces. Although bearing a negative electrostatic charge, actin filaments are assumed to be uncharged for all applications in this thesis because of its Debye length of  $\sim 1\text{nm}$  [107] in ionic solutions.

External electric or magnetic fields can be applied in order to analyze biomolecules such as proteins or nucleic acids. The electrophoretic analyses of deoxyribonucleic acids (DNA) by means of computer simulations (e.g., [111, 112]) are an interesting future topic, but are only of limited interest here.

## 2.5 Discretization

In this section, a brief outline of the discretization procedure will be given, which is applied in order to numerically model both filaments and linkers in space and time. By no means, a detailed derivation of the discretized terms is attempted. Rather the following pages summarize which force and moment contributions have to be accounted for in order to arrive at a comprehensive dynamic micromechanical model of a filament. If in need of a more detailed description of viscous and stochastic terms, the reader is referred to [33, 38]. The vast and complex topic of nonlinear, geometrically exact, three-dimensional beam (element) formulations, is well discussed by [29] as well as in preceding publications of [192, 193] and [30, 103].

### 2.5.1 Weak form

As a first step towards a FE discretization, the equations of motion given by Equation (2.6) have to be reformulated such that they allow for a variational approach, which is necessary when applying the finite element method (FEM). The general idea behind a variational approach is to formulate the (physical) problem in a way which allows for the minimization of some characteristic problem-specific error term. In the context of mechanics, this idea leads to the formulation of *virtual work* expressions, which state that the work done by an infinitesimal perturbation of the system must vanish. In structural mechanics, one may think of these perturbations as displacements. The term *weak form* reflects the less strict requirements towards differentiability of the testing functions as well as the fact, that the balance equations only need to be satisfied in their integral form. Arbitrary nodal weighting functions

$$\mathbf{W}_t(s) = \mathbf{W}_r(s) = [\text{diag}(W^{[1]}(s)), \text{diag}(W^{[2]}(s)), \dots, \text{diag}(W^{[K]}(s))] \quad (2.21)$$

chosen from a sufficiently large function space are used to reformulate the translational Equation (2.6a) and the rotational Equation (2.6b). Both matrices share a layout equal to that of the interpolation function matrix  $\mathbf{l}_t$  from Equation (2.25). With infinitesimal virtual translational and rotational displacements  $\delta\mathbf{u}$  and  $\delta\boldsymbol{\vartheta}$ , one may rewrite these equations to take on the form of virtual work expressions

$$\delta\mathbf{u}^T \int_0^L \mathbf{W}_t^T \mathbf{f}'_s ds = \delta\mathbf{u}^T \int_0^L \mathbf{W}_t^T (\mathbf{f}_{\text{stoch}} + \mathbf{f}_{\text{visc}} + \mathbf{f}_{\text{ext}}) ds, \quad (2.22a)$$

$$\delta\boldsymbol{\vartheta}^T \int_0^L \mathbf{W}_r^T (\mathbf{m}'_s + \mathbf{x}' \times \mathbf{f}_s) ds = \delta\boldsymbol{\vartheta}^T \int_0^L \mathbf{W}_r^T (\mathbf{m}_{\text{stoch}} + \mathbf{m}_{\text{visc}} + \mathbf{m}_{\text{ext}}) ds. \quad (2.22b)$$

The weak form of Equations (2.22) can be obtained by an integration by parts such that eventually, the weighted residuals read

$$\int_0^L \mathbf{W}_t^T \mathbf{f}_s ds = \int_0^L \mathbf{W}_t^T (\mathbf{f}_{\text{stoch}} + \mathbf{f}_{\text{visc}} + \mathbf{f}_{\text{ext}}) ds + [\mathbf{W}_t^T \mathbf{f}_\Gamma]_0^L, \quad (2.23a)$$

$$\int_0^L \mathbf{W}_r^T \mathbf{m}_s - \mathbf{W}_r^T \mathbf{x}' \times \mathbf{f}_s ds = \int_0^L \mathbf{W}_r^T (\mathbf{m}_{\text{stoch}} + \mathbf{m}_{\text{visc}} + \mathbf{m}_{\text{ext}}) ds + [\mathbf{W}_r^T \mathbf{m}_\Gamma]_0^L \quad (2.23b)$$

with boundary terms  $(\cdot)_\Gamma$ .

## 2.5.2 General remarks on discretization in space and time

According to [33], the SPDE (2.6) can be discretized with FEs in space and by an Implicit Euler scheme in time. The integration of an SPDE is a theoretically intricate endeavor with many potential pitfalls, such as, e.g., the choice of an appropriate integral convention. The reiteration of the entire derivation and proof of principle of the here used method goes well beyond the scope of this work. Readers in search for a more detailed lecture are referred to topical publications [33, 38]. Without detailing the derivation, the following sections' intention simply is to provide an overview of BD/FE simulations with beam elements.

The formulaic goal is the discretized form of the SPDE, which reads

$$\mathbf{F}_s^i = \mathbf{F}_{\text{stoch}}^i + \mathbf{F}_{\text{visc}}^i + \mathbf{F}_{\text{ext}}^i, \quad (2.24a)$$

$$\mathbf{M}_s^i = \mathbf{M}_{\text{stoch}}^i + \mathbf{M}_{\text{visc}}^i + \mathbf{M}_{\text{ext}}^i + \mathbf{M}_s^i \quad (2.24b)$$

at a discrete time  $t^i = i\Delta t$  with  $i \in \{0, 1, 2, \dots, l\}$  and a step size  $\Delta t = T_{\text{sim}}/l$ , where  $T_{\text{sim}}$  marks the upper bound of the interval of simulated time  $[0; T_{\text{sim}}]$ . This interval is subdivided into  $l+1$  equidistant points in time. For discrete quantities, the convention is introduced of denoting them with sans-serif typeface.

The one-dimensional parameter space  $[0; L]$ , within which the neutral line of the continuum is described, is discretized with  $K$  nodes, which are equally spaced at a distance  $h = L / (K - 1)$ . Each node is located at its respective discrete line parameter position  $s^{[k]}$  with  $k \in \{1, 2, \dots, K\}$ . Furthermore, the  $k^{\text{th}}$  node at the  $i^{\text{th}}$  time step has associated vectors  $\mathbf{x}^{i[k]} \in \mathbb{R}^3$ ,  $\boldsymbol{\theta}^{i[k]} \in \mathbb{R}^3$ , which hold the approximated positions and rotations according to Equations (2.4a) and (2.4b), respectively. Unless explicitly required, the superscripted  $i$  will be from here on omitted in favor of a slender notation as it is implied that the discussed equations are evaluated at discrete time  $t^i$ . The interpolation schemes of translational and rotational quantities usually differ from each other in  $\mathbb{R}^3$ . The interpolation of translational DOFs is realized following an isoparametric approach for  $K - 1$  linear elements with  $K$  nodes. Using an interpolation matrix

$$\mathbf{l}_t(\mathbf{s}) = \left[ \text{diag}(\mathbf{l}_t^{[1]}), \text{diag}(\mathbf{l}_t^{[2]}), \dots, \text{diag}(\mathbf{l}_t^{[K]}) \right] \in \mathbb{R}^{3 \times 3K} \quad (2.25)$$

with nodal interpolation blocks  $\text{diag}(\mathbf{l}_t^{[k]}) \in \mathbb{R}^{3 \times 3}$  and polynomials functions  $\mathbf{l}_t^{[k]}$  (here: Lagrange polynomials) as well as the nodal position vector

$$\mathbf{X} = [(\mathbf{x}^{[1]})^T, \dots, (\mathbf{x}^{[K]})^T]^T, \quad (2.26)$$

the interpolated translational positions at time  $t^i$  can be written as

$$\mathbf{x}(\mathbf{s}) = \mathbf{l}_t(\mathbf{s})\mathbf{X}. \quad (2.27)$$

The nodal interpolation functions  $\mathbf{l}_t^{[k]}$  can be chosen equal to the nodal weighting functions  $W_t^{[k]}$ . The vector of nodal rotations

$$\Theta = \left[ (\theta^{[1]})^\top, \dots, (\theta^{[K]})^\top \right]^\top \quad (2.28)$$

cannot in general be interpolated as conveniently as its translational counterpart Equation (2.26). Rotational quantities require different and more elaborate means of interpolation [103, 179], which will be discussed in more detail in Chapter 3. The current beam model meets two fundamental mathematical and mechanical requirements: *path-independence* and *strain-invariance*. Path-independence in the context of conservative vector fields demands equality of all integrals along arbitrary paths for fixed integral bounds. Mechanically, this property means that all path-independent load cases are reproducible as such by the beam formulation. For example, imagine the simple static case of a beam, that is straight in its relaxed state, with statically defined support, which is subject to a lateral load  $F$  leading to a deformed configuration. If a sequence of  $n_F$  load steps adding up to  $F$  does not depend on the order of its individual steps, then the order must not matter for the beam model as well. Strain-invariance refers to the objectivity of the strain measure, which means it remains unimpaired by constant motion or rigid body rotations [30].

The employment of rather complex generalized interpolation functions for the interpolation of rotations is essential in order to fulfill these conditions. They have to enable the computation of an approximate representation  $\theta(s)$  of the exact rotation field  $\theta(s)$  from Equation (2.28) in a way that fulfills the two essential requirements given above. Such an interpolation scheme in general leads to a nonlinear relation between  $\vartheta(s)$  and  $\vartheta^{[k]}$

$$\theta(s) = \mathbf{f}(\theta^{[k]}, s). \quad (2.29)$$

If an interpolation scheme meets these requirements, it can be applied to a FE discretization in space combined with an implicit time integration scheme. Further details on the interpolation of rotations will be given in Chapter 3, where they enable the formulation of appropriate rotational constraints for extended filament and linker models. Implicit time integration requires the mathematical means to arrive at an iterative solution of a nonlinear system of equations. Therefore, the linearized form of the differential equations is evaluated using a *Newton* scheme. The term linearization is used equivalently to a Taylor series expansion truncated after the linear term.

With the simplest implicit time integration scheme, the *Implicit Euler* method, the translational velocity field can be approximated by

$$\dot{\mathbf{x}}(s) \approx \mathbf{l}_t(s) \frac{\mathbf{x}^i - \mathbf{x}^{i-1}}{\Delta t} \quad (2.30)$$

and the rotational velocity field (node-wise) by

$$\dot{\theta}(s) \approx \frac{\Delta \theta^i(s)}{\Delta t}. \quad (2.31)$$

with an implicitly defined nodal rotation increment

$$\Delta \Lambda(\Delta \theta^i) = \Lambda^i (\Lambda^{i-1})^{-1}, \quad (2.32)$$

which describes the rotational difference from the old to the current step. As before in the continuous case, the abbreviation  $\mathbf{\Lambda}^{(\cdot)} := \mathbf{\Lambda}(\boldsymbol{\theta}^{(\cdot)})$  is used. Instead of a common Newton-Raphson scheme, a method called *pseudo-transient continuation* (PTC) is utilized [38, 56], which increases the convergence radius of the conventional Newton scheme by heuristic means. The inclined reader is referred to [38, Appendix I] as further explications do not greatly contribute in the present context.

### 2.5.3 Discretized forces and moments

Equations (2.24) can be detailed in terms of their individual discretized force and moment contributions. The discretized weighted residuals read

$$\underbrace{\int_0^L \mathbf{W}_t^T \mathbf{f}_s \, ds}_{\mathbf{F}_s} = \underbrace{\int_0^L \mathbf{W}_t^T \mathbf{f}_{\text{stoch}} \, ds}_{\mathbf{F}_{\text{stoch}}} + \underbrace{\int_0^L \mathbf{W}_t^T \mathbf{f}_{\text{visc}} \, ds}_{\mathbf{F}_{\text{visc}}} + \underbrace{\int_0^L \mathbf{W}_t^T \mathbf{f}_{\text{ext}} \, ds}_{\mathbf{F}_{\text{ext}}} + [\mathbf{W}_t^T \mathbf{f}_\Omega]_0^L, \quad (2.33a)$$

$$\underbrace{\int_0^L \mathbf{W}_r^T (\mathbf{m}_s - \mathbf{x}' \times \mathbf{f}_s) \, ds}_{\mathbf{M}_s} = \underbrace{\int_0^L \mathbf{W}_r^T \mathbf{m}_{\text{stoch}} \, ds}_{\mathbf{M}_{\text{stoch}}} + \underbrace{\int_0^L \mathbf{W}_r^T \mathbf{m}_{\text{visc}} \, ds}_{\mathbf{M}_{\text{visc}}} + \underbrace{\int_0^L \mathbf{W}_r^T \mathbf{m}_{\text{ext}} \, ds}_{\mathbf{M}_{\text{ext}}} + [\mathbf{W}_r^T \mathbf{m}_\Omega]_0^L \quad (2.33b)$$

Theoretically, any set of weighting functions satisfying Equation (2.23) is suitable. In practice, weighting functions  $\mathbf{W}_t$  and  $\mathbf{W}_r$  are often chosen equal to interpolation functions  $\mathbf{l}_t$  (*Bubnov-Galerkin* approach). However, this statement exclusively applies to translational DOFs and does not cover the interpolation of finite rotations, for which special interpolation functions are employed.

**Inertial forces and moments** What separates the mechanics of microscopic from that of macroscopic structures is the dominance of viscous and stochastic forces over inertia. In fact, in overdamped microscopic systems, inertial effects may be neglected completely [88] leading to a simplified form of *Langevin dynamics*, which commonly referred to as *Brownian dynamics* (BD). What remains, is an SPDE of first order in time.

**Elastic forces and moments** Elastic forces and moments result from the discretization of the weak form as presented in [30, 103]. After intricate derivations involving a special treatment of rotations in three-dimensional Euclidean space, the authors arrive at a strain-invariant, path-independent nonlinear, geometrically exact beam formulation, whose description would by far exceed the scope of this thesis. The model itself is well-established and has the capability of fully accounting of the most essential elastic effects occurring in slender structures such as actin filaments: axial extension, bending, shear, and torsion. Due to the specificities of rotational

interpolation, it is practical writing down the discretized elastic forces and moments in a node-wise form. In brief, without further detailing the derivation, the discretized elastic forces and moments read

$$\mathbf{F}_s^{[k]} = \int_0^L \mathbf{W}_t'^{[k]} \mathbf{\Lambda} \mathbf{C}_f \boldsymbol{\gamma} ds, \quad (2.34)$$

$$\mathbf{M}_s^{[k]} = \int_0^L \mathbf{W}_t'^{[k]} \mathbf{\Lambda} \mathbf{C}_m \boldsymbol{\kappa} - \mathbf{W}_t^{[k] \circ} \mathbf{\Lambda} \mathbf{C}_f \boldsymbol{\gamma} ds, \quad (2.35)$$

where  $\boldsymbol{\gamma}$ ,  $\boldsymbol{\kappa}$  denote material strains and  $\mathbf{I}_t^{[k]}$  denotes the  $k^{\text{th}}$   $3 \times 3$  nodal block of  $\mathbf{I}_t$ .

**Viscous forces and moments** Due to the time discretization by an Implicit-Euler scheme, Equations (2.13) are discretized as

$$\mathbf{F}_{\text{visc}} = \int_0^L \mathbf{W}_t^T \mathbf{D}_t \mathbf{I}_t ds \frac{\mathbf{X}^i - \mathbf{X}^{i-1}}{\Delta t}, \quad (2.36a)$$

$$\mathbf{M}_{\text{visc}} = \int_0^L \mathbf{W}_r^T \mathbf{D}_r \frac{\Delta \boldsymbol{\theta}^i}{\Delta t} ds. \quad (2.36b)$$

Note that the damping matrices  $\mathbf{D}_t$  and  $\mathbf{D}_r$  are constant, i.e., strictly speaking, they apply only to straight, rigid rods. In view of the small curvature of the individual beam elements, this approximation is acceptable.

**Stochastic forces and moments** The discretized, stochastic, translational and rotational excitations are given by

$$\mathbf{F}_{\text{stoch}} = \sqrt{2k_B T} \int_0^L \mathbf{W}_t^T \mathbf{S}_t \frac{\partial^2 \mathcal{W}_t(s, t^i)}{\partial s \partial t} ds \approx \sum_{\text{IP}} \sqrt{\frac{2k_B T w_{\text{IP}}}{\Delta t}} [\mathbf{W}_t^T \mathbf{S}_t]_{s_{\text{IP}}} \boldsymbol{\mathcal{Z}}(0, 1), \quad (2.37a)$$

$$\mathbf{M}_{\text{stoch}} = \sqrt{2k_B T} \int_0^L \mathbf{W}_r^T \mathbf{S}_r \frac{\partial^2 \mathcal{W}_r(s, t^i)}{\partial s \partial t} ds \approx \sum_{\text{IP}} \sqrt{\frac{2k_B T w_{\text{IP}}}{\Delta t}} [\mathbf{W}_r^T \mathbf{S}_r]_{s_{\text{IP}}} \boldsymbol{\mathcal{Z}}(0, 1). \quad (2.37b)$$

Index IP loops over integration points,  $w_{\text{IP}}$  represent quadrature weights, and  $s_{\text{IP}}$  localizes the integration points in parameter space. Finally,  $\boldsymbol{\mathcal{Z}}(0, 1)$  denotes a vector-valued Gaussian random variable with zero mean and unit variance for each of its vector entries. The approximation of the stochastic terms is supported by theoretical considerations, which demonstrate the validity of a coarse-graining applied to  $\mathcal{W}$ . This coarse-graining results in piecewise constant stochastic contributions in space and time [37], which in turn lead to the formulae of Equation (2.37).

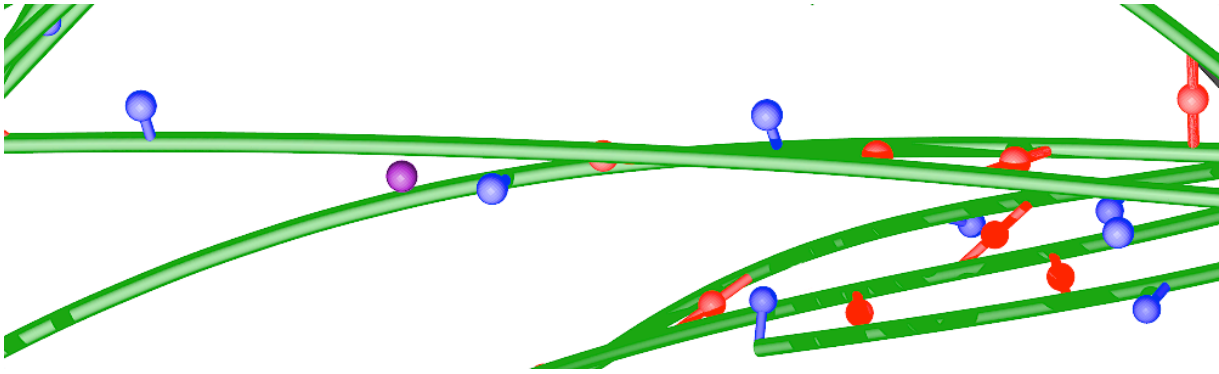


**Figure 2.2** All possible chemical states of a linker molecule: a *free* linker, which moves through the fluid driven by stochastic excitations and damped by viscous forces (●). *Singly bound* linkers are attached filaments with one of their reactive domains (●). Finally, linkers that have established a crosslink between two filaments, are called *doubly bound* (●).

**Deterministic external forces and moments** External forces and moments can be directly adopted from textbooks in the case of being accounted for by deterministic Neumann boundary conditions [29]. The evaluation of mechanical contact requires a discretized distance measure, that evaluates the existence of contact, and which is commonly referred to as the *gap function*. In case that contact is detected, the repulsion forces resulting from the contact interaction of contacting bodies are evaluated in their discrete form. Electrostatic interactions for now remain unconsidered due to being effectively shielded by the surrounding fluid.

## 2.6 Mechanical and chemical model of a linker molecule

In experiments, biomolecules, that can act as transient, reversible crosslinks, establish non-covalent connections with actin filaments [137]. Usually such linker molecules have two actin binding domains separated by a linker-specific distance  $2R_l$ . There are linkers with more than two actin binding domains. However, such variants are not accounted for at this point. In reality, linkers consist of more than just their chemically active domains and feature more complex geometries. As pointed out in Section 2.3.1, a simplified model is often sufficient and will be employed in the following.

### 2.6.1 Chemical states of a linker

In this idealized model, a linker can be found in three distinct chemical conditions, which are all present in Figure 2.2. Initially, a linker is a solute of the fluid phase and thus *free*. When it enters the vicinity of a potential binding site located on a filament, there is a certain probability of establishing a chemical bond to that filament. A linker, that has established one connection to a filament, is called *singly bound*. If the second reactive domain of linker happens to also bind to a filament, it is referred to as *doubly bound*. The linker then constitutes a *crosslink* between two filaments and contributes to the mechanical behavior of the network.

## 2.6.2 Free linkers in solution

A free linker, i.e., one which is not attached to any filament, can be modeled as a point-like particle in solution, which is why the notation immediately follows the discrete typeface convention. It has a centroid position  $\mathbf{x}_l$  and a velocity  $\dot{\mathbf{x}}_l$ . Around the position of the centroid, the linker model assumes a reaction volume in the shape of a spherical shell including radii  $R \in [R_l - \Delta R_l; R_l + \Delta R_l]$ . A linker is subject to stochastic thermal forces, viscous drag, and, in some cases, external forces of some kind. Its equation of motion reads

$$\mathbf{f}_{\text{visc},l}(\mathbf{x}_l, \dot{\mathbf{x}}_l, t^i) = \mathbf{f}_{\text{stoch},l}(\mathbf{x}_l, t^i) + \mathbf{f}_{\text{ext},l}(\mathbf{x}_l, t^i). \quad (2.38)$$

Subscripts follow the principle set up in Section 2.4.1, such that  $\mathbf{f}_{\text{visc},l}$ ,  $\mathbf{f}_{\text{stoch},l}$ , and  $\mathbf{f}_{\text{ext},l}$  denote forces due to viscous drag, stochastic forces, and deterministic external forces, respectively.

**Viscous forces** A free linker moving through the fluid phase feels viscous drag forces. Again, the effect of the fluid on linker is only modeled in terms of appropriate drag laws, neglecting whatever more complex interaction between fluid and solid particle might occur. Hence, the viscous force vector reads

$$\mathbf{f}_{\text{visc},l} = \zeta_l(\dot{\mathbf{x}}_l - \mathbf{v}(\mathbf{x}_l)) \quad (2.39)$$

with an effective friction coefficient  $\zeta_l = 6\pi\eta R_l$  in accordance to *Stoke's law* (cf. [88, Table 6.2]).

**Stochastic forces** A free linker performs Brownian motion in a thermal bath. As in the case of filaments, stochastic forces acting on a linker molecule can be modeled by a standard Wiener process  $\mathcal{W}_l(t^i) \in \mathbb{R}^{3 \times 1}$ . Then

$$\mathbf{f}_{\text{stoch},l} = \sqrt{2k_B T \zeta_l} \dot{\mathcal{S}}_l(t^i). \quad (2.40)$$

From Equations (2.39) and (2.40), it can be deduced that in absence of external forces and assuming a constant friction coefficient, one may simply update the spatial position of a linker during the current time step by

$$\mathbf{x}_l^i = \mathbf{x}_l^{i-1} + \sqrt{\frac{k_B T \Delta t}{\zeta_l}} \Delta \mathcal{W}_l^i, \quad (2.41)$$

where  $\Delta \mathcal{W}_l^i = \mathcal{W}_l(t^i) - \mathcal{W}_l(t^{i-1})$  is the increment of the Wiener process.

**External forces** In general, external forces due to excluded volume effects, electrostatic forces, or the application of some external force field influence the dynamics of a linker molecule. Such force contributions are neglected for now as the volume fraction of filaments and linkers combined is low, electrostatic effects are considered marginal in the context of semiflexible networks (cf. Section 2.4.2), and other deterministic external forces are not applied in order to keep the problem simple and the results interpretable.

### 2.6.3 Singly bound linkers

**Reaction kinetics** In Section 2.6.1, the chemical states of a linker have been described in general. The two-staged reaction involving linkers L and filaments F reads



with an experimentally measured chemical association rate constant  $k_+$  and a respective dissociation rate constant  $k_-$ . The association rate constant of this second order reaction depends on the reactants' concentrations and is given in units of  $M^{-1}s^{-1}$ , where  $M \equiv \text{mol/L}$  represents the molar concentration of a substance. The dissociation rate constant is given in  $s^{-1}$  owing to the reverse reaction being of order one.

Values for rate constants are mostly drawn from either in vivo and in vitro experiments or, alternatively, from MD simulations. Experimental values can be drawn from a variety of sources in literature, e.g., [152] provides experimentally measured rate constants for actin-myosin bonds ( $k_+ \sim 10^{-6} M^{-1}s^{-1}$ ,  $k_- \sim 0.1-1s^{-1}$ ). Other biologically relevant linker species like fascin,  $\alpha$ -actinin, or filamin feature dissociation rate constants on a similar range [133].

At this point, the question arises how to include the experimentally observed global rate constants  $k_+$  and  $k_-$  in a numerical model that explicitly accounts for the dynamics of single linker molecules. The single molecule association rate constant needs to model the likelihood of a binding event, when a linker and an unoccupied binding site enter each others' reaction volumes. In order to break reaction kinetics down to the level of single molecules, a modified rate constant  $k_{\text{on}}$  is required, which is deduced from chemical kinetics. The rate equation of the association of linkers to filaments reads

$$r_{LF} = k_+[L][F] \quad (2.43)$$

with bracketed terms denoting concentrations of the respective species. The requirement for the single molecule association rate is

$$k_{\text{on}} = Ck_+, \quad (2.44)$$

where  $C$  takes on the dimension of a concentration. The nature of this prefactor is readily explicable; it is the concentration corresponding to a *single* linker having entered the reaction volume  $V_{\text{react}}$  of a binding site, which is located on a filament (hence the "1" in Equation (2.45)). Consequently the unit of the modified rate constant is  $s^{-1}$ . Eventually, the in silico rate constants can be written as

$$k_{\text{on}} = N_A \frac{1}{V_{\text{react}}} k_+, \quad k_{\text{off}} = k_- \quad (2.45)$$

with Avogadro constant  $N_A = 6.022 \times 10^{23} \text{mol}^{-1}$ .  $V_{\text{react}}$  is a parameter of the numerical model and does not have a direct real-life equivalent. Isolated within  $V_{\text{react}}$ , the reaction can be interpreted as a pseudo-first order reaction, during which the linker switches from its free to its bound state. This assumption is valid here since the availability of a binding site at this stage is *guaranteed*. In other words, the concentration of binding sites within  $V_{\text{react}}$  can be considered so large that it can be factored in the rate constant.

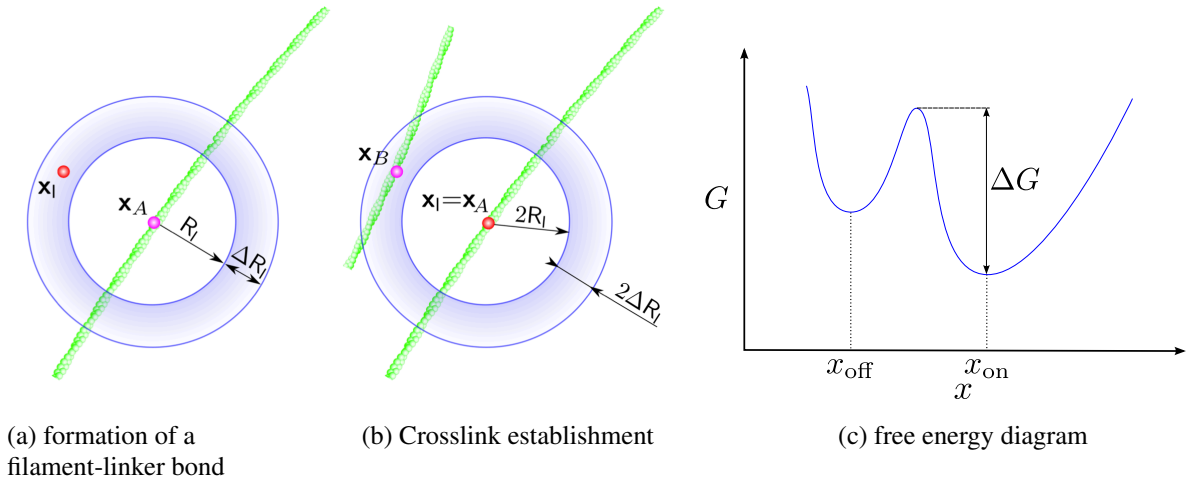


**Figure 2.3** Free linkers that are considered for the establishment of chemical bonds to binding sites on filaments have to fulfill a simple geometrical condition: (a) the linker molecule needs to enter the reactive volume of the binding site located at  $\mathbf{x}_A$ , which is modeled as a spherical shell with finite thickness but is only represented in 2D here for clarity. (b) The establishment of a crosslink adheres to the same pattern, only with a second binding site at location  $\mathbf{x}_B$ . However, the radius is changed corresponding to a linker that is free to swivel around its joint. Sketch of the free energy diagram clarifying the binding energy  $\Delta G$  of the chemical reaction.

**Binding events** When a free linker arrives in the vicinity of a binding site as illustrated in Figure 2.3 and their distance is  $\Delta_l = R_l \pm \Delta R_l$ , the binding probability can be calculated as

$$p_{\text{on}} = 1 - \exp(-k_{\text{on}}\Delta t), \quad (2.46)$$

which is the probability of a unit Poisson process with mean  $\mu = k_{\text{on}}\Delta t$  [180]. The probabilistic evaluation of the reaction potential on the level of single molecules is a common procedure in stochastic simulations (cf. [6]). As the linker is now attached to one filament (singly bound), its position is no longer updated independently, but is coupled to the movement of the filament. Binding to a second filament follows the same procedure.

Linkers attached to one filament may already change its hydrodynamic cross section, thus altering filament dynamics. However, it is assumed that this kind of alteration does not fundamentally change the dynamic behavior of a single filament in a way, that additional physical phenomena (e.g., fluid-structure interaction) have to be taken into account. Thus, such effects of singly bound linkers on a filament are neglected here. If need be, the effect may be incorporated into the model by modifying the filament's damping matrices  $\mathbf{D}_t$  and  $\mathbf{D}_r$  depending on the bonding status of the linker.

**Unbinding events** The chemical bond between a linker and a filament is reversible in most cases unless the reverse reaction is inhibited in some way. The bond F-actin and heavy meromyosin (HMM) ,e.g., can be made permanent by addition of glutaraldehyde [137]. This reverse reaction is modeled again as a Poisson process and the dissociation potential is given by

$$p_{\text{off}} = 1 - \exp(-k_{\text{off}}\Delta t). \quad (2.47)$$

Having introduced both binding and unbinding events, it is now possible to characterize the strength of the chemical bond by means of its binding energy

$$\Delta G = \ln \left( \frac{k_{\text{on}}}{k_{\text{off}}} \right). \quad (2.48)$$

The free energy diagram of this reaction helps visualizing  $\Delta G$  (Figure 2.3c): it represents the height of the energy wall that needs to be overcome in order to return the linker to its free state.

### 2.6.4 Doubly bound linkers: crosslinks

When linkers establish bonds with two filaments, they constitute *crosslinks*, i.e., they are doubly bound. As such, they alter the mechanical behavior of the network. On the one hand, they provide additional pathways for load transfer. On the other hand, they reduce the number of thermally excited eigenmodes of filaments, which entails structural stiffening.

These properties demand for a more complex model. As a consequence, a doubly bound linker is no longer modeled only as a point-shaped particle but as rod-like continuum. The underlying mechanical description is that of a beam with an adequate constitutive law and material parameters. The mechanical model described in Section 2.4 can be applied to doubly bound linkers as well. Hence, linkers can be discretized with finite beam elements applying the same principles as in the case of filaments. At this point, mechanical connections between separate filaments can be established between *nodes* of elements on separate filaments only. In Chapter 3, this restriction will be lifted by introducing extended models for both filaments and linkers.

## 2.7 Periodic boundary conditions

The filament model and the linker model as well as their chemical and mechanical interaction model stand ready to be applied. Using an unbounded simulation volume, however, leads to dispersion of filaments and linkers alike. In the context of discrete fiber simulations (e.g., [94, 115, 167]), periodic boundary conditions are a popular means to guarantee time- and – with respect to the control volume – space-invariance of an observed quantity, and to improve and facilitate statistics. In the following, mainly cubic simulation volumes with an edge length  $H$  will be used. By convention, the simulation box is located in the first octant and occupies the three-dimensional interval  $[0; H] \times [0; H] \times [0; H]$ . Any spatial position  $\bar{x}$  compliant to periodic boundary conditions can be given for each spatial component  $i$  by

$$\bar{x}_i = x_i - \lfloor H^{-1}x_i \rfloor H, \quad (2.49)$$

where  $x_i$  denotes the position before application of periodic boundary conditions and  $\lfloor \cdot \rfloor$  is the floor function. Rotations remain unaffected. A sensible ratio between the characteristic dimensions of a structure (e.g., the length of filaments) and the periodic repeat  $H$  helps to avoid *finite size effects* dominating the simulation outcome.

## 2.8 Concluding remarks

In this chapter, the methodic foundations of the numerical experiments presented in the following chapters have been laid. Mechanical models for filaments and linkers have been introduced. Both species interact with each other by means of a simple chemical reaction model as well as, if chosen, by mechanical contact. The high computational efficiency of the model allows for the simulation of large complex network structures over time intervals that cover most of the relevant processes within eukaryotic cells.

Based upon this numerical framework, further modeling steps are discussed in Chapter 3 and Chapter 4. While the former chapter recovers the molecular structure of filaments previously lost due to mechanical coarse-graining, the latter presents an approach to modeling molecular motor activity in biopolymer networks. In Chapter 5 and Chapter 6, which focus on advances in physics by means of simulations, theory, and experiments, the mechanical and chemical models provides the basis for all simulation-based research presented in this thesis.

# 3 Extended micromechanical approach – the reintroduction of sub-continuum microstructure

Any act of abstraction is inevitably accompanied by a loss of detail. The micromechanical model of Chapter 2 gains numerical efficiency by abstraction of its microstructure, which represents the essence of any mechanical continuum approach. Expressed most generally, it trades short length scales for long time scales. This chapter is about the retrieval of length scales *lost in abstraction*.

To this end, the filament model as well as the linker model are extended. The first extension provides geometrical information reminiscent of the monomeric architecture of the coarse-grained, and thus microstructurally featureless filament model. Obviously, the chemical topology of the filament is directly affected. The second extension enables the linker model to profit from the first. The joint goal of all measures to be presented is to gain access to a new set of biophysical problems without abandoning the advantages of the original approach.

This chapter is the second in a series of three methodic chapters and comprises three main parts. It will first elaborate in more detail on the necessity of model enhancements, including a brief discussion of a few shortcomings, that the current model still suffers from, and a selection of possible areas of application (Section 3.1). Subsequently, the reader will be acquainted with the methodic realization (Sections 3.2 and 3.3). Finally, both phenomenological and quantitative comparisons will be drawn between the original and the extended model in order to ensure equivalence (or more) in their capability to tackle problems on the network scale (Section 3.4).

## 3.1 Decoupling chemical and mechanical resolution

The original model in principle suffers from the same deficiency that eliminates MD simulation as a candidate for micromechanically modeling entire biopolymer network structures on the scale of 1 - 10 $\mu$ m: the inseparableness of the mechanical resolution from the chemical resolution, i.e., each mechanical base unit (in MD, a single molecule) is generally capable of chemical interaction. This property limits MD approaches to length scales well below the dimensions of a cell and to insufficiently large time scales for most cellular processes. The very same property also diminishes or in some cases may even nullifies one of the main advantages of the original FE approach [38]: computational efficiency gained by mechanical coarse-graining. In cases, where a fine chemical discretization is mandatory, the original model has to refine its mechanical discretization as well. The investigation of the mechanics of filament bundles often requires such a refinement (cf. [80]) in order to adequately model their *chirality*. The term chirality was first introduced by LORD KELVIN in [204] and applies to objects which cannot be superimposed on their mirror images. The human hand is perhaps the most prominent example

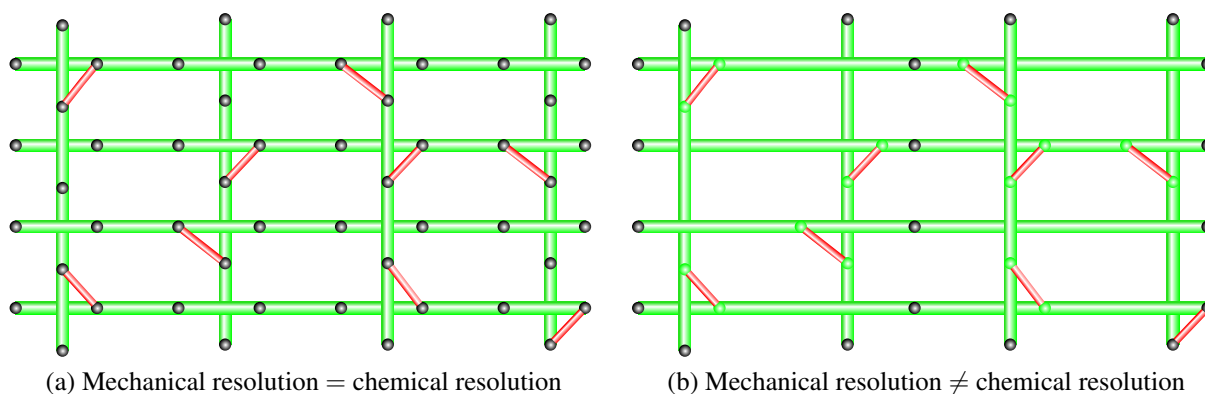


**Figure 3.1** Sketch of the basic modeling idea. (a) FE discretization and chemical resolution are equivalent. (b) the chemical resolution remains the same, while the mechanical discretization is chosen coarser.

for chirality. The helical geometry of F-actin has been shown to play an important role in the assembly of single filaments into chiral bundles [64]. Depending on the linker species, bundle systems can be self-limiting: the competing effects of chiral (over-)twist of the bundle and the bending of individual filaments result in an energetic trade-off, that becomes manifest in a finite bundle diameter. Self-limiting bundle systems have been observed experimentally [23, 190] and elaborated theoretically [63, 80, 85]. Their findings suggest that helicality can be crucial to the mechanism of self-limitation, which implies the necessity of resolving the monomeric structure of a filament. Globular actin, the monomeric subunit of F-actin, is a few nanometers in size. The resolution of this length scale with the original FE model would require the refinement of the discretization down to monomer level, which easily exceeds refinement factors of 50. Not only would the computational cost quickly increase to the point of infeasibility, but also would this step result in compromising the intention of the continuum approach, which definitely has not been introduced meticulously only to return to modeling monomers.

In light of this predicament, the straight-forward remedy lies with decoupling the chemical topology from the mechanical discretization of a filament. First of all, this means that the size of single beam elements discretizing a filament should remain constant at the very least, or – if possible – be increased further. Simply put: adjacent nodes should be placed as far apart from each other as possible while keeping the errors due to discretization within acceptable bounds. The considerations above can be condensed to formulate two basic modeling requirements:

- (I) Capability of placing discrete chemical interaction sites, whose location is independent of the location of FE nodes.
- (II) Capability of a linker beam element to establish a mechanical connection between two arbitrary locations on (not necessarily two separate) filaments.

If executed correctly, a computational framework including these two features allows for the simulation of high chemical resolutions at a nearly unchanged computational cost. On the other hand, it allows for an even coarser mechanical discretization in case of problems that the original approach could already handle, but for which an unnecessarily fine mechanical discretization had to be chosen.

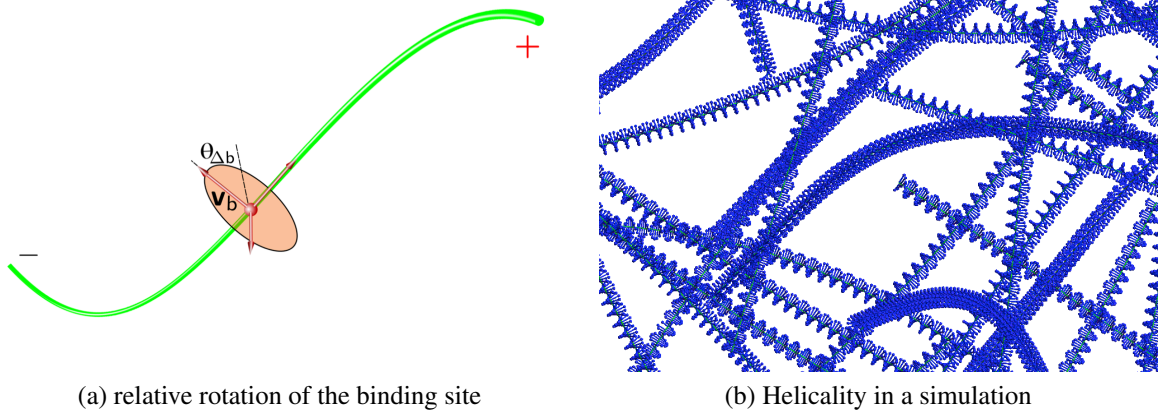


**Figure 3.2** (a) binding site orientation is considered fixed at a relative angle  $\theta_{\Delta b}$  with respect to the second principal axis  $\mathbf{v}_b$  of the material triad at the corresponding position. The first principal direction by convention points towards the (+)-end of the filament. (b) In silico semiflexible network with  $N_f = 104$  filaments, and  $L_f = 4 \mu\text{m}$ , corresponding to a filament concentration  $c_f = 2 \mu\text{M}$  and a molar ratio  $R = 1.0$  ( $N_l \approx 1.5 \times 10^5$  linkers). Binding sites with a spacing  $d_b = d_g = 2.77 \text{ nm}$  (i.e., all monomers are binding sites) are entirely occupied by singly bound linkers.

## 3.2 Extended filament model

First, the numerical model of the actin filament will be enhanced. It is the prelude to the subsequent and significantly more intricate extension of the numerical linker model in Section 3.3 and provides the chemical reaction sites, that become mechanical connections along the interpolated filament geometry, i.e., *between* physically existing FE nodes. All required instruments are readily available from the standard filament model presented in Chapter 2.

### 3.2.1 Parametrization of the monomeric structure of F-actin

Chapter 1 has already expanded on the molecular structure of actin filaments. Hence only properties directly related to model parameters are recalled here.

An actin filament consists of globular actin monomers (G-actin) organized in a structure, that can be seen either as a right-handed double helix with an offset of one monomer between the two strands or as a left-handed single helix [88]. See Figure 1.2d for a sketch of the helical arrangement of monomers, that constitute the filament. In the following, the latter description is used owing to its geometrical simplicity. A straight actin filament in its stress-free state features a rotation angle of  $\alpha \approx 166^\circ$  between one monomer of the helix to the next. The translational increment between two such consecutive G-actin units is  $d_g = 2.77 \text{ nm}$  [196]. The periodicity of the helix is  $D = 72 \text{ nm}$ , which corresponds to  $n_D = 26$  monomeric subunits per period. Although different linker species establish bonds with different chemical binding domains on the filament and do not necessarily bind equally to all monomers, the most generic case of a linker is portrayed here, which means it can in principle establish chemical bonds with an arbitrary monomer. In order to quantify the hypothesis of Section 3.1, the following example is given. The ratio of the FE length used later on in Chapter 5 and the monomeric distance mentioned above amounts to  $h_f/d_g \approx 45$ . Extrapolating this to a filament of length  $L_f = 5 \mu\text{m}$  implies discretizing it with  $N_e = 1805$  beam elements. Finally, considering not only one but hundreds of

simulated filaments, a refinement of this magnitude heavily affects the computational performance. With a rising number of DOFs, the overall simulation time is increasingly dominated by the linear solver. At this point, the only means to effectively increase computational efficiency is the reduction of system size, i.e., a reduction of DOFs.

The remedy for this shortcoming in terms of the filament model is simple, as the solution only requires making use of inherent features of the filament's continuum description. In the following, requirement (I) of Section 3.1 will be realized. To this end, it is necessary conveying helicity as a geometrical feature of the filament down to its constituting beam elements, i.e, the handling of interpolated joints (binding sites), rests with the respective finite element. Thus, with filament length  $L_f$  and the local element line parameter  $\xi \in [-1; 1]$ , a general map that links global (filament) parameter space to local (element) parameter space

$$\xi : [0; L_f] \rightarrow [-1; 1], s \mapsto \xi(s, L_f) \quad (3.1)$$

is defined, resulting in the availability of inter-nodal binding sites as illustrated by Figure 3.1. This simple measure already provides independent handles on binding site resolution and the mechanical discretization.

In a second step, binding sites are associated with an orientation, which can be motivated considering the helical structure of the actin filament and potential applications (cf. Section 3.1). The parametrization of rotations will be described in more detail in the subsequent Section 3.3. At this point, however, it is sufficient to state that each material point of the continuum has an associated orthonormal triad  $\mathbf{\Lambda}(s) \in \mathbb{R}^{3 \times 3}$  with base vectors  $\{\mathbf{u}, \mathbf{v}, \mathbf{w}\}$ , which describes the orientation of the (planar) cross section at location  $s$ . In analogy to Equation (3.1), a map is introduced governing the connection between location and orientation of the binding sites. It is generally defined as

$$\mathbf{\Lambda}_b : \xi(s) \mapsto \mathbf{\Lambda}_b(\xi(s)) \quad (3.2)$$

and can be practically realized by one of various mathematical parametrizations (e.g., rotation vectors, quaternions, Euler angles). Having the efficient and ready-to-use framework of the beam formulation at hand, orientations are treated by means of pseudo-vector representations. Hence, making use of Equations (3.16) and (3.17), one can describe the orientation of a binding site at local parameter  $\xi_b = \xi(s_b)$  as

$$\mathbf{\Lambda}_b(\xi_b) = \underbrace{\exp(\overset{\circ}{\boldsymbol{\theta}}_{\Delta b}(\xi_b))}_{=:\mathbf{\Lambda}_{\Delta b}} \mathbf{\Lambda}(\xi_b), \quad (3.3)$$

where the  $L^2$ -norm of the pseudo-vector  $\boldsymbol{\theta}_{\Delta b} = \|\boldsymbol{\theta}_{\Delta b}\|$  describes the angular difference to the second base vector of the interpolated triad, i.e., the material normal. The axis of rotation is given by  $\boldsymbol{\theta}_{\Delta b}/\boldsymbol{\theta}_{\Delta b} = \mathbf{u} = \mathbf{u}_b$ . The triad  $\mathbf{\Lambda}(\xi_b)$  denotes the material triad at the current binding site position. Recall from Section 2.4.2 that the  $\circ$ -operator denotes the skew-symmetric matrix representation of a pseudo-vector. In order to have the second base vector  $\mathbf{v}_b(s_b)$  of the associated triad describe a left-handed single helix,  $\boldsymbol{\theta}_{\Delta b}$  has to obey

$$\boldsymbol{\theta}_{\Delta b}(\xi_b) = \alpha \xi_b / d_b. \quad (3.4)$$

The distance between two consecutive binding sites on a filament  $d_b \geq d_g$  depends on the modeled linker species: HMM for example is known to bind to actin every  $d_b = 36$  nm [88], which corresponds to half a periodic repeat of F-actin. By design, the filament model is now chiral, which is illustrated by the simulation snapshot in Figure 3.2b.

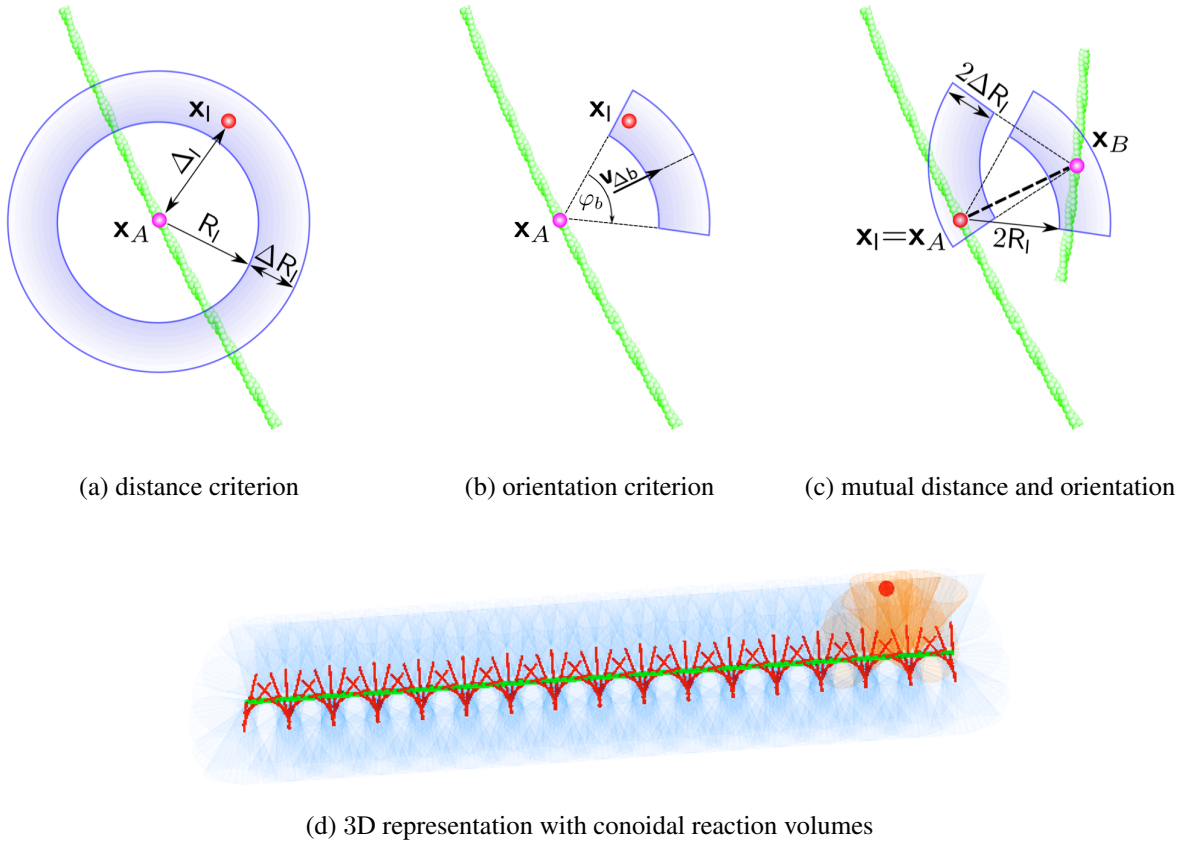


**Figure 3.3** Establishment of chemical filament-linker bonds with helically oriented reaction volumes: considered binding site (●) and free linker (●) lie apart  $R_l - \Delta R_l \leq \Delta_l \leq R_l + \Delta R_l$  (a). The linker is located in a cone with axial vector  $\mathbf{v}_{\Delta b}$  and may bind to the filament (b). The singly bound linker adopts the perspective of its binding site at  $\mathbf{x}_A$ . When its reaction volume and one of another binding site at  $\mathbf{x}_B$  overlap mutually as given, a crosslink is established. The thick dashed line indicates the linking direction (c). The volumes are reduced to 2D representations for clarity. A three-dimensional representation of a filament with physiologically spaced binding sites ( $d_b = d_g = 2.77$  nm) and conoidal reaction volumes (pale blue), some of which (orange) have just been entered by a linker (red). The reaction volumes' orientations  $\mathbf{v}_{\Delta b}$  are depicted as red lines (d).

### 3.2.2 Binding events and modified reaction volumes

Now that chirality has been introduced to the mechanical filament model from Section 2.4, the orientations of the reaction volumes treated accordingly. Theoretical work done on the subject of bundle size control assumes explicit orientations of binding sites [80]. An extension of the chemical reaction model of Section 2.6 will be presented, which incorporates all necessary means for the simulation of helically oriented binding sites and their respective reactive domains. Figure 3.3 illustrates the entire (reversible) reaction process, at which end a double bond between two binding sites  $\mathbf{x}_A, \mathbf{x}_B$  of two separate filaments is established.

- (I) *Distance criterion*: a linker with position  $\mathbf{x}_l$  has to be located in the reaction volume of a binding site (at position  $\mathbf{x}_A$ ), a spherical shell, satisfying  $R_l - \Delta R_l \leq \Delta_l \leq R_l + \Delta R_l$  (Figure 3.3a). The binding potential is given by Equation (2.46).

- (II) *Orientation criterion*: the conoidal reaction volume has an opening angle  $\varphi_b$  (Figure 3.3b). Only linkers located in this subvolume of the initial spherical shell are eligible for linking.
- (III) *Mutual overlap criterion*: In order to establish a crosslink between two filaments, the reaction volumes of the linker and the free binding site have to overlap in a way such that a binding corridor exists between positions  $\mathbf{x}_I$  and  $\mathbf{x}_B$  (Figure 3.3c).

### 3.2.3 Structural polarity of filaments

Actin filaments are polar macromolecules due their monomers being polar and oriented in the same direction. Filaments thus have two different ends, (+) and (–). Polarity affects polymerization rates as well as the traveling direction of myosin molecules, that attach to the filament. In view of modeling motor proteins such as myosin II (cf. Chapter 4), structural polarity is an essential property that needs to be accounted for. Polarity as a model feature is easily included by defining the direction of the first principal axis  $\mathbf{u}_b$  of triad  $\mathbf{\Lambda}_b$  as pointing towards the (+)-end (Figure 3.2a).

## 3.3 Extended linker model

The centerpiece of this chapter is a computational approach which allows linkers – or rather their beam element representations – to establish mechanical connections at positions that are located in between the FE nodes of filaments. The approach accomplishes this by enforcing equality of positions and orientations between the linker element and the binding site position on the filament.

### 3.3.1 Design concept

Simply put, a linker attaches to a filament and remains at its attachment site (until random detachment), which entails the formulation of a most basic and very intuitive requirement: the location of each of the two reactive domains of a linker must coincide with the location of the respective binding site of the filament for the duration of their chemical bond. The locations of the reactive domains are determined by the dynamics of the beam element representing the linker. The locations of the binding sites can be computed using the interpolation schemes of the BFE formulation of the filaments. Having determined both locations, a constraint must be defined, that relates these two locations in a way which reflects the kinematical and kinetic properties of the connection. An analogous train of thought leads to the definition of an appropriate rotational constraint.

### 3.3.2 Geometrical and mechanical interpolation and constraint formulation for a two-noded beam element

The applied BFE formulation coincides with the one used to discretize filaments (cf. Section 2.3.1), the main reason for this choice being its consistent and reliable handling of interpolated rotations in three-dimensional scenarios. Since it discretizes a crosslink, it is labeled element  $C$  from here on (cf. Figure 3.4a).

**Introduction of essential quantities and notation** Throughout the remaining chapter, it is advantageous to distinguish between two sets of quantities. Quantities attributed to the first set exist only implicitly in the frame of the interpolation and tying procedure. They will be indicated by the fractal letter  $\mathfrak{v}$  ( $\rightarrow$ virtual). The second set of quantities comprises everything that is accounted for by or explicitly leads to entries in the global system of equations. This second type will be marked with the fractal letter  $\mathfrak{r}$  ( $\rightarrow$ real). Element  $C$  establishes a mechanical connection between two beam elements  $A$  and  $B$  with two nodes, which usually (not necessarily!) belong to two separate filaments as depicted in Figure 3.4a. In principle, higher order Lagrange interpolation functions can be applied leading to a larger number of nodes for elements  $A$  and  $B$ . The advantage of higher order interpolation function lies with a reduced error due to discretization. Element  $C$  has two nodes, which is sufficient due to the high stiffness of the linker. These two nodes will eventually *not* factor into the global system of equations due to mathematical considerations presented later on. The nodal positions are given by vectors  $\mathbf{x}_{\mathfrak{v}A}$  and  $\mathbf{x}_{\mathfrak{v}B}$ . These rather elusive virtual nodes will be labeled  $\mathfrak{v}_A$  and  $\mathfrak{v}_B$ . The indices reflect that each interpolated node is assigned to one of the filaments' elements  $A$  or  $B$ . The computed mechanical quantities of nodes  $\mathfrak{v}_A$  and  $\mathfrak{v}_B$  are distributed onto four real nodes  $\mathfrak{r}_A^{[k]}$  and  $\mathfrak{r}_B^{[k]}$ , respectively, with superscripted nodal index  $k = \{1, 2\}$ . The locations of the virtual nodes in terms of the local scalar line parameters  $\xi_A$  and  $\xi_B$  are denoted as  $\tilde{\xi}_A$  and  $\tilde{\xi}_B$ . In general, from here on, the fractal characters  $\mathfrak{v}$  and  $\mathfrak{r}$  will indicate virtual and real quantities.

The method will only be discussed for the simplest case of Reissner beam elements  $A$  and  $B$  having two nodes. In principle, it is applicable to beam elements with an arbitrary number of nodes. In fact, it is independent of the type of beam element. Although there is a need to account for model-specific characteristics (e.g., the type of shape functions, the number of nodes per finite element, DOFs accounted for, or the technique of rotation interpolation, etc.), the fundamental idea is universal. It could thus be loosely referred to as *beam tying*, since geometrically *non-matching* nodes are mechanically tied together by a mathematical mapping procedure. The mechanical coupling between virtual and real nodes is achieved by

- (i) Formulation of suitable geometrical constraints concerning both translational and rotational DOFs of virtual nodes  $\mathfrak{v}_A$  and  $\mathfrak{v}_B$ , that are tied to the interpolated positions at  $\tilde{\xi}_A$  and  $\tilde{\xi}_B$  by these constraints.
- (ii) Linearization of the resulting nonlinear equations of motion.
- (iii) Elimination of the DOFs of the virtual nodes such that only the contributions of nodes  $\mathfrak{r}_A^{[k]}$  and  $\mathfrak{r}_B^{[k]}$  enter the global discretization.

In accordance to Equations (2.4), the translational position vector field and the rotation vector field of the continuum, which is discretized by element  $A$ , are given by  $\mathbf{x}_A(\xi_A) \in \mathbb{R}^{3 \times 1}$  and  $\mathbf{\Lambda}_A(\xi_A) \in \mathbb{R}^{3 \times 3}$ , respectively. For the continuum discretized by element  $B$ , analogous vector fields are denoted as  $\mathbf{x}_B(\xi_B)$  and  $\mathbf{\Lambda}_B(\xi_B)$ .

### 3.3.3 Linearized system of equations for a tied two-noded Reissner beam element

As a first step and for the purpose of a later application in the linearization of the modified residual, the linearized system of equations needs to be determined for a standard three-dimensional,

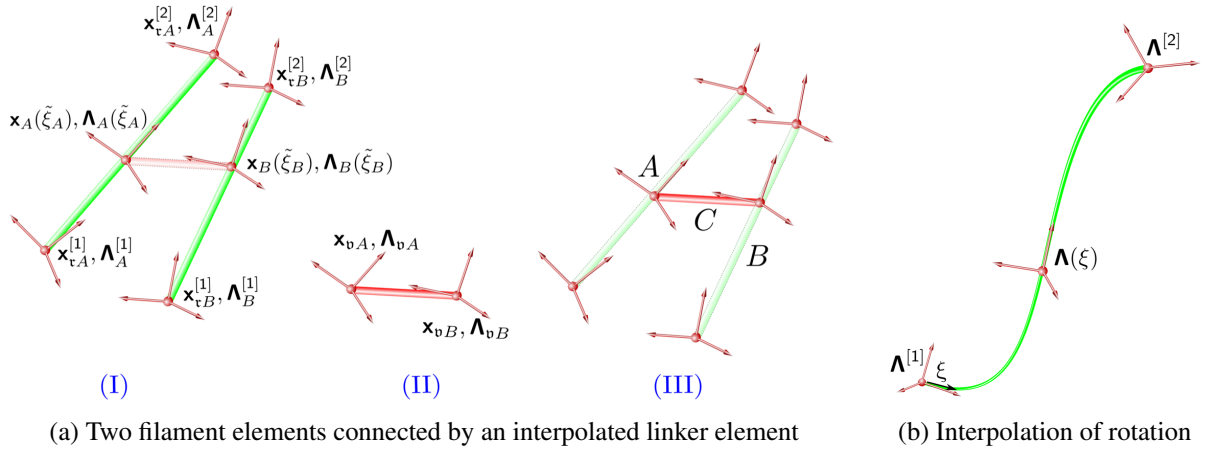


**Figure 3.4** (a) Internodal connectivity. (I) Two arbitrary beam elements  $A$  and  $B$  with interpolated triads  $\mathbf{\Lambda}_A(\tilde{\xi}_A)$ ,  $\mathbf{\Lambda}_B(\tilde{\xi}_B)$  at their interpolated (binding site) positions  $\mathbf{x}_A(\tilde{\xi}_A)$ ,  $\mathbf{x}_B(\tilde{\xi}_B)$ . (II) A two-noded crosslinker beam element with virtual nodal triads  $\mathbf{\Lambda}_{vA}$ ,  $\mathbf{\Lambda}_{vB}$  at their virtual node positions  $\mathbf{x}_{vA}$ ,  $\mathbf{x}_{vB}$ . (III) Virtual node positions and orientations are coupled to the interpolated positions and rotations of the four real nodes  $\mathbf{x}_{t\varepsilon}^{[k\varepsilon]}$ . (b) Sketch of the Interpolation of rotational triads along the line parameter  $\xi$  by means of rotation matrices  $\mathbf{\Lambda}$ .

geometrically exact, nonlinear Reissner beam element with two nodes. Here, the concrete example of the beam formulation by [103] is discussed.

**General remarks** In order to solve a nonlinear system of equations implicitly, one requires an iterative scheme, which minimizes a residual with respect to a (well-)chosen control quantity. The minimization procedure evaluates a linearized form of the system of nonlinear equations in a series of  $J \in \mathbb{N}^+$  iterative steps  $j$ . If the control quantity measuring the quality of the numerical approximation – usually a vector norm of the residual displacements and/or the residual itself – meets a given threshold during the  $J^{\text{th}}$  step, the scheme is considered converged. The residual represents the imbalance between all present internal and external forces due to the approximate character of numerical schemes in general. In many cases, *Newton methods* represent an adequate choice. However, aiming for increased efficiency and robustness in order to enable simulations on time intervals spanning several hundreds of seconds, additional measures in the form of a PTC scheme are taken [38, 56], modifying the tangential stiffness matrix  $\mathbf{K}$  by addition of artificial damping terms, that fade away once convergence within a  $J$  iterative steps is most probable. Essentially, increasing efficiency is synonymous to achieving larger time step sizes without deterioration of numerical accuracy. Increased robustness results in the recovery of convergence of the Newton scheme even if the informed guess of the predictor step or any of the following iterations is such that the radius of convergence is exceeded. As the discussion of iterative solution schemes does not substantially promote the understanding of the mechanical model, the reader is referred to [38, Appendix I], where the PTC scheme is presented in sufficient detail.

**Linearization procedure** The linearized problem for the interpolated element  $C$  can be denoted as a truncated Taylor series expansion around expansion point  $\mathbf{d}_v^{[j]}$ , i.e., all higher order terms are neglected leaving only the linear term involving the directional derivative of the

residual. Hence, the system of linearized equations

$$\mathbf{K}_v^{\{j\}} \Delta \mathbf{d}_v^{\{j\}} = -\mathbf{r}_v^{\{j\}} \in \mathbb{R}^{6 \times 1} \quad (3.5)$$

features the directional derivative

$$\mathbf{K}_v^{\{j\}} = \left. \frac{\partial \mathbf{r}_v^{\{j\}}}{\partial \mathbf{d}_v} \right|_{\mathbf{d}_v^{\{j\}}} \in \mathbb{R}^{6 \times 6}, \quad (3.6)$$

which is identified as the tangential element stiffness matrix of element  $C$  for the  $j^{\text{th}}$  iterative step. For the remaining part of this section, the superscript  $j$  is dropped from quantities, that obviously depend on the iterative step number. Hence, unless explicitly specified, all symbols (except for the interpolation function matrices) relate to the  $j^{\text{th}}$  iterative step. The tangential stiffness matrix is obtained by linearization of the weak form. The linearized residual of the interpolated beam element  $C$  reads

$$\text{Lin } \delta \Pi = \underbrace{\begin{pmatrix} \delta \mathbf{u}_v \\ \delta \boldsymbol{\vartheta}_v \end{pmatrix}}_{=\delta \mathbf{d}_v}{}^T \overbrace{\left[ \underbrace{\begin{pmatrix} \mathbf{r}_{vt} \\ \mathbf{r}_{vr} \end{pmatrix}}_{=\mathbf{r}_v} + \underbrace{\begin{bmatrix} \mathbf{K}_v^{uu} & \mathbf{K}_v^{u\vartheta} \\ \mathbf{K}_v^{\vartheta u} & \mathbf{K}_v^{\vartheta\vartheta} \end{bmatrix}}_{=\mathbf{K}_v} \underbrace{\begin{pmatrix} \Delta \mathbf{u}_v \\ \Delta \boldsymbol{\vartheta}_v \end{pmatrix}}_{=\Delta \mathbf{d}_v} \right]}_{\text{Lin } r \stackrel{!}{=} 0} = 0. \quad (3.7)$$

As before, the index  $v$  indicates quantities attributed to the virtual nodes of the interpolated beam element  $C$ . The variations of the nodal translational and rotational displacements of the virtual nodes as well as the linearized displacements are given by

$$\delta \mathbf{d}_v = \left( \delta \mathbf{u}_v^{[1]T} \quad \delta \mathbf{u}_v^{[2]T} \quad \delta \boldsymbol{\vartheta}_v^{[1]T} \quad \delta \boldsymbol{\vartheta}_v^{[2]T} \right)^T \in \mathbb{R}^{12 \times 1}, \quad (3.8a)$$

$$\Delta \mathbf{d}_v = \left( \Delta \mathbf{u}_v^{[1]T} \quad \Delta \mathbf{u}_v^{[2]T} \quad \Delta \boldsymbol{\vartheta}_v^{[1]T} \quad \Delta \boldsymbol{\vartheta}_v^{[2]T} \right)^T \in \mathbb{R}^{12 \times 1}. \quad (3.8b)$$

Furthermore, the vector of residual forces is denoted as  $\mathbf{r}_v$ , and  $\mathbf{K}_v$  is the element stiffness matrix. The individual terms of the element stiffness matrix are given in Appendix A.

Next, in order to tie the interpolated beam element  $C$  to beam elements  $A$  and  $B$  at arbitrary inter-nodal positions, constraints must be formulated that keep element  $C$  fixed to its positions and orientations at its locations on these elements.

### 3.3.4 Constraint formulations

**Translational constraints** The enforcement of translational constraints is by far easier than it is for rotations, which is why it will be discussed first. Both elements  $A$  and  $B$  in principle receive the same mathematical treatment, that is to say their mechanical interaction with element  $C$  is modeled the same way. Hence, from here on, instead of writing down equations twice, the placeholder  $\mathcal{E} \in \{A, B\}$  will indicate relevance for both elements. Let the vector

$$\mathbf{x}_{\tau \mathcal{E}}^i = \left( \mathbf{x}_{\tau \mathcal{E}}^{[1]T} \quad \mathbf{x}_{\tau \mathcal{E}}^{[2]T} \right)^T \in \mathbb{R}^{6 \times 1} \quad (3.9)$$

with nodal positions  $\mathbf{x}_{\tau \mathcal{E}}^{[k]} \in \mathbb{R}^{3 \times 1}$ , that hold the values of the FE approximation of the continuous solution  $\mathbf{x}_{\mathcal{E}}$ . The superscripted  $i$  marks the  $i^{\text{th}}$  discrete time step as introduced in Chapter 2.

As before, from here on throughout this chapter, temporal index  $i$  will be omitted in order to maintain an as simple as possible notation. Using interpolation function matrix  $\mathbf{l}_t(\xi) \in \mathbb{R}^{3 \times 6}$ , the interpolated positions in  $\mathbb{R}^3$  may be readily calculated by

$$\mathbf{x}_\varepsilon(\xi_\varepsilon) = \mathbf{l}_t(\xi_\varepsilon)\mathbf{X}_{\tau\varepsilon}, \quad (3.10)$$

where matrix  $\mathbf{l}_t$  is in principle given by Equation (2.25) and contains linear nodal shape functions  $l_t^{[1]} = (1 - \xi)/2$  and  $l_t^{[2]} = (1 + \xi)/2$ . Note that  $s \in [0; L_e]$  is commonly used in the literature on beams (e.g., [103]). It needs to be mapped to FE parameter space  $\xi \in [-1; 1]$  with the help of  $\tilde{\mathcal{J}} = ds/d\xi = \|\mathbf{x}_{0,\xi}\|$ . The notation  $(\cdot)_{,\xi}$  means the derivative with respect to  $\xi$ . In some cases, an explicit dependence on the global line parameter  $s$  instead of  $\xi$  is required (e.g. for the rotational interpolation in Equation (3.24)). Whenever possible, the local parameter will be applied.

One may now formulate a vector-valued translational constraint, that ensures a fixed distance between the positions of the two nodes and the respective interpolated positions. With the position vector of the virtual nodes of element  $C$ ,  $\mathbf{X}_v = (\mathbf{x}_{vA}^T \quad \mathbf{x}_{vB}^T)^T$ , and the nodal position vector of the real nodes  $\mathbf{X}_\tau = (\mathbf{X}_{\tau A}^T \quad \mathbf{X}_{\tau B}^T)^T$ , the constraint reads

$$\mathbf{H}_t = \mathbf{X}_v - \tilde{\mathbf{X}} = \begin{bmatrix} \tilde{\mathbf{1}} & -\tilde{\mathbf{l}}_t \end{bmatrix} \begin{bmatrix} \mathbf{X}_v \\ \mathbf{X}_\tau \end{bmatrix} \in \mathbb{R}^{6 \times 1}, \quad (3.11)$$

where  $\tilde{\mathbf{X}}$  denotes the vector of interpolated positions and  $\tilde{\mathbf{1}} \in \mathbb{R}^{6 \times 6}$  an appropriately dimensioned identity matrix in order to fit the interpolation function matrix

$$\tilde{\mathbf{l}}_t = \begin{bmatrix} \mathbf{l}_t(\tilde{\xi}_A) & \mathbf{0} \\ \mathbf{0} & \mathbf{l}_t(\tilde{\xi}_B) \end{bmatrix} \in \mathbb{R}^{6 \times 12}, \quad (3.12)$$

which in conjunction with  $\mathbf{X}_\tau$  determines the interpolated coupling positions on elements  $A$  and  $B$ . The formulation of translational constraints clearly does not pose a problem and is readily implemented. Note that the constraint is given in a general way, leaving open how exactly the constraint is fulfilled. In the most simple case of equality constraints,  $\mathbf{H}_t = \mathbf{0}$ .

Accordingly, the variation of the translational constraint can be written as

$$\delta\mathbf{H}_t = \delta\mathbf{u}_v - \delta\tilde{\mathbf{u}} = \begin{bmatrix} \tilde{\mathbf{1}} & -\tilde{\mathbf{l}}_t \end{bmatrix} \begin{bmatrix} \delta\mathbf{u}_v \\ \delta\mathbf{u}_\tau \end{bmatrix} = \mathbf{0} \in \mathbb{R}^{6 \times 1}. \quad (3.13)$$

with the variations of the four *real* nodes  $\delta\mathbf{u}_\tau = (\delta\mathbf{u}_{\tau A}^T \quad \delta\mathbf{u}_{\tau B}^T)^T$ . In order to complete the translational constraint formulation, its linearization with  $\Delta\mathbf{u}_\tau = (\Delta\mathbf{u}_{\tau A}^T \quad \Delta\mathbf{u}_{\tau B}^T)^T$  is given by

$$\Delta\mathbf{H}_t = \begin{bmatrix} \tilde{\mathbf{1}} & -\tilde{\mathbf{l}}_t \end{bmatrix} \begin{bmatrix} \Delta\mathbf{u}_v \\ \Delta\mathbf{u}_\tau \end{bmatrix} = \mathbf{0} \in \mathbb{R}^{6 \times 1}. \quad (3.14)$$

**Rotational constraints** Mathematical measures constraining the orientation of the linker cross section are more complicated than their translational analogs. The interpolation of rotations requires specific procedures, which are only briefly outlined in the course of the chapter as

this topic is as vast as it is intricate. The following procedure applies to the beam formulation of [103], which is used throughout the chapter. The basic course of action, however, remains the same as in the translational case.

As an essential requirement, interpolated triads need to be accessible by means of an unambiguous parametrization. This is achieved as follows. The parameter describing the rotational field is the local rotational pseudo vector  $\boldsymbol{\psi}_{l\mathcal{E}}(\xi_{\mathcal{E}})$ . It is conveniently interpolated between nodes  $\mathbf{r}_{\mathcal{E}}^{[1]}$  and  $\mathbf{r}_{\mathcal{E}}^{[2]}$  by

$$\boldsymbol{\psi}_{l\mathcal{E}}(\xi_{\mathcal{E}}) = \mathbf{I}_t(\xi_{\mathcal{E}}) \left[ (\boldsymbol{\psi}_{l\mathcal{E}}^{[1]})^T \quad (\boldsymbol{\psi}_{l\mathcal{E}}^{[2]})^T \right]^T \in \mathbb{R}^{3 \times 3} \quad (3.15)$$

The reader's attention is directed towards the fact that linear interpolation *is* possible without the loss of objectivity in the case of the *local* pseudo vector, which represents the rotation with respect to a reference frame  $\boldsymbol{\Lambda}_R$  fixed to the element. By contrast, this interpolation is incorrect for the case of *global* rotation vectors. The local pseudo vectors  $\boldsymbol{\psi}_{l\mathcal{E}}^{[1]}$  and  $\boldsymbol{\psi}_{l\mathcal{E}}^{[2]}$  represent the rotations of triads fixed at nodes  $\mathbf{r}_{\mathcal{E}}^{[1]}$  and  $\mathbf{r}_{\mathcal{E}}^{[2]}$ . The interpolated rotational field can be described by a compound rotation

$$\boldsymbol{\Lambda}_{\mathcal{E}}(\xi_{\mathcal{E}}) = \boldsymbol{\Lambda}_{R\mathcal{E}} \exp(\overset{\circ}{\boldsymbol{\psi}}_{l\mathcal{E}}(\xi_{\mathcal{E}})) \quad (3.16)$$

with a reference triad

$$\boldsymbol{\Lambda}_{R\mathcal{E}} = \boldsymbol{\Lambda}_{\mathcal{E}}^{[1]} \exp(\overset{\circ}{\boldsymbol{\phi}}_{1/2}) \quad (3.17)$$

as illustrated in Figure 3.4b. In principle, the referential orientation can be chosen arbitrarily. Here, by definition, the relative rotation  $\boldsymbol{\phi}_{1/2} := 0.5 \boldsymbol{\phi}_{\mathcal{E}}^{[12]}$  is chosen, which describes the state of rotation halfway between both nodes [30]. It can be computed from the rotation from the first onto the second node

$$\exp(\overset{\circ}{\boldsymbol{\phi}}_{\mathcal{E}}^{[12]}) = \boldsymbol{\Lambda}_{\mathcal{E}}^{[1]T} \boldsymbol{\Lambda}_{\mathcal{E}}^{[2]} \quad (3.18)$$

with the two nodal rotation matrices  $\boldsymbol{\Lambda}_{\mathcal{E}}^{[k]} \in \mathbb{R}^{3 \times 3}$ . The interpolated triad from Equation (3.16) can be expressed by other means, e.g., by the corresponding rotational pseudo-vector  $\boldsymbol{\theta}_{\mathcal{E}}(\xi_{\mathcal{E}})$ .

The variety of possible parametrizations of rotations entails an equally large variety of potential constraint formulations. One such formulation will be presented, which enforces constraints on the basis of pseudo-vector representations of rotations. To this end, rotation couplings  $\{\boldsymbol{\Lambda}_{vA}, \boldsymbol{\Lambda}_A(\tilde{\xi}_A)\}$  and  $\{\boldsymbol{\Lambda}_{vB}, \boldsymbol{\Lambda}_B(\tilde{\xi}_B)\}$  have to be created by constraining rotation differences  $\boldsymbol{\Lambda}_{\Delta A}$  and  $\boldsymbol{\Lambda}_{\Delta B}$ , respectively. In advance, the reader is again reminded of the notation  $\mathcal{E} \in \{A, B\}$ , which avoids repetition of formulae due to elements  $A$  and  $B$  being treated equally. As stated above, the approach constrains the mechanical system in terms of the rotation difference  $\boldsymbol{\Lambda}_{\Delta\mathcal{E}}$ , which is computed from

$$\boldsymbol{\Lambda}_{\Delta\mathcal{E}} = \boldsymbol{\Lambda}_{v\mathcal{E}} \boldsymbol{\Lambda}_{\mathcal{E}}^T(\tilde{\xi}_{\mathcal{E}}). \quad (3.19)$$

Given a matrix representation of the rotation difference  $\boldsymbol{\Lambda}_{\Delta\mathcal{E}}$  and its pseudo-vector counterpart  $\boldsymbol{\theta}_{\Delta\mathcal{E}} \in \mathbb{R}^{3 \times 1}$ , the constraint function can be defined in general as

$$\mathbf{H}_{r\mathcal{E}} : \mathbb{R}^{3 \times 3} \rightarrow \mathbb{R}^{3 \times 1}, \boldsymbol{\Lambda}_{\Delta\mathcal{E}} \mapsto \boldsymbol{\theta}_{\Delta\mathcal{E}}. \quad (3.20)$$

In the present case,  $\mathbf{H}_{r\mathcal{E}} = \mathbf{0}$ . Individual constraints have to be formulated for each of the two interpolated nodes tied to elements  $\mathcal{E}$ . Each nodal constraint reads

$$\boldsymbol{\Lambda}_{v\mathcal{E}} \stackrel{!}{=} \boldsymbol{\Lambda}_{\mathcal{E}}(\tilde{\xi}_{\mathcal{E}}) = \boldsymbol{\Lambda}_{R\mathcal{E}} \exp(\overset{\circ}{\boldsymbol{\psi}}_{l\mathcal{E}}(\tilde{\xi}_{\mathcal{E}})). \quad (3.21)$$

The variation of this rotational constraint is best expressed by means of spin variables. It is given by

$$\delta\boldsymbol{\vartheta}_{v\mathcal{E}} \stackrel{!}{=} \delta\boldsymbol{\vartheta}_{\mathcal{E}}(\tilde{\xi}_{\mathcal{E}}) = \mathbf{I}_{t\mathcal{E}}(\tilde{\xi}_{\mathcal{E}})\delta\boldsymbol{\vartheta}_{t\mathcal{E}} \in \mathbb{R}^{3 \times 1}, \quad (3.22)$$

where  $\delta\boldsymbol{\vartheta}_{t\mathcal{E}} = (\delta\boldsymbol{\vartheta}_{t\mathcal{E}}^{[1]\top} \quad \delta\boldsymbol{\vartheta}_{t\mathcal{E}}^{[2]\top})^\top$  denotes the variations of the nodal spin variables of element  $\mathcal{E}$ . Note that the nodal translational interpolation function  $\mathbf{I}_{t\mathcal{E}} \in \mathbb{R}^{3 \times 3}$  (cf. Equation (2.25)) is applicable here. The linearization of the rotational constraint yields

$$\Delta\boldsymbol{\vartheta}_{v\mathcal{E}} \stackrel{!}{=} \Delta\boldsymbol{\vartheta}_{\mathcal{E}}(\tilde{\xi}_{\mathcal{E}}) = \mathbf{I}_{r\mathcal{E}}(\tilde{\xi}_{\mathcal{E}})\Delta\boldsymbol{\vartheta}_{t\mathcal{E}} \quad (3.23)$$

with the matrix of nodal rotational shape functions of element  $\mathcal{E}$  as  $\mathbf{I}_{r\mathcal{E}} = [\mathbf{I}_r^{[1]} \quad \mathbf{I}_r^{[2]}] \in \mathbb{R}^{3 \times 6}$ . According to [103], the linearized spin variables  $\Delta\boldsymbol{\vartheta}_{t\mathcal{E}} = (\Delta\boldsymbol{\vartheta}_{t\mathcal{E}}^{[1]\top} \quad \Delta\boldsymbol{\vartheta}_{t\mathcal{E}}^{[2]\top})^\top$  cannot be interpolated as conveniently as their variations from Equation (3.22), in which case a simple linear interpolation scheme is sufficient. As stated in [103], the shape function  $\mathbf{I}_{r\mathcal{E}}$  allows for the interpolation in the  $SO(3)$  and preserves objectivity. The shape function of the  $k^{\text{th}}$  node is given by

$$\mathbf{I}_r^{[k]}(\xi) = \boldsymbol{\Lambda}_{R\mathcal{E}} \left[ \left( \mathbf{1} - \mathbf{T}^{-1}(\boldsymbol{\psi}_{l\mathcal{E}}(s)) \mathbf{I}_t^{[k]}(\xi) \mathbf{T}(\boldsymbol{\psi}_{l\mathcal{E}}^{[k]}) \right) \mathbf{V}^{[k]} + \mathbf{I}_t^{[k]}(\xi) \mathbf{T}^{-1}(\boldsymbol{\psi}_{l\mathcal{E}}(\xi)) \mathbf{T}(\boldsymbol{\psi}_{l\mathcal{E}}^{[k]}) \right] \boldsymbol{\Lambda}_{R\mathcal{E}}^\top \quad (3.24)$$

with the transfer matrix

$$\mathbf{T}(\boldsymbol{\theta}) = \frac{\boldsymbol{\theta}\boldsymbol{\theta}^\top}{\theta^2} + \frac{\theta/2}{\tan(\theta/2)} \left( \mathbf{E} - \frac{\boldsymbol{\theta}\boldsymbol{\theta}^\top}{\theta^2} \right) - \frac{1}{2} \mathring{\boldsymbol{\theta}} \in \mathbb{R}^{3 \times 3}, \quad (3.25)$$

which relates the additive nodal variations  $\delta\boldsymbol{\theta}$  to the non-additive nodal variations  $\delta\boldsymbol{\vartheta}$  by

$$\delta\boldsymbol{\theta} = \mathbf{T}(\boldsymbol{\theta})\delta\boldsymbol{\vartheta}. \quad (3.26)$$

The inverse of Equation (3.25) is denoted as

$$\mathbf{T}^{-1}(\boldsymbol{\theta}) = \frac{\sin \theta}{\theta} \mathbf{1} + \frac{1}{\theta^2} \left( \mathbf{1} - \frac{\sin \theta}{\theta} \right) \boldsymbol{\theta}\boldsymbol{\theta}^\top + \frac{1}{2} \left( \frac{\sin(\theta/2)}{\theta/2} \right)^2 \mathring{\boldsymbol{\theta}}. \quad (3.27)$$

Finally, the summarized contributions of the node-to-node rotation  $\boldsymbol{\Phi}^{[12]}$  are given node-wise by

$$\mathbf{V}^{[1]} = \frac{1}{2} \left( \mathbf{1} + \frac{1}{\boldsymbol{\Phi}^{[12]}} \tan \frac{\boldsymbol{\Phi}^{[12]}}{4} \right) \mathring{\boldsymbol{\Phi}}^{[12]}, \quad \mathbf{V}^{[2]} = \frac{1}{2} \left( \mathbf{1} - \frac{1}{\boldsymbol{\Phi}^{[12]}} \tan \frac{\boldsymbol{\Phi}^{[12]}}{4} \right) \mathring{\boldsymbol{\Phi}}^{[12]}. \quad (3.28)$$

The symbol  $\mathbf{1} \in \mathbb{R}^{3 \times 3}$  denotes an identity tensor. The transfer matrix in Equation (3.25) arises from rather lengthy derivations and, for example, can be found in [17, 99]. In contrast to translational interpolation schemes, the rotational interpolation functions (3.24) explicitly depend on the current, deformed configuration.

The final step towards the completion of the new formulation introduces the rotational tying matrix  $\tilde{\mathbf{I}}_r$ , which is a block-diagonal matrix of the form

$$\tilde{\mathbf{I}}_r = \begin{bmatrix} \mathbf{I}_r^{[1]}(\tilde{\xi}_A) & \mathbf{I}_r^{[2]}(\tilde{\xi}_A) & \mathbf{0} & \mathbf{0} \\ \mathbf{0} & \mathbf{0} & \mathbf{I}_r^{[1]}(\tilde{\xi}_B) & \mathbf{I}_r^{[2]}(\tilde{\xi}_B) \end{bmatrix} \in \mathbb{R}^{6 \times 12}. \quad (3.29)$$

This matrix assembles the known nodal interpolation functions  $\mathbf{l}_r^{[k]}$  into a form which facilitates the incorporation into the linearized system of equations. At this point, all pieces of the puzzle have been gathered. The next and final step is to piece them together in order to acquire the linearized form of the constrained problem.

Before proceeding to the linearized problem, the element spin variables as well as their variations and increments are assembled in the respective spin variable vectors  $\boldsymbol{\vartheta}_\tau = (\boldsymbol{\vartheta}_{\tau A}^\top \quad \boldsymbol{\vartheta}_{\tau B}^\top)^\top$ ,  $\delta\boldsymbol{\vartheta}_\tau = (\delta\boldsymbol{\vartheta}_{\tau A}^\top \quad \delta\boldsymbol{\vartheta}_{\tau B}^\top)^\top$ , and  $\Delta\boldsymbol{\vartheta}_\tau = (\Delta\boldsymbol{\vartheta}_{\tau A}^\top \quad \Delta\boldsymbol{\vartheta}_{\tau B}^\top)^\top$ .

### 3.3.5 Linearized system of equations of the constrained problem

The constraints demand the equality of positions and orientations of virtual and real nodes, which is expressed by  $\mathbf{H}_t = \mathbf{H}_r = \mathbf{0}$ . The modified stiffness matrix can be written as

$$\mathbf{K}_\tau(\mathbf{d}_\tau) = \begin{pmatrix} \tilde{\mathbf{l}}_t^\top \\ \tilde{\mathbf{l}}_r^\top \end{pmatrix} \begin{bmatrix} \mathbf{K}_b^{uu} & \mathbf{K}_b^{u\vartheta} \\ \mathbf{K}_b^{\vartheta u} & \mathbf{K}_b^{\vartheta\vartheta} \end{bmatrix} \begin{pmatrix} \tilde{\mathbf{l}}_t \\ \tilde{\mathbf{l}}_r \end{pmatrix}, \quad (3.30)$$

which for the case of two-noded beam elements has the dimension  $\mathbb{R}^{24 \times 24}$ . The element force vector is given by

$$\mathbf{r}_\tau(\mathbf{d}_\tau) = \begin{pmatrix} \tilde{\mathbf{l}}_t^\top \mathbf{r}_{bt} \\ \tilde{\mathbf{l}}_r^\top \mathbf{r}_{br} \end{pmatrix}. \quad (3.31)$$

In the end, the tangential stiffness matrix  $\mathbf{K}_\tau$  and the element force vector  $\mathbf{r}_\tau$  solely depend on the displacement vector  $\mathbf{d}_\tau = (\mathbf{u}_\tau^\top \quad \boldsymbol{\vartheta}_\tau^\top)^\top \in \mathbb{R}^{24 \times 1}$  of the four real nodes  $\mathbf{r}_\tau^{[k]}$ . With its variation  $\delta\mathbf{d}_\tau = (\delta\mathbf{u}_\tau^\top \quad \delta\boldsymbol{\vartheta}_\tau^\top)^\top$  and the linearization  $\Delta\mathbf{d}_\tau = (\Delta\mathbf{u}_\tau^\top \quad \Delta\boldsymbol{\vartheta}_\tau^\top)^\top$ , the resulting linearized residual reads

$$\text{Lin } \delta\Pi_\tau = \delta\mathbf{d}_\tau^\top \underbrace{[\mathbf{r}_\tau(\mathbf{d}_\tau) + \mathbf{K}_\tau \Delta\mathbf{d}_\tau]}_{\text{Lin } \mathbf{r}_\tau} = 0 \Rightarrow \mathbf{r}_\tau(\mathbf{d}_\tau) + \mathbf{K}_\tau \Delta\mathbf{d}_\tau = \mathbf{0}. \quad (3.32)$$

This linearized formulation can be readily incorporated into a FE framework in accordance to standard textbook procedures (e.g., [234]).

### 3.3.6 A preview on constraint enforcement by Lagrange multipliers

It has been emphasized that the chosen constraints  $\mathbf{H}_t = \mathbf{H}_r = \mathbf{0}$  are the most simple ones to enforce and effectively do not even require the introduction of additional DOFs, which was demonstrated in the course of this chapter. However, the physical reality might not always be as simple as it fortunately is for the case of chemical bonds which are fixed to their bonding location. With increasing kinematical and kinetic complexity, the formulation of the constraint has to be more sophisticated as well.

At this point, it seems worthwhile introducing the fundamental ideas behind Lagrange multipliers, which can be utilized in the formulation of constrained optimization problems. In a mathematical sense, optimization seeks to find the best solution out of some problem-specific

set of possible solutions. To this end, Lagrange multipliers represent a popular means of minimizing an objective function

$$y(\mathbf{x}) : \mathbb{R}^{N_d} \rightarrow \mathbb{R}, \quad N_d \geq N_c, \quad (3.33)$$

whose solution space is constrained by a secondary function  $\mathbf{c}(\mathbf{x}) = \mathbf{0}$  containing constraints in  $N_c$  dimensions. In the context of the previously presented application, these constraints arise from the requirement of spatial and orientational congruence of pairs of material points. However, as implied, more complex constraint function could be required. Eventually one arrives at the formulation of a constrained optimization problem

$$\min_{\mathbf{x}} (y(\mathbf{x}) | \mathbf{c}(\mathbf{x})). \quad (3.34)$$

The introduction of Lagrange multipliers  $\boldsymbol{\lambda} \in \mathbb{R}^{N_c}$  leads to a modified objective function

$$y_{mod}(\mathbf{x}, \boldsymbol{\lambda}) = y(\mathbf{x}) + \boldsymbol{\lambda} \cdot \mathbf{c}(\mathbf{x}). \quad (3.35)$$

In order to minimize this expression, one has to find  $\mathbf{x}^*$  such that the variation of  $y_{mod}$

$$\delta y_{mod}(\mathbf{x}) = \delta y(\mathbf{x}) + \delta \boldsymbol{\lambda} \cdot \mathbf{c} + \boldsymbol{\lambda} \cdot \delta \mathbf{c}(\mathbf{x}) \stackrel{!}{=} 0. \quad (3.36)$$

In-depth information on the formulation of constraints in numerics can be drawn from [146].

**Incorporation into the weak form** Lagrange multipliers are introduced into the system of equations as additional unknowns. They appear as an additional summand in a modified potential, which reads

$$\Pi_{mod} = \Pi + \boldsymbol{\lambda}^\top \mathbf{H} \quad (3.37)$$

and which leads to a so-called *saddle-point problem*, as a submatrix of zeros is introduced into the graph of the stiffness matrix due to the additional DOFs. By means of static condensation, the number of secondary Lagrange-multiplier-based DOFs may be reduced depending on the problem. In fact, the simplistic problem presented in this chapter can be conceived as the result of a complete condensation of the Lagrange multiplier DOFs.

The variation of the modified potential with respect to the primary unknowns, displacements  $\mathbf{d}$ , and secondary unknowns  $\boldsymbol{\lambda}$  is given by

$$\delta \Pi_{mod} = \delta \Pi + \delta \boldsymbol{\lambda}^\top \mathbf{H}(\mathbf{d}) + \delta \mathbf{H}(\mathbf{d})^\top \boldsymbol{\lambda}. \quad (3.38)$$

The minimization of  $\Pi_{mod}$  with respect to  $\mathbf{d}$  in the presence of  $\boldsymbol{\lambda}$  requires this variation to vanish for arbitrary  $\delta \mathbf{d}$  and  $\delta \boldsymbol{\lambda}$ , meaning

$$\delta \Pi_{mod} = 0 \quad (3.39)$$

ensuring an exact satisfaction of the constraint at the cost of additional DOFs introduced by  $\boldsymbol{\lambda}$ . Often one can identify  $\boldsymbol{\lambda}$  and  $\mathbf{H}(\mathbf{d})$  as work conjugate, which makes Equation (3.38) a virtual work expression. This convenient feature of the Lagrange multiplier method makes it an especially popular tool for the derivation of weak forms in the FE context.

Constraints, that exceed the present ones in terms of their intricacy, could be employed in more demanding problems such as the modeling of *processive* and *non-processive* enzymes. For example, the non-processive behavior of *myosin-II* involves multiple time-variant phases. Myosin II can *slide along* the filament and reattach firmly at some point [4]. The description of this biological process can be more or less directly translated into a constraint formulation, that is a function of both space and time. Other examples would be the *walk* of *kinesin* on microtubules or the activity of *dynein* (cf. the subsequent Chapter 4), which both are highly processive molecular machines [233]. They are able to travel along a microtubule without dissociating from it, which is a key aspect of processivity. As motor activity such as mentioned above involves complex molecular kinematics, appropriate constraints may be formulated more easily if the general (theoretical) framework of a Lagrange-multiplier-based method is used as a starting point rather than the condensed version of the underlying system of equations. Further development of the approach towards more complex (processive) constraint formulations is deemed a promising field of research in the future, as it could help understand mechanisms of intracellular transport or cell division on a larger scale than, e.g., molecular dynamics approaches are able to handle. Cooperative effects of different well-understood molecular motors could be studied and quantified (e.g., [199]), leading to a better understanding of how different motor species team up to boost their efficiency .

## 3.4 Numerical examples

In this section, both quantitative and a qualitative numerical examples will be presented. The first example demonstrates path-independence and objectivity of the interpolated beam element. The second example reproduces all principal network architectures found in [35] with the original beam formulation for filaments and linkers. Finally, the new approach is tested on two linear rheology problems. While the first example simply tests whether the approach works (testing the interpolation and the (virtual) constraints), the latter examples will additionally feature performance tests to document the development of computational cost, and ascertain its possible use in rheological studies.

It is noted beforehand that detailed discussions on the subjects of self-assembly and the rheology of networks follow in Chapters 5 and 6, respectively. The examples of this section simply serve the purpose of validating the extended filament and linker models with respect to their fundamental operativeness and correct implementation.

### 3.4.1 Validation of constraint enforcement

As already implied above, the present example rather aims at verifying the correctness of the implementation and constraint enforcement than at an evaluation of the beam model itself, for which path-independence and objectivity were proven by [103]. Here, examples 1 and 3 from [103] are computed for the current implementation using the simplest possible geometry of two two-noded *filament beam elements* and one two-noded *linker beam element* ties to the other two as depicted in Figure 3.4a. As stated during the previous derivations, all involved elements are based upon the same path-independent and objective beam formulation. The exemplary beam has a cross section area  $A = 0.1 \mu\text{m}^2$ , moments of inertia of the principal directions

of the cross section  $I_2 = I_3 = 8.38 \times 10^{-5} \mu\text{m}^4$ , Young's modulus  $E = 1.2 \times 10^8 \text{ Pa}$ , Poisson's ratio  $\nu = 0.3$ , and a shear correction factor  $\gamma = 1.1$ . The nodes of the filament beam elements have the coordinates  $\mathbf{x}_{\tau A}^{[1]} = [0, 0, 0]^T$ ,  $\mathbf{x}_{\tau A}^{[2]} = [0, 1, 0]^T$ ,  $\mathbf{x}_{\tau B}^{[1]} = [1, 0, 0]^T$ , and  $\mathbf{x}_{\tau B}^{[2]} = [1, 1, 0]^T$ . The tying positions are located at  $\xi_{vA} = -0.1$  and  $\xi_{vB} = 0.8$ , which are given in the FE parameter space  $\xi \in [-1; 1]$  defined in section 2.4.1. For the sake of completeness, it is stated that the real nodes do *not* additionally belong to conventional beam elements in contrast to the initial problem description in Section 3.1. Nodes  $\tau_A^{[1]}$  and  $\tau_A^{[2]}$  are subject to translational Dirichlet boundary condition enforcing zero displacement. All four nodes are subject to prescribed rotations

$$\boldsymbol{\theta}_{\tau A}^{[1]} = \begin{bmatrix} 1 \\ -0.5 \\ 0.25 \end{bmatrix}, \quad \boldsymbol{\theta}_{\tau A}^{[2]} = \begin{bmatrix} 1.25 \\ -0.75 \\ 0.1 \end{bmatrix}, \quad \boldsymbol{\theta}_{\tau B}^{[1]} = \begin{bmatrix} -0.4 \\ 0.7 \\ 0.1 \end{bmatrix}, \quad \boldsymbol{\theta}_{\tau B}^{[2]} = \begin{bmatrix} -0.45 \\ 0.5 \\ 0.2 \end{bmatrix}. \quad (3.40)$$

Note that these rotations do not equal the prescribed rotations chosen by [103], thus leading to different results. The demonstration of path-independence requires equality of results upon application of different rotation increments. Test case (a) makes the beam rotate by application of a single rotation. Test case (b) applies two different rotations in sequence, which are  $0.25 \boldsymbol{\theta}_{\tau A}^{[1]}$ ,  $0.2 \boldsymbol{\theta}_{\tau A}^{[2]}$ ,  $0.5 \boldsymbol{\theta}_{\tau B}^{[1]}$  and  $0.6 \boldsymbol{\theta}_{\tau B}^{[2]}$  followed by  $0.75 \boldsymbol{\theta}_{\tau A}^{[1]}$ ,  $0.8 \boldsymbol{\theta}_{\tau A}^{[2]}$ ,  $0.5 \boldsymbol{\theta}_{\tau B}^{[1]}$  and  $0.4 \boldsymbol{\theta}_{\tau B}^{[2]}$ . Table 3.1 lists the rotational strains  $\boldsymbol{\kappa}$  at the center of the beam, i.e.,  $\xi = 0.0$  and the interpolated displacements  $\mathbf{u}_{vB}$  at the free end of the beam. Strain-invariance is verified by a third test case (c) superimposing a rigid body rotation  $\boldsymbol{\theta}_\circ = [0.2, 1.2, -0.5]^T$  on the prescribed deformation enforced by Equation (3.40). The resulting rotations for test case (c) can be extracted from  $\mathbf{\Lambda}_{(c)} = \exp(\dot{\boldsymbol{\theta}}_{(c)}) = \exp(\dot{\boldsymbol{\theta}}_\circ) \exp(\dot{\boldsymbol{\theta}}(\xi_{\tau B}))$ . The results presented in Table 3.1 do not grant new insights recalling that a verified beam element provides the mathematical foundation of the model. However, they demonstrate the reliability of the interpolation of the virtual nodes and thus serve as a proof of concept.

### 3.4.2 Network morphologies in crosslinked semiflexible networks

The second study seeks to recreate all four network morphologies presented and discussed in Chapter 5: homogeneous-isotropic, bundle, cluster, and lamellar networks (cf. Figure 5.2). The structural polymorphism of crosslinked semiflexible networks such as the cytoskeleton relies heavily on the linker species involved, which are distinguished by their preferred binding angle  $\phi$ , and the linker-to-binding site ratio  $n_l$  (see Table 3.2). In addition, the computational performance is investigated for all morphologies at different numbers of elements  $N_e$  discretizing

test sequence	$\kappa^1(L/2)$	$\kappa^2(L/2)$	$\kappa^3(L/2)$	$\mathbf{u}_{vB}^1$	$\mathbf{u}_{vB}^2$	$\mathbf{u}_{vB}^3$
(a) 1 increment	-1.32303	0.263443	-1.43698	0.17273	0.08015	-0.35218
(b) 2 increments	-1.32303	0.263443	-1.43698	0.17273	0.08015	-0.35218
(c) Rigid body rot.	-1.32303	0.263443	-1.43698	–	–	–

**Table 3.1** Components of the rotational strain  $\boldsymbol{\kappa}(L/2)$  and the displacement  $\mathbf{u}_{vB}$  at the free tip of the beam for the different rotation incrementation sequences. Note that in (c)  $\mathbf{u}_{vB}$  are not given as problem (c) differs from problems (a) and (b), which results in different values that are not comparable.

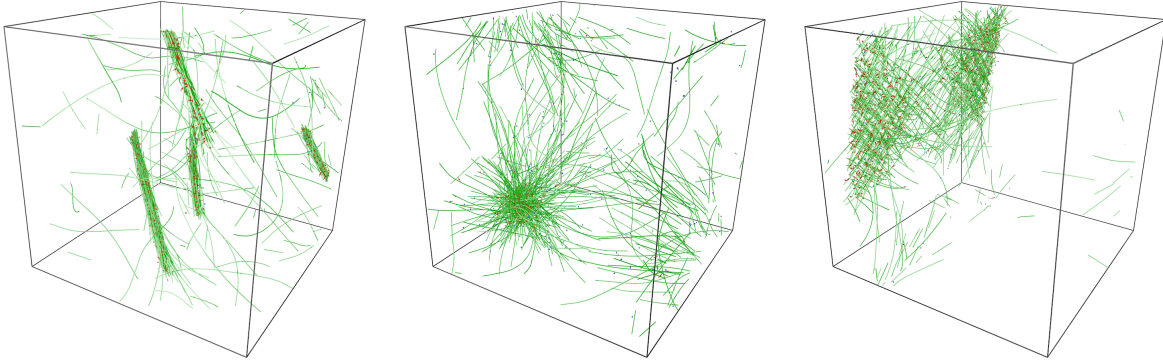


**Figure 3.5** Network morphologies that emerge from simulations with the new linker beam element. Each of the filaments (green) of length  $L_f = 4 \mu\text{m}$  is discretized with  $N_e = 8$  beam elements. All four principal network phases found in Chapter 5 are reproducible: homogeneous isotropic phase (not shown), bundle phase, cluster phase, and lamellar phase. For better visibility, filaments with a diameter of 5-7 nm are visualized with doubled thickness.

a single filament. The referential quantity for all conducted simulations is the total number of binding sites on filaments,  $N_b$ , which is kept constant for all simulations. Five different discretizations are evaluated with respect to computation time needed to reach 30000 time steps, which equals a simulated time of  $T_{\text{sim}} = 300 \text{ s}$  at a step size  $\Delta t = 0.01 \text{ s}$ . The simulated time interval is large enough to ensure the development of all network morphologies. All discretizations have a common number of  $N_f = 208$  filaments, which corresponds to a filament concentration of  $c_f = 4 \mu\text{M}$ . Filament length is set to a constant  $L_f = 4 \mu\text{m}$ . Filaments discretization varies and takes on values of  $N_e \in \{8, 16, 24, 32\}$  FEs per filament, which corresponds to discretization lengths  $h_f \in \{0.5 \mu\text{m}, 0.25 \mu\text{m}, 0.167 \mu\text{m}, 0.125 \mu\text{m}\}$ . The original FE formulation without extensions (see Chapter 2) and  $h_f = 0.125 \mu\text{m}$  as well as  $N_b = 6864$  binding sites is chosen as a reference. Other key simulation parameters include  $H = 5 \mu\text{m}$  as edge length of the cubic simulation volume, dynamic viscosity of the surrounding fluid  $\eta = 10^{-3} \text{ Pa}\cdot\text{s}$ , and the thermal energy of the system  $k_B T = 4.045 \times 10^{-3} \text{ aJ}$ . A comprehensive list of simulation parameters can be found in Tables D.1 and D.2 in the appendices.

As discussed in Section 5.2, the encountered network morphologies are sensitive to the preferred binding angle  $\phi$ , which is the angle enclosed by the filaments' tangents at the binding sites. Relative linker concentration  $n_l$  and  $\phi$  are chosen according to the phase diagram established in Chapter 5 (cf. Figure 5.5). Their respective values for each simulation are provided in Table D.3 of the appendix. Results for  $N_e = 8$  show the emergence of the expected network morphologies, which are illustrated in Figure 3.5. For low linker concentrations, the network stays isotropic and homogeneous with respect to both filaments and linkers. Above a certain

parameter	description	homogeneous	bundle	cluster	lamellar
$n_l = N_l / N_b$	relative linker concentration	0.058	0.204	0.138	0.204
$\phi \pm \Delta\phi$	preferred binding angle	$\frac{7}{16}\pi \pm \frac{\pi}{16}$	$\frac{\pi}{16} \pm \frac{\pi}{16}$	$\frac{7}{16}\pi \pm \frac{\pi}{16}$	$\frac{7}{16}\pi \pm \frac{\pi}{16}$

**Table 3.2** Simulations with different FE discretizations feature tuples of relative linker concentrations  $n_l$  and preferred binding angles  $\phi$ , that lead to one of the morphologies found in Chapter 5.

linker concentration, the so-called *crosslink saturation threshold*, one witnesses the formation of aggregates. For linkers that prefer crosslinking parallel filaments, bundles are observed. Linkers with a preference for orthogonal filaments create clusters at intermediate linker concentrations and highly ordered orthogonal lattices or lamellar aggregates. It is demonstrated, that the same morphologies can be reproduced, however, at a lower computational cost due to the reduced number of global DOFs. This effect, which reflects one of the essential advantages of the extended formulation, will be studied in detail in the following. Figure 3.6 summarizes the results of a numerical study, which focuses on the computational effects of choosing coarser filament discretizations. The presented data results from data evaluation on the time interval  $t \in [100 \text{ s}; 300 \text{ s}]$ . The lower interval boundary is chosen such that the respective network structure has already developed its characteristic shape.

First, simulations yielding homogeneous isotropic networks are discussed, which are illustrated in the first column of Figure 3.6. The comparison of homogeneous isotropic networks shows that the computational effort for the case with interpolated linkers and  $N_e = 32$  is  $\approx 20\%$  higher than the simulation using standard node-to-node linkers at an equal number of elements per filament  $N_e = 32$ . This is hardly surprising since the interpolation of positions and rotations and the set-up of element stiffness matrices needs to be performed for each linker element. The additional effort of providing inter-nodal binding sites entails the observed increase in computation time. Throughout all simulations, only  $\sim 100$  crosslinks are constantly present at any time for all discretizations – too small a number to significantly affect the total computation time. However, investigating the total number of linker elements, the satisfactory conclusion can be drawn that the interpolated linker approach does not significantly alter the statistics of binding and unbinding events, i.e., the number of crosslinks is independent of the discretization (within the studied bounds, of course). Linker administration (running search algorithms, evaluating binding potentials, interpolation of nodal positions/rotations, etc.) is more costly, which is understandable considering the increased effort of handling a doubled number of DOFs per linker molecule. However, in view of computation times decreasingly contributing to the overall temporal effort with increasing mesh refinement, one may state that this matter of expense is a minor one. Moreover, remedies to this problem are readily available in standard literature and do not directly affect mechanics. The summed temporal costs per time step for the use of linear and – as a consequence – the non-linear solver in Figure 3.6 again scale nearly linearly.

The picture changes upon examination of the other morphologies, which are linker-dominated. The bundle phase is the most demanding network structure in terms of computational cost. This is only natural as it provides a maximal number of potential binding sites for crosslinks. Generally, isotropic linkers, i.e. without binding angle limitations, the emerging network architecture will always be bundles. Imagine sitting at a filament binding site close to the neutral line of a bundle. Potential binding partners then include all binding sites within a sphere of radius  $R_l$ . This statement is also true for a cluster. However, the radially oriented filaments lead to a quick depletion of binding partners with increasing distance from the cluster core. Although the number of simulated linker molecules is more than three times higher than in the homogeneous isotropic case, linker administration takes about the same amount of time. The reason for this seemingly paradox outcome is simple. For reasons of efficiency, doubly bound linkers may be skipped by linker management routines since their location and mechanical behavior is now completely defined by their FE model. Studying the second column of Figure 3.6, one can easily identify the cost driver: the solution procedure of the linearized system of equations

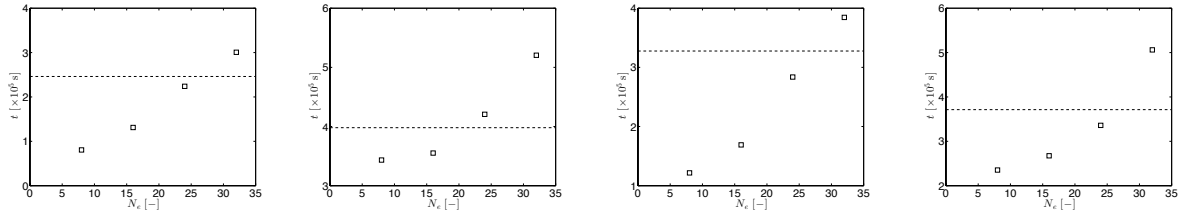
homogeneous isotropic

bundle network

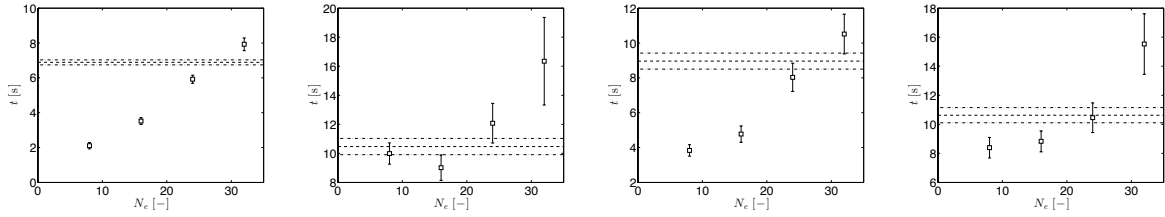
cluster network

lamellar network

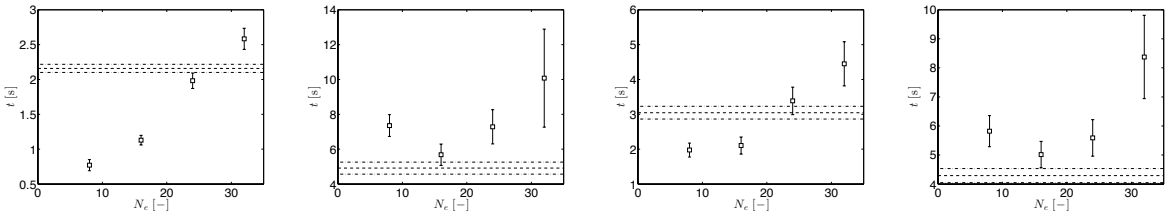
Total simulation time



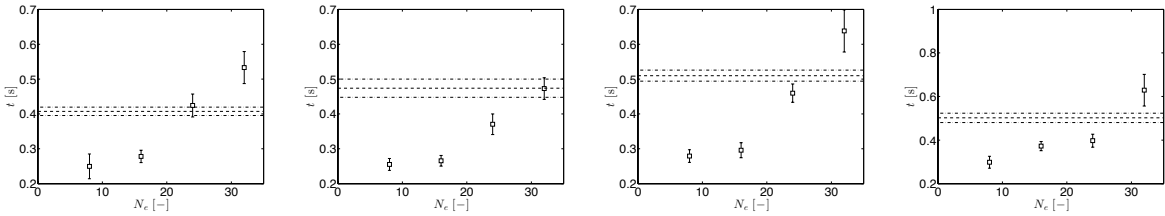
Nonlinear solver time



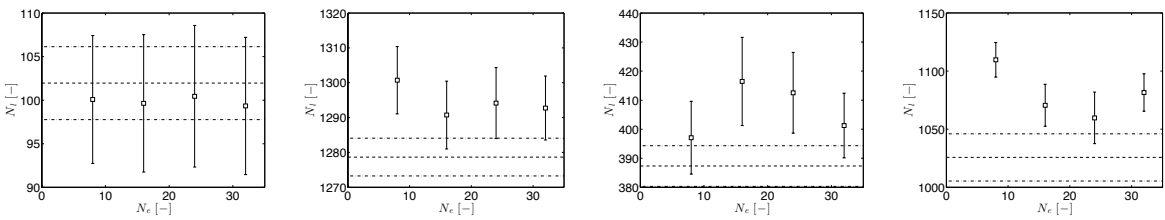
Linear solver time



Linker administration time



Number of crosslinks



Total number of elements

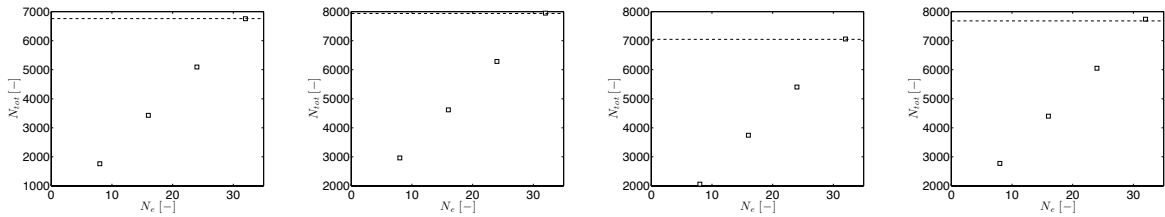


**Figure 3.6** Columns: Network morphologies. Rows: Total simulation time for various discretizations, PTC time per time step, linear solver time/timestep, linker administration time (search algorithms, linking/unlinking, addition/deletion of elements), average number of linker elements, and total number of FEs. Dashed lines depict values for the standard linker case, dash-dotted lines provide errors.

are responsible for more than 60% of the total time consumption of the iterative solutions procedure. The cause is straight-forward. Since linker elements in general increase the degree of nodal connectivity, off-diagonal entries in the global system of equations increase in number as well. The incorporation of four instead of only two nodes per linker element amplifies this problem and thereby further diminishes the performance of the solution procedure. Off-diagonal terms are counterproductive in terms of solver efficiency as they lead to ill-conditioned stiffness matrices. Due to the limited scope of this thesis, efforts to increase solver efficiency by means of an optimized and problem-specific treatment of the global stiffness matrix have not been undertaken. However, putting the hypothetically possible leap in performance and the practical outcome into perspective, the need for improvement is obvious and implies possibilities for future improvements. Another noteworthy observation is the variance in linear solver times for finer filament discretizations, which is caused by the stochastic nature of the problem. Due to stochastic binding-/unbinding events, the graph of the global stiffness matrix is subject to random changes in each time step. Favorable matrix layouts lead to short solution times, while extremely unfavorable ones lead to a noticeable increase in the solution time increase (up to  $\sim 13$  s for  $N_e = 32$ ). In general, the spread of solution times increases with the number of elements per filament  $N_e$ .

Finally considering the average number of linker elements, a slight increase by 1-1.5% is recorded. In view of the fact that only one simulation has been performed per discretization, this minor aberration may be excused. One possible explanation might be rooted in the loss of an increasing number of explicitly simulated thermal fluctuations with decreasing  $N_e$ . The present two-noded Reissner beam element interpolates positions only linearly. The quality of the approximation deteriorates with decreasing  $N_e$ , as all transverse modes of fluctuation between two FE nodes of a filament are omitted. As a consequence, the number of available binding sites increases, since the set of possible geometrical configurations of the filament is drastically reduced. A more accurate interpolation scheme would most probably alleviate this shortcoming. See this chapter's outlook (Section 3.5) for a slightly more detailed elaboration of the problem.

The cluster network with its approximately 400 linker elements exhibits a near linear scaling of the total simulation time (cf. the third column of Figure 3.6). Other measures, such as the nonlinear solver time, behave according to expectations as well. The number of linker elements varies more noticeably than in the previously discussed cases, that is, the deviation amounts to about 5% depending on  $N_e$ . However, with respect to the total number of binding sites  $N_b$ , it still represents only a minor influence on the overall simulation as the bottom row of Figure 3.6 shows. The scaling of the total number of elements in the simulations is overall linear.

The lamellar phase offers high number of potential double-binding sites for linkers as well and in this respect resembles the bundle phase. The fourth column of Figure 3.6 thus in principle displays a similar behavior as the bundle phase with a slightly less pronounced nonlinear scaling of the computational effort. However, the flat geometry leaves less binding site combinations than the bundle does, resulting in a slightly lower computational cost due to a smaller average number of linker elements.

Overall the numerical bottleneck can be pinned on the linear solver. As expected, the higher connectivity due to the involvement of four instead of two FE nodes per linker element leads to noticeably higher overall simulation times. For discretizations tested here, the superiority of the original node-to-node linker is not surprising. However, the selling point of this linker formulation is found elsewhere. The new linker element becomes the economically sensible

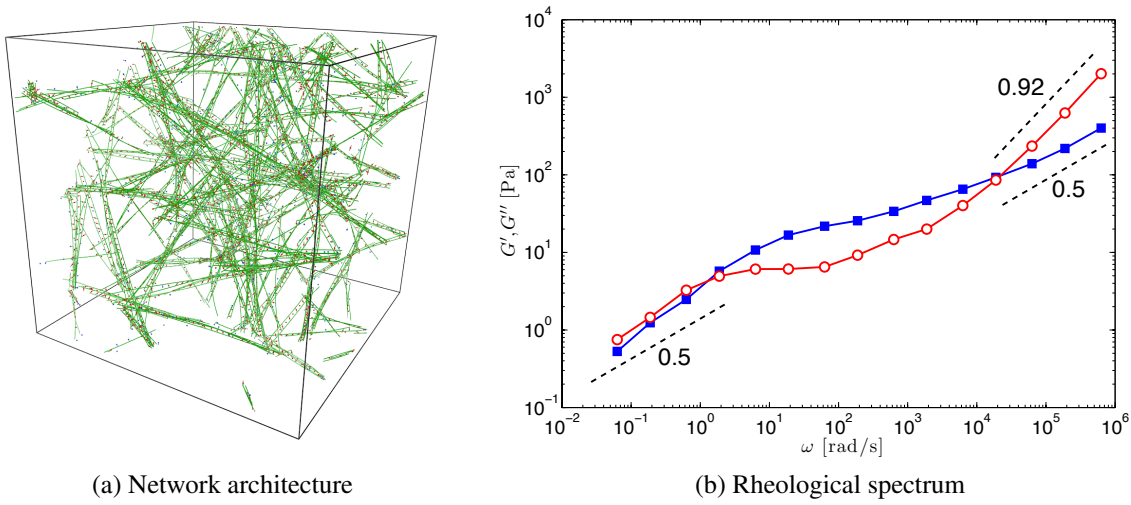


**Figure 3.7** Rheological spectrum of a bundled semiflexible network, which is modeled using interpolated linker elements. Storage modulus (*blue*) and loss modulus (*red*) show the expected scaling relation, which differs from the classic  $\{G', G''\} \sim \omega^{3/4}$  at high frequencies. Furthermore, the slight dip in  $G''$  as well as the low frequency scaling  $\{G', G''\} \sim \omega^{1/2}$  are also reproduced. Note the intersection of  $G'$  and  $G''$  at 1rad/s as assumed in Section 2.3.3 of [133].

choice, when the total number of binding sites  $N_b$  is increased. The global system size remains constant for the new linker element independent of  $N_b$ , while the original approach entails an increase of DOFs. Eventually, a further refinement of the mechanical discretization becomes computationally infeasible, which makes a good case for the new linker.

### 3.4.3 Linear rheology of semiflexible bundle networks

The final validation of the overall operativeness of the new linker model is performed by means of rheological simulations. The goal is to recreate the joint mechanical effects of thousands of simultaneous crosslinks. The results are cross-checked against validated results presented in Chapter 6. A network consisting of  $N_f = 360$  filaments ( $c_f = 4 \mu\text{M}$ ) with  $N_e = 12$  elements per filament is probed on a broad frequency interval  $f \in [3 \times 10^{-3}; 3 \times 10^5] \text{Hz}$ . The number of binding sites  $N_b = 11880$  is chosen equal to the examples in Chapter 6, which corresponds to a distance  $d_b = 0.125 \mu\text{m}$  between two adjacent filament binding sites. The network was prepared by letting the network self-assemble for  $\sim 1200 \text{s}$  until it reached a geometrical state that almost exclusively consisted of bundles (see Figure 3.7a). The cubic simulation box with edge length  $H = 6 \mu\text{m}$  contains  $N_l = 9000$  linker molecules, of which approximately 6000 are doubly bound within the bundles. A comprehensive parameter list is provided in Table D.9.

As Figure 3.7b demonstrates, all characteristic features of the generic rheological spectrum of a bundle network from Chapter 6 are reproduced. For high frequencies, the moduli display the typical power law behavior native to bundle networks of semiflexible filaments. The frequency-dependent scaling of  $G' \sim \omega^{0.95}$  differs noticeably from that of  $G'' \sim \omega^{0.55}$  and both are thus in contrast to the classic understanding of the high frequency scaling of semiflexible networks, which is  $G', G'' \sim \omega^{3/4}$  [59, 118]. The intermediate frequency regime shows a very subtle inflection resulting in a local maximum for  $G''$  at a frequency of about 1Hz. This observation is in agreement with experiments [14, 138]. Furthermore, the low-frequency square root scaling can

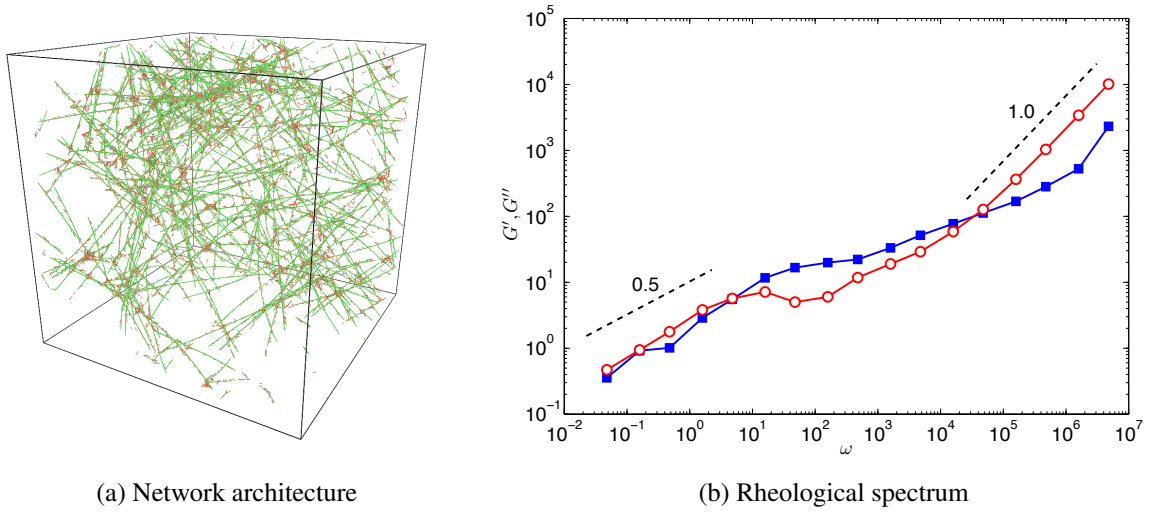


**Figure 3.8** (a) homogeneous, isotropic network made of single filaments, that are decorated by linker molecules. (b) rheological spectrum of a homogenous-isotropic network with storage modulus  $G'$  (blue) and loss modulus  $G''$  (red). At entanglement points, linkers establish crosslinks to other filaments. Compared to bundle networks, the minimum in  $G''$  at intermediate frequencies is slightly more pronounced in accordance to experiments [137]. The low-frequency square-root scaling is recovered. At high frequencies, the moduli's scaling behavior is  $G', G'' \sim \omega$ .

be seen, which again is in agreement with experiments mentioned before. The loss modulus exceeds the storage modulus for this particular sample, meaning that viscous dissipation exceeds elasticity. This second intersection – the first having occurred in the high-frequency regime – is a feature that is hinted at in [133], yet has not been directly observed there due to a comparatively low dissociation rate constant  $k_{\text{off}} \approx 0.07 \text{ s}^{-1}$  (in vivo) mentioned in [134]. Whether or not a second intersection of  $G'$  and  $G''$  is observed most probably depends on crosslink density. The lower this density is in a bundle, the greater the dissipative contribution to the complex modulus. Eventually at sufficiently low linker densities, viscous effects exceed elasticity.

### 3.4.4 Linear rheology of homogeneous isotropic networks

HMM is known to constitute crosslinked actin networks made up of single filaments. These networks remain homogeneous and isotropic regardless of linker concentration [137, 203]. This property can presumably be attributed to HMM attaching itself to an actin filament with both its S1 domains, blocking two binding sites, which leads to a decrease of the number of binding site pairs eligible for crosslinks between separate filaments. Only at filament entanglement points can crosslinks be established, which is a somewhat trivial statement but, given that HMM constitutes homogeneous, isotropic networks, stresses the fact that such a network offers less opportunities for double bonds than, e.g., a bundle network.

Simulations are set up with an almost identical parameter set as the bundle network example in Section 3.4.3: among others, the size of the simulation box ( $H = 6 \mu\text{m}$ ), filament concentration  $c_f = 4 \mu\text{M}$  and the number of linkers  $N_l = 9000$  remain unchanged (cf. Table D.9). The linkers are, however, not isotropic anymore, but exhibit a binding angle preference of  $3\pi/8 \leq \phi \leq \pi/2$  when establishing crosslinks between two separate filaments, and are explicitly allowed to bind to the same filament with both their reactive sites. Additionally the distance

between two adjacent filament binding sites is reduced to  $d_b = 15.625$  nm and filaments are chiral. In the present case, chirality plays only a minor role due to large linkers ( $2R_l = 100$  nm), which find enough binding opportunities regardless of the binding site orientation. The network in Figure 3.8a, which is used for linear rheology simulations, has undergone evolution for a simulated time of  $\sim 800$  s. Figure 3.8b shows the frequency-dependent viscoelastic response of the network in the regime of small deformations. Clearly, the local maximum of  $G''$  at intermediate frequencies ( $\sim 10$  rad/s) is more prominent than it is for bundle networks, i.e., the difference between the dip in  $G''$  and its local maximum is larger. In contrast to bundle networks, the local maximum in  $G''$  at the characteristic frequency  $\omega_c$  is not shifted to  $\omega_c/2\pi < k_{\text{off}}$ , but rather equals the off-rate, which again is in agreement with experiments [137]. Absolute values of the maxima are comparable with  $G''(\omega_c) \approx 0.7$  Pa, the difference between the  $G''$ -minimum and the maximum. This distinction between the two network morphologies is in agreement with experiments on actin/HMM networks [137] and actin/fascin bundle networks (e.g., [138]). It can be understood by the decreased number of crosslinks between filaments, which makes the unbinding of a single linker weigh more in a homogeneous isotropic network than in a bundle. If an intra-bundle crosslink detaches, there are still plenty of crosslinks left in the bundle cross section. In homogeneous isotropic networks, however, the detachment of a linker may already mean the loss of a crosslinked entanglement point, i.e. the free filament length at the unbinding site grows leading to increased dissipation. In the low frequency regime, the scaling  $G', G'' \sim \omega^{1/2}$  is observed, which serves as another proof for a generic power law regime, which is not only limited to bundle networks as discussed in Chapter 6. At high frequencies, both moduli seem to approach a common power-law scaling  $G', G'' \sim \omega$ .

## 3.5 Conclusions and outlook

In this chapter, the BD/FE framework of Chapter 2 has been extended. The modeling augmentations allow for a decoupled handling of the molecular topology and the mechanical description. As a result, the superior computational efficiency of the FEM can be exploited while simultaneously resolving macromolecular details far below the mechanical discretization length.

This chapter's innovation is founded on two separate developments, that are closely linked together and access their full potential only when applied in conjunction with one another. An enhancement of the numerical model of the filament enables mechanical connections along the entire geometry and not only at nodes of a finite element. Without a complementary linker model, however, the extension of the filament model is pointless. Therefore linkers have been enabled to crosslink filaments at arbitrary binding positions along their geometry.

Biological macromolecules such as F-actin or microtubules consist of discrete molecular subunits, which provide chemical binding sites for linkers. Knowing their molecular structure, the topology of binding sites may be designed in order to meet the specifications of one or the other filament species. Here, the design procedure has been discussed for the chiral biopolymer F-actin as it is closely connected to the topic of this thesis. However, it can be easily transferred to meet the structural specifications of the molecular geometry of other slender polymers like triple-helical collagen or microtubules, which consist of helically arranged tubulin subunits. The only adjustments concerns the adaption of the constitutive properties and the binding site map

by means of orientations  $\mathbf{\Lambda}_b$ .

Two primary model-related and methodic aspects as well as two secondary problems need to be considered in view of future developments:

- (I.1) Increase of the accuracy of the interpolated geometry by means of more fitting interpolation procedures, i.e. the employment of alternative beam element formulations
- (I.2) Improvement of the solution procedure regarding the efficiency of the linear solver
- (II.1) Application of an efficient load balancing between the participating processors during parallel computation
- (II.2) Efficient search algorithms

With respect to item (I.1), one may consider switching to an alternative beam element formulation. Fortunately, the tying method is adaptable to principally any beam or rod model. Nonlinear, geometrically exact *Kirchhoff* beam elements appear to be the method of choice [155, 156]. Beam elements of this type have only two nodes but interpolate the translational DOFs using *higher-order Hermite polynomials*. The current FE model of the filament is based upon a Reissner beam formulation, which interpolates the translational displacement field using *Lagrange polynomials*. The polynomial order  $p$  of Lagrange polynomials is connected to the number of nodes  $K$  by  $p = K - 1$ . Due to the more complex interpolation scheme, the Kirchhoff beam element offers a better geometrical approximation than the Reissner beam element for an equal number of DOFs. As a consequence, one can choose a coarser discretization in order to achieve the same accuracy as the current Reissner beam discretization. There are further advantages. The Kirchhoff theory omits shear, which is an acceptable simplification for beams with a high slenderness ratio. This leads to a reduction in model complexity. Furthermore, Reissner beam elements suffer shear locking and an ill-conditioned stiffness matrix. Lastly, in view of a future application of beam contact formulations, the  $C^1$ -continuity of the centerline of the Kirchhoff beam element is of great advantage.

In conjunction with an appropriate beam model, solver performance can be improved as postulated by (I.2). In this chapter, only the general feasibility of the approach has been evaluated using an iterative GMRES solver for the linearized system with an ILU factorization for the pre-conditioning of the global stiffness matrix. Optimized pre-conditioner settings and problem-specific linear solver parameters are expected to improve computational performance. In network simulations, the global stiffness matrix is subject to change in each time step as the random addition and subtraction of linker elements affects matrix entries and may lead to an ill-conditioned problem. Therefore, the adequacy of the initial set of solver parameters is questionable with respect to the evolved network geometry. The application of numerical methods that aim to reduce the matrix bandwidth (e.g., based on the ideas of [32]) can yield a beneficial effect.

Concerning (II.1): parallelized simulations require the definition of processor boundaries, that divide the global problem into processor-specific subdomains. The stochastic nature of network simulations can lead to an imbalance between the individual processor loads due to an increasingly non-uniform distribution of elements among the participating processors. As a consequence, the global computational efficiency suffers from increased solver times, which

result from increased inter-processor communication due to the high degree of connectivity among elements and nodes. The continued evaluation of the sensibility of processor domains during runtime as well as their controlled redefinition, i.e. the redistribution of all DOFs and elements, can entail an increase in computational efficiency.

Lastly, concerning (II.2) and bearing in mind that a physiological actin filament consists of thousands of monomers, i.e., potential binding sites, efficient search routines are an essential component of any network simulation. In the frame of this thesis, search algorithms using octree data structures and binning strategies have been implemented and are capable of handling the complexity of the system (cf. Appendix B.2). However, in order to further decrease search and matching times, an improved parallelization of the search routines can be considered.

The extended computational approach can be applied to a variety of biophysical problems such as actin bundle assembly. Here, phenomena on length scales below a numerically feasible filament discretization determine the mechanics on the scale of single bundles. Alternatively, the approach can be applied to increase the physical dimensions of the problem. One can exploit the reduced number of DOFs per filament in order to explore effects of larger filament concentrations in enlarged volumes. Chapter 5 will feature one such example, where the characteristic length scale of the system (the edge length of the cubic simulation box) is increased to 10  $\mu\text{m}$ . Being able to access this dimension also means that modeling and simulating systems the size of single cells cannot be considered a far-fetched goal any longer.

The decoupling of the chemical topology from the FE discretization may also help modeling polymerization processes without having to discretize molecular subunits. Due to the fact that polarity is already implicitly modeled by the orientation of the beams' material triads, biological processes like the *treadmilling* of actin filaments or the contraction of both polar and apolar bundles may be the subject of future study, to which the here presented approach can contribute greatly.

The subsequent Chapter 4 utilizes the here introduced methods and applies them to the modeling of molecular motors. Furthermore, they will be picked up in Chapter 5 for an enhanced study of linker-induced self-assembly in order to assess the effect of both a finer chemical resolution as well as the effect of chirality.



# 4 A beam-element based model of a molecular motor

Life's maybe most defining characteristic is *autonomous movement* driven by metabolic activity. Complex motion patterns – from facial expressions to a javelin throw – are the result of a mechanical amplification of over ten orders of magnitude in length. What manifests in the form of macroscopic mechanical work and kinetic energy is the joint effect of myriads of motor proteins, *molecular machines*, which convert chemical free energy into mechanical work and heat. They *make things move* [215].

Chapters 2 and 3 have laid the methodic foundations for the present chapter, where a simplified model of a molecular motor will be motivated, discussed methodically, and validated numerically. As the focus of this work lies with networks consisting of semiflexible filaments, the design of the motor will be inspired by skeletal muscle myosin. However, the goal of this chapter is not to recreate the complex kinematics of single motor proteins or even to account for their distinct chemical cycles, but rather aims at providing an instrument, which allows for direct mechanical insights of how the exertion of forces on biopolymer structures alter their mechanical behavior on a larger scale.

This chapter begins with a short introduction to the vast topic of motor proteins and their functions, which includes a brief discussion of the main motor protein families *myosin*, *kinesin*, and *dynein* (Section 4.1). The introduction is followed by the description of a myosin-inspired numerical model of a molecular motor based on BFEs. More precisely, the motor activity of a single myosin head domain serves as the archetype of the motor (Section 4.2). Based on this fundamental building block, more complex motor units like myosin thick filaments may be realized in the future. In a final section, the presented approach is applied in the simulation of so-called in vitro motility assays, which in the past provided essential experimental information on the biochemical and mechanical properties of the myosin molecule [88] (Section 4.3). A slightly enhanced outlook will briefly hypothesize about a modeling approach for myosin thick filaments and their application in the simulation of contractile bundles and active biopolymer networks.

## 4.1 Molecular machines

Motor proteins such as myosin or kinesin are the driving force behind an abundant variety of intracellular processes, which have been discovered and studied in the past decades. They play their part in such essential tasks as muscle contraction [97, 98], vesicular transport and endocytosis [165], mitosis and meiosis (cf. [145]) or mechanosensing [109]. The defining purpose of molecular motors is the amplification and acceleration of biological processes, which in their absence would be driven by mere diffusion. According to [88], any motor protein propelled

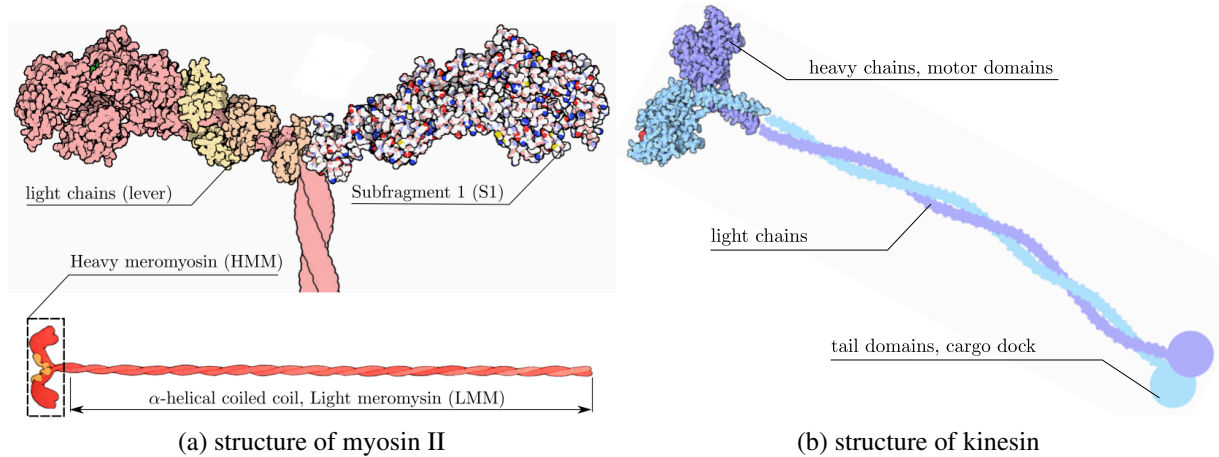


**Figure 4.1** Essential motor proteins. (a) *actin-associated* motor protein myosin II, most prominent member of the myosin superfamily, is the eponym of the family as it was discovered first. It is localized in muscle cells, where it assembles into *thick filaments*. It binds to actin filaments with its heavy chains (images modified from [61]). In experiments involving single myosin molecules or parts of it, often only Heavy meromyosin (HMM) or the subfragment 1 (S1) of HMM are used. (b) *microtubule-associated* motor proteins kinesin and dynein (not depicted) exhibit complex kinematic patterns during force exertion. Since kinesin’s motion resembles a *walking biped*, it was named the *kinesin walk*. The motor domains attach to the microtubule, the tail domains attach to cargo, e.g., vesicles (image modified from [62]).

by the hydrolysis of *adenosine triphosphate* (ATP) can be characterized in general by three characteristic distance measures:

- (I) **working distance**  $\delta_w$  describes the distance covered during each step of the molecular motor. It consists of a fraction  $\delta_+$  attributed to the power stroke and  $\delta_-$  attributed to motor being dragged along by the filament after the power stroke and before detachment, which is referred to as *drag stroke*.
- (II) **path distance**  $\delta_p$  quantifies the distance between two consecutive substrate locations that a motor attaches itself to.
- (III) **distance per ATP**  $\delta_{ATP}$  represents the distance that is covered during the hydrolysis of a single ATP.

These quantities can readily be converted into meaningful parameters of the here presented model of a motor protein. A fourth, temporal quantity of great importance when characterizing

Motor	Ref.	working distance $\delta_w$	path distance $\delta_p$	distance/ATP $\delta_{ATP}$	duty ratio $r$
Myosin II	[88]	5	36	200-400	0.05
Kinesin	[88]	8	8	16	$\geq 0.5$
Dynein	[177]	$\pm 8$	8	16	$\geq 0.5$

**Table 4.1** Characteristic distance measures for the three main motor proteins. Distances are given in units of nm, the duty ratio is dimensionless.

motor proteins is the *duty ratio*

$$r = \frac{\tau_{\text{on}}}{\tau_{\text{on}} + \tau_{\text{off}}}, \quad (4.1)$$

which describes the fraction of a full cycle, during which the motor is attached to its substrate. Here,  $\tau_{\text{on}}$  denotes the temporal fraction of the cycle during which the motor is attached to the filament. The complementary time  $\tau_{\text{off}}$  then represents the time that the motor spends detached from the filament. This value varies greatly among different types of motors as there exist *processive* and *non-processive* motor proteins. Processive proteins like kinesin stay attached to their substrate for many steps. Hence their duty ratio is high, usually  $r \sim 0.5$  and above. Most myosins on the other hand detach after each hydrolytic event, which makes them non-processive. Consequently their duty ratios are reported to be low at  $r \sim 0.01-0.1$  [87]. Literature values for the three most prominent motor proteins are listed in Table 4.1 [88].

### 4.1.1 Actin motors

**Molecular taxonomy** The myosin superfamily consists of about 20 different motor proteins, which share filamentous actin as their binding partner. All of them are capable of force generation via ATP hydrolysis, an exothermic reaction that severs the terminal inorganic phosphate and produces *adenosine diphosphate* (ADP). Given a sufficiently high ATP concentration, myosin motors exhibit either processive or non-processive behavior depending on the species. Myosin V is processive, while myosin II is not. Here, myosin II will be treated in more detail since it will loosely pose as the archetype for the numerical model. Hence, from here on, the term *myosin* will refer to type II of the superfamily. It consists of two heavy chains (the head domains) and as four light chains of amino acids (the necks and the tail), of which sketches are provided in Figure 4.1a. Initially being thought to exist only within muscle cells (hence the prefix *myo*), myosin II became the eponym for an entire family of motor proteins, which in the following decades was identified in many other cell types as well, e.g., in cells of stereocilia in the inner ear (myosin I, [9]) or in retinal cells (myosin III, [143]).

**Force generation** Muscle contraction is attributed to the motor activity of myosin, which is driven by ATP hydrolysis. The reaction lead to a series of conformational changes in the protein's head domains [195]. Myosin exhibits a cyclic motor activity, which can be divided into five distinct states (cf. textbooks such as [4], alternatively [194]). The initial, yet short-lived state is called *rigor configuration*, where one of the two heavy chain head domains is attached to the filament. This state is depicted in Figure 4.2a. ATP attaching to a specific binding pocket of the head domain of myosin causes a small conformational change, which results in the myosin head detaching from the filament. At this point, the head is free to slide along the actin filament (Figure 4.2b). ATP hydrolysis subsequently entails a large conformational change, which makes the head domain move  $\delta_w \approx 5 - 15$  nm in (+)-direction [145, 226] (Figure 4.2c). It then reattaches to the next binding site (Figure 4.2d). Myosin does not follow the helical path laid out by the actin monomers but rather maintains a translation parallel to the filament axis [88]. It hydrolyzes one ATP per step, so that the working distance equals the distance per ATP:  $\delta_w = \delta_{\text{ATP}}$ . Having reattached to the filament, the severed phosphate is set free resulting in another large conformational change, which is commonly referred to as *power stroke*. The stroke is not explicitly depicted. Rather, it represents the transition from Figure 4.2e to Figure 4.2e.

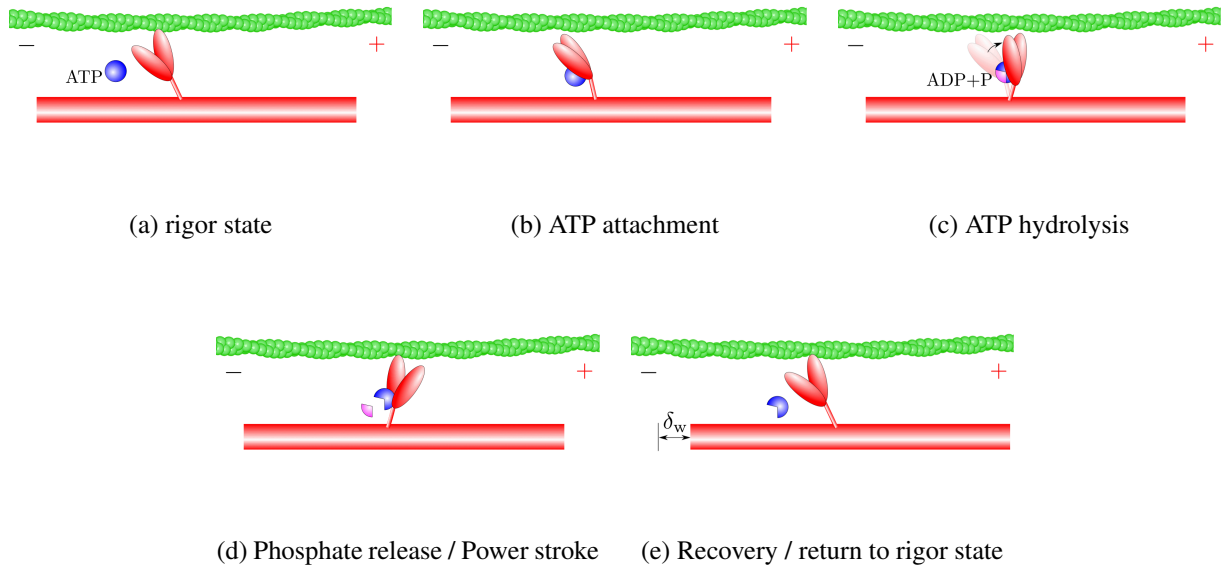
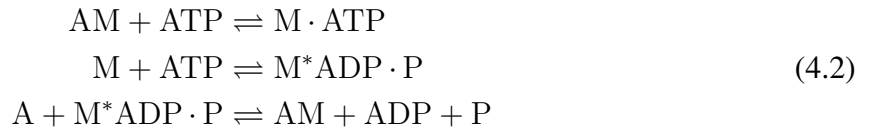


**Figure 4.2** Sketch of the enzymatic cycle of myosin: (a) rigor configuration, where one of the myosin heads is firmly attached to actin (green). (b) ATP (blue) binds to myosin. (c) In the wake of ATP hydrolysis to ADP and phosphate (purple), the head domain undergoes a conformational change. It slides along the filament. (d) The head domain reattaches to the next available F-actin binding site, triggering a conformational change, which causes the ejection of the phosphate. This causes another large conformational change, the power stroke. (e) Recovery of the initial (rigor) configuration at the new position after a relative translation of  $\delta_w$ .

During a major part of the cycle, however, the myosin head spends in a slow conformational change, which reproduces the initial rigor configuration at the new binding position, which is illustrated in Figure 4.2e. Expressed in terms of formulae, the consecutive steps describing the reaction kinetics of actomyosin interaction according to [148] read



with A, M, and P representing the chemical species actin, myosin, and phosphate, respectively. As Figure 4.2 shows, only one of the two myosin heavy chains is involved actively at a time.

The structural polarity of F-actin is of essential importance as it controls the direction of movement of the myosin motor. Except for type VI, all myosins move towards the *barbed* or (+) end of the actin filament. Through their catalytic activity, which leads to molecular movement, motors exert forces, which can be measured in experimental set-ups. Their range of magnitude is given by 1-7 pN with a mean force  $F_{av} = 3.4 \pm 1.2$  pN [52]. Other sources report similar values of 2-6 pN [16, 68]. The path distance is reported to be  $\delta_p = D/2 \approx 36$  nm, which corresponds to half an F-actin repeat. Corresponding experiments have also shown that myosin motors do not follow the helically winding path of actin monomers but rather move parallel to the filament's axis [88].

Under certain environmental conditions, e.g., at low salt concentrations, myosin molecules clot together forming thick filamentous structures at whose ends active domains with numerous

single myosin motors can be found. These *thick filaments* can be found in muscle cells, where the first myosin structures to be discovered and usually comprise  $\approx 600$  myosin heads. They enable actin displacements of up to  $0.7\mu\text{m}$  per cycle [88, 194], which are essential to muscle contraction as well as to contractility in apolar actin bundles [131, 132, 205].

### 4.1.2 Microtubule motors

As previously mentioned, proteins of the kinesin and the dynein superfamily are the main molecular motors associated with microtubules. Their main task is the vesicular transport of proteins, nutrients, and metabolites, but also entire organelles, which is paramount to the overall operativeness of a cell's metabolism. Kinesins predominantly move towards the (+)-end of the microtubule, while dyneins move in the opposite direction.

**Kinesin** Kinesin was first described by [216] and is an *ATPase* like myosin, converting chemical energy by ATP hydrolysis. It supports cell division (mitosis and meiosis), and carries cargo though the cell towards its destination (e.g., *anterograde transport* of cargo in axons, i.e. center $\rightarrow$ periphery). It is a dimer consisting of two heavy chains of amino acids, which bind to two light chains. The light chains form an  $\alpha$ -helical coiled coil structure, to whose tail domains cargo vesicles usually, but not exclusively, attach (cf. Figure 4.1b). The motion pattern of kinesin is believed to be a *hand-over-hand* mechanism [231], which is slightly reminiscent of a waddling duck (cf. Figure 4.1b). With each step and while hydrolyzing ATP, kinesin covers a distance of  $\delta_w \approx 8\text{ nm}$  along a microtubule, where it attaches to tubulin subunits [188]. Hence, depending on the tubulin dimer ordering, kinesin either walks parallel to the axis or in a helical fashion.

**Dynein** Dynein is predominantly localized in the cytoplasm [147] but it can also be found in axonemes, that enable the motility of cilia and flagella [174]. For example, it provides the means for *retrograde transport* of vesicles and organelles in axons [187]. Dynein consists of two heavy chains, which contains the active head domains, six intermediate chains, as well as several light chains. It is a processive enzyme, which means that at least one of its two head domains is bound to a tubulin subunit at a time during its enzymatic activity. The precise crystal structure of the dynein heads has only very recently been resolved [120]. The two heads capacitate dynein of actively walking down a microtubule. It has the same working distance as kinesin, but can also walk backwards and sideways [177].

## 4.2 Numerical model of a non-processive molecular motor

In this section, a kinematically abstracted model of a molecular motor is presented, which can be used to study effects of motor proteins on structures on a larger length scale, e.g., on the scale of biopolymer networks. It models non-processive motor activity. Therefore, it bears resemblance to myosin motors, or, more precisely, to the active part containing the heavy chains, HMM. In one respect, it stays loyal to the original concept presented by A. F. HUXLEY [96], which has

only two states: *on* and *off*. However, it additionally incorporates a basic idea concerning motor kinematics in the sense, that a rotatory motion is performed, which resembles the swinging cross-bridge model (cf. [195]) and the swinging lever arm hypothesis (cf. [82]). With regard to the significantly more complex motion patterns of the processive microtubule motors kinesin and dynein, more demanding procedure are without a doubt required in order to account for their kinematics. In this case, the Lagrange-multiplier approach from Chapter 3 may present a methodical solution by adjusting both the geometrical information passed to the filament model and the constraint formulation of the motor element such that both agree with the molecular structure of the microtubule on the one side and with the motor's cyclic pattern on the other. The following sections, however, are restricted to the case of non-processivity and leave the above mentioned for future research.

### 4.2.1 Modeling strategy

**Geometrical and kinematic abstraction** The modeling of the kinematics of motor proteins is a difficult endeavor if performed on the level of their molecular structure. Both actin and microtubule motors undergo complex conformational changes, which are not completely understood to date. The geometrical and kinematic abstraction of the molecular motor bears the risk of oversimplification *if* crucial details of the motor mechanism are omitted. Nonetheless, it represents a necessary step towards modeling motors as one-dimensional continua.

By no means, a precise reproduction of a motor protein's motion pattern is attempted in this thesis. Rather this chapter proposes the model of a contractile, rotating rod-like unit, which mimics the properties of a myosin head in a way that allows for the principal re-creation of its motor activity. This contractile unit will be discretized with a single geometrically exact beam element in conjunction with the constraint-based interpolation approach of Chapter 3. As such, it is capable of resolving the length scale of the path distance  $\delta_p$  of myosin, while it simultaneously profits from the much coarser mechanical discretization in terms of computational efficiency. The decision to model a non-processive motor is owed to the focus of this thesis, which lies on actin-based biopolymer networks. Myosin motor activity dominates in actin structures, which further supports the decision of making it the centerpiece of this chapter.

**Model of the power stroke mechanism** Some controversy surrounds the actual mechanism, by which force is generated. There are two main propositions, that are in fundamental contradiction to each other. One proposition is that the interaction of the motor head domain with ATP only provides a corset, that channels thermal excitations (e.g., [25, 150, 178]), hence playing the role of a *Maxwell daemon*. This description is often referred to as *thermal ratchet*, which assumes that the power stroke is a purely thermal effect. On the other hand, the power stroke may be triggered by a large conformational change itself. Before releasing the energy stored in a spring-like mechanism, the apparatus would need to be cocked. Such an approach is described in [88] and is found to be favorable, when modeling actomyosin bonds [66, 67]. Again, there exist several theories on how a motor arrives at this cocked state, either by a slow conformational change or a less extreme thermal ratchet mechanism than the one mentioned first. In [86], a mixed model is proposed, which takes the lever for a thermal ratchet, while simultaneously speculating about the existence of *hidden* spring elements providing elasticity. Although the discovery of muscular contraction due to myosin activity dates back more than

half a century, there are noticeable gaps in the knowledge on the exact mechanism of myosin motors. It appears to be still open to speculation, which part of the motor actually provides the property of a spring (cf. [86, 89]). For example, the successful observation of the so-called recovery stroke dates back only a few years [198].

In light of the variety of propositions, all of which have been shown to account for certain properties of motor proteins, the numerical model will adhere to its strong mechanical foundation. As the mechanical features considered above can be readily recreated using the present beam element formulation, the question is, how to consistently reproduce the effect of a motor rather than its detailed inner workings. Hence, conformational changes will be modeled using different reference configurations, that refer to one or the other molecular conformation. Their reaction kinetics will be portrayed similarly to the existing framework for filament-linker interaction from Chapter 2 and 3. Forces and step lengths are load-dependent [200], i.e. the enzymatic cycle depends on mechanical loading as well, which is not included in the present model.

**Model of conformational change** The model, which is going to be elaborated in the following, combines the idea of the spring element of the power stroke model and a rotational motion reminiscent of the swinging cross-bridge model or its successor, the swinging lever arm hypothesis [82]. In the first model, the entire S1 subfragment (i.e. the head domain) of myosin is involved in the rotation, while in the latter, only the light chain of the neck region rotates. The reason for this combination can be readily explained. A simple contraction of the beam modeling the motor tends to just pull the filament towards the motor's joint location  $\mathbf{x}_m$ . A simultaneous rotation about  $\mathbf{x}_m$ , however, allows for a tangential transport trajectory of the filament. As a consequence of these modeling assumptions, an appropriate parametrization of the motor geometry leads to working distances very well comparable to real motors such as myosin. Details are given in Section 4.2.4.

In extension of previously introduced methods, the modification leading to an actively contracting and relaxing rod-like continuum is quickly accomplished. Based on the general frame of the model elaborated above and the analysis of the cyclic activity discussed in Section 4.1.1, one may design an activity pattern that mimics the actual behavior of a myosin head or – further enhancing the model – a thick filament (cf. Section 4.4.2).

## 4.2.2 Force-dependent model of chemical bonds

As previously introduced, the likelihood of a bond establishing or dissociating is evaluated by Boltzmann probabilities (2.46) and (2.47). In many cases, however, the dissociation rate constant  $k_{\text{off}}$  is affected by a tension or compression of magnitude  $F$  acting on the bond. The so-called *Bell model* [10] incorporates this force-dependence in order to arrive at the relation

$$k_{\text{bell}} = k_{\text{off}} \exp\left(\frac{F \Delta x}{k_B T}\right) \quad (4.3)$$

between the reference off-rate  $k_{\text{off}}$  in the absence of force and the force-dependent off-rate  $k_{\text{bell}}$ . The effect of force on the dissociation reaction can be thought of as a change in height of the energy barrier between two chemical states. For a catch bond as in the present case, this property is

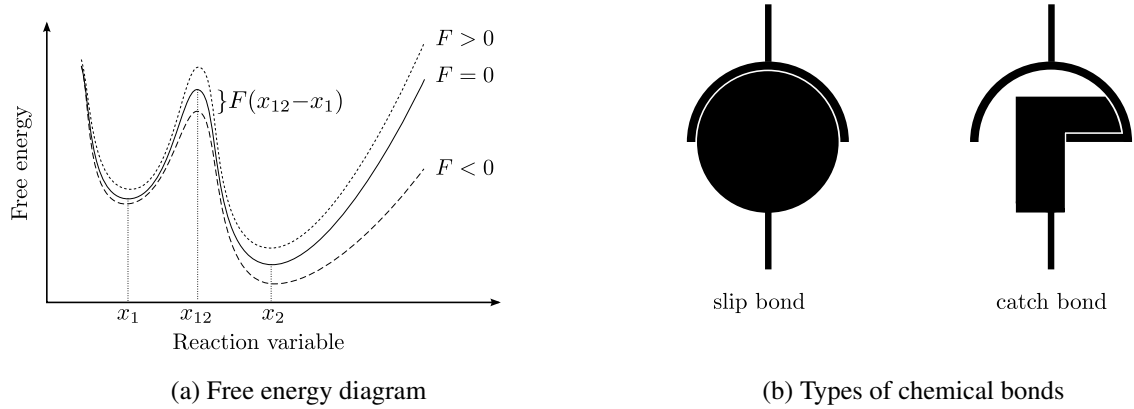


**Figure 4.3** (a) The effect of an applied force to a catch bond. If the bond is compressed, the transition state  $x_{12}$  becomes easier accessible and the reaction is accelerated. If the bond is put under tension, the barrier is heightened and the transition becomes less favorable. (b) pictograms conveying an intuitive understanding of the nature of the two bond types.

reflected in the sketched free energy diagram of Figure 4.3. Tensile forces strengthen the bond, which is expressed in a heightened energy barrier between the states 1 and 2. Compression on the other hand leads to bond weakening, which is reflected in a lowered barrier. The characteristic distance  $\Delta x$  depends on the type of chemical bond, commonly has the magnitude of several nanometers, and can be drawn from experiments (e.g., [222]). The behavior of  $k_{\text{bell}}$  depends on whether the chemical bond in question is under tension or compression. This information is readily available in simulations and can be directly drawn from the beam model representing the motor. As the Bell model describes a one-dimensional relation, the question arises, which force measure to apply in the three-dimensional case. Candidates are the magnitude of internal translational forces  $\mathbf{F}_1$  of the linker element or the contribution with respect to a certain direction of the material frame (e.g., normal forces at the nodes). Taking into account the axial strain  $\varepsilon$ , the force  $F_1$  entering Equation (4.3) is given by

$$F_1 = \begin{cases} |\mathbf{F}_1| & \text{if } \varepsilon > 0, \quad \text{tension} \\ -|\mathbf{F}_1| & \text{if } \varepsilon < 0, \quad \text{compression} \end{cases} \quad (4.4)$$

Depending on the characteristic distance  $\Delta x$ , a chemical bond can be characterized by

$$\Delta x = \begin{cases} > 0 & , \text{slip bond} : \text{tension weakens bond} \\ < 0 \mid F_1 \leq \bar{F}_1 & , \text{catch bond} : \text{tension strengthens bond up to } \bar{F}_1 \\ = 0 & , \text{force-independent} , k_{\text{bell}} = k_{\text{off}} \end{cases} \quad (4.5)$$

The chemical bond between the motor head domain and the filament can be modeled as a *catch bond* with the characteristic distance of  $\Delta x = -2.5 \pm 0.6$  nm entering the Bell model (4.3), when ADP is bound to the head domain [68]. A fairly simplified, yet intuitive way of thinking about the character of slip bonds and catch bonds is depicted in Figure 4.3b: a tensile force acting on a slip bond has a purely destructive effect on the bond, while the same tensile force evokes self-locking in a catch bond. The threshold force was quantified experimentally as  $\bar{F}_1 \approx 6$  pN [68], beyond which  $k_{\text{bell}}$  increases with load. There are more advanced and complex

approaches (e.g., [222]) than the Bell model for the description of the influence of mechanical load on chemical reactions. However, due to its simplicity and the availability of experimental values for  $\Delta x$ , the Bell model is often assumed to be a good approximation when modeling force-dependence. Choosing  $\Delta x < 0$ , the Bell model describes catch bond behavior [173]. Eventually, these considerations lead to a force-dependent probability of bond dissociation

$$p_{\text{bell}} = 1 - \exp(-k_{\text{bell}}\Delta t). \quad (4.6)$$

### 4.2.3 Cyclic motor activity and motor-filament interaction

In this section, key features of the model will be introduced, which aim to recreate the cyclic activity of a molecular motor. Furthermore, light will be shed on the specifics of the interaction between motor and filament.

**The enzymatic cycle** Reaction equations (4.2) have to be made available to the mechanical model. In order to mimic the *effect* of the conformational changes rather than their chemical or kinematic details, the reactive cycle is simplified. ATP is not explicitly simulated but is taken into account implicitly by its probability of attachment to the motor domain by means of a Poisson process. The following two steps, i.e., the separation of the phosphate and its release, which triggers the power stroke, are jointly modeled in the wake of the attachment process. What remains, are two basic conformations: a long state  $l$  and short state  $s$  of the motor's head domain, which are interrelated by chemical transitions with effective reaction rate constants  $k_{ls}$  and  $k_{sl}$ . The probability of the chemical transition and its reversal are given by

$$p_{ls} = 1 - \exp(-k_{ls}\Delta t), \quad p_{sl} = 1 - \exp(-k_{sl}\Delta t). \quad (4.7)$$

This way, the activity of the motor can be tuned according to the implicitly given ATP concentration. Attachment to filaments only occurs in the long, cocked state  $l$ , which is followed by contraction to the short state  $s$  at some proximal, post-attachment point in time (of course, given a finite contraction rate constant  $k_{ls}$ ). Between attachment and the subsequent power stroke, a motor may detach based on Equation (4.6). Furthermore, the power stroke model does not allow for detachment during the stroke or, in other words, until the motor has completely performed its stroke, displacing the filament by stroke distance  $\delta_+$ . The stroke distance of the motor is included in its working distance  $\delta_w$ . If the motor detaches at zero strain,  $\delta_+ = \delta_w$ . The difference  $\delta_- = \delta_w - \delta_+$  is called the *drag stroke distance* and accounts for the distance that the still attached motor is dragged along with the moving filament. During the drag stroke, which typically last for  $\leq 1$  ms, the motor is compressed [88], leading to a significant increase of  $k_{\text{off}}$  (reported value:  $k_{\text{off}} \sim 2000\text{s}^{-1}$ , [88]), leading to a strongly increased likelihood of detachment from the filament. The recovery stroke, during which the motor head is detached from the filament, is only accounted for by the off-time  $\tau_{\text{off}}$ , that determines reattachment time scale. At the end of recovery, the motor returns to state  $l$ , another cycle begins. In order to achieve this recovery behavior, one may in principle employ one of two approaches, by either directly declaring a time slot of duration  $\tau_{\text{off}}$  or, which is more elegant, leave the recovery to probabilistic instruments. The definition of the recovery rate constant is given by

$$k_{sl} = 1/\tau_{\text{off}}, \quad (4.8)$$

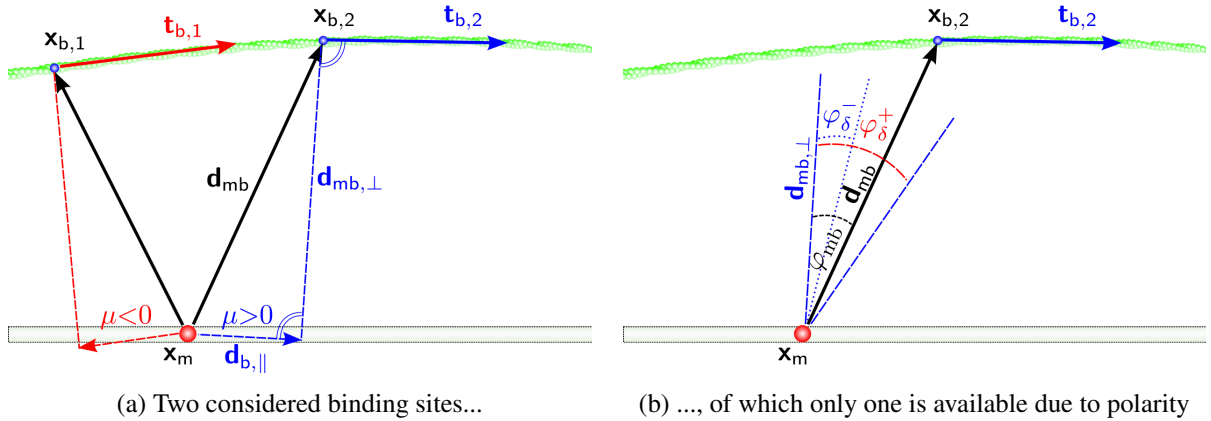


**Figure 4.4** Structural polarity of filaments is modeled with the help of material triads at the binding sites. Here, only the tangents are depicted. (a) Two potential binding sites, of which one fulfills the polarity condition with respect to motor position  $\mathbf{x}_m$  (blue,  $\mu > 0$ ), while the other does not (red,  $\mu < 0$ ). (b) Additionally, the considered binding site is tested for compliance with angle interval  $[\varphi_\delta^-; \varphi_\delta^+]$ .

which means that a recovery stroke is expected to take place with a probability  $p(i_r \Delta t \geq \tau_{\text{off}}) = 1$  with  $i_r \in \mathbb{N}^+$  denoting the number of recovery time steps, i.e. since the latest detachment. In Section 4.1, the duty ratio has been reported to be of the magnitude  $r \sim [0.01; 0.1]$ . In the following, this ratio will be set to an intermediate  $r = 0.05$ , such that  $\tau_{\text{off}} = 38$  ms.

**Polarity criterion** The establishment and the maintenance of a chemical bond between motor and filament depends on filament polarity. A motor is only able to bind to a filament if the orientation of the filament with respect to the motor's current position allows for it. The orientation and the polarity of a filament is determined by means of the orientation of its material triads. The  $3 \times 3$  binding site triad  $\mathbf{\Lambda}_b$  can be extracted from the beam model using Equation (3.3), where the first column represents the unit tangent  $\mathbf{t}_b$  of the filament at this particular location (see Figure 4.4a). The definition of the (+)-end of the filament to be located in the direction of  $\mathbf{t}_b$  enables the formulation of a polarity condition in a fairly straight-forward way. For a given pair of locations  $\mathbf{x}_b$  for the binding site and  $\mathbf{x}_m$  for the motor, it reads

$$\mu = (\mathbf{x}_b - \mathbf{x}_m) \cdot \mathbf{t}_b = \begin{cases} \geq 0, & \text{fulfilled} \\ < 0, & \text{not fulfilled} \end{cases} \quad (4.9)$$

and represents the signed scale of the vector contribution parallel to  $\mathbf{t}_b$ .

**Geometrical criteria** Apart from structural polarity, the model of the motor is required to adhere to a set of geometrical criteria. The formulation of these criteria is motivated by geometry (i.e. motor size) and kinematics (i.e. possible motor configurations). The first criterion demands a certain proximity of the motor and the considered binding site, which is expressed by  $\|\mathbf{d}_{mb}\| = \|\mathbf{x}_b - \mathbf{x}_m\| \in [L_m - \Delta L_m; L_m + \Delta L_m]$  and has been introduced in Section 2.6.3. Here,  $L_m$  denotes the size of the motor,  $\Delta L_m$  is a heuristically chosen tolerance. The second criterion further diminishes the set of potential binding sites. It is motivated by the need to inhibit the establishment of bonds that most likely do not occur with actual motor proteins due to geometrical and kinematic restrictions. In other words, this criterion implicitly excludes unwanted

and unnatural motor positions without modeling the exact (molecular) geometry of the motor. Assuming a working distance  $\delta_w = 5$  nm, one may give an estimate of the angular restriction of both the motor's and the binding site's reaction volumes. In fact, the means used to create helically oriented binding sites presented in Section 3.2 (cf. Figure 3.3) can be directly applied to this problem, where both binding partners have to lie in each other's scope.

Next, the dimension of the motor unit needs to be quantified. In the case of a myosin head, there exists an  $\alpha$ -helical structure of length  $d_l \approx 8.5$  nm, which serves the purpose of a lever [226]. During the large conformational change, this lever rotates by approximately  $70^\circ$  covering a distance of  $\sim 10$  nm in the process [88]. The length of the entire head domain can be roughly approximated by  $\sim 2 - 3 d_l$ , which provides an appropriate estimate for the motor size  $L_m$ . In order to achieve working distance  $\delta_w$  by means of a longitudinal contraction, the angle covered by the rod during the power stroke – from state  $l$  to  $s$  – needs to be in the range of  $\theta_{ls} \approx 15^\circ$ . A good estimate for an upper angular bound is given by  $\varphi_\delta^+ \sim \arcsin(\delta_w/L_m)$ , which helps excluding improbable, yet possible motor-substrate pairings within the limits set by structural polarity. The actual value in simulations should be chosen such that  $\varphi > \varphi_\delta^+$ . The enforcement of this angular restriction is ensured by simply evaluating the enclosed angle

$$\varphi_{mb} = \arccos(d_{mb,\perp}/d_{mb}), \quad (4.10)$$

where  $d_{mb} = \|\mathbf{d}_{mb}\|$  and  $d_{mb,\perp} = \|\mathbf{d}_{mb,\perp}\|$  are the  $L^2$ -norms of the difference vector between motor position  $\mathbf{x}_m$  and binding site location  $\mathbf{x}_b$  and its projection orthogonal to the binding site tangent  $\mathbf{t}_b$ , respectively. Finally, in order to avoid the motor simply pulling down the filament instead of tangentially displacing it, the motor's reaction volume is additionally bounded by  $\varphi_\delta^-$  at the lower end. Its value should be small (geometrical considerations imply  $< \varphi_\delta^-/10$ ). Motors are allowed to bond to filaments within the angular interval  $[\varphi_\delta^-; \varphi_\delta^+]$ , which upon attachment results in slanted motors as Figure 4.4b implies. The choice of these angles influences reaction kinetics as the reactive volume depends on them. Making the interval too narrow makes chemical activity cease.

#### 4.2.4 Modeling of conformational change

**Continuum mechanics interpretation of conformational change** The mechanical part of force generation triggered by the reaction model from Section 4.2.3 is accomplished by an update of the translational and orientational reference configurations. What seems at first like a primitive meddling with basic model parameters, can in fact be motivated in a very satisfying, since fundamental way. Conformational change is the effect observed during the translation from one local free energy minimum to another. The two states are separated by an energy barrier of some reaction-specific height. The energy needed to overcome that barrier between the two states is provided by ATP hydrolysis in the case of motor proteins (or by thermal fluctuations depending on the model). Having eventually overcome the barrier, the new conformation seeks to stabilize at its local free energy minimum. A change in the reference configuration of the beam model achieves an analogous behavior. The Poisson process (4.7) modeling the arrival and hydrolysis of ATP provides the trigger for the change of reference configuration, creating an off-balance restoring force, that drives the beam to approach its new unstrained configuration. On its way there, the beam displaces the filament as does the real

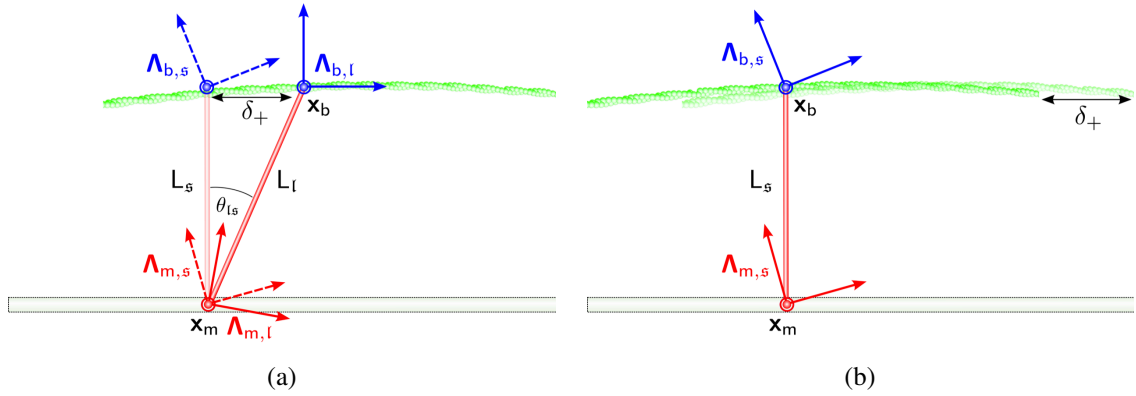


**Figure 4.5** A longitudinal contraction in conjunction with a rotation of the reference material triad results in an updated reference configuration that enables a power stroke covering the targeted working distance  $\delta_+$ . *Left:* Reference configurations *pre* and *post* power stroke. *Right:* The filament is pushed along by the motor, which has deformed towards its updated reference configuration.

myosin head. Hence, the (re)set of the reference state not only has the same effect on the filament as a conformational change, but also adheres to the same energy principle.

**Parametrization of conformational change** The power stroke will be modeled by a contraction  $\lambda$  and a rigid body rotation by an angle  $\theta_{ls}$  of the motor element. The aim is to enable a motor-driven filament trajectory which is parallel to the filament's tangent  $\mathbf{t}_b$  at the motor attachment site. Such a modeling decision may vary from reality but entails a few geometrical properties that facilitate the parametrization of the power stroke. The motor is assumed to attach itself to a filament in a slanted configuration (cf. Figure 4.5a). The new reference length is then calculated such that the beam's stress-free configuration is perpendicular to  $\mathbf{t}_b$ .

As the power stroke model considers the source of the stroke to be a quadratic spring potential  $W = E_m A_m \delta_w^2 / (2L_s)$  with Young's modulus  $E_m$ , cross section  $A_m$ , and the short target reference length  $L_s$ , the energy stored in the cocked state  $l$  may simply be released by altering the (relaxed) reference length  $L_l$  of the rod-like continuum representing the motor. Note the difference between the power stroke model and the beam model at state  $l$ : while the power stroke model *is* actually strained and locked in that configuration, the beam model is instantaneously strained, when the reference configuration is set to state  $s$ . The updated reference length of the beam is given by

$$L_s = \lambda L_l \quad (4.11)$$

with  $L_l$  being the length of the long, cocked state. The scale factor is then easily calculated as  $\lambda = d_{mb,\perp} / d_{mb}$ . A sensible choice of the binding angle interval  $[\varphi_\delta^-; \varphi_\delta^+]$  as well as adhering to the geometrical criteria formulated above (also, cf. Figure 4.4), the working distance of the motor model can be tuned to values around the experimentally observed working distance  $\delta_w$ , but may vary depending on the geometrical situation.

In a simultaneous step, material triads  $\Lambda_m$  and  $\Lambda_b$  of the current configuration are utilized to compute the updated referential rotations of the beam element representing the motor. As the degree of contraction is governed by  $\lambda$ , so is the rotation of triads  $\Lambda_m$  and  $\Lambda_b$ . As depicted in

Figure 4.5a, the angle by which the triads need to be rotated is given by

$$\theta_{ls} = \varphi_{mb} = \cos^{-1} \lambda, \quad (4.12)$$

which directly relates to the geometry described by Equation (4.10). The axis of rotation can be determined bearing in mind that vector  $\mathbf{d}_{mb}$  needs to be rotated to come to lie in the direction of  $\mathbf{d}_{mb,\perp}$ . The rotation can be parametrized by its pseudo-vector representation

$$\boldsymbol{\theta}_{ls} = \theta_{ls} \frac{\mathbf{d}_{mb} \times \mathbf{d}_{mb,\perp}}{\|\mathbf{d}_{mb} \times \mathbf{d}_{mb,\perp}\|}, \quad (4.13)$$

with which one may retrieve the orthonormal triad describing the associated rotation

$$\mathbf{\Lambda}_{ls} = \exp(\overset{\circ}{\boldsymbol{\theta}}_{ls}). \quad (4.14)$$

The updated rotation, where the power stroke is expected to terminate, can thus be formulated as

$$\mathbf{\Lambda}_{m,s} = \mathbf{\Lambda}_{ls} \mathbf{\Lambda}_{m,l}, \quad \mathbf{\Lambda}_{b,s} = \mathbf{\Lambda}_{ls} \mathbf{\Lambda}_{b,l} \quad (4.15)$$

with matrices  $\mathbf{\Lambda}_{(\cdot),l}$  and  $\mathbf{\Lambda}_{(\cdot),s}$  denoting orientations of entity  $(\cdot)$  in their respective long and short conformation.

This modeling step somewhat reflects the idea of the *swinging cross-bridge*. Both the swinging cross-bridge model as well as the swinging-lever-arm hypothesis feature slightly more complex kinematics than the here proposed model (cf. [82, 195]). However, the following section will argue that such a kinematic simplification is acceptable for mesoscale simulations. There exists another mechanically motivated reason for the incorporation of rotations. The applied beam formulation allows for the transduction of moments. This needs to be accounted for by an alteration of the referential rotations, since otherwise the longitudinal contraction has to do work against the bending stiffness of the two joints, which has not been reported to occur for the actomyosin bond (and probably never will be due to the difficulty of such a measurement).

The entire update procedure is depicted in Figure 4.5, which illustrates the general mechanism leading to a translation of the filament. As a consequence of changing the reference orientation, the beam experiences restoring moments in  $\mathbf{x}_m$  and  $\mathbf{x}_b$ . Eventually, the superposition of contraction and rotation yields the desired stroke distance  $\delta_+$  as illustrated in Figure 4.5b. Using the inverse relation of Equation (4.15), the update can be undone if necessary, e.g. if the return to state  $l$  is explicitly modeled. For all subsequent numerical examples, however, this behavior is not considered, since the motor detaches from the filament and recovers its long state without being represented by a beam element.

With this relation, one may transcend from one to the other basic conformation and exert forces on filaments to which the motors are currently attached. From [88], it is known that the entire power-stroke sequence lasts for about 1ms, of which a portion of  $\tau_- \approx 0.4\text{ms}$  can be attributed to the drag stroke. The remaining time  $\tau_+$  represents the temporal fraction, during which the motor is active. This time scale is used to quantify the rotation increment for a given time step size  $\Delta t$ , which simply is

$$\Delta\theta_{ls} = \begin{cases} \theta_{ls} & \text{if } \Delta t \geq \tau_+ \\ \frac{\Delta t}{\tau_+} \theta_{ls} & \text{if } \Delta t < \tau_+ \end{cases}. \quad (4.16)$$

The valid objection remains that the cocked state of the power stroke model is pre-stressed and the beam in the present model is not as its reference length is  $L_l$ . This minor deficit seems tolerable considering the already significant degree of abstraction of the model as compared to a real motor. Also, the spring of HMM has yet to be discovered. Lastly, the primary intention is the modeling of an effect rather than the precise properties of molecular motors. In summary, the model is deemed adequate for its designated purpose.

### 4.2.5 Comprehensive incorporation of all modeling aspects into the existing finite element framework

In principle, the functionalities introduced in the preceding sections of this chapter can be applied in conjunction with an arbitrary nonlinear, geometrically exact beam element, that accounts for rotations in some way. However, there are consequences resulting from the chemical resolution, which require additional measures.

The computational bottleneck is characterized by the path distance of myosin, which is  $\delta_p = 36$  nm. The standard network model introduced in Chapter 2 requires direct nodal connectivity and thus a mechanical discretization that matches the path distance of the molecular motor. In order to put things into perspective, this particular value for  $\delta_p$  entails a mesh refinement by a factor of 3.5 as compared to the numerical experiments conducted in chapters 5 and 6. This implies an increase in the total number of DOFs by the same factor. While the additional computational effort for modeling myosin may in some cases still be handled efficiently by means of adequate search algorithms and a sensible parallelization of computational processes, the gap between the chemically required and the mechanically needed discretization length takes on disadvantageous proportions, especially, when the path distance is reduced to meet the value of kinesin  $\delta_p \approx 5.5$  nm and each tubulin subunit on a microtubule represents a potential binding site.

However, a remedy to this predicament has been introduced in Chapter 3, where chemical binding sites do not have to coincide with FE nodes anymore. Hence, the simulation of motor-filament assemblies is enabled by a triad of measures, which comprises the discretization of the motors with interpolated beam elements (cf. Section 3.3), the provision of inter-nodal binding site positions on filaments in order to keep their mechanical discretization acceptably coarse, and, lastly, the model that governs the reaction kinetics and the enzymatic cycle of the molecular motor.

## 4.3 Numerical examples

For the purpose of model validation, an experiment with well-defined properties has been chosen: an *in vitro* actin/HMM *motility assay*. Motility assays like the ones shown in Figure 4.6 represent commonly used experimental set-ups (cf. [4]) and are often employed in order to study the properties of motor proteins and how they affect their cargo under well-controllable lab conditions (e.g., [68, 121, 189]). The aim of this chapter is to demonstrate that a sensible choice of parameters for *in silico* motors leads to observations on the filament scale, which are well comparable to *in vitro* values. Two quantities will serve the purpose of model validation: *forces* exerted by the linkers (or, as a matter of fact, their internal forces) and the *average ve-*

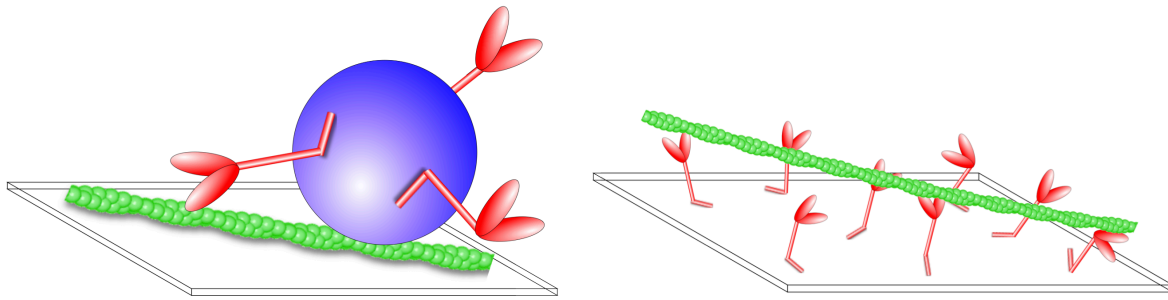


**Figure 4.6** The two basic motility assay set-ups. *Left*: Bead assay with motors (red) attached to a microbead and filaments (green) attached to the microscope coverslip. *Right*: Gliding assay with motors attached to the coverslip and filaments which are free to move.

*locity* of transportation of single filaments. A particular choice of model parameters such as the contraction factor  $\lambda$  or the rod length  $L_f$  entails parameter-specific forces and velocity values. By choosing parameters carefully, one may then tailor the motor model such that it reflects the effect of motors on their cargo as known from a great variety of experiments (e.g., [52, 183, 189], see also Table 4.2 and Table 4.3).

In the subsequent sections, two numerical experiments will be conducted, of which the first resembles an experiment by [214] as it is restricted to one-dimensional diffusion (Section 4.3.2). The second example is of more complex nature and simulates a two-dimensional motility assay as depicted in Figure 4.8b (Section 4.3.3). All relevant simulation parameters are listed in Tables D.4 (basic motor parameters), D.5 (quasi-1D assay), and D.6 (2D-assay).

### 4.3.1 Motility assays in experiments

Motility assays have two components: motors and their cargo. There are two basic assay geometries: *bead assays* and *gliding assays*, their discriminating feature being which species is movable and which is fixed. In bead assays, filaments are fixed and motors are attached to a microbead, which is pushed around by motor activity (Figure 4.6a). In gliding assays, filaments are transported across a lawn of fixed motors (Figure 4.6b). Here, numerical representations of gliding assays are studied and compared to experiments, where HMM serves as the motor, while its affiliate filament F-actin is the cargo. HMM comprises the two globular head domains and their  $\alpha$ -helical levers and is chemically severed from its tail domain, light-meromyosin (LMM), prior to being used in the assay. The assay itself consists of a microchamber with a volume of usually some tens of  $\mu\text{L}$ , which is filled with a fluid containing ATP. The motors are attached to a microscope coverslip (see the cartoon in Figure 4.8a). Fluorescence-labeled filamentous actin is added in order to track the motor-driven path of motion. The snapshot depicted in Figure 4.8a shows some fluorescent actin filaments (most of the filaments, however, remain unlabeled). Filament density  $\rho_f$  is usually chosen as the control parameter for the assay. Depending on  $\rho_f$ , the system can be characterized as a *low-density* motility assay or a *high-density* motility assay. At low densities, filaments are disordered. With increasing density, however, polar patterns emerge and collective motion can be observed. In [183], the filament threshold density is located at

about  $\rho_f^* = 20\mu\text{m}^{-2}$ . The example in Section 4.3.3 will recreate the low-density phenomenology of this kind of experimental set-up.

The presence of certain chemical additives in the buffer solution alter the dynamic behavior of filaments, which allows for the evaluation of otherwise inaccessible information. One such additive is *methyl cellulose*, which is a highly viscous synthetic chemical compound (*trivia*: methyl cellulose is used in movies for the representation of slime, ooze, or lava). Its effect on actin filaments is very useful for studying motor transport velocities even at very low motor densities. In direct sequence to this section, numerical results will be presented that recreate the  $\rho_m$ -dependent transport velocity of filaments in a one-dimensional problem. Afterwards, a more complex simulation of a two-dimensional motility assay is discussed.

### 4.3.2 Transport velocity of filaments in one-dimensional in silico motility assays

As mentioned in Section 4.3.1, the diffusive behavior of actin filaments can be altered by chemical additives to ease the experimental quantification of motor activity. The effect of such additives can be reproduced computationally, which leads to a very simplistic, yet equally informative in silico problem, which is going to be outlined below.

**Experimental background** One of the experiments reported by [214] (data plotted in [88, p. 221, Figure 13.3]) evaluates actin filament transport velocities  $v_f$  depending on myosin motor surface density  $\rho_m$  using an in vitro gliding assay. The addition of the thickener methyl cellulose increases the viscosity of the buffer solution to values in the range of  $\eta = 0.05\text{-}0.1$  Pas. It is reported to greatly slow down lateral diffusion while having nearly no effect on the longitudinal transport velocity of filaments. The reason for the use of methyl cellulose is to keep filaments close to the motor-covered surface of the coverslip. As a consequence, transport velocities can be measured far below the threshold surface density  $\rho_m^*$ , which is the density, above which motor activity is observable for a filament of a certain length (see [88, p. 200] for exemplary values).

**Problem description** The simplest way of reproducing the experiments of [214] is to restrict the filament to its longitudinal DOF, which can be easily accomplished by a prescription of zero-displacement conditions on the Dirichlet boundary. The purpose of this series of simulations is the calibration of the motor model, which eventually leads to a sensible set of modeling parameters.

A visualization of three distinct temporal configurations is depicted in Figure 4.7a, where a filament is transported in direction of its  $(-)$ -end. In analogy to the experiment, the filament length is set to  $L_f = 2\mu\text{m}$ . It is discretized with 10 BFEs and features binding sites spaced  $d_b = 36\text{ nm}$  corresponding to the path distance  $\delta_p$  of myosin. The given motor surface density  $\rho_m$  translates to a corresponding line density  $\rho_{m,1D} = \sqrt{\rho_m}$ , which is varied to account for different motor densities ranging on the interval  $[30; 3000]\mu\text{m}^{-2}$ . A periodic boundary condition is employed in global  $x$ -direction (i.e. the direction of filament translation) with a periodic repeat of  $H = 10\mu\text{m}$ . Temperature is set to  $T = 303.15\text{ K}$  in order to recreate the lab conditions reported in [214]. The viscosity of the surrounding buffer solution is raised to  $\eta = 0.05\text{ Pas}$  to account

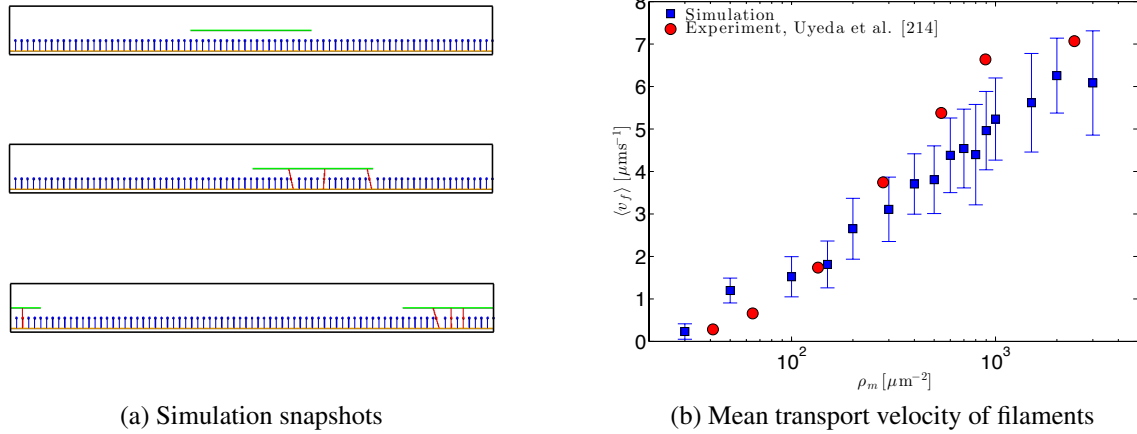


**Figure 4.7** (a) Snapshots from three different points in time illustrating the transportation of the green filament in (–)-direction by motors (blue, red) and across the periodic boundary. Motors are attached to the ground, which is modeled by beam elements as well (orange). The pictures show larger than usual linkers ( $L_m = 85$  nm) for visual clarity. (b) Mean filament transport velocity  $\langle v_f \rangle$  depending on the motor density  $\rho_m$  in the presence of methyl cellulose [88, 214] for linkers of length  $L_m = 20 \pm 10$  nm.

for the addition of methyl cellulose. The simulated time is given as  $T_{\text{sim}} = 20$  s with a time step size of  $\Delta t = 5 \times 10^{-4}$  s.

**Motor parameters** The size of a motor is set to  $L_m = 20 \pm 10$  nm in order to be close to the actual size of a myosin head, which is about 20-30 nm [88] assuming a lever length of 8.5 nm and a head of approximately double that size. The variation determines the distance interval of the reactive volume of the linker and might also be loosely considered as a size variance of the motors. The stroke distance in the unloaded case is set to  $\delta_{+,0} = 10$  nm. The actual distance  $\delta_+$  in simulations varies from this value as the new relaxed state is not necessarily reached. The local rate constant modeling the probability of attachment of a motor to a filament is chosen to be  $k_{\text{on}} = 180 \text{ s}^{-1}$  and the corresponding off-rate  $k_{\text{off}} = 0.09 \text{ s}^{-1}$  as given for HMM by [152]. The latter rate constant is relevant to detachment processes without a prior power stroke, i.e., it models spontaneous detachment of the motor from the filament. The rate constant governing the probability of a power stroke is set to  $k_{\text{ts}} = 800 \text{ s}^{-1}$ . Note that this parameter is set heuristically here in order to ensure a quick contraction after attachment to the filament, i.e., a high ATP concentration is assumed. The motor’s cycle time is set to  $\tau_c = 40$  ms, which determines the recovery rate constant  $k_{\text{sl}}$  by means of Equation (4.8). The duty ratio is chosen as  $r = 0.05$ . The stiffness of HMM has been experimentally determined by [219] as  $c_m = 0.69 \pm 0.47 \text{ pN/nm}$ . From data by [202], the motor model’s circular cross section can be calculated as  $A_m = 4.75 \times 10^{-6} \mu\text{m}^2$ , which results in a Young’s modulus in the range of  $E_m = 3.0 \times 10^6 \text{ pN}/\mu\text{m}^2$ .

**Motor forces** The magnitude of forces exerted by the motors in the direction of the filament tangent  $\mathbf{t}_b$  during their power stroke phase is found to be  $2.5 \pm 1.0$  pN, which overall compares acceptably well to experimental data by [52], bearing in mind that the filament was held fixed there while the simulated filament is translated. Forces reported by other sources are in the same range and are listed in Table 4.2. Furthermore, compressive forces during the drag stroke phase are found to be in the range of  $-1.55 \pm 0.8$  pN. Some motors are tensed before having

performed their power stroke. They experience forces of  $\sim 0.45$  pN. A more detailed discussion will follow for the case of the two-dimensional motility assay.

**Transport velocities** With the present parametrization, one arrives at a reasonably close match to reported experimental values as Figure 4.7b proves. The density-dependent increase of  $v_f$  is captured well by the numerical model as well as the onset of saturation for  $\rho_m > 1000 \mu\text{m}^{-2}$ . Values at high densities  $\rho_m$  are found to be slightly lower than reported in experiments. However, apart from the difference being moderate also in absolute values, it can be argued that the remaining difference may result from the simulation being strictly one-dimensional. Although methyl cellulose inhibits lateral diffusion, it certainly does not inhibit motors from participating in filament transport, which do not lie in the direction of motion but are slightly displaced laterally. As a consequence, a larger number of motors propels the in vitro filament leading to a higher velocity than in the case of the strictly one-dimensional in silico example. Being able to model individual active components, which adequately approximate the known kinematic and kinetic properties of a non-processive molecular motor, one may utilize this base unit to build more complex motors resembling, e.g., the shape and function of myosin thick filaments (cf. Section 4.4).

### 4.3.3 Simulation of a two-dimensional motility assay

The second example features a two-dimensional field of motors, which propels a number of single filaments. While the long-term goal could be large-scale simulations of the collective movement of filaments involving contact interactions, the short-term goal simply is the examination and validation of the model for low-density assays.

**Problem description** As the experiment can be conceived more or less as a two-dimensional problem (ignoring the fact that the fluid film on top of the coverslip has a finite thickness), the filaments in the simulation are confined within the  $xy$ -plane. The visualization in Figure 4.8b shows  $N_f = 100$  single filaments of length  $L_f = 4 \mu\text{m}$ , which are distributed in an area measuring  $6 \times 6 \mu\text{m}^2$ . This implies a filament density of  $\rho_f \approx 3 \mu\text{m}^{-2}$ . A filament is discretized with  $N_e = 16$  BFEs as described in Chapter 2. All filaments are initially straight. Temperature is set to a constant  $T = 293.15$  K. The simulated volume is equipped with periodic boundary conditions. As stated in [88], the distance between two adjacent binding sites on a filament is chosen to equal the path distance of myosin II,  $\delta_p = 36$  nm. Accordingly, the matrix of motors is chosen to have a square layout with a distance between two neighboring motors of  $d_b = \delta_p$  as well. The resulting motor density is  $\rho_m = 770 \mu\text{m}^{-2}$  ( $N_m = 27777$  motors), which is well beyond the threshold density  $\rho_m^*$  (cf. [88, p. 220],  $\rho_m^* = 600 \mu\text{m}^{-2}$  to move a filament with a length of  $1.1 \mu\text{m}$ ). The microscope coverslip is modeled by a parallel array of BFEs with inter-filament spacing  $d_s = \delta_p$ , which are spatially fixed by means of Dirichlet boundary conditions. Each coverslip filament has a length  $L_s = 6 \mu\text{m}$ . It is discretized with  $N_{e,s} = 20$  BFEs of the same type as the free filaments and has motors attached at predefined binding positions. If a mechanical connection is established between a filament and a motor, an interpolated beam element as introduced in Chapter 3 is temporarily added between the free filament and the fixed filament until the power stroke is terminated. The motors are confined and spatially fixed in a plane parallel to

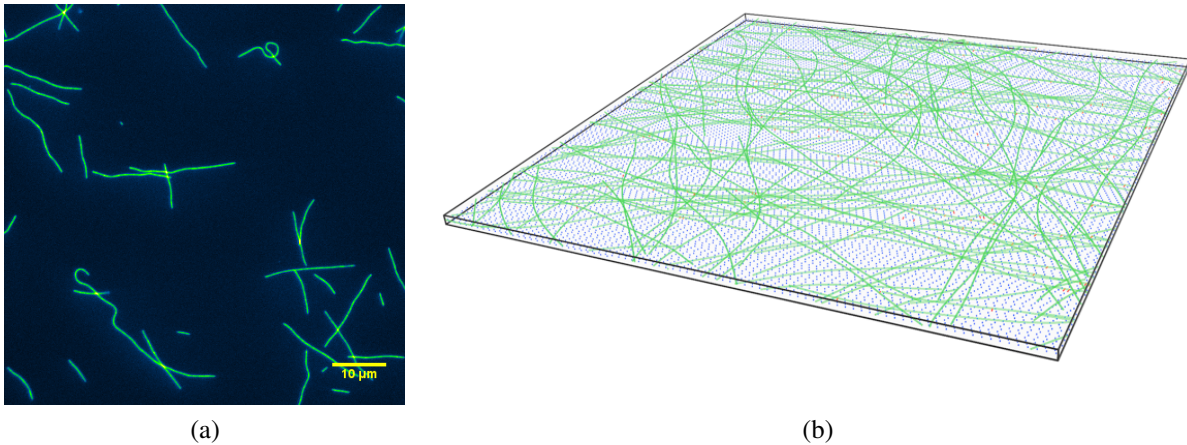


**Figure 4.8** *Left:* Snapshot of fluorescence-labelled filaments in an in vitro gliding motility assay (modified from [151]). *Right:* Perspective view of an in silico motility assay with  $N_f = 100$  free filaments (green),  $N_m \approx 28000$  motor units/active linkers (blue), of which a certain number form short-lived mechanical connections with filaments (red).  $N_m$  corresponds to a motor surface density  $\rho_m \approx 770 \mu\text{m}^{-2}$ . The fixed filaments, to which the motors are permanently attached, are not shown. The problem is constrained to two dimensions and neglects excluded volume effects.

the filaments' plane of motion with a separation of 20 nm, which equals the motor size  $L_m$ . The simulation covers a time interval  $T_{\text{sim}} = 20$  s at a step size of  $\Delta t = 5 \times 10^{-4}$  s. Further simulation parameters like the filament's material properties are summarized in Table D.7.

**Motor parameters** Motor properties are chosen equal to those for simulations of one-dimensional motility assays described in Section 4.3.2.

**Remark on excluded volume effects/mechanical contact** The collective motion of filament assemblies beyond  $\rho_f^*$  in [183] is greatly influenced by excluded volume effects. In Chapter 5, a method for modeling beam contact based on an Augmented Lagrange scheme will be applied to prevent filaments from overlapping in three-dimensional space. This approach does not cover the exception of perfectly parallel contacting beams. Perfect parallel alignment of filaments is a possible, yet highly unlikely scenario, and for that matter has been considered negligible. In two dimensions, however, the chosen approach is not applicable as contact between parallel beams or the collision of a beam's tip with another beam's side are highly likely scenarios. The former case represents a geometrical exception and is not covered by the contact algorithm as the evaluation of the closest-point-projection fails, while the latter case is inconsistent with the theory of one-dimensional continua. One alternative to this beam contact formulation is a FE approximation of the *Lennard-Jones potential*, which theoretically enables the realization of excluded volume effects for fully arbitrary orientations of contact pairs. Other approaches for contact detection and evaluation capture the exception of parallel contacting beams and treat it adequately [41, 42]. However, both alternatives do not solve principal problems such as a lack of numerical robustness in case of very slender beams or the undetected cross-over of beams between iterative steps. As this numerical study purely aims at the evaluation of the motor model, the additional complexity introduced by mechanical contact is neglected for now, but undoubtedly must be accounted for in the future.

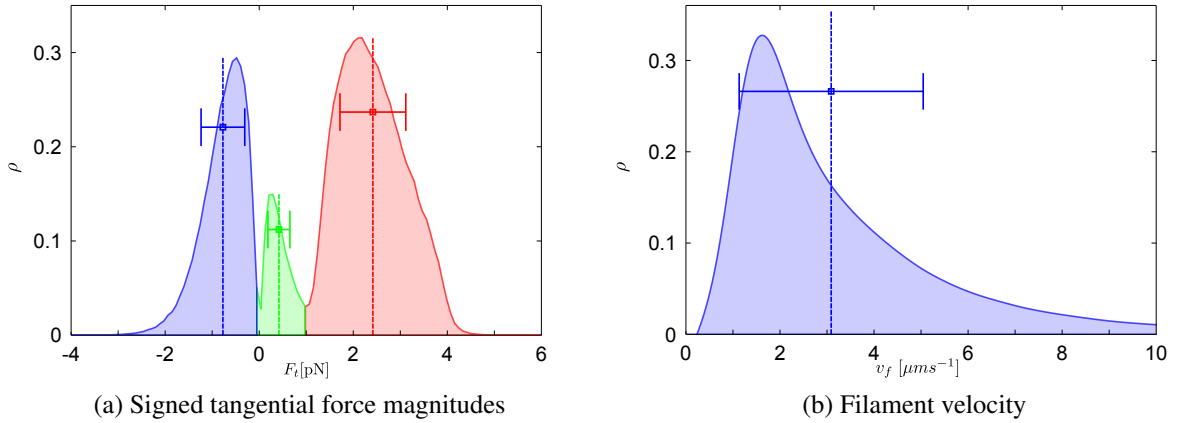


**Figure 4.9** (a) Distribution of exerted motor forces. Three distinct regimes are observed. From left to right: The drag-stroke-regime (blue) with negative strains  $\varepsilon$ , where motors experience compression with a mean force of  $F_t = -0.77 \pm 0.46$  pN. A smaller peak with a mean value of  $F_t = 0.44 \pm 0.23$  pN represents motors that are tensed, yet have not yet performed their power stroke (green). The third regime (red) represents motors being underway of performing their power stroke but still remain in the power-stroke-phase as  $\varepsilon > 0$ . The mean force is found to be  $F_t = 2.44 \pm 0.7$  pN. All three mean values are depicted as dashed vertical lines accompanied by error bars. (b) distribution of filament transport velocities  $v_f$  for filaments of length  $L_f = 4 \mu\text{m}$  gathered over a simulated time of  $T_{\text{sim}} = 20$  s. The average velocity is computed as  $\bar{v}_f = 3.1 \pm 1.9 \mu\text{m/s}$  and is again represented in the graph by the dashed vertical line along with error bars.

The absence of contact between beams leads to unordered, criss-crossing filaments independent of their concentration as they do not interact with each other at all given the present hydrodynamic model. The only implicit influence of filaments on each other is the fact that the total number of *free* motors available for chemical binding is reduced by a growing number of filaments. However, this is unproblematic as long as  $\rho_f < \rho_f^*$  since the gradual depletion of free motors occurs in reality as well.

It is safe to assume that the dynamics of a low-density motility assay can be approximated by the described numerical set-up. An increase in the number of simulated filaments would simply improve the statistical quality of statements on filament velocities and motor forces. Although more complex phenomena such as collective motion patterns and their cause can currently neither be observed nor explained, the basic functionality of the motor model may be assessed very well.

**Motor forces** In view of the gap in geometrical complexity between the beam formulation and the Bell model, the question arises which computed forces actually do enter the Bell model as input parameters (cf. Section 4.2.2). Several candidates arise. A satisfactory answer to this question can be found by studying how data was ascertained experimentally. The measurement of forces for single motors is commonly performed using optical traps or mechanical setups. In the former case, a microbead with attached motors is fixed to a microscope coverslip while a filament is strung between two optically trapped beads. The motor displaces the filament leading to a displacement of the bead. The exerted force is measured by an atomic force microscope. In the latter case, the motor is fixed to the coverslip and the filament is held by a thin glass fiber, that serves the purpose of miniature tweezers. Both set-ups tend to measure forces in direction of the filament. Force values typically lie in the  $10^0$  pN-range. The measurement of the motor

force contribution pointing in tangential direction of the filament seems the most faithful way of data evaluation. In addition, with regard to the Bell model, it is of interest, whether the motor is tensed or compressed. This information can be easily drawn from the mechanical model itself in terms of the longitudinal strain  $\varepsilon$ .

**Discussion** Figure 4.9a features the distribution of tangential force magnitudes  $F_t$ . Forces  $F_t$  are enriched by information on the strain state. If  $\varepsilon < 0$ , the motor is compressed and the sign turns negative. Vice versa, if  $\varepsilon > 0$ , the motor is tensed and the force values are given as positive. As a consequence of this convention, the Figure is dominated by the peaks of three well-distinguishable subdistributions corresponding to the three basic states a motor takes on while being attached to a filament. A first peak arises for negative force values, which accounts for the motors being compressed after the power stroke is performed. The mean value is calculated as  $-0.77 \pm 0.46$  pN. Motors that are compressed exhibit a much higher unbinding probability according to the model presented in [88] and are very likely to detach from the filament. These motors are currently engaged in the drag-stroke fraction  $\delta_-$  of their working distance  $\delta$ .

The second peak corresponds to motors that have attached to filaments but have not yet performed their power stroke. The average force of  $0.44 \pm 0.23$  pN that is exerted on the filament, stems from motors being slightly tensed due to filament motion. Finding a motor in this state is more unlikely than finding it in one of the other states. The relative height of the peak and the variance of the distribution are controlled by  $k_{ig}$ . Low values result in a higher peak and a broader distribution as motors then are more likely to remain in the pre-stroke state.

Finally the regime on the right can be attributed to motors currently performing their power stroke. These motors are under tension ( $\varepsilon > 0$ ). The average force exerted on filaments during the power stroke phase can be quantified as  $2.44 \pm 0.7$  pN. To the author's knowledge, no reliable experimental data has been reported on the magnitude of forces of pre-power stroke linkers or in the drag-stroke regime, so that a comparison with numerical data is impossible. However, there are plenty of single motor force measurements in literature, which correspond to the third regime shown in Figure 4.9a. With model parameters chosen reasonably close to actual motor dimensions and reaction kinetics, a very good agreement between experimentally measured forces and their numerical counterpart is observed. The higher force values and the

Reference		purpose	myosin type	force [pN]
Simulation		-	-	$\geq 2.44 \pm 0.7$
MOLLOY <i>et al.</i>	[158]	measurement of single-motor forces	■,●	$\geq 1.8$
WARSHAW <i>et al.</i>	[226]	verification of lever arm hypothesis	■,■*	$1.6 \pm 0.3$
FINER <i>et al.</i>	[52]	measurement of forces & step length	■	$3.4 \pm 1.2$
TAKAGI <i>et al.</i>	[200]	force & step dep. on dynamic load	▲	$\leq 9.0$

**Table 4.2** Myosin motor forces found in simulation and experiments. Different rabbit skeletal muscle myosin II parts are examined (filament ▲, HMM ■, HMM mutants ■\*, S1 fragment ●, cf. Figure 4.1a). Mutants differ from wild type myosin by the length of their neck domains. The values give a good impression of the range of exerted forces per motor.

smaller tolerances in experiments can be explained by the difference in set-up. Forces in most experiments are measured with the help of a fixed filament and are restricted to one motor-filament pair. Forces extracted during the simulation of a gliding assay obviously assess the acting forces in a state of dynamic equilibrium, i.e. the compliances of all bound motors factor in the equilibrium forces of each other. Of course, the reasonable matching of simulation and experiment is not a surprise per se as simulation parameters may be chosen such that they meet the observations. However, it is an encouraging finding that a reasonable choice of parameters leads to comparable results albeit the considerable abstraction the model has undergone. Force values found in various experiments are listed in Table 4.2.

**Transport velocity of filaments** Finally the effect of motor activity on the movement of filaments is evaluated for this larger example. In analogy to Section 4.3.2, the transport velocity of filaments is studied in order to assess the appropriateness of the chosen set of model parameters. Figure 4.9b presents the result of this simulation. It depicts the normalized distribution of transport velocities  $v_f$ . Velocities were evaluated for time intervals of  $\Delta t_{\text{eval}} = 10\Delta t$  in order to smoothen filament motion. A peak in the distribution can be seen at  $v_f = 2 \mu\text{m/s}$  followed by a smooth drawn-out descent towards higher velocities. The average transport velocity is  $\bar{v}_f = 3.1 \pm 1.9 \mu\text{m/s}$  and thus lies in the range of values reported in experiments. The comparatively broad dispersion of filament velocities is surprising at first but seems to be present also in experimental literature. In [189], measured velocities are found to be 2-6  $\mu\text{m/s}$  revealing a rather large variance, which the authors attribute to different myosin preparation. Apart from a preparation-based dispersion of quantities, velocities vary greatly depending on the myosin type and its origin ( [88] reports values of  $\sim 60 \mu\text{m/s}$  for myosin XI in algae). Furthermore, the ATP concentration in the buffer solution as well as the pH of the buffer solution have a strong influence on motor performance. Thus within the bounds of experimental uncertainties, the numerical motor model seems to perform rather well. Table 4.3 lists velocities reported literature.

Reference	assay	myosin	origin	$L_f[\mu\text{m}]$	$\rho_m[\mu\text{m}^{-2}]$	$v_f[\mu\text{m/s}]$
Simulation	gliding	-	-	4	$\sim 770$	$3.1 \pm 1.9$
SHEETZ <i>et al.</i> [189]	bead	▲	△, □, ○	-	-	2-6
KRON <i>et al.</i> [121]	gliding	▲	△, ○	$\sim 10$	-	1-4
SCHALLER <i>et al.</i> [183]	gliding	■	△	$\sim 5$	$\sim 600$	$4.8 \pm 0.5$
UYEDA <i>et al.</i> [214]	gliding	■	△	$\sim 2$	40-2400	$\leq 7$
TOYOSHIMA <i>et al.</i> [207]	gliding	▲, ■, ●	△	$\sim 10$	$\sim 500$	$\sim 8$

**Table 4.3** Comparison of the simulated transport velocity with various experimental values. Different parts of myosin (entire filament ▲, HMM ■, S1 fragment ●) from several organisms and organs (rabbit muscle △, turkey gizzard □, slime mold ○) as well as different fragments of the myosin filament are listed. Depending additionally on environmental conditions (motor density, ATP concentration, pH, etc.), the dispersion of velocities is large, which implies that there is the need to individually fit the motor model to the species to be modeled.

### 4.3.4 Conclusions

The effect of motor proteins on filaments depends on a multitude of both intrinsic as well as external parameters. Filament length  $L_f$ , motor density  $\rho_m$ , temperature, ATP concentration, as well as the origin of the myosin motor influence the way motors interact with their cargo. Choosing a parametrization close to physiological conditions, the numerical motor model allows for a good approximation of single-motor behavior. Hence, as long as motors share a common mechanism (kinematics, enzymatic properties) as in the case of the myosin superfamily, the model may be fitted to experimental findings with the help of an individual set of parameters. In summary, the presented numerical model fulfills all requirements in order to be applied in more complex studies as it reproduces the fundamental behavior of a motor protein. The forces it exerts on filaments as well as the velocity of filaments resulting from motor activity are in the range of physiological motors.

## 4.4 Outlook

In this chapter, a model for a non-processive molecular motor has been presented, which can act as a basic building block for a number of scientific applications. Given robust and efficient algorithms for contact detection and evaluation, the presented model may be utilized to study the evolution of polar patterns of motor-driven filaments in more detail, which enhances the knowledge of actomyosin interactions (in extension, e.g., of [183]). One may use this simple model to build larger and more complex motor units, which have been key components in a number of theoretical [122, 131] as well as experimental endeavors [132, 205] to elucidate the mechanism of active bundle contraction. Bundle contractility is indeed a very interesting topic of vivid and ongoing research as these structures provide the means for force generation within cells. Here, myosin filaments play a vital role in both ordered and disordered filament-motor assemblies, e.g., in sarcomeres and the contractile ring, respectively. Ordered assemblies are crucial to muscle contraction, disordered ones play a pivotal role in cell division.

In this slightly extended outlook, ideas will be presented on how to expand the existing motor model in order to tackle problems revolving around cellular force generation.

### 4.4.1 Future model refinements

The current model represents only the first step towards portraying the activity of single molecular motors such as myosin. It is known for example, that the rate of ATP hydrolysis is coupled to the amount of mechanical loading a myosin motor or an entire muscle experiences, a phenomenon called the *Fenn effect* [49], which expresses itself in heat generation proportional to contraction. This relation is currently not reflected in the numerical model of the molecular motor but can be included by coupling the contraction rate constant  $k_{15}$  to the forces acting on the motor element. In principle, this simply entails an additional force-dependence similar to the Bell model, which governs the strength of the motor-filament bond.

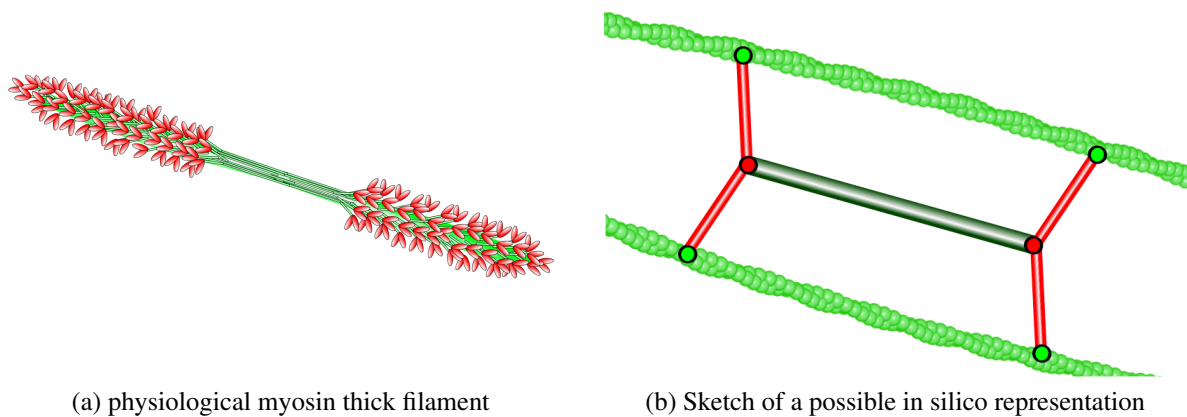


**Figure 4.10** *Left:* illustration of a physiological myosin thick filament. It has two ends with antiparallel motor arrays and a bare zone in its middle section. The red, ribbon-shaped entities represent motor head domains. *Right:* simplified model of a thick filament with four motor units, which consists of four individual beam elements representing the motors (red), and one beam element representing the filament backbone (dark green).

#### 4.4.2 Towards modeling myosin thick filaments

Under certain physiological solvent conditions, single myosin filaments assemble into agglomerates, which can be characterized as rather thick filaments [4]. The light chain tail domains of single myosin molecules assemble into bundles and create an axisymmetric filament with two structurally identical halves. The heavy chains containing the motor units are therefore divided into two groups of several hundreds of motor head domains each, which have antiparallel working directions (see Figure 4.10a). In view of the goal to study the influence of motor activity on the scale of networks, efficiency dictates not to model single myosin head domains by means of individual beam representations. Rather, the first strategic modeling decision has to sum up the joint mechanical effect of all heads and condense it into a reduced set of active motor units as shown in Figure 4.10b. The building blocks for such a motor model have all been introduced and discussed in chapters 2 to 4. At this point, it is merely a matter of combining the fundamental filament model from Chapter 2 with the extended model from Chapter 3 in order to provide a sufficient resolution of binding sites required for motor activity, and finally create the motor geometry of Figure 4.10b using four contractile beam elements introduced in the present Chapter 4. That alone might already be sufficient to model the motor activity of myosin thick filaments. However, [132] reports that bundle contractility can be attributed to filament buckling caused by motors with a certain statistical dispersion in their contraction rates, their transport velocities, and probably their sizes as well. These uncertainties may be readily included in the model by definition of appropriate tolerances for rates and other statistically dispersed quantities, which may then be randomly attributed to individual motor units and which are drawn from an assumed governing probability distribution. Having introduced a certain dispersion to some of the characteristic quantities, it would be possible to predict the amount of contractility in terms of statistical measures, which would help ascertain the validity of some of the claims about what parameter actually enables contractility.

### 4.4.3 Simulation of contractile bundles and active networks of bundles

In a further expansion of the model, the myosin thick filament representation may be applied in the self-assembly of bundles of filaments in conjunction with other (passive) linkers. Such cooperative setups have been observed in the contractile ring [128] and different stress fibers [206], where myosin II and  $\alpha$ -actinin simultaneously interact with actin filaments. Thick filaments are known to alter the mechanical properties of actin networks [119, 210], e.g. affecting their rheological properties.

In the future, using the presented model, rheological studies as conducted in Chapter 6 could be expanded to active networks, e.g., in order to compare results to theoretical predictions on active polar gels (cf. [104]).



# 5 Equilibrium morphologies of semiflexible, transiently crosslinked biopolymer networks

The exploration of thermodynamically equilibrated network morphologies emerging from the interaction of semiflexible filaments and linkers is the main focus of this chapter. The equilibrated states of networks are virtually unobservable in *in vitro* experiments due to their extremely long equilibration times, which is why simulations present the only available means to study these structures phenomenologically. The main achievement of the chapter is the establishment of an equilibrium phase diagram incorporating all observed morphologies of semiflexible biopolymer networks with transient linkers. It is based on results presented in [35, 163] and comprises all network phases observed so far in *in vitro* systems [135, 140, 213] (see Figure 5.1 for experimental images). Each of the network morphologies is discussed on the basis of detailed structural information, which demonstrates how vast changes in network architecture are triggered by fine-tuning linker concentration. It has been proposed by [13], that small changes of key quantities (e.g., the binding energy, a second linker species, or filament length) result in a large scale reorganization of the network structure. Having acquired detailed on linker-mediated network evolution, one may precisely create networks by manipulation of a minimal parameter set, which includes filament and linker concentration as well as the linker type. These findings are invaluable for the subsequent Chapter 6, where the detailed understanding of self-assembly processes within the simulated system allow for the generation of rheological samples with precisely tunable mechanical properties.

It is of great interest to biophysicists, biologists, and bioengineers alike to understand how eukaryotic cells organize and make use of their structures of networked stiff biopolymers, which define the cell's mechanical properties. The cytoskeleton, for example, creates vast F-actin networks, which are involved in a great variety of essential cellular processes. At network entanglement points, individual filaments are often connected to each other by crosslinks, which are established by small linker molecules. Such composite materials are often encountered in both natural and man-made materials. The linkers determine the macroscopic mechanical response of a network to a large extent. In natural organic matter, crosslinks are usually established by small proteins, but in other cases also intermolecular interactions like hydrogen bonds or multivalent cations serve as linkers [161]. First steps in understanding polymer networks were undertaken, however, in the wake of creation of synthetic polymer structures commonly known as rubber [208]. The main interest of prior research endeavors lay in a general understanding of these artificial organic materials. P.-G. DE GENNES proposed a phase diagram for dilute solutions of polymers in order to predict their structure [39] with linkers only posing as attraction agents between polymers. Given a sufficiently high linker concentration (at the so-called *crosslink saturation threshold* [172]), theory predicts a *phase transition* accompanied by *den-*

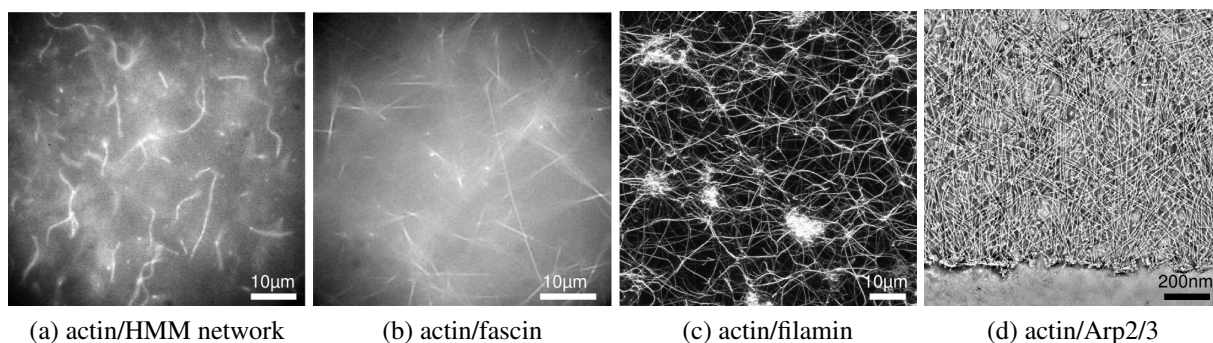


**Figure 5.1** Different F-actin network architectures arise in vitro depending on the linker species. (a) homogeneous isotropic actin/HMM network (molar ratio  $R = 1.2$ ), (b) actin/fascin network consisting purely of bundles ( $R = 1.1$ ), (c) actin/filamin cluster network ( $R = 0.1$ ), (d) electron tomogram of the front region of lamellipodia. Images in Figures (a)-(c) were kindly provided by K. M. Schmoller and A. R. Bausch [2]. The image in Figure (d) is used with kind permission of M. Vinzenz and J. V. Small [1].

*sity fluctuations* and *elastic stress variations*. In recent years, research on materials consisting of biological polymers has increased tremendously and has led to noteworthy developments in numerous scientific fields such as biochemistry, biophysics, medicine, and biomedical engineering [8].

Like man-made polymers, biological polymers can be organized in networks by crosslinking. The eukaryotic cytoskeleton is a prominent example. Polymerized actin filaments are its main mechanical constituent. They are often connected among each other by transient crosslinking proteins. In order to understand key aspects of cytoskeletal functionality, it is often necessary to reduce system complexity. Experiments, theory, and simulations thus mostly put their focus on two-component model systems. F-actin solutions and their viscoelastic behavior have been amply examined in experiments using macroscopic rheology [81] as well as microrheology [5, 55, 58]. Experimental findings received a thorough theoretical treatment (e.g., [53, 149]) and were the subject of numerical studies (e.g., [176]). Crosslinked F-actin networks, however, have far more interesting properties, which as well have been the topic of numerous scientific contributions over the past few years. A variety of experiments on actin networks focuses on the different network architectures, e.g., bundle networks (e.g., [54, 134, 136, 191]), homogeneous isotropic networks [137, 203], or structurally polymorphic networks (e.g., [139, 186]). Theorists have studied, amongst others, the kinetics of random fiber networks (e.g., [77, 78]), the consequences of microstructure on macroscopic elasticity [79], or the mechanics of fiber bundles (e.g., [76, 80]). Finally, a large number of numerical studies have mainly examined short time scale effects like strain-stiffening (e.g., [7, 93, 94, 115]) and high-frequency linear viscoelasticity [116]. Hitherto, there is a lack of numerical experiments on network evolution over long time scales, which can in detail explain the mechanisms behind network self-assembly as well as geometrically and mechanically analyze the emerging network structures. This chapter presents a first step towards closing this gap as linker-induced network aggregation will be studied on larger time scales in the range of biologically relevant processes such as cell division or migration. Filament aggregation depends on the concentration of linkers. Earlier attempts to explain, e.g., the aggregation of F-actin crosslinked by  $\alpha$ -actinin in the context of the de Gennes phase diagram [201] may be inadequate due to the following reasons.

1. Experiments clearly show different architectures depending on the linker species. Linkers dictate whether the resulting network consists of F-actin *bundles* [22, 23], *clusters* [186], and even *lamellar structures* as seen in the presence of counter ions [227] or the Arp2/3 complex in live lamellipodia [154]. A structural polymorphism such as observed in vitro is supposed to play an important part in the organization the spatial structure of the cytoskeleton in living cells [135, 197].
2. Compared to flexible polymers, semiflexible polymers are much stiffer. Due to their high stiffness, local phase separation as predicted by DE GENNES is rather unlikely. The separation of single semiflexible filaments from the aggregate while still being crosslinked would require large bending deformations, that cannot be achieved only by thermal effects. Furthermore, as the orientation of semiflexible filaments is auto-correlated over distances up to  $\sim 10 \mu\text{m}$ , orientational preferences of linker molecules can be transmitted over longer distances. Therefore, crystalline meshes as in liquid crystals are more likely to occur.
3. Thermal fluctuations of single filaments are increasingly suppressed by an increasing amount of filament crosslinking. As filaments become more ordered, their entropy is reduced, i.e., the number of possible geometrical states is decreased. Within such networks, the entropy of the linker molecules themselves may no longer be ignored.

## 5.1 Simulation of Network Evolution

The simulation of network evolution towards the point of thermal equilibrium poses a considerable challenge. Popular models like bead-spring or bead-rod representations of slender polymers in conjunction with an explicit time integration may be intuitive and easy to implement, yet inefficient and often methodically questionable. In fact, various micromechanical numerical studies examined predominantly, if not exclusively, phenomena on short time and length scales. The simulation of time intervals on the scale of several hundreds up to thousands of seconds is simply impossible for most, if not all, presented computational approaches to date. The BD/FE method by [34, 38] finally enables long-term studies, which allow for the establishment of an equilibrium phase diagram of semiflexible filament networks. Depending on a linker's orientational preference when connecting two filaments, four different prototypical network morphologies are predicted by computational model.

In order to ensure physical consistency between real filaments and their numerical representations, sensible simulation parameters have to be employed. The cubic simulation volume (as shown in Figure 5.2) with sides of  $H = 5 \mu\text{m}$  and periodic boundary conditions is occupied by  $N_f = \{52, 105, 208, 416\}$  filaments. If recalculated, these filament numbers correspond to  $c_f = \{1, 2, 4, 8\} \mu\text{M}$  filament concentrations, respectively. Temperature is set to  $T = 293.15 \text{ K}$  and the viscosity to  $\eta = 10^{-3} \text{ Pas}$ . The filaments' cross-sectional area is  $A_f = 1.9 \times 10^{-5} \mu\text{m}^2$ , the Young's modulus is given by  $E_f = 1.3 \times 10^9 \text{ pN}/\mu\text{m}^2$ , and the moment of inertia is set to  $I_3 = I_3 = 2.85 \times 10^{-11} \mu\text{m}^4$ . For a comprehensive list of parameters, the reader is referred to Table D.7. At this point, it is worthwhile to briefly touch the topic of accuracy of data gained from experiments and other sources tapped for reasonable simulation parameters. The measurement of the persistence length of F-actin may serve as an example. According to [65], sample

preparation clearly affects the mechanical properties. Fluorescent markers like rhodamine and phalloidin tend to stiffen the actin filament. Directly labeled actin is reported to have a persistence length of  $\sim 8 \mu\text{m}$ , rhodamine increases this value to  $9.1 \pm 0.5 \mu\text{m}$ . Phalloidin stiffens the filament by a factor of  $\sim 1.9$ , so that several sources in literature [100, 130, 169] arrive at values between  $16 \mu\text{m}$  and  $18 \mu\text{m}$ . The value predominantly chosen for simulations presented here is  $9.2 \mu\text{m}$ . Eventually, variations of the persistence length of this magnitude do not matter in most cases as they do not entail significantly different physical conclusions. The reader is therefore advised to interpret these parameters as a *well informed guess*, which represents a reasonable choice within given physical and physiological boundaries.

Linker molecules are the second simulated species and interact chemically and mechanically with the filaments. Initially, they are randomly distributed within the simulation volume. The linker size is set to  $0.08 \mu\text{m} \leq R_l \leq 0.12 \mu\text{m}$ . Important material and geometrical parameters comprise the cross section area  $A_l = 4.75 \times 10^6 \mu\text{m}^2$ , Young's modulus  $E_l = 2.56 \times 10^6 \text{ pN}/\mu\text{m}^2$ , and the linkers' moment of inertia  $I_l = 4.49 \times 10^{-11} \mu\text{m}^4$ . Additional parameters are summarized in Table D.7. Reaction sites on the filaments coincide with the finite element nodes which are equally distributed over a filament every  $h_f = 0.125 \mu\text{m}$ . The size of the linkers is in the range of real linker proteins like filamin or  $\alpha$ -actinin [50]. The central assumption concerning the nature of a linker is its preference for a certain enclosed angle  $\phi$  between the two filaments it connects. Being discretized with BFEs, crosslinks can transmit forces and moments and thus tend to maintain their preferred binding angle. Excluded volume interactions are taken into account by the application of an *Augmented-Lagrange* approach for the mechanical evaluation of contact between B-FEs (cf. [129, Chapter 6]). Entanglement is only partially modeled by this method since the combination of a large time step with highly slender structures requires further methodical steps such as a modified gap function, a cross-over detection, and a more robust numerical evaluation of beam contact interaction in general. However, the present approach already guarantees that the volumetric overlap of filaments is minimized.

## 5.2 The fundamental network morphologies of crosslinked semiflexible filament networks

### 5.2.1 Preliminary remarks on nomenclature

In the course of this chapter, some terms are going to be used frequently such that they require an a priori explanation. Linkers, which favor crosslinks between two filaments enclosing an angle of about  $\phi = \pi/2$  will be called *orthogonal linkers* from here on. In analogy, linker with an angular preference of about  $\pi/3$  are termed *hexagonal linkers*, and linkers with a preference for small inter-filament binding angles shall be called *parallel linkers*. Finally, linkers without any orientational preference towards the filaments it connects, are referred to as *isotropic linkers*.

Network architectures showing a pronounced point-symmetric character will be referred to as *clusters*, while sheet-like morphologies will be called *lamellae*. The terms *bundles* and *homogeneous isotropic gel* are self-explanatory. This terminology will be used whenever possible in an unambiguous way, e.g., *cluster* is synonymous to *cluster phase* or *cluster structure*.

## 5.2.2 Network morphologies

Given a linker concentration below the crosslink saturation threshold, the filaments in the volume form a homogeneous isotropic gel, see Figure 5.2a. Gels like these exhibit the well-elaborated power law behavior of  $\{G', G''\} \sim \omega^{3/4}$  (see Chapter 6, Figure 6.3b). The network mesh size, i.e., the average distance between two entanglement points, in such a network is given by  $\xi = 4.5 \times 10^{-2} L_p$ , which is significantly smaller than the persistence length of a single filament. An increase in linker concentration beyond the saturation threshold leads to filament aggregation. Depending on the preferred binding angle interval  $[\phi - \Delta\phi; \phi + \Delta\phi]$ , different network morphologies develop. For angles  $\phi < \pi/4$  and a tolerance  $\Delta\phi = \pi/16$ , phase separation occurs characterized by thick bundles of filaments in a dilute phase of single filaments. Initially, seeds of aggregation in different places of the simulation box may lead to several smaller bundles. However, these separate bundles finally aggregate into one large bundle which is depicted in Figure 5.2b. If  $\phi > \pi/4$ , a different structure emerges, the cluster. It has a radial symmetry and comprises all filaments in the volume, which results in its size being limited by the length of the incorporated filaments and thus to a maximal diameter of  $2L_f$ . The spatial distribution of linkers is highly non-uniform as Figure 5.2c illustrates. While the cluster core contains a very high concentration of doubly bound linkers, the outer corona of the structure is nearly devoid of linkers. It is therefore not surprising that filaments in the cluster core are so tightly crosslinked that their thermal fluctuations are almost completely suppressed, whereas filaments can freely fluctuate in the more remote regions of the cluster corona. With increasing distance  $r$  from the cluster core, the mesh size  $\xi$  increases following the relation

$$\xi(r) = r(4\pi/N_r)^{1/2}, \quad (5.1)$$

where  $N_r = N_f$  is the number of radial rays originating from the center of the cluster. The relation is visualized in Figure 5.3a. Due to this radial symmetry, the corona of the cluster phase can be considered self-similar. The mesh size of the cluster core is constant and is comparable to the linker length  $R_l$ . Making use of this fact, it is possible to estimate the core mesh size

$$\xi^* = R_l(4\pi/N_r)^{-1/2}. \quad (5.2)$$

Figure 5.3b provides complementary information on linkers. Here, the relative linker concentration is denoted as  $n_{l,rad} = N_{l,rad}/N_b$  with  $N_{l,rad}$  being the number of linkers found in a spherical shell with a volume  $V_s$ , thickness  $\Delta r$ , and center  $s_l$ . As one would expect in view of relation (5.1), a scaling behavior  $n_{l,rad} \sim R^{-5}$  is observed since the volume of the spherical shell scales with  $r^2$  for  $r \gg \Delta r$  and the spherical volume, whose surface is tangential to radially oriented rays, scales with  $r^3$ . The latter volume represents the space that filaments need to penetrate so that a linker may establish a crosslink. Linker concentration with respect to the radial coordinate thus has to scale inversely.

The question remains whether this cluster state is in thermodynamic equilibrium or if it represents a kinetically trapped intermediate state, as which it has been interpreted in experiments with the linkers filamin [186] and  $\alpha$ -actinin [140]. In these experiments, however, clusters consist of bundles of actin filaments rather than single filaments, which means that the first phase transition (from homogeneous isotropic gel to bundles) has already taken place at some lower linker concentration. It cannot be determined if another transition eventually occurs but the experimental clusters most probably are not equilibrated. In the end, it might very well be that

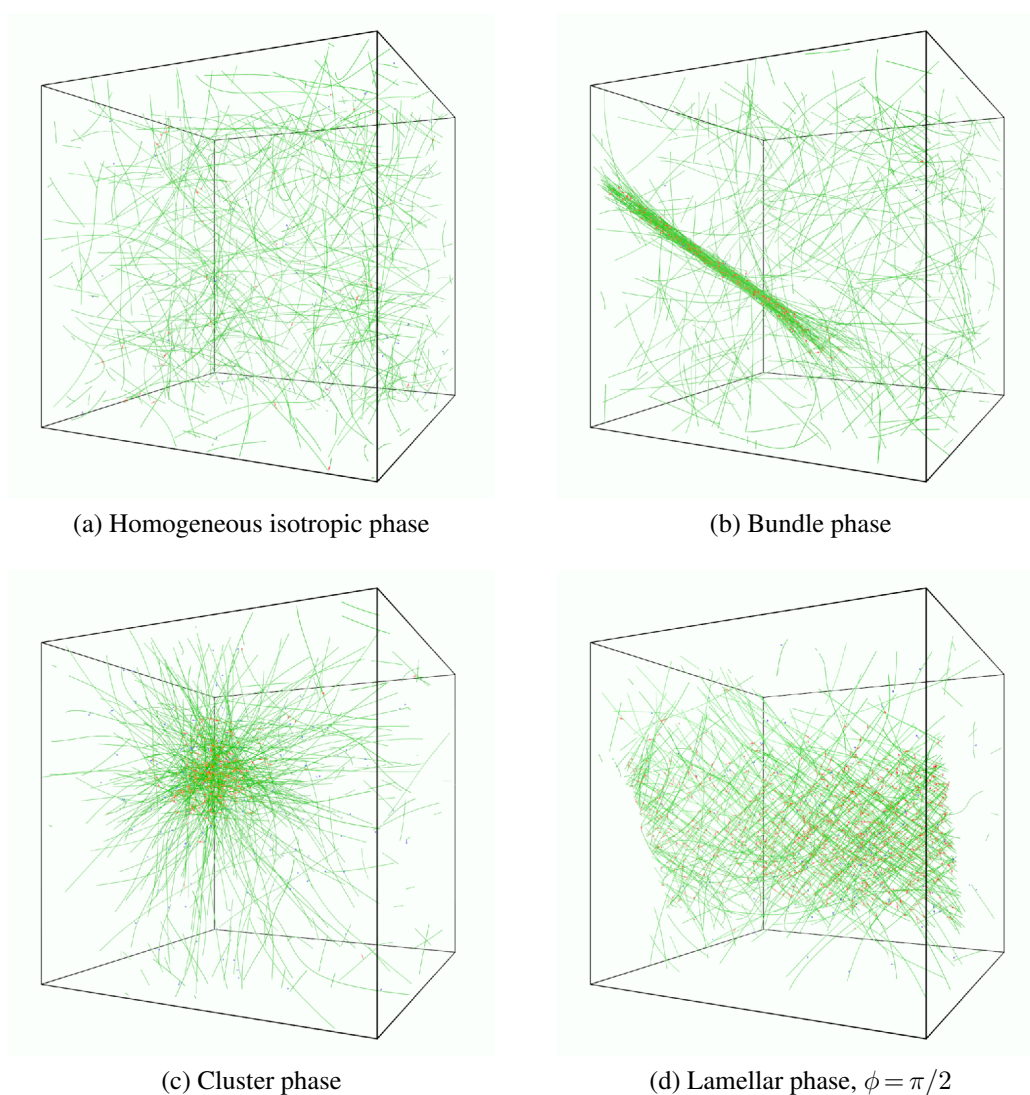


**Figure 5.2** Network phases observed in simulations. The cubic simulation volume contains semiflexible filaments (green), singly bound linkers (blue), and doubly bound linkers (red). Unbound linkers are not shown.

the experimental and the simulated clusters only share shapes, but differ in their thermodynamic states.

In order to verify either the equilibrium or non-equilibrium state of the cluster, first the constitution of lamellae is simulated. Lamellae establish at very high linker concentrations and represent a state of maximal geometrical order of filaments. At one point in time, usually several hundreds of simulated seconds, where the lamellae have arrived in a stationary state, a certain number of linkers is removed permanently from the simulated volume. The linkers left within the volume cannot maintain the lamellar structure. The subsequent process of reorganization of the filaments leads back to a structurally and temporally stable cluster. In analogy, linkers are added to a stationary homogeneous isotropic gel. Again, a stable cluster emerges. As a consequence, it is rather safe to assume that the cluster is in a state of thermodynamic equilibrium given the linker specifications chosen.

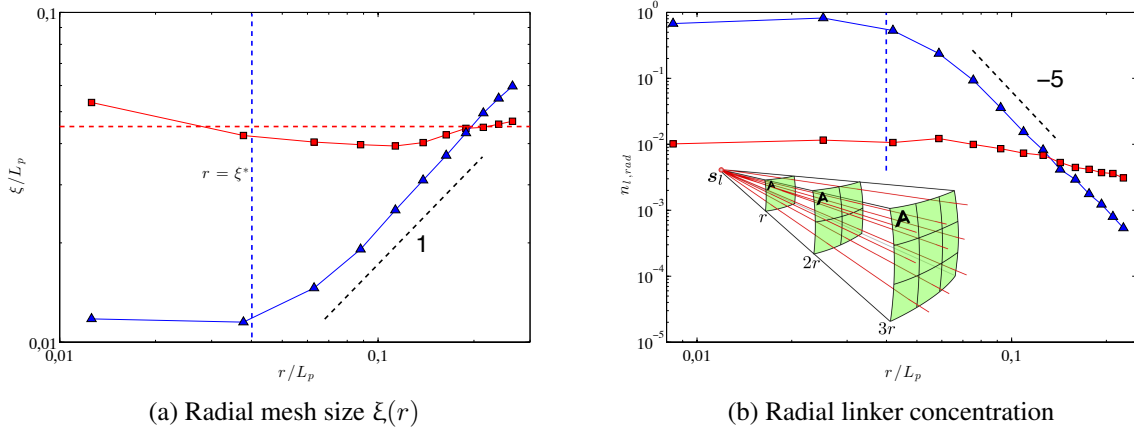


**Figure 5.3** (a) Local mesh size  $\xi(r)$  as a function of the radial distance  $r$  from the center of mass  $s_l$  of an isotropic-homogeneous gel (■) and a cluster (▲). While the homogeneous isotropic gel has a mesh size close to the uniform mesh size (red dashed line), the cluster’s mesh size is constant and comparable to the linker size  $R_l$  at the core. In the outer region with  $r > \xi^*$ , it can be described by  $\xi(r) = r(4\pi/N)^{1/2}$  (black dashed line), which is the mesh size of a spherical bundle of rays (see inset in (b)). (b) Radially measured relative linker concentration  $n_{l,rad} = N_{l,rad}/N_b$  of the same network phases as in (a). Not surprisingly,  $n_{l,rad}$  is nearly constant for the isotropic-homogeneous gel. The cluster, however, features a decreasing  $n_{l,rad} \sim r^{-5}$ .

A further increase of linker concentration leads to the formation of lamellae. Filaments are compacted in a sheet-like assembly with either a six-fold or a four-fold broken orientational symmetry as depicted in Figure 5.4. The corresponding binding angle intervals are given as  $5\pi/16 \leq \phi < 7\pi/16$  for the former and  $7\pi/16 \leq \phi \leq \pi/2$  for the latter case. The linker molecules that establish these network architectures are unordered with respect to their position within the lamellar phase. Yet they introduce bond-orientational order in accordance to [18]. Information on bond-orientational order travels across rather large distances due to the high bending stiffness of the filaments, which stabilizes the linker-induced order of the filaments. The observed structures correspond to two-dimensional hexatic and squaratic liquid-crystalline mesophases [110]. Here, these lamellae are limited in size due to a finite number of available filaments and linkers. Theoretically, however, lamellae can expand indefinitely by adding more filaments.

### 5.2.3 Parameter dependence of network morphologies

Claiming universal validity of the phase diagram – at least within chosen specifications – one is confronted with the necessity of proving the invariance of the qualitative behavior with respect to the most important system parameters. In a first step, these parameters were varied in a sensible and reasonable range. Linker stiffness plays only a negligible role in the formation of the phases. As long as it does not drop below values too small to guarantee sufficient torsional and axial stiffness, no noteworthy differences in the emerging network phases are observed. The variation of the length of the linkers leads to shifts in the linker saturation thresholds. Yet, the fundamental observation of the existence of four prototypical morphologies remains unaltered. It goes without saying that in the limit of either very short or very long linkers, observations deviate from the statement made above. In either case, aggregation does not take place at all.

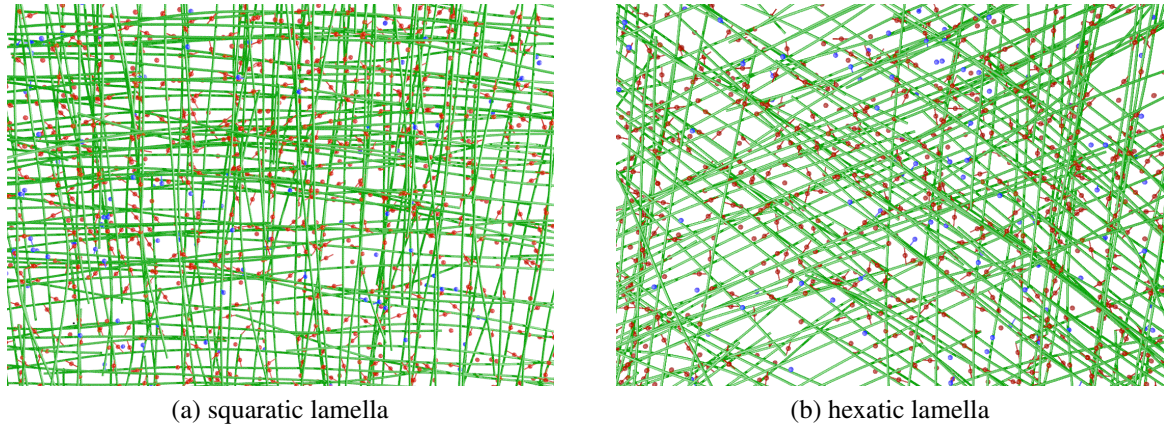


**Figure 5.4** Two kinds of lamellar morphologies emerge depending on the preferred binding angle  $\phi$ , either a four-fold symmetry (a) or a six-fold symmetry (b) develops.

While long linkers lack the ability to impose orientational order, short linkers may yet be able to aggregate filaments given enough free binding sites.

Interestingly, systems with isotropic linkers, i.e., without angular binding preference, always tend to form bundles, or as a matter of fact, a network of bundles, which is in a very slowly changing state of non-equilibrium. The network's slowed down evolution towards the free energy minimum, a single big bundle, can be explained by the enlarged pool of possible crosslinking sites as a consequence of lifting the angular constraint. The network of bundles is effectively frozen, at least for the duration of observation.

Furthermore the effect of the persistence length of the filaments was tested on an interval of  $[0.1L_p; 10L_p]$ . While the saturation threshold varied slightly from case to case, no fundamental differences were observed. Contact interaction played a minor role. Considering the small filament radius compared the linker length, i.e.,  $\sqrt{A_f/\pi} \ll R_l$ , the negligible effect of contacting filaments on network morphology can be readily explained. The linkers serve – at least in the present simulations – as spacers between the filaments and thus prevent filament contact in most cases. Only a linker with a length comparable to the filament diameter entails more pronounced excluded volume effects. However, in order to observe aggregation for small linkers, the number of potential binding sites on filaments has to be increased as well. With the BD/FE approach introduced in [34], where filament binding sites coincide with finite element nodes, the resolution of these length scales inevitably leads to a much finer mechanical discretization. Hence, the advantage of coarse-graining the filament is lost. In this thesis, a method enabling the establishment of inter-nodal crosslinks is presented in Chapter 3 that resolves this issue by decoupling the chemical from the mechanical discretization. An enhanced study using this method will be presented in Section 5.6. Another parameter whose effect on network morphology was thoroughly studied is the concentration of filaments  $c_f$  in the simulated volume. Within a concentration interval of  $[1 \mu\text{M}; 8 \mu\text{M}]$ , neither are new morphologies encountered nor do any of the previously found structures disappear [33]. Among all parameters, it is the binding angle deviation  $\Delta\phi$  that has the most pronounced impact on network morphology. An increase of  $\Delta\phi$  towards  $\Delta\phi = \pi/2$  leads to a reduction of possible network morphologies. The bundle regime grows until – in the limit of no angular preference – only two observable domains remain: ho-

mogeneous isotropic gels for low linker concentrations and bundles above the linker saturation threshold.

## 5.3 Equilibrium phase diagram of semiflexible filament networks with transient linkers

### 5.3.1 Establishment of the phase diagram

The phenomenological observations of Section 5.2.2 can be condensed into a phase diagram, which is shown in Figure 5.5. It presents the equilibrium network morphology as a function of the preferred binding angle of the linkers and the relative linker concentration  $n_l = N_l/N_b$ . For this particular realization of the phase diagram, filament length was chosen  $L_f = 4 \mu\text{m} = 0.43L_p$ , the binding angle tolerance was set to  $\Delta\phi = \pi/16$ , and the initial mesh size to  $\xi = 0.41 \mu\text{m}$  ( $= 4.5 \times 10^{-2}L_p$ ) (for additional parameters, see Table D.7; standard values are underlined). As linkers seek to maximize the number of their potential filament binding sites,  $n_l$  seems an appropriate measure for the tendency towards filament aggregation. Experimentalists often refer to a molar ratio  $R = c_l/c_g$ , where  $c_l$  is the linker concentration and  $c_g$  represents the concentration of globular actin that are subsequently polymerized to filaments. In a well controllable *in silico* environment as the present one,  $n_l$  can easily be understood as a related quantity. In order to obtain the information needed to establish Figure 5.5, the linker concentration  $n_l$  was increased by steps of  $\Delta n_l = 0.015$ , which in the case of a  $4 \mu\text{M}$  network corresponds to  $\Delta N_l = 100$  linkers. The gradual increase of linker concentration was performed for discrete preferred binding angles  $(i_\phi - 1)\pi/16 \leq \phi \leq (i_\phi + 1)\pi/16$ ,  $i_\phi = 1, \dots, 7$ . In order to ascertain the precise transition concentration,  $n_l$  was fine-tuned in steps of  $\Delta n_l = 4 \times 10^{-3}$  ( $\rightarrow \Delta N_l = 25$ ).

Having studied all relevant simulation parameters contributing to equilibrium structure formation and bearing in mind the relative insensibility of the qualitative findings towards these parameters, the phase diagram presented in this chapter can be interpreted in a rather general sense as being representative for networks made of semiflexible polymers like F-actin with transient linker molecules.

### 5.3.2 Discussion

Figure 5.5 predicts structural mesophases at high linker concentrations. These phases take the form of bundles for small  $\phi$ , which then gradually transcend into lamellae for increasing values of  $\phi$ . First a continuous flattening of the bundles can be observed until  $\phi \approx \pi/4$ , where filaments aggregate into an intermediate state between bundle and lamella. Subsequently the network structure spreads out shaping a layer-like network. Mesophases like the ones observed arise due to the high stiffness of semiflexible polymers as compared to flexible polymers. The large persistence length of the filaments allows for angular preferences of the linker molecules to be conveyed over distances that are in the range of the filaments' persistence length. Mesophase formation has been predicted in a theoretical paper [13]. Their prediction of a *cubic* phase, which represents the three-dimensional expansion of the lamellar phase, could not be examined in the present study as it was not observed. By contrast, both lamellar morphologies have recently been predicted in [110], where they are referred to as *tetratic* and *hexatic*.

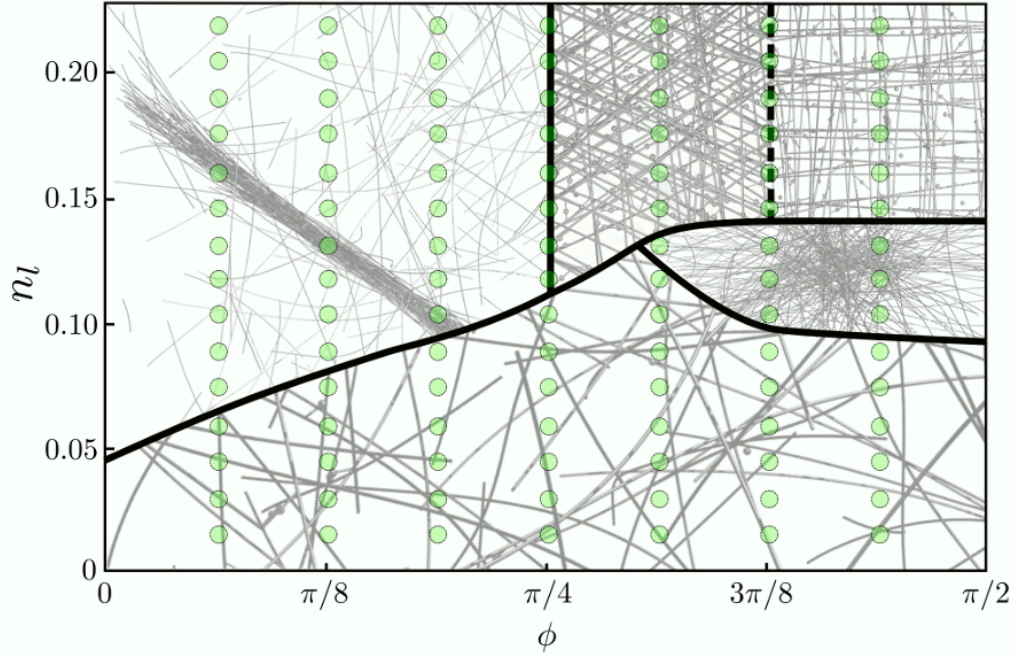


**Figure 5.5** Equilibrium phase diagram as a function of the preferred binding angle  $\phi$  and the ratio  $n_l = N_l/N_b$  of the number of linkers and the total number of binding sites on the filaments in the volume for an angular tolerance  $\Delta\phi = \pi/16$ , filament length  $L_f = 4\mu\text{m} = 0.43L_p$ , and  $N_f = 208$  filaments. The pale green spots mark data points, each of which represents the outcome of a simulation.

Simulations with filament length  $L_f = 4\mu\text{m}$  and  $H = 5\mu\text{m}$  leading to the formation of a cluster always result in this cluster incorporating all filaments. It is reasonable to question this finding as it is obviously connected to the simulation box size and the finite filament concentration. Previously, studies involving a significantly increased simulation box size were computationally infeasible [35]. However, the methodic extensions introduced in Chapter 3 now allow for such simulations. While keeping filament length  $L_f$ , filament and linker concentration  $c_f$  and  $c_l$  constant, the box size was increased to  $H = 10\mu\text{m}$ , which in fact becomes comparable to the size of a small cell (parameters given in Table D.8). Following the argumentation in [35], the cluster radius has to be similar to the length of a filament. Thus an increase of the simulated volume is predicted to lead to the formation of multiple co-existing clusters.

The enlarged simulated volume contains  $N_f = 1664$  filaments ( $N_e = 8$  elements per filament) and  $N_l = 7200$  linkers, which corresponds to a linear scaling of previous simulations, for which clusters were observed. Figure 5.5 indicates a relative linker concentration of  $n_l \approx 0.13$  for this case. The increase in system size requires an efficient search algorithm, which manages the matching of linkers to potential binding sites. A geometrical binning strategy has therefore been introduced (cf. appendix B.2).

Figure 5.6 depicts several structures confined in the enlarged simulation box. Three lamellae as well as two clusters can be seen. The coexistence of lamellae and clusters can be explained by a competition for linkers among the structures, which leads to spatial linker density fluctuations. As will be elaborated later in Section 5.3.3, lamellae, compared to clusters, offer the greater number of binding site pairs that are potential crosslinking sites between two filaments. As a consequence, the probability of finding a doubly bound linker molecule in a lamella is higher than in clusters.

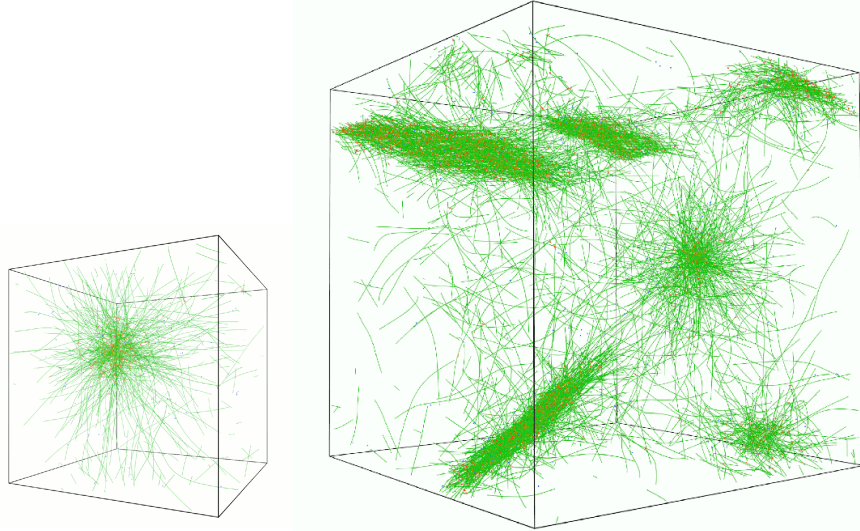


**Figure 5.6** Result of a simulation featuring an enlarged simulation box ( $H = 10 \mu\text{m}$ ). Filament concentration  $c_f$ , filament length  $L_f$  as well as linker size  $R_l$  remain unchanged compared to previous studies in this chapter. At  $t = 350 \text{ s}$  multiple lamellar structures and two cluster structures have developed. All of them are in a (nearly) stationary state as they have not undergone significant morphological changes for over 150 s. In order to be able to simulate a system of this size, the extended linker beam element formulation of Chapter 3 has been applied. For comparison, a *regular* simulation box ( $H = 5 \mu\text{m}$ ) is depicted as well.

In Section 5.2.2, numerical evidence has been presented that clusters are thermally equilibrated. However, they are fragile constructs judging from the small phase domain, in which they exist according to Figure 5.5. Once disturbed, e.g., by a small change in the local linker density, they dissolve and reassemble into another morphology. Such disturbances occur in environments large enough to host multiple different structures such as depicted in Figure 5.6. Here, clusters are eventually bound to be incorporated into larger superstructures, as the net flux of linkers for clusters is negative, i.e., they lose linkers in competition with lamellae until they cannot maintain their form anymore. As a consequence, one might have to weaken the claim of thermally equilibrated clusters. Their existence as a thermodynamically stable morphology depends, apart from filament persistence length, on the filament length  $L_f$  itself, and, as a matter of fact, on its environment. A desolate cluster is stable, two clusters, however, can unite and most probably will form a lamella.

### 5.3.3 Impact of linker entropy on network morphology

Here, the effect of linker entropy on network morphology will be discussed. The concept of a linker saturation threshold for flexible polymers introduced in [172] can be shown to maintain its validity also in the case of semiflexible polymers. Isotropic homogeneous gels represent the thermodynamically favored architecture at low linker concentration. In this case,  $N_b \gg N_l$ . Hence, conformational fluctuations of the filaments by far dominate the free energy. Filament entropy is maximized when the distribution of filament orientations is uniform, which is equivalent to White noise.

Raising the linker concentration entails drastic changes. Since each finite element node is a potential binding site for linkers, the total number of node pairs eligible for the establishment of crosslinks factors into filament aggregation. The maximal number of these node pairs depends on the network morphology and therefore on linker concentration. A quick estimation of the density of such binding site pairs in an homogeneous isotropic gel with isotropic linkers reveals  $\rho_{db,iso} \sim R_l/\xi^4$ . This estimate can be motivated on the one hand by the density of filament-filament crossings in the volume, which is  $1/\xi^3$ . On the other hand, there is the distance criterion set by the size of the linker  $R_l$ , which dictates that the probability of two filament binding sites crossing each other at a distance  $R_l$  can be written as  $R_l/\xi$ . In the case of the presented simulations,  $\rho_{db,iso}$  corresponds to a linker to binding site ratio  $n_l \approx 0.03$ . This threshold separates the homogeneous isotropic gel from other network aggregates, where thermal fluctuations of the filaments are effectively quenched by linkers. All of these aggregates have in common that they provide a significantly higher number of potential sites for crosslinks. Depending on the linkers' angular preference, the architecture providing the greatest number of these sites are either bundles or lamellar aggregates. The cluster network can be characterized as an intermediate stage. While it offers a higher number of potential crosslinks than the homogeneous isotropic gel, it still offers significantly less combinations of crosslinks than the lamellar phase. It represents a trade-off only possible on a rather narrow intermediate interval of linker concentration. As a hard rule, the resulting network morphology is always the one offering the greatest number of potential crosslinks under the constraint of the present linker concentration. In other words, the favored network type represents the maximal degree of order, which all linkers together can energetically afford. All aforementioned observations and interpretations thereof lead to the conclusion that *linker entropy* determines how filaments are condensed into one or the other network morphology.

### 5.3.4 Experimental support of in silico results

In literature, plenty of experimental examples can be found that partly or wholly support the numerical results. Homogeneous isotropic gels are known to be the predominant network morphology at low linker concentrations. This state is independent of the linker species. In case of isotropic linkers such as  $\alpha$ -actinin, [26] reports a network of branched bundles. If one follows the argument of [48], these kind of networks are long-lived non-equilibrium architectures. Such networks were first reported in [185, 186] and agree well with the presented simulation results. There are cases, where bundle networks formed by small linkers like fascin [26] may very well be more preferable energetically than one single bundle. As argued in [23, 64], chirality of the involved filaments play a role. Due to the fact that F-actin filaments do not possess a perfect double-helical structure, bundle growth beyond a certain diameter becomes energetically unfavorable due to an increase of strongly bent filaments. Hence, filament chirality may act as a stabilizer of a network made of bundles. Polyvalent counter-ions such as  $Mg^{2+}$  or  $Al^{3+}$  can be argued to have an orthogonal angular preference which originates from close-range electrostatic repulsion of filaments [227]. In fact, there are linkers like the Arp2/3 complex that actually exhibit a distinct angular preference: in lamellipodia, the preferred angle is explicitly known to be  $\phi \approx 70^\circ$  [154, 213]. Finally, networks with clusters have been reported, too, but deemed to be kinetically trapped rather than equilibrium structures [139, 186].

## 5.4 Structural analysis of network morphologies and their phase transitions

So far, the general phenomenology of the four fundamental equilibrium network morphologies has been discussed. The subsequent Section 5.5 will thus be dedicated to a more detailed structural examination of these morphologies and their phase transitions, which are indicated in Figure 5.5. Prior to the discussion of phase transitions, however, it is worthwhile giving a basic understanding of the nature of phase transitions as well as an introduction to the analytical tools applied to examine them.

### 5.4.1 On the order of phase transitions

Transitions between different thermodynamic states of a system can be classified by their transition order. First-order transitions display a discontinuity in the first derivative of the free energy with respect to a thermodynamic variable. In case of this variable being the temperature of the system, a discontinuity in the system's order parameter can be observed. A further characteristic of such transitions is revealed: the temperature of the system stays constant. Melting is a prototypical example for such a phase transition. In contrast to first-order transitions, second-order transitions feature a smooth first derivative of the free energy with respect to the thermodynamic variable of interest. Returning to the example above, the order parameter develops continuously with temperature. The Curie point, which separates paramagnetic and ferromagnetic materials, marks a second-order phase transition.

### 5.4.2 Analytical tools for the structural and mechanical analysis of crosslinked networks

**Morphology-dependent local coordinate systems** All three inhomogeneous network morphologies (clusters, bundles, and lamellae) correspond to geometrical primitives (point, line, and plane). Their characterization may thus be facilitated by defining morphology-dependent local coordinate frames  $(x_1, x_2, x_3)$  aligned with the respective geometric primitive in a suitable way. The origin of the cluster-specific coordinate frame is placed in the center of mass  $s_i$  along with an arbitrary orientation of the coordinate frame. For bundle networks, this origin is put on the bundle's centerline at its center of gravity and the  $x_1$ -direction is defined orthogonal to it. Finally, for the lamellae, the  $x_1$ -direction is chosen orthogonal to the plane in which they lie. Their local frames' origin is located at  $s_i$ . The coordinate frames are shown as insets of Figures 5.7b, 5.8b, and 5.11b, respectively.

**Orientalional distribution of filaments** The distribution of filament orientations is a characteristic measure for any kind of filamentous network. Using spherical coordinates  $(\varphi, \psi)$ , these orientations may be described by means of the orientation density functions

$$\rho(\varphi) = \left\langle \frac{1}{N_f L_f} \sum_{n=1}^{N_f} \int_0^{L_f} \delta[\varphi - \varphi_n(s)] ds \right\rangle, \quad \rho(\psi) = \left\langle \frac{1}{N_f L_f} \sum_{n=1}^{N_f} \int_0^{L_f} \delta[\psi - \psi_n(s)] ds \right\rangle, \quad (5.3)$$

where  $\langle . \rangle$  denotes the time average,  $\delta$  the Dirac-Delta-function and  $\varphi_n(\mathbf{s})$  and  $\psi_n(\mathbf{s})$  the orientation angles of the tangent of the  $n^{\text{th}}$  filament at the material point  $\mathbf{s}$ . The azimuth angle  $\varphi \in [0; 2\pi[$  is measured against the  $x_2$ -direction, the polar angle  $\psi \in [0; \pi]$  against the  $x_1$ -direction (cf. Figure B.2a). The functions  $\rho(\varphi)$  and  $\rho(\psi)$  are a direct measure for the degree of the orientational anisotropy of filaments in the network. In view of the following analyses of filament orientations, the reader is referred to Appendix B.3 for the correct interpretation of orientations by means of the angles  $\varphi, \psi$ .

**Orientation correlation among filaments** Linkers with a preferred binding angle tend to impose an orientation correlation between filaments close to each other. Let the position of the  $m^{\text{th}}$  binding site on the  $i^{\text{th}}$  filament be  $\mathbf{x}_b^{[i][m]}$ . Then,

$$\mathcal{I} = \{(i, m, j, n) : R_l - \Delta R_l \leq \left\| \mathbf{x}_b^{[i][m]} - \mathbf{x}_b^{[j][n]} \right\| \leq R_l + \Delta R_l, i \neq j\} \quad (5.4)$$

is the set of all index tuples belonging to pairs of binding sites on different filaments, which are in the appropriate distance to be connected by a linker. Some of them may indeed be chemically crosslinked, while others are not due to the lack of a linker molecule in their vicinity. Let  $\mathbf{t}_b^{[i][m]}$  be the filament tangent vector of a binding site. Then, the correlation of orientations of neighboring filaments can be written as the orientation correlation function (OCF)

$$O(\theta) = \sum_{(i,m,j,n) \in \mathcal{I}} \delta \left( \theta - \cos^{-1} \left| \mathbf{t}_b^{[i][m]} \cdot \mathbf{t}_b^{[j][n]} \right| \right), \quad (5.5)$$

where  $\theta$  denotes the angle enclosed by the tangents. Given a network with perfectly random filament orientations, the linker-mediated interactions between neighboring filaments are negligible. The distribution function  $O(\theta)$  is then expected approach  $O(\theta) = \sin(\theta)$ ,  $\theta \in [0; \pi/2]$  due to the geometric preference for angles close to  $\pi/2$  between randomly oriented straight lines. By contrast, in case of strong, linker-mediated filament-filament interactions and linkers with a preferred binding angle  $\phi$ , one expects a pronounced maximum at  $\theta \approx \phi$ .

**Filament order parameter** The order parameter of a nematic liquid crystal is commonly given as a scalar value

$$S = \langle P_2(\cos \vartheta) \rangle = \frac{1}{2} \langle 3(\cos \vartheta)^2 - 1 \rangle \quad (5.6)$$

and represents the ensemble average of the second Legendre polynomial  $P_2$  at a specific point in time. Usually,  $\vartheta$  represents the enclosed angle between the direction of rigid rod-like molecules and a global director. In general, Equation (5.6) describes the degree of order of a nematic liquid crystalline phase [18]. Whereas  $S = 0$  indicates uncorrelated angles,  $S > 0$  and  $S < 0$  indicate a predominance of small and large  $\vartheta$ , respectively.

Here, the focus lies on the orientation of long semiflexible polymers in networks rather than with short rigid rods as common for liquid crystals. Thus, Equation (5.6) is altered in a way which allows to capture the varying orientation along the axis of filaments. Additionally, one would like to compare the local filament orientation not with a given preferred direction, but rather with the orientation of all other filaments in the network depending on their respective

distance  $d$ . To this end, the modified order parameter reads

$$S(d) = \frac{1}{(N_f^2 - N_f)L_f^2} \left\langle \sum_{i=1}^{N_f-1} \sum_{j=i+1}^{N_f} \int_0^{L_f} \int_0^{L_f} \delta(d - \|\mathbf{x}_i(s_i) - \mathbf{x}_j(s_j)\|) (3\vartheta_{ij}^2 - 1) ds_i ds_j \right\rangle, \quad (5.7)$$

where  $d$  is a distance and  $\mathbf{x}_{(\cdot)}(s_{(\cdot)})$  marks the spatial position of the  $(\cdot)^{\text{th}}$  filament. Furthermore,  $\vartheta_{ij} = |\mathbf{t}_i(s_i) \cdot \mathbf{t}_j(s_j)|$  with tangents  $\mathbf{t}_{(\cdot)}(s_{(\cdot)})$ .

**Strain energy of the network** Depending on the beam formulation, the internal elastic energy or strain energy can consist of individual energy terms stemming from axial, bending, shear, and torsional deformation. The here applied Reissner beam [30, 103] accounts for all of these deformations, whereas recently developed Kirchhoff beam formulations [155, 156] omit shear deformation and might be the more efficient modeling choice due to the high slenderness ratio of the filaments and linkers. Here, based on [103], the energy

$$E_{int} = \frac{1}{2} \sum_{i_f}^{N_f} \int_0^{L_f} \boldsymbol{\gamma}_{mat}^T \mathbf{C}_f \boldsymbol{\gamma}_{mat} + \boldsymbol{\kappa}_{mat}^T \mathbf{C}_m \boldsymbol{\kappa}_{mat} ds \quad (5.8)$$

sums up the strain energy contributions of individual filaments in what can be understood as the joint strain energy stored in the network. The strain measures  $\boldsymbol{\gamma}_{mat}$  and  $\boldsymbol{\kappa}_{mat}$  are defined with respect to the material frame [103]. The constitutive matrices  $\mathbf{C}_f$  and  $\mathbf{C}_m$  are defined by equations (2.12).

**Two-point density-density correlation function of linkers** The spatial distribution of the linkers is an important characteristic of the network and is quantified as follows. Let the position vectors of the  $N_{db}$  doubly bound linkers (i.e., crosslinks) be  $\mathbf{x}_{db}^{(k)}$ ,  $k = 1, \dots, N_{db}$  with components  $x_{db,i}^{(k)}$ ,  $i = 1, 2, 3$ . Then, according to [18], the number density operator

$$n(x_i) = \sum_{k=1}^{N_{db}} \delta(x_i - x_{db,i}^{(k)}) \quad (5.9)$$

is a measure for the spatial density of doubly bound linkers and the distribution of these linkers can be characterized by the so-called two-point density-density correlation function (DDCF)

$$C_i(x_i, \hat{x}_i) = \langle n(x_i) n(\hat{x}_i) \rangle = \left\langle \sum_{k=1}^{N_{db}} \sum_{k'=1}^{N_{db}} \delta(x_i - x_i^{(k)}) \delta(\hat{x}_i - x_i^{(k')}) \right\rangle, \quad (5.10)$$

with non-identical linker positions  $\mathbf{x}^{(k)}$  and  $\mathbf{x}^{(k')}$  and two non-identical variable points in space  $\mathbf{x}$  and  $\hat{\mathbf{x}}$ . In slight variation of  $C_i(x_i, \hat{x}_i)$ , one may simply evaluate the mutual distance between two given doubly bound linkers by

$$C_i(d_i) = \langle n(x_i) n(\hat{x}_i) \rangle = \left\langle \sum_{k=1}^{N_{db}} \sum_{k'=1}^{N_{db}} \delta(d_i - |x_i - \hat{x}_i|) \delta(x_i - x_i^{(k)}) \delta(\hat{x}_i - x_i^{(k')}) \right\rangle. \quad (5.11)$$

**Structure function** Complementary information to Equation (5.10) is given by its Fourier transform, which can be measured directly in diffraction experiments and reads

$$I_{x\hat{x}}(q_i) = \int e^{-iq_i(x_i - \hat{x}_i)} C_i(x_i, \hat{x}_i) dx_i d\hat{x}_i \quad (5.12)$$

with imaginary unit  $i = \sqrt{-1}$ . This expression is typically referred to as structure function. Finally,  $\mathbf{q}$  – with the components  $q_i$  – is called the *scattering wave vector*. It describes the difference between incoming and scattered waves in experimental investigations (e.g., via *small angle x-ray scattering*). It may be interpreted as the frequency of spatial occurrences of detected particles, which allows for its direct application to the analysis and classification of arbitrary linker patterns. The structure function as the Fourier transform of Equation (5.11) is given by

$$I_i(q_i) = \int e^{-iq_i d_i} C_i(d_i) dd_i. \quad (5.13)$$

## 5.5 Fundamental phase transitions

All transitions are studied by gradually increasing linker concentration until morphological changes become apparent. In the following, transitions from homogeneous isotropic gels to bundles, clusters, and lamellae are examined, as well as transitions from clusters to lamellae.

### 5.5.1 The bundle transition

As illustrated in Figure 5.7, the phase transition from a homogeneous isotropic gel to a bundle network is accompanied by an abrupt change of the network morphology at a critical linker concentration rather than by a continuous transition. Bundling is observed for linkers that favor connections between filaments whose axes enclose small angles up to  $\phi = 3/16\pi$ , i.e., parallel linkers. For the case discussed here, a binding angle  $\phi = 1/16\pi$  and a deviation of  $\Delta\phi = 1/16\pi$  are defined. Within the narrow concentration interval  $n_l \in [0.058; 0.062]$  (i.e.,  $N_l \in [400; 425]$ ), the DDCF  $C_1(d_1)$  in (normal)  $x_1$ -direction in Figure 5.7a suddenly changes from a uniform distribution to a peaked distribution with a sharp maximum around zero (and  $H$  because of the periodicity of the system). The width of this peak is comparable to the bundle diameter. At concentrations only slightly above the critical linker concentration, phase separation is observed: a single bundle is surrounded by free filaments devoid of linkers. Increasing the linker concentration further leads to a state where almost all filaments available in the simulated volume are bound within the bundle. The corresponding structure functions  $I_1(q_1)$  in  $x_1$ -direction in Figure 5.7b can be interpreted as follows. A homogeneous isotropic gel ideally exhibits only a constant contribution, which is hardly surprising since a flat power spectral density of the distances  $d$  between two linkers is detected, i.e., there are no spatial density fluctuations. Entering the bundle regime, a sudden rise in the amplitudes of higher frequency contributions can be seen. This phenomenon is the consequence of a steep gradient when linker concentration drops to values close to zero outside of the bundle. Similarly and as expected, the orientational distribution for homogeneous isotropic networks with  $n_l \leq 0.058$  is uniform. In Figure 5.7c, the perfect uniform distribution of azimuth angles is represented by a circle with radius  $1/\sqrt{\pi}$ . For  $n_l > 0.062$ , the distribution exhibits pronounced maxima in two opposite directions, which

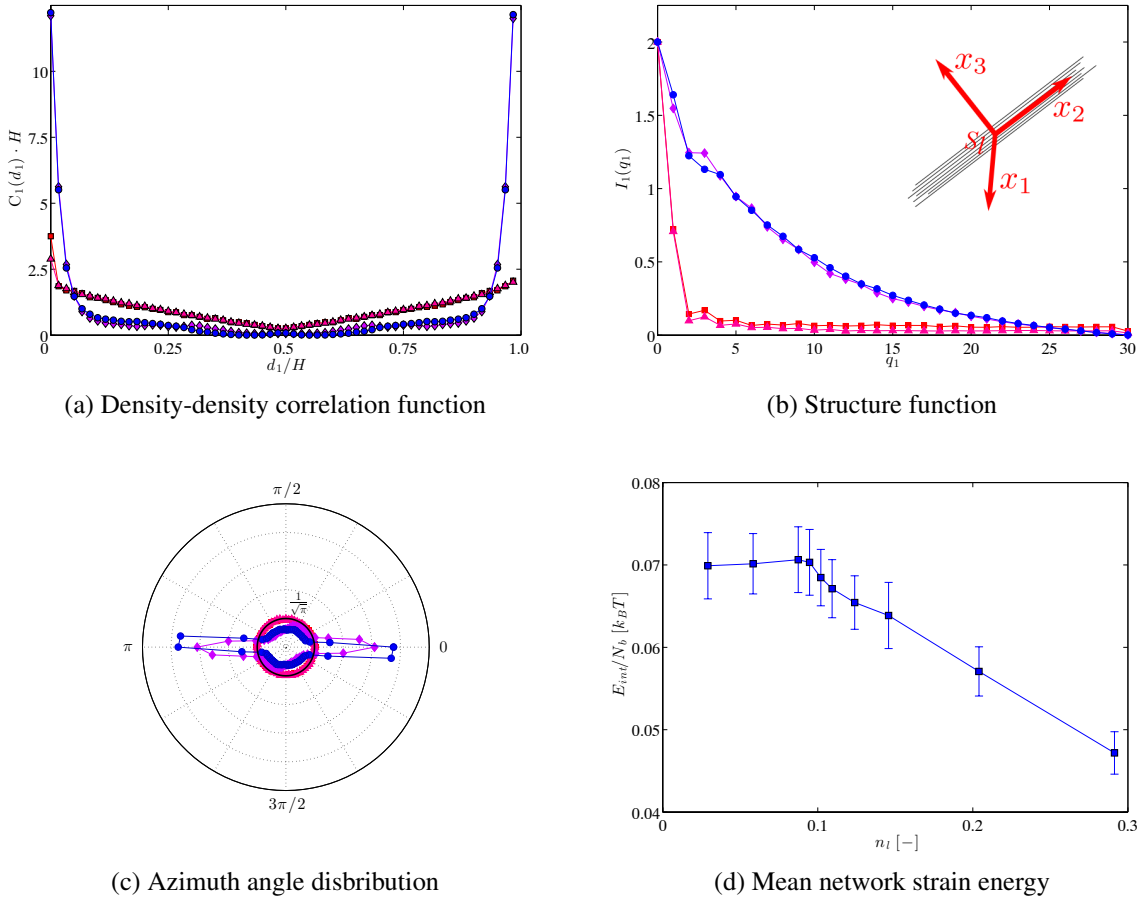


**Figure 5.7** Transition from homogeneous isotropic gel to bundle network. The binding angle interval is  $0.0 \leq \phi \leq \pi/8$ . DDCF  $C_1(d_1)$  in (normal)  $x_1$ -direction (a), its structure function  $I_1(q_1)$  (b), and azimuth angle distribution  $\rho(\varphi)$  (c) for  $n_l \approx 0.044$  (■),  $0.058$  (▲),  $0.062$  (◆), and  $0.073$  (●) corresponding to a total number of  $N_l = 300, 400, 425,$  and  $500$  linkers, respectively. The continuous black circle with radius  $1/\sqrt{\pi}$  in (c) marks the uniform distribution. The inset in (b) illustrates the orientation of the coordinate frame. In (d), the normalized mean strain energy of the network (d) for  $N_f = 104$  filaments ( $c_f \approx 2\mu\text{M}$ ) is depicted.

is to be interpreted as a strong uniaxial orientational preference. The axial  $x_2$ -direction is not discussed as it does not hold valuable information.

The normalized mean internal elastic energy of all filaments, i.e., the network mean strain energy, changes noticeably upon phase transition as Figure 5.7d clearly shows. For this particular analysis, a network with a smaller number of  $N_f = 104$  filaments ( $c_f \approx 2\mu\text{M}$ ) was chosen. In order to arrive at comparable values across different filament concentrations, the energy is normalized by the total number of filament binding sites  $N_b$ . The lower filament concentration leads to a more pronounced effect of bundling on the strain energy of the network as will be explained now. For higher filament concentrations, the drop in network strain energy cannot be detected clearly because of phase separation, where a bundle consisting only of a part of the filaments is surrounded by an increasing number of loose filaments. The contribution of the free filaments masks the effect of the aggregation. The time interval, over which energies are averaged, is given by  $[2000 \text{ s}; 2400 \text{ s}]$  of simulated time. The transition from a homogeneous isotropic gel to the bundle phase between  $n_l = 0.097$  and  $n_l = 0.112$  coincides with a linker-induced drop of the

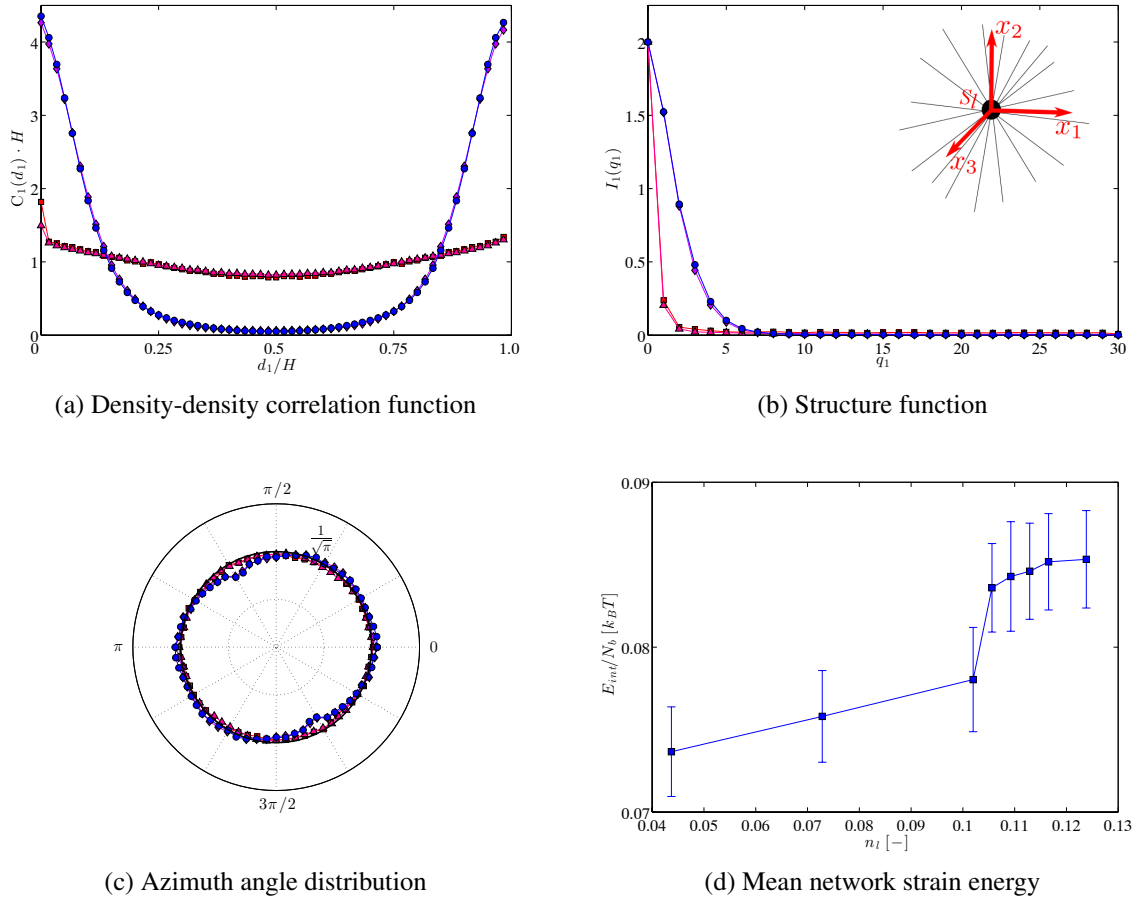


**Figure 5.8** Transition from homogeneous isotropic gel to a cluster network with preferred binding angle interval  $6\pi/16 \leq \phi = \pi/2$ . DDCF  $C_1(d_1)$  (a), structure function  $I_1(q_1)$  (b), and azimuth angle distribution  $\rho(\varphi)$  (c) for  $n_l \approx 0.044$  (■), 0.102 (▲), 0.106 (◆), and 0.117 (●) corresponding to  $N_l = 300, 700, 725$ , and 800 linkers. The continuous black circle in (c) with radius  $1/\sqrt{\pi}$  represents the uniform distribution. The inset illustrates the orientation of the coordinate frame. In (d), the normalized mean network strain energy the shown.

strain energy of the filaments by approximately 5%. Freely fluctuating semiflexible filaments deform and thus store energies of a few  $k_B T$  mainly in their bending modes [88]. Filaments in a bundle, however, align in a nearly straight way under the constraining effect of the linkers, which greatly reduces the strain energy of the filaments.

## 5.5.2 The cluster transitions

Again changes in the DDCF, the structure function, and the orientational distribution were studied for increasing linker concentrations and for different parameter settings. Typical results are depicted in Figure 5.8 and Figure 5.9 for preferred binding angles  $\phi \in [3\pi/8; 3\pi/2]$  and  $\phi \in [\pi/4; 3\pi/8]$ , respectively. These angular intervals represent the cases for which linkers at very high concentrations eventually induce squaratic or hexatic order (cf. Section 5.5.4). At intermediate linker concentrations investigated here, however,  $\phi$  does not yet exert its full influence on the order of filaments as for very high concentrations. Crossing a critical concentration of orthogonal linkers (see Figure 5.8 between  $n_l = 0.102$  and  $n_l = 0.106$ ), the network morphol-

ogy abruptly changes. This change is marked by a peaked density-density correlation instead of a hitherto nearly uniform spatial distribution of the linker molecules (Figure 5.8a). The width of this peak is comparable to the cluster diameter. This aspect reinforces the idea of a linker-rich core and a corona which is almost free of linkers. The structure functions of cluster networks in Figure 5.8b exhibit finite-amplitude frequency contributions up to about the 5<sup>th</sup> harmonic, which suggests increased spatial fluctuations in linker density. The quick monotonous decline of the structure function, however, is a sign of a smooth decrease in linker concentration when moving away from the cluster core.

Figure 5.8c shows the distribution of azimuth angles of the filaments. Across the phase boundary, no significant changes are detected, which is an observation that also holds for the polar angle as Figure 5.12f points out later on. Apparently, the cluster transition does not noticeably affect the distribution of filament orientations. In Figure 5.9, the same phase transition is illustrated for hexagonal linkers. The structure emerging in excess of the critical concentration between  $n_l = 0.113$  and  $n_l = 0.117$  ( $N_l \in [775; 800]$ ) can be classified as a cluster. It exhibits a slightly more pronounced geometrical anisotropy as compared to clusters with orthogonal linkers. While the general tendency expressed by an abrupt morphological reorganization is maintained as the DDCFs in Figure 5.9a suggest, the subsequent development towards higher  $n_l$  differs from clusters with orthogonal linkers. On the broad concentration interval bounded by  $n_l = 0.117$  and  $n_l = 0.131$ , the DDCFs show signs of a smooth transition in normal  $x_1$ -direction. Indeed, at higher concentrations, a continuous flattening of the cluster can be observed. This observation is reflected in Figure 5.9b, too, where the structure functions of networks with  $n_l = 0.117$  to  $n_l = 0.131$  exhibit continuously increasing amplitudes for higher harmonics. The effect is still minor, though, as the distribution of azimuth angles in Figure 5.9c implies that filament orientations do not significantly change on both sides of the phase boundary. Yet, Figure 5.13f reveals a preference for a polar angle of  $\psi = \pi/2$  already in the cluster phase. In local coordinates, the polar angle is measured against the  $x_1$ -direction. Hence, the smoothly increasing peak at  $\theta = \pi/2$  confirms the flattening mentioned above.

It is important to note that despite the fundamental structural changes shown in Figure 5.8a and Figure 5.8b, the orientation of the filaments – on a global level – remains nearly uniformly distributed. Figure 5.10a features OCFs of a homogeneous isotropic gel as well as two clusters, one with orthogonal linkers, the other with hexagonal linkers. It reveals that clusters with orthogonal linkers are indeed nearly rotationally symmetric. The data points for the homogeneous isotropic gel and this cluster are almost congruent and both very close to the analytical uniform distribution of orientations. Clusters with hexagonal linkers do not entirely maintain rotational symmetry. Here, the OCF peaks slightly at  $\theta \approx \pi/3$  and thus deviates from the uniform distribution.

At short distances, both clusters exhibit order parameter values  $S(d) > 0$ , i.e., a local angular correlation between filaments is detected due to the presence of crosslinks (Figure 5.10b). Neighboring filaments are expected to include angles comparable to the preferred linker binding angle  $\phi$ . This angle for clusters is always  $\phi > \pi/4$  (cf. Figure 5.5) and direct linker interactions are limited to short distances  $d \leq R_l$ . Clusters with hexagonal linkers have a higher structural order than clusters with orthogonal linkers, judging by their larger order parameter over a larger distance interval. The order parameter quickly decreases to zero with increasing distance  $d$  from the center of mass, which shows that filaments become uncorrelated outside of the cluster

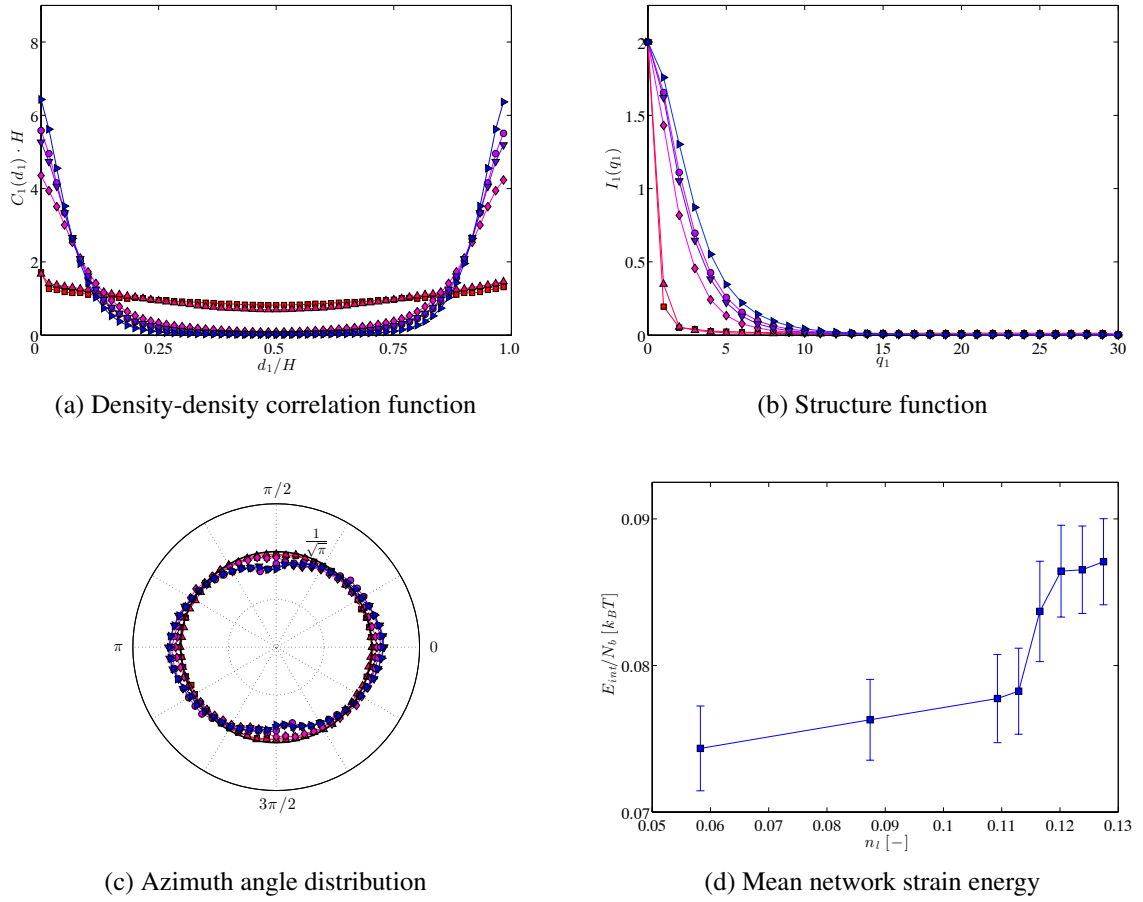


**Figure 5.9** Transition from homogeneous isotropic gel to a cluster with hexagonal linkers, i.e.,  $\pi/4 \leq \phi \leq 3\pi/8$ . DDCF  $C_1(d_1)$  in (normal)  $x_1$ -direction (a), its structure function  $I_1(q_1)$  (b), and azimuth angle distribution  $\rho(\varphi)$  (c) for  $n_l \approx 0.058$  (■), 0.113 (▲), 0.117 (◆) and 0.120 (●), 0.124 (▼), and 0.131 (►) corresponding to  $N_l = 400, 775, 800, 825, 850,$  and  $900$  linkers, respectively. The continuous black circle in (c) with radius  $1/\sqrt{\pi}$  represents the uniform distribution. The normalized mean network strain energy in (d) behaves in analogy to an orthogonal cluster (cf. Figure 5.8d).

core. The small negative values around  $S(d \approx H/2)$  are noteworthy as they are characteristic for assemblies with radial symmetry (ideal point symmetry results in  $S(d) = -0.5$ ).

The cluster transition, in contrast to the bundle transition, leads to an abrupt increase of the mean network strain energy by approximately 7% both for hexagonal and orthogonal linkers as shown in Figure 5.8d and Figure 5.9d. Both cluster types can be understood as intermediate stages towards the highly ordered lamellae with nearly straight filaments. At this intermediate stage, the number of linkers is already sufficient to condense filaments, yet it is not sufficiently high to bring them to a state of higher order as in the case of lamellae. In clusters, linkers strive towards an increased number of spots where they can connect two filaments *by bending them*, thereby increasing their strain energy.

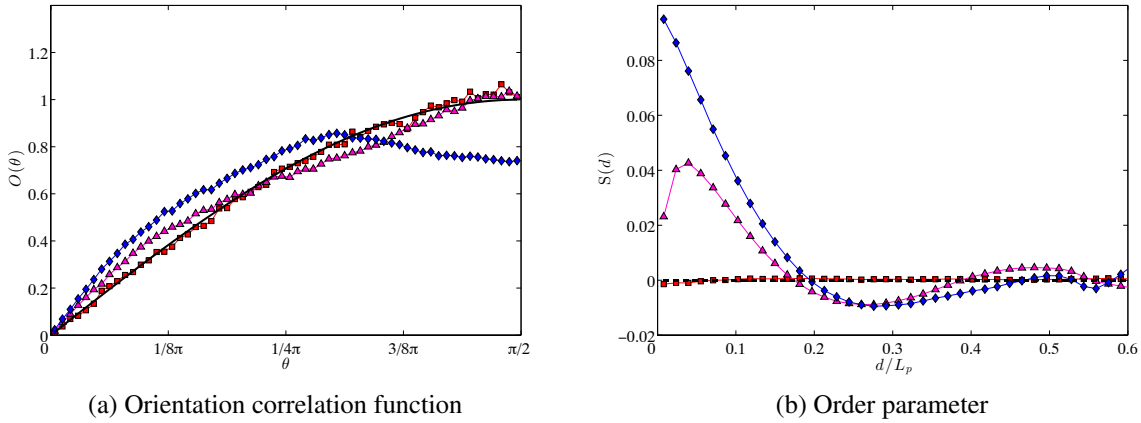


**Figure 5.10** OCFs and order parameter for cluster networks. (a) OCFs  $O(\theta)$  and (b) the corresponding order parameters  $S(d)$  for a homogeneous isotropic network with  $n_l \approx 0.015$  ( $N_l = 100$ ,  $\blacksquare$ ), a cluster network with  $3\phi/8 \leq \phi \leq \pi/2$  and  $n_l = 0.120$  ( $N_l = 825$ ,  $\blacktriangle$ ), a cluster network with  $\pi/4 \leq \phi \leq 3\pi/8$  and  $n_l \approx 0.117$  ( $N_l = 800$ ,  $\blacklozenge$ ). The dashed black line represents the uniform distribution of filament orientations ( $O(\theta) = \sin \theta$  and  $S(d) = 0$ ).

### 5.5.3 The lamella transition

Figure 5.5 reveals yet another phase transition. Leaving the phase diagram at the tip of the cluster region towards smaller angles in the interval  $\phi \in [\pi/4; 3\pi/8]$ , one encounters a small interval of angles in which a homogeneous isotropic gel directly transcends to a lamella without entering cluster phase space. Again, an initial network is chosen which has a smaller number of  $N_f = 104$  filaments ( $c_f \approx 2 \mu\text{M}$ ). The DDCFs in Figure 5.11c suggest that a compaction of filament takes place in the in-plane directions but that it is moderate in comparison to the direction normal to the surface of the lamella (Figure 5.11a). Here, at concentrations between  $n_l = 0.291$  and  $n_l = 0.299$ , a sudden and steep rise in linker density for small distances is detected, which goes along with the depletion of linkers for distances  $d_1 \gtrsim R_l$ . The structure functions reflect the extent of morphologic change more clearly. While changes in the structure functions for the in-plane directions (Figure 5.11d) are marginal, the normal direction (Figure 5.11b) features drastically increased amplitudes for higher harmonics. Within the geometrical limits of the lamella, the linker distribution remains constant, whereas perpendicular to the lamellar phase, the linker concentration rapidly and almost instantaneously decreases to very low values. The lamella exhibits a well-defined six-fold symmetry, which leads to a hexagonal distribution of azimuth angles of the filaments in Figure 5.11e. The distribution of polar angles (Figure 5.11f) peaks at  $\psi = \pi/2$  due to the choice of the local coordinate frame.

The normalized mean network strain energy plotted in Figure 5.11g exhibits a similar behavior as observed for the transitions from homogeneous isotropic gels to clusters and finally to the hexagonal lamella (cf. Figure 5.9d and Figure 5.13g). In general, the reduction of filament concentration (i.e.  $N_f, c_f$ ) gradually diminishes the cluster phase (cf. Figure 6.11 from [33]). Below a certain concentration threshold, the cluster might even vanish completely from the phase diagram (which was not observed for the chosen filament concentrations). As a consequence, the interval of linker concentrations shrinks which features an elevated strain energy level – a distinct characteristic of the cluster phase. It vanishes for filament concentrations as low as  $N_f = 104$  ( $c_f \approx 2 \mu\text{M}$ ).

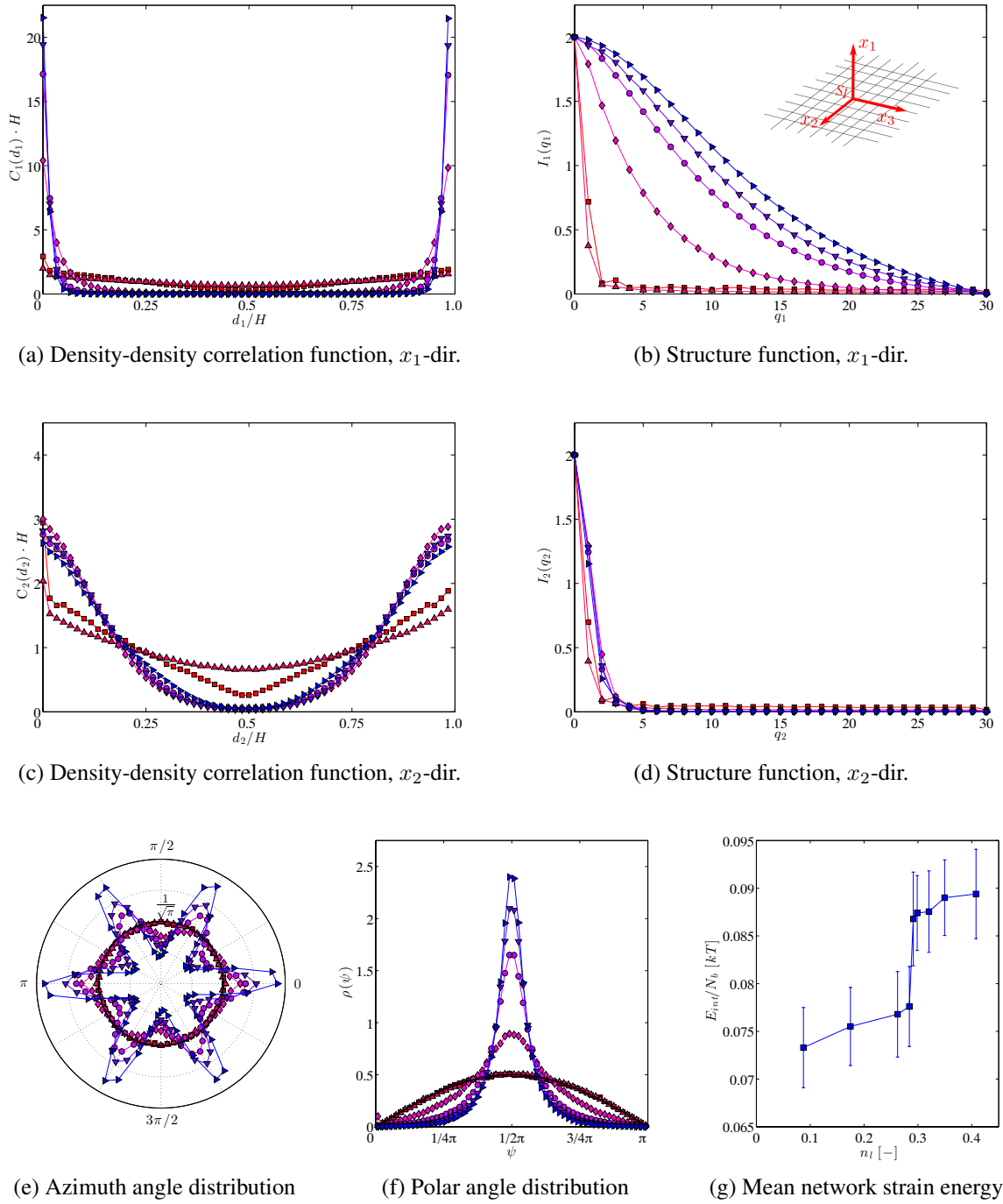


**Figure 5.11** Transition from homogeneous isotropic gel to a lamella with hexagonal linkers, i.e.,  $\pi/4 \leq \phi \leq 3\pi/8$ . In this case,  $N_f = 104$ . *Top row*: DDCF  $C_1(d_1)$  in (normal)  $x_1$ -direction (a) and its structure function  $I_1(q_1)$  (b). *Middle row*: density-density-correlation function  $C_2(d_2)$  in (tangential)  $x_2$ -direction (c) and its structure function  $I_2(q_2)$  (d). *Bottom row*: azimuth angle distribution  $\rho(\varphi)$  (e) and polar angle distribution  $\rho(\psi)$  (f). The networks have  $n_l = 0.044$  (■), 0.071 (▲), 0.073 (◆) and 0.075 (●), 0.080 (▼), and 0.087 (▶) corresponding to  $N_l = 600, 975, 1000, 1025, 1100$ , and 1200 linkers. The continuous black circle with radius  $1/\sqrt{\pi}$  in (e) and the black line with  $\rho(\psi) = \sin(\psi)/2$  in (f), respectively, represent the uniform distribution. In contrast to the transitions from the cluster to the lamellar phase (cf. Section 5.5.4), the normalized mean network strain energy rises during the transition.

### 5.5.4 The cluster-lamella transitions

If the linker concentration in cluster networks is increased further, clusters transcend into either a squaratic or a hexatic lamella. Lamellae are highly ordered filament condensates, which are densely crosslinked and thus are dominated by linker-filament interaction, which effectively quench thermal fluctuations of single filaments.

The transition from cluster to lamella with orthogonal linkers is characterized by a single discontinuous condensation event. Clusters with orthogonal linkers are rather insensitive to a rising linker concentration until they abruptly flatten and become lamellae, which is shown in Figure 5.12. No noticeable change in geometry is detected on a rather broad concentration interval  $n_l \in [0.131; 0.157]$ . Then, a minor additional increase of the linker concentration to  $n_l = 0.160$  leads to a large-scale reorganization of the network, which is detected by two abruptly expressed orthogonal preferential orientations in Figure 5.12d. A four-fold symmetry develops. It should be emphasized that this angular preference is not prescribed in a strong sense but rather represents the most favorable configuration in the presence of orthogonal linkers. The polar angle is measured against the normal  $x_1$ -direction of the lamella and peaks at  $\psi = \pi/2$  upon transition, which is a natural consequence of the cluster's condensation into a more or less two-dimensional structure (Figure 5.12e). The reorientation of filaments is accompanied by strong spatial density fluctuations in  $x_1$ -direction, which are shown in Figure 5.12a and Figure 5.12b. There, the density-density correlation suddenly peaks for low linker distances, which suggests a rapid condensation. These peaks have a width of  $\sim R_l$ , which is about the thickness of the lamellar phase. The corresponding structure function responds to this abrupt condensation by exhibiting large amplitude high-frequency contributions. The in-plane  $x_{2,3}$ -directions experience the flattening as a sudden homogenization in linker density, which is detected by the density-density correlation and corresponding structure function (Figure 5.12c and Figure 5.12d). The cluster spreads out and as a consequence, linkers become uniformly distributed within the emerging lamella. A macroscopic example resembling this transition is the pressure-induced bursting of a water-filled balloon placed on a table. The balloon membrane keeps the water in a spherical form. When more water is added, the shape does not change until the membrane yields. Then, the water is released and finds its new surface energy minimum by spreading out on the table (assuming gravity, of course).

In contrast to orthogonal linkers, hexagonal linkers invoke a more complex transition. Based on the data presented in Figure 5.13, the transition can be divided into two separate stages. The initial abrupt flattening of the cluster on the interval  $n_l \in [0.131; 0.135]$  ( $N_l \in [900; 925]$ ) is followed by a smooth rearrangement of filaments over a much broader linker concentration interval  $n_l \in [0.135; 0.189]$  ( $N_l \in [925; 1300]$ ). In  $x_1$ -direction, both the density-density correlation (Figure 5.13a) and the structure function (Figure 5.13b) display first an abrupt change between  $n_l = 0.131$  and  $n_l = 0.135$  followed by a continuous evolution from a (flat) cluster to a lamella. The first stage can be interpreted as a first-order transition, which is followed by a seamless evolution of the network structure bearing the characteristics of a second-order phase transition. The in-plane DDCF ( $x_2$ -direction, Figure 5.13c) and its structure function (Figure 5.13d) show the expansion of the lamella by a smooth decline of the low-distance peaks and the amplitudes of the harmonics, respectively. Interestingly, these two instruments are insensitive with respect to the initial morphological change. With increasing linker concentration, the preferred hexagonal order becomes apparent (Figure 5.13e). Meanwhile, the polar angle (Figure 5.13f) develops

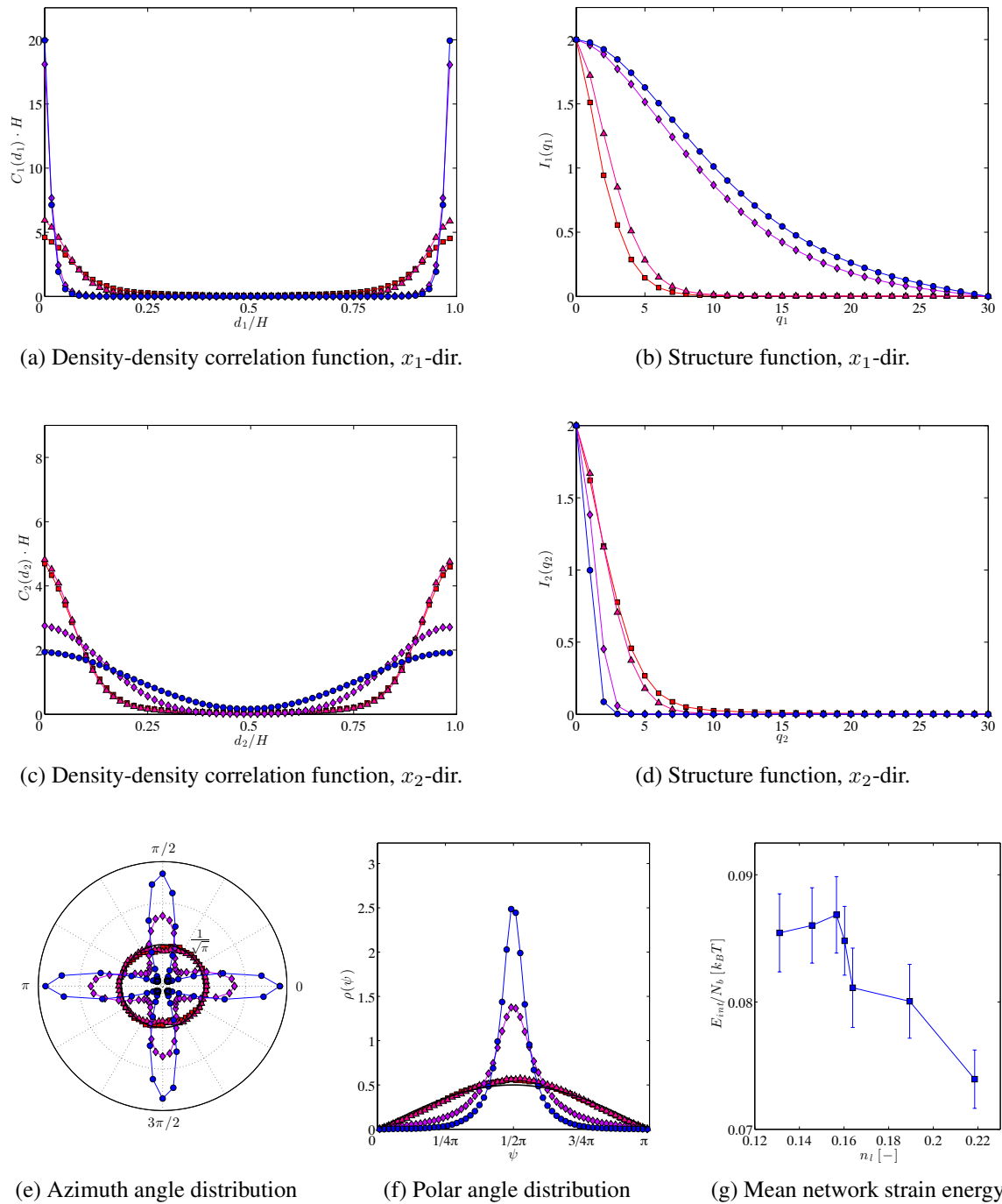


**Figure 5.12** Transition from a cluster network to a lamellar network with a preferred linker binding angle interval  $3\pi/8 \leq \phi \leq \pi/2$ . *Top row*: DDCF  $C_1(d_1)$  in  $x_1$ -direction perpendicular to the lamellar phase (a) and its structure function  $I_1(q_1)$  (b). *Middle row*: DDCF  $C_2(d_2)$  in (tangential)  $x_2$ -direction (c) and its structure function  $I_2(q_2)$  (d). *Bottom row*: azimuth angle distribution  $\rho(\varphi)$  (e) and polar angle distribution  $\rho(\psi)$  (f). The normalized mean network strain energy drops abruptly during transition (g). Linker concentrations:  $n_l \approx 0.131$  (■),  $0.157$  (▲),  $0.160$  (◆) and  $0.212$  (●) corresponding to  $N_l = 900, 1075, 1100,$  and  $1500$  linkers.

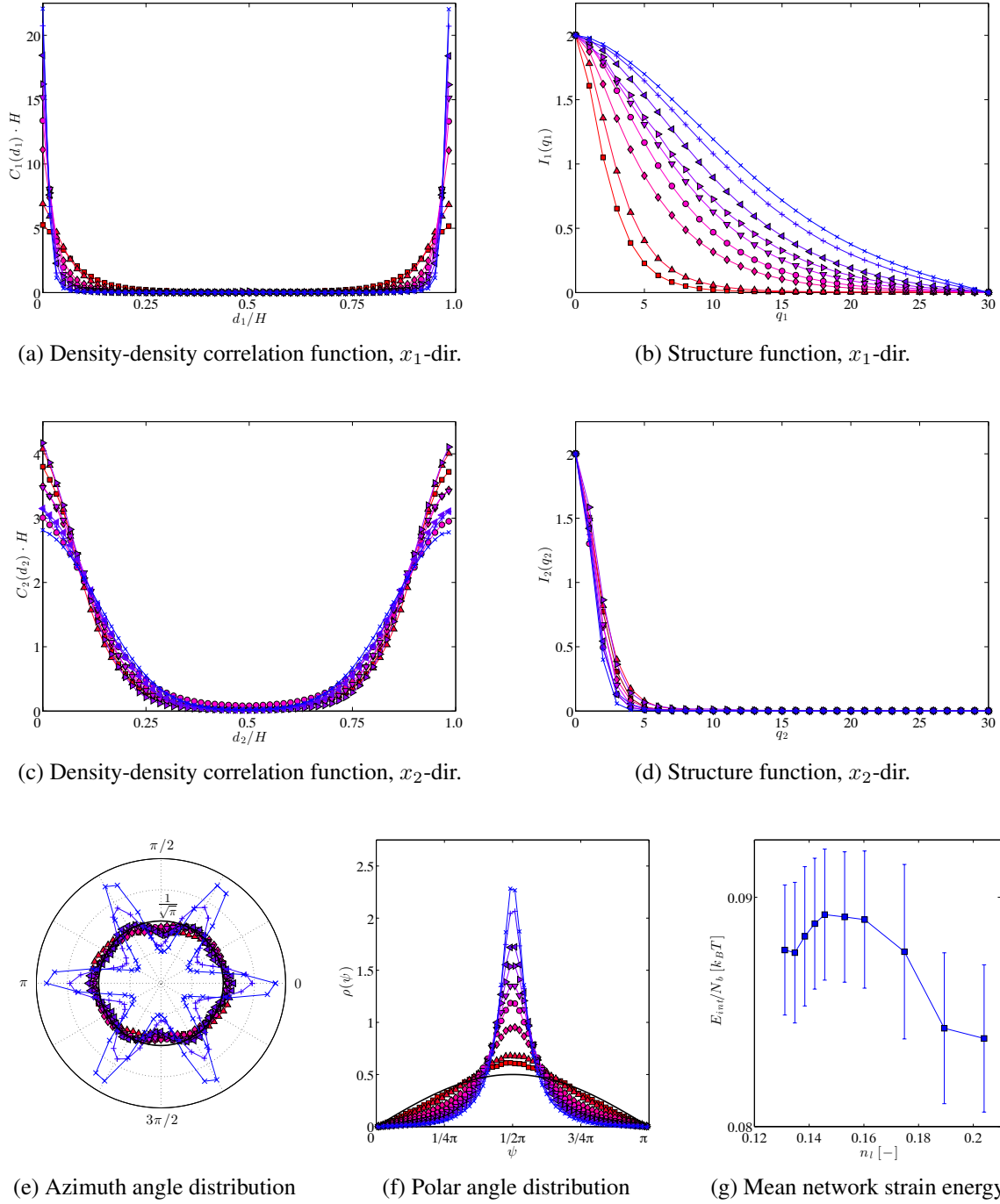


**Figure 5.13** Transition from a cluster network to a lamellar network with a preferred linker binding angle interval  $\pi/4 \leq \phi \leq 3\pi/8$ . *Top row*: DDCF  $C_1(d_1)$  in (normal)  $x_1$ -direction (a) and its structure function  $I_1(q_1)$  (b). *Middle row*: DDCF  $C_2(d_2)$  in (tangential)  $x_2$ -direction (c) and its structure function  $I_2(q_2)$  (d). *Bottom row*: azimuth angle distribution  $\rho(\varphi)$  (e) and polar angle distribution  $\rho(\psi)$  (f). Linker concentrations:  $n_l = 0.124$  (■), 0.131 (▲), 0.135 (◆), 0.138 (●), 0.146 (▼), 0.153 (►), 0.160 (◄), 0.175 (+), and 0.189 (×) corresponding to  $N_l = 850, 900, 925, 950, 1000, 1050, 1100, 1200$ , and 1300 linkers, respectively. The normalized mean network strain energy behaves somewhat differently than in the case of the orthogonal lamellar network (cf. Figure 5.12g). It rises towards the transition and then smoothly decreases (g).

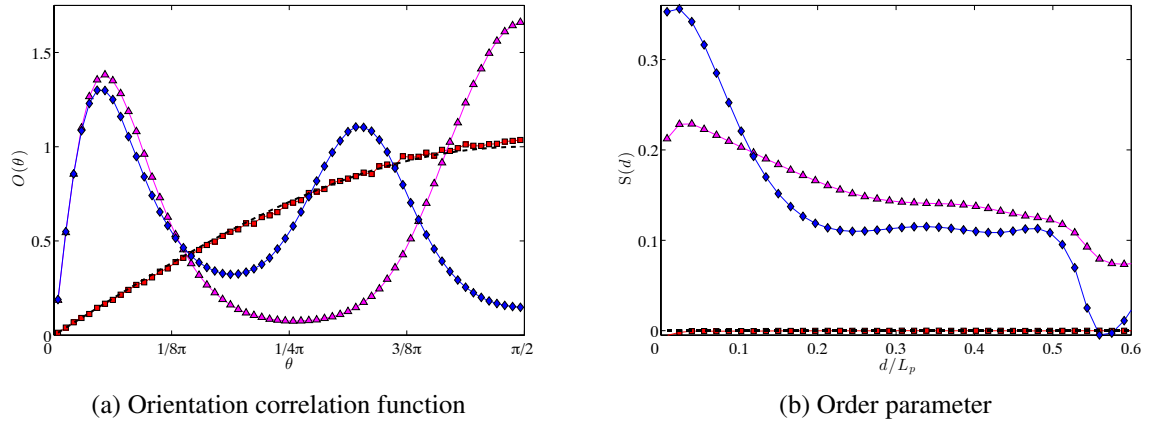


**Figure 5.14** (a) OCFs  $O(\theta)$  and (b) the corresponding order parameters  $S(d)$  for a homogeneous isotropic gel (■), a lamellar network with  $3\pi/8 \leq \phi \leq \pi/2$  and  $n_l = 0.189$  ( $N_l = 1300$ , ▲), and a lamellar network with  $\pi/4 \leq \phi \leq 3\pi/8$  and  $n_l = 0.189$  (◆). The dashed black line represents the uniform distribution of filament orientations ( $O(\theta) = \sin \theta$  and  $S(d) = 0$ ).

towards the limit of a Dirac impulse at  $\psi = \pi/2$ , as already seen in Figure 5.12f. In contrast to orthogonal linkers in squaric lamellae, hexagonal linkers do not immediately impose a six-fold symmetry. The post-transition lamella merely exhibits the onset of an orientational preference.

Clearly, both lamellae represent the most favorable configurations that their linkers are able to establish. They offer maximal combinatoric freedom for crosslinking while constraining filaments to a minimum in positional and orientational freedom. As illustrated in Figure 5.14a, the preferred linker binding angle induces two peaks in the OCFs  $O(\theta)$  (cf. Equation (5.5)), one close to  $\theta = \phi$ , the other close to  $\theta = 0$ . The first peak reflects the linker-mediated orientational preference of the filaments, while the second peak simply reflects the geometrical necessity of having, on average, equal numbers of filaments enclosing  $\phi$  and parallel filaments. The different heights of the peaks are a result of finite size effects (i.e., finite  $N_f, H$ ). Due to the large persistence length of the filaments, linkers impose global orientational order in lamellae, which is reflected by the non-negative order parameter  $S(d)$  (cf. Equation (5.7)) even at greater distances  $d$  (Figure 5.14b).

The different modes of transition become most apparent when examining the mean network strain energy. Whereas a cluster reduces its mean network strain energy by approximately 7% upon transition to a squaric lamella (see Figure 5.12g), the transition to a hexatic lamella does not display such a discontinuity (see Figure 5.13g). On the contrary, the mean network strain energy first rises slightly even beyond the transition concentration, which can be attributed to the strongly bent filaments within the lamella. In other words, the network has a hard time deciding whether it is still a cluster or already a lamella. The end of the energy plateau ( $n_l \approx 0.145$ -0.16) marks the end of this intermediate stadium. Once further filament bending becomes energetically unfavorable in excess of  $n_l \approx 0.15$ , the filaments are reordered into the “classic” hexagonal geometry. From this point on, the network strain energy decreases rather smoothly as the ordering effect of the linkers begins to dominate.

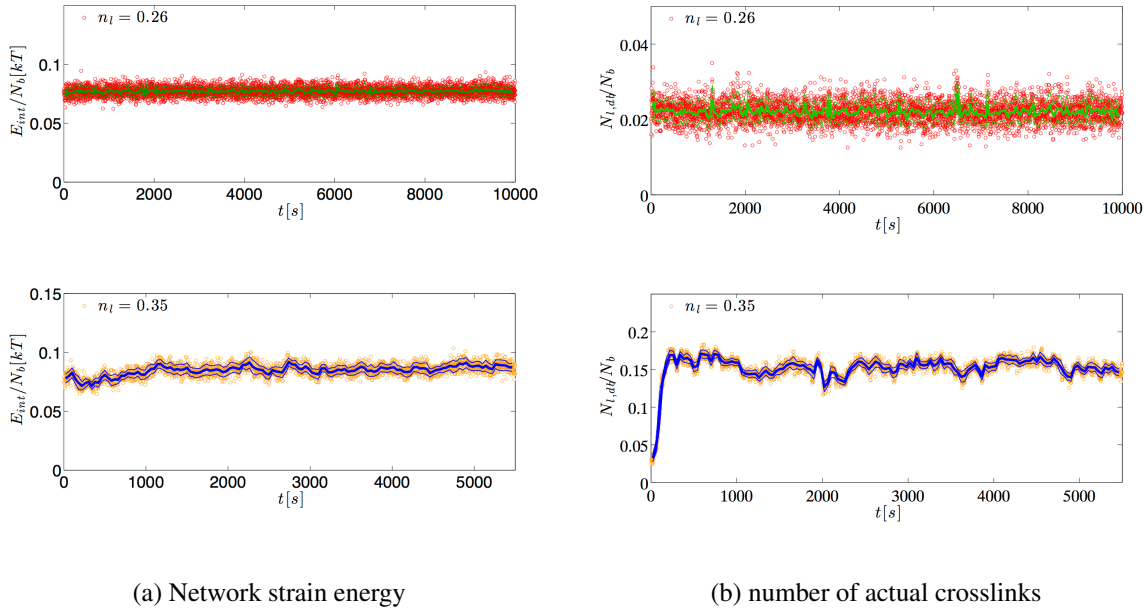


**Figure 5.15** (a) Network strain energy for a homogeneous isotropic gel (top) and a hexagonal lamella (bottom). (b) The number of doubly bound linkers  $N_{l,db}$  with respect to the total number of available binding sites  $N_b$ . The network has  $N_f = 104$  filaments and  $N_b = 3432$  binding sites.

### 5.5.5 Energy conservation during network evolution

A most fundamental criterion for any kind of numerical simulation is the conservation of energy in the system (in absence of sources, drains, and energy leakage across the system boundary). The amount of thermal energy in the system is determined by temperature, which for the presented approach expresses itself only implicitly in terms of effective thermal forces and moments. In the context of modeling, they are simple vector-valued random variables with zero mean and a certain variance (cf. Chapter 2). Although there exist known problems concerning the accurate generation of pseudo-random numbers, the possibility of the random number generator creating an off-balance in energy is neglected. What remains is the energy stored by the system's structural constituents in form of elastic energy as well as kinetic energy. An increase or decrease in kinetic energy would result in a violation of the Einstein-Smoluchowski relation  $\mathcal{D} = \zeta/k_B T$  as the diffusion coefficient  $\mathcal{D}$  would be affected. This source of error has been ruled out theoretically and heuristically in a previous work [33] by means of long term numerical studies on diffusive properties. The principle of equipartition of energy predicts the average kinetic energy of a particle with a certain (arbitrary) mass to be  $\langle E_{kin} \rangle = 3k_B T/2$ , which is thus only dependent on temperature. Since the effect of temperature is controlled by the underlying stochastic processes of the BD method, the conservation of kinetic energy is not an issue here.

Since the evaluation of the internal elastic energy in the system has been put forth as being important to the process of filament self-assembly, it seems worthwhile to monitor this quantity over the course of a simulation. In Figure 5.15, the results of this survey are presented for two representative simulations. Figure 5.15a depicts the temporal development of the summed elastic energies of all filaments in the simulation volume for an isotropic-homogeneous network ( $n_l = 0.26$ ) and a hexagonal lamellar network ( $n_l = 0.35$ ). The first case demonstrates

the stationary nature of  $E_{int}$  over a time interval of  $T_{sim} = 10000$  s, which corresponds to  $10^6$  time steps. In the second case, network evolution is witnessed, a process, that comes to end at  $t \approx 1500$  s. The effect of transient crosslinking becomes apparent. Compared to a homogeneous isotropic gel, strain energy fluctuations are more pronounced as the space/time-variant set of crosslinks affects filament bending. Moreover, linker unbinding events may randomly lead to a release of a portion of the stored strain energy of the filaments. As discussed in Section 5.5.3, the mean internal elastic energy of the network increases, when it transcends from the homogeneous isotropic gel phase to the hexatic lamellar phase. This increase by approximately 12% is observed in the evolutionary phase. Afterwards, the reaction between filaments and linkers has reached chemical equilibrium. The internal elastic energy enters the stationary phase, which is observed to be stable for more than 4000 s of simulated time. Figure 5.15b shows the number of doubly bound linkers over the course of the simulations. It detects a constant degree of crosslinking for the homogeneous isotropic phase. For the lamellar phase, however, noticeable fluctuations are observed (e.g., the drop at  $t = 2000$  s). One notices that the temporal development of the strain energy and the crosslink coverage are not correlated in an obvious way. Although the number of crosslinks fluctuates at  $t \approx 2000$  s, the energy curve remains rather unaffected. Most likely, the amount of stored mechanical energy is maintained also with a smaller number of linkers if the previous loss of crosslinks is evenly distributed throughout the structure. This statement probably does not hold for more inhomogeneous structures, where the breakage of a few bonds may already yield a larger effect (e.g., the breakage of inter-bundle connections). In conclusion, the numerical approach appears to be energetically stable within the time scales of interest.

## 5.6 The effect of chirality on the formation of semiflexible network structures

F-actin is known to have a left-handed, helical molecular structure [88]. As elaborated in Chapter 3 and discussed in both experimental [23] and theoretical literature (e.g., [80,85]), the molecular geometry limits the number of binding site pairs, which are available for crosslinking. This leads to interesting effects like the limitation of bundle diameter for some linker species. The focus of this section lies on the influence of the helical structure on the equilibrium phase diagram.

For this study, the previously chosen geometrical specifications of the filaments leading to Figure 5.5 are altered according to Section 3.2. The distance between two consecutive binding sites on a filament  $d_b = 15.625$  nm is *eight times* smaller than in previously discussed simulations. Computational cost rises only slightly due to the use of the interpolated linker beam element introduced in Chapter 3. The  $d_b$  of physiological F-actin is again five times smaller. However, the present refinement should be sufficient to capture the effect of chirality due to the following argument. Since chirality is a geometrical feature, its consequences for self-assembly should be the same for a larger  $d_b$  if linker size  $R_l$ , linker stiffness, and the persistence length of the filament  $L_p$  are scaled accordingly. Previously,  $L_p$  has been ruled out as a strong influence because a variation over two orders of magnitude did not change the essence of the phase diagram. For large, flexible linkers like filamin, chirality supposedly does not have a noticeable influence but shorter and stiffer linkers should “feel” chirality. Linker size is thus set to an

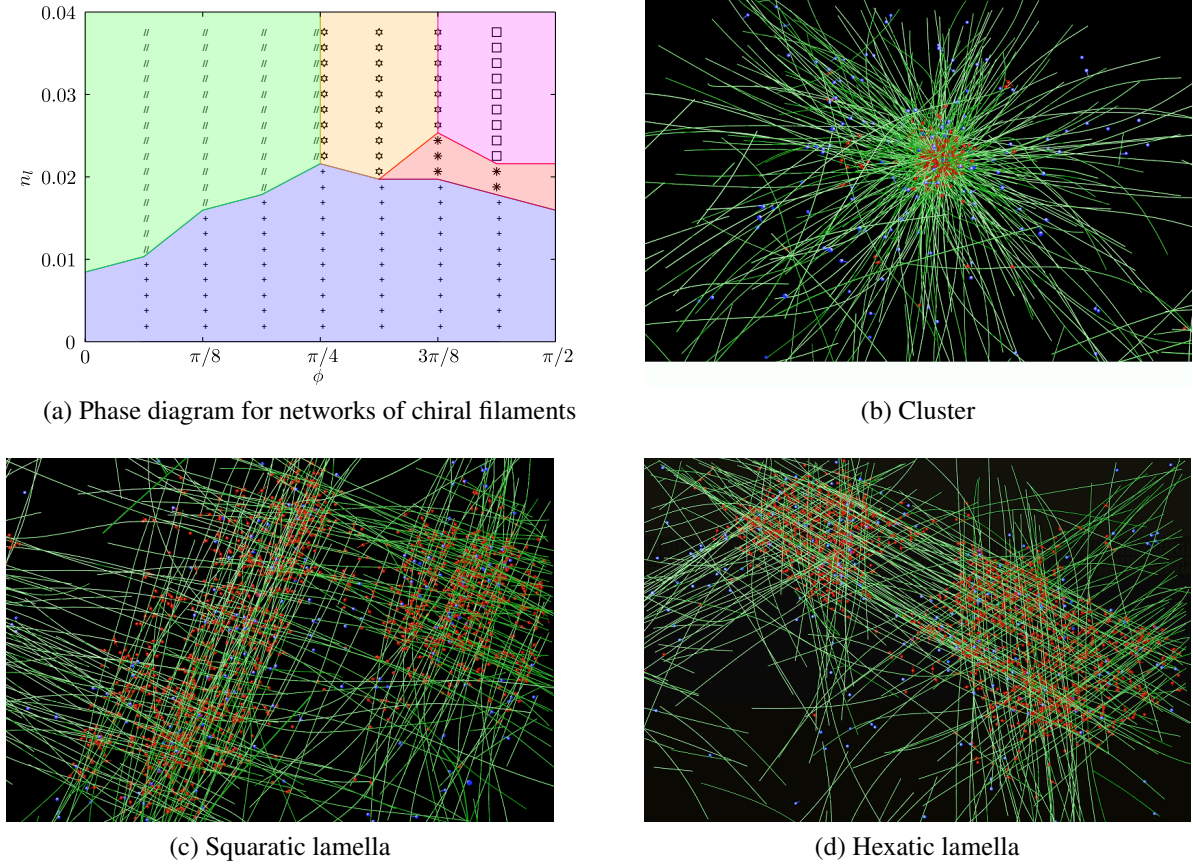


**Figure 5.16** (a) Phase diagram in presence of chiral filaments. Chirality is accounted for by helically arranged conoidal reactive volumes (cf. Section 3.2). The spacing between binding sites is  $d_b = 15.625$  nm. Phase transitions occur at lower relative linker concentrations  $n_l$  mainly due to increased number of binding sites. Furthermore, the hexatic lamellar phase expands into the orthogonal lamellar phase regime compared to Figure 5.5. Markers within the phase domains represent single simulations. (b) Cluster structure with  $n_l = 0.019$  ( $N_l = 1000$ ), (c) squaratic and (d) hexatic lamellae with  $n_l = 0.038$ . Due to a smaller  $d_b$ , the cluster core is much denser than before. At higher  $n_l$ , lamellar patches are observed. Due to filament chirality, the problem-specific crosslink saturation threshold is shifted to slightly higher values of  $N_l$ .

intermediate value of  $R_l = 0.06 \pm 0.02$   $\mu\text{m}$ . The left-handed rotation of  $\alpha \approx 167^\circ$  per monomer is adopted for this study and the opening angle of each binding site is set to  $\varphi_{bs} = \pi/3$ . The Young's modulus of the linkers is raised to  $E_l = 5 \times 10^6$  pN/ $\mu\text{m}^2$ .

### 5.6.1 Effects on the equilibrium phase diagram

First results regarding the effect of chirality on the phase diagram are presented in Figure 5.16. Most importantly, none of the principal morphologies vanish and no additional ones emerge, which on the one hand is slightly disappointing given the effort of including chirality into the numerical model. On the other hand, the finding is reassuring that the phase diagram is of general character.

Studying the phase diagram of chiral filament networks, features distinct from the previous phase diagram become apparent. The hexagonal lamellar phase domain grows compared to previous numerical studies without chirality as does the cluster phase. The reduced value for  $d_b$

results in the transition being shifted to lower relative linker concentrations  $n_l$ . This statement might seem trivial at first. However, it also means, that the critical linker concentration does not scale intuitively (i.e., linearly) with the number of available binding sites  $N_b$ . Rather the transitions occur at very similar total linker numbers  $N_l$ . The right part of Figure 5.16 explains the observation. A cluster structure with a densely crosslinked core as well as two lamellar structures with  $\phi = \pi/3$  and  $\phi = \pi/2$  are depicted. As stated in previous sections, linkers strive to maximize the number of binding sites available for crosslinking by gathering filaments around them. The maximal binding site density depends on the discretization length of the filament model. In previous studies,  $h_f = d_b = 0.125 \mu\text{m}$ . With reduced  $d_b$ , linkers are able to increase the density of potential crosslinking sites in their vicinity. By doing so, they invoke the phase transition at a comparable  $n_l$ , yet only more localized. Hence, one witnesses the emergence of a dense cluster as well as lamellar networks showing patches of highly localized linker clouds, that bring filaments into their preferred order. Without chirality, but the same reduced binding site distance  $d_b$ , the lamellae appear to be more densely packed, most probably as a consequence of their greater binding site reaction volumes, that allow for a larger number of crosslinking opportunities.

The effect of chirality on bundling has been the subject of a variety of publications with theoretical and experimental focus (see Section 3.1 for some prominent examples). The main claim is that chirality leads to a self-limiting system in the sense that it forces crosslinked filaments into geometrical configurations that allow only for a limited radial growth of bundles. Indeed, a different, much slower bundle evolution than in the case of achiral filaments is observed. Even after several hundreds of seconds, where simulations with achiral filaments have already aggregated into one single bundle, there are still several bundles of very similar thickness present in the case of chiral filaments. However, this observation must not be overrated by any means. Bundle evolution could simply be significantly slowed down as a consequence of the smaller reaction volumes of the binding sites. Another aspect is the greater total number of binding sites on filaments, which also contributes to a slowed down evolution. Lastly, no detailed assessment of the degree of filament bending and bundle torsion has taken place. At this point, without a comparison of the strain energies of chiral and achiral bundle assemblies and a quantification of their differences, a reliable statement cannot be made.

It goes without saying that some simulation parameters have a more pronounced effect on self-assembly than others. With very short linkers below 5 nm, self-assembly processes come to a hold. Bundling occurs even with very short linkers but even this structure is not observed anymore beneath this size threshold. Another crucial parameter is the opening angle  $\varphi_{bs}$  defined in Section 3.2.2, which restricts the *perspective* of a filament binding site. For the present simulations, values above  $\pi/18$  were required. Otherwise, no self-assembly is observed. The angle chosen for the presented set of simulations has been found to represent a good choice because allows for aggregation of filaments but the chiral structure of the filament is still strongly expressed. In general, the chiral model slows down equilibration due to a more restricted reaction volume surrounding filament binding sites and the consideration of binding site orientation.

## 5.7 Conclusions

In this chapter, an equilibrium phase diagram of transiently crosslinked, semiflexible polymers has been established. The phase diagram predicts four main network morphologies. At sufficiently low linker concentrations, the formation of isotropic homogeneous gels is observed, which are independent of the linker species. For small preferred binding angles  $\phi$ , a bundle phase is predicted. Beyond a certain binding angle, clusters and lamellar aggregates emerge. Furthermore, it was verified that  $\phi$  represents the only parameter which significantly affects network morphology assuming the linkers to be stiff elastic rods. The results suggest that linker entropy plays a major role in filament aggregation phenomena and dictates the shape of equilibrium structures. The occurrence of predicted structures in experimental observations is encouraging.

In a more detailed study, the microstructure of the four network morphologies and the phase transitions between them were studied by means of mathematical instruments from condensed matter physics. All relevant phase transitions exhibit clearly visible (linker-)concentration-dependent discontinuities in the density distribution of the networks, i.e., they are first-order transitions (cf. section 5.4.1). Both the two-point DDCFs and their structure functions provide ample evidence of these abrupt spatial density fluctuations. The only exception: the transition from the cluster phase to the hexatic lamellar phase, where, in addition to an initial discontinuous structural change, a smooth development of the network's spatial density distribution ensues. This second stage can be considered a second-order phase transition.

For isotropic-homogeneous gels and bundles, the expected structural features, e.g., the strong uniaxial anisotropy of the bundle, were confirmed but no essential additional properties were observed in the course of the structural characterization. The microstructure of the cluster phase and the lamellar phases, however, have not yet been the subject of a careful examination. In this respect, the computational analysis presented in this chapter is the first comprehensive source of information. The cluster phase was demonstrated to exhibit a local orientational correlation between the filaments on short distances introduced by linker-mediated interactions. Yet on a global level, the cluster structure is nearly isotropic, which is an important property, e.g., when incorporating cluster phases in a continuum-mechanical setting by means of microstructurally informed constitutive laws. Lamellae were found to exhibit either a hexagonal or an orthogonal symmetry depending on the linker species. Further investigation revealed that besides this orientational order, there is no in-plane position order of the linkers in these phases, i.e., they are anisotropic, but homogeneous. The large stiffness of the filaments allows linkers to convey their orientational preference over long distances on the scale of the filament's persistence length. Lamellae are not composed of a variety of small patches, each with its own anisotropic orientational order. Rather, there is one global anisotropy and orientational order in the whole layer of filaments. The observation of dense patches for chiral filaments does not contradict this statement as the orientations of all patches are equal. This might change once larger volumes with sides  $H \gg L_f$  can be simulated. Still, this finding remains valuable when modeling lamellae on a larger length scale by suitable anisotropic constitutive laws, e.g., in the case of lamellipodia – subcellular structures strongly involved in cell migration [154]. In fact, in view of the  $\sim 70^\circ$ -preference of Arp2/3 in lamellipodia and the computational results on lamellae, there could exist an Arp2/3-mediated, thermally equilibrated actin cluster.

The simulations demonstrate that different morphologies are composed of filaments in a different mean stress state: in bundles as well as in lamellae, thermal fluctuations seem to be quenched out effectively. As a consequence, internal stresses are reduced. In cluster phases, however, filaments even exhibit an elevated mean stress state. This information can be of importance for the design of suitable strain energy functions, that characterize the dependence of the elastic energy in these morphologies as a function of the state of deformation. On the basis of the detailed computational study presented here, a new class of constitutive models for cell mechanics may be designed incorporating thermodynamic phase transitions and thereby allowing for significantly more realistic homogenization approaches. Also owing to a previous lack of detailed information on phase transitions between morphologies and the microstructures of cytoskeletal networks, continuum mechanical approaches to cell mechanics so far largely ignore the changes of the mechanical properties due to structural reorganization ([170,212], cf. [124] for more references). In view of the highly dynamic interior of cells, these rather inflexible approaches seem questionable at least.

Cytoskeletal networks and their mechanical properties are largely determined by their structural polymorphism, which allows biological cells to adapt their properties flexibly by means of thermodynamic phase transitions. The results support the idea that biological cells are able to trigger an extensive reorganization of their cytoskeleton by only slightly tuning linker concentration (cf. [13]). These changes induced by thermodynamic phase transitions are an effect which cells can exploit, e.g., for cell motility, the assembly of stress fibers, or cell adhesion.

At least for the parameter space probed in this chapter, filament chirality did not play a crucial role in self-assembly. All previously observed morphologies were present also when assuming chiral filaments. Phenomena like the limitation of bundle diameter due to helical twist have not been studied yet beyond first observations of a slowed down bundling process, the cause of which is still rather obscure. However, the introduction of chirality in Chapter 3 has laid the foundations for further investigations and are a promising area of future research and development.

The immediate practical use of what has been presented in the course of this chapter is having gained in-depth knowledge of network self-assembly. Knowing key parameters, that reliably entail the emergence of a certain kind of microstructure, is of great advantage to the study of mechanical properties of networks. In the following Chapter 6, this knowledge will be put to use in order to generate isotropic bundle networks, which are ubiquitous in living cells, occurring, e.g., in stress fibers, filopodia, in microvilli, or stereocilia. Having *produced* such network samples, one may proceed and probe their rheology in the linear and nonlinear deformation regime and eventually gain new insights into the mechanics of crosslinked fiber networks.

## 6 Rheology of semiflexible biopolymer bundle networks

The mechanical properties of cells are largely determined by the cytoskeleton, which often takes on the form of a network of bundles. The principal constituent of these networks is the biopolymer F-actin [46], a semiflexible filament. Bundle networks are ubiquitous structures in the cells of eukaryotic organisms, where they are crucially involved in cell migration and adhesion [4], contractility [205], and mechanosensing [72, 190]. Due to the high linker density within bundles, the average distance between two consecutive crosslinks is short compared to the persistence length. Bundle networks are therefore referred to as *semiflexible networks*. The mechanical properties of semiflexible networks are distinct from the better known gels of synthetic and highly flexible polymers [71].

Purified F-actin networks have served as a model system and have been thoroughly investigated in recent years (see, e.g., [138, 185, 203]). On the one hand, this kind of network allows for the examination of key features of cellular biomechanics. On the other hand, the behavior of semiflexible networks in general can be studied. A further, practical advantage is that F-actin networks can be reliably reconstituted from monomeric actin under controlled *in vitro* conditions. The elasticity of these network structures has drawn the interest of theoretical physicists leading to a profound understanding of networks in thermal equilibrium [5, 81, 160]. It is well-established that small transverse thermal deflections account for the majority of the observable filament compliance and dominate the high-frequency rheology of semiflexible networks. This initial idea paved the way for two key discoveries. First, at high loading frequencies, a universal power law rheology was first predicted theoretically [59] and then confirmed in experiments [58]. Second, a nonlinear dependence of the elastic moduli on filament concentration could be shown [55, 102, 149].

There is, however, increasing evidence that this theory does not convincingly explain the rheology of bundle networks. This particular network morphology is encountered in *in vitro* systems at high linker concentrations [135]. In the case of transient linkers, the network is in a *non-equilibrium* state and very slowly evolves towards its free energy minimum. For the simulated networks, this state of minimum corresponds to a single bundle because the filaments are *achiral*. This energy minimum is not reached within the computationally probed time scales. Some *in vitro* bundle networks with *chiral* filaments are thought to evolve towards a different free energy minimum. In these cases, bundle growth becomes energetically unfavorable in excess of a certain diameter. Although the bundle size is limited, experiments have shown that these network structures *age*, i.e., they, too, are in non-equilibrium [138]. The non-equilibrated nature of bundle structures suggests that there are no universal properties to be expected. One would expect a low frequency rheology that is sample-dependent and non-universal, with a cross-over to Newtonian rheology at very low frequencies, while for high frequencies, one would expect to recover the results for single filament rheology.

This chapter aims to prove otherwise. It presents the results of large *in silico* studies, which help categorizing bundle network rheology in a generic way. The results imply the presence of three rheological regimes with distinct properties. At high frequencies, linkers can be assumed permanent such that the linear response is dominated by the mechanics of single bundles, leading to a universal scaling behavior distinct from that of single-filament networks. At lower frequencies the mechanical response begins reflecting that the stress release caused by linker unbinding events dominates the dissipative stress [230]. Significant sample-to-sample variations are observed, which can be explained by a non-universal dependence of the mechanical response on sample geometry and the strong influence of linker/filament reaction kinetics. At even lower frequencies, again a universal scaling behavior is observed, which is caused by the dissolution of bundles over long time intervals and the *large-scale collective motion* of structures within the network, which have a non-equilibrium origin.

## 6.1 General remarks on rheology

Rheology means the study of *flowing matter*. Flow implies transience and transience is inevitably coupled to the concept of time. On first thought, matter in its liquid state comes to mind, which is only natural because what is commonly termed a liquid is the kind of matter that flows on time scales which are easily perceptible by humans. Yet, not only fluids flow but also solid matter does. Creeping lead pipes are a commonplace example. On geological time scales, mountain ranges and continents flow. On the other hand, liquids can be perceived as solids as well given a short enough observation time (anyone having done a belly-flop from the spring board of a swimming pool can tell). A characteristic measure for the fluidity of a material is the so-called *Deborah number*  $De = t_c/t_p$ , which is the quotient of a material's characteristic relaxation time  $t_c$  (i.e., the time scale on which it yields to applied stresses) and the observation or probing time  $t_p$ .

As the following sections will demonstrate, biopolymer networks flow as well, a fact, which is reflected in time-scale-dependent material properties. The complex modulus  $G^*$  is a mechanical measure that accounts for this time-dependence and will be applied in the following examination of the linear rheology. Materials that exhibit a time-dependence of stresses and strains, which is expressed in a temporal phase shift between these two quantities, are called viscoelastic as they exhibit elastic as well as viscous properties. The here studied networks are highly viscoelastic materials. The inclined reader is referred to textbooks such as [125] for a more detailed lecture.

## 6.2 Micromechanical simulation of network rheology

### 6.2.1 Parametrization

First, the simulation box is set up in accordance with the definition of the global orthonormal basis  $B = \{e_x, e_y, e_z\}$  with  $e_{\{x,y,z\}} \in \mathbb{R}^{3 \times 1}$ . The simulation box occupies a cubic volume  $V := \{\mathbf{x} \in \mathbb{R}^3 \mid 0 \leq x_{\{x,y,z\}} < H\}$  with an edge length of  $H = 6 \mu\text{m}$ .

The faces of the cube are equipped with periodic boundary conditions. Temperature is set to  $T = 293.15 \text{ K}$ . The  $N_f = 360$  filaments are modeled as nonlinear, geometrically exact, three-dimensional Reissner beams with a circular cross section of area  $A_f = 1.9 \times 10^{-5} \mu\text{m}^2$ , Young's

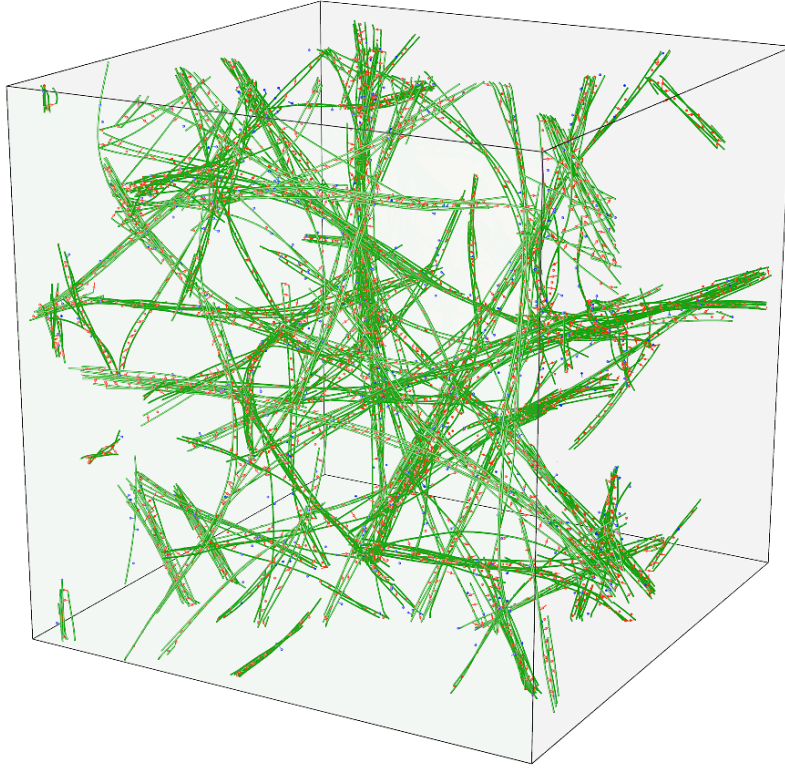


**Figure 6.1** Representative in silico bundle network, which was prepared for rheological simulations. The cubic simulation box has a volume of  $V = 216 \mu\text{m}^3$  and is equipped with periodic boundary conditions. It incorporates 360 (green) filaments at a corresponding concentration of  $c_f = 4 \mu\text{M}$ , which are in chemical equilibrium with linkers at a relative linker concentration  $n_l \approx 0.75$ . Red linkers have established crosslinks between filaments. Blue linkers are bound to only one filament. Unbound linkers are not visualized for reasons of clarity.

modulus  $E_f = 1.3 \times 10^9 \text{ pN}/\mu\text{m}^2$ , and moment of inertia  $I_2 = I_3 = 2.85 \times 10^{-11} \mu\text{m}^4$ . They are discretized with finite beam elements of length  $h_f = 0.125 \mu\text{m}$ . As in Chapter 5, the length of a single filament is set to  $L_f = 4 \mu\text{m}$  and its persistence length to  $L_p = 9.2 \mu\text{m}$ , which is close to experimental values found for pure actin without any kind of chemical stabilizer (cf. Section 5.1). Linkers are also modeled as rod-like microstructures and, like the filaments, are discretized with Reissner BFEs. A total number of  $N_l = 9000$  linkers are initially distributed randomly within volume  $V$ , which translates to a concentration of linkers  $c_l = 0.07 \mu\text{M}$ . Considering the approximately 12000 binding sites (which coincide with finite element nodes), the *simulated* ratio between linkers and binding sites in the volume can be calculated as  $n_l = N_l/N_b \approx 0.75$ . In *experiments*, however, the molar ratio  $R$  is given as the ratio of linker concentration and *actin monomer* concentration, which necessitates a recalculation of  $n_l$  into a molar ratio  $\bar{R}$ . Ideally, all monomers are polymerized to F-actin (which is not the case in experiments). For the purpose of estimation and in order to make numerical and experimental values slightly more comparable, a molar ratio resembling the experimental value may be calculated as  $\bar{R} = N_l D / (N_f L_f n_D)$  with  $D = 0.072 \mu\text{m}$  the helical repeat of F-actin and  $n_D = 26$  the number of actin monomers per repeat [88]. According to this formula, the bulk of the simulated networks feature an approximated molar ratio of  $\bar{R} \approx 0.018$ . The most important linker parameters comprise a circular

cross section  $A_l = 4.75 \times 10^{-6} \mu\text{m}^2$ , a Young's modulus  $E_l = 2.6 \times 10^6 \text{ pN}/\mu\text{m}^2$ , moment of inertia  $I_l = 8.9 \times 10^{-11} \mu\text{m}^4$ , and a linker size within the interval  $0.08 \mu\text{m} \leq R_l \leq 0.12 \mu\text{m}$ . The two chemical reaction sites of the linker are located at the ends of the linker molecule. Their chemical counterparts are equally spaced along the filament. The reactions between linkers and binding sites are modeled by Poisson processes with fixed, force-independent rate constants  $k_{\text{on}}, k_{\text{off}}$ , which are related by

$$k_{\text{off}} = k_{\text{on}} \exp\left(-\frac{\Delta G}{k_B T}\right) \quad (6.1)$$

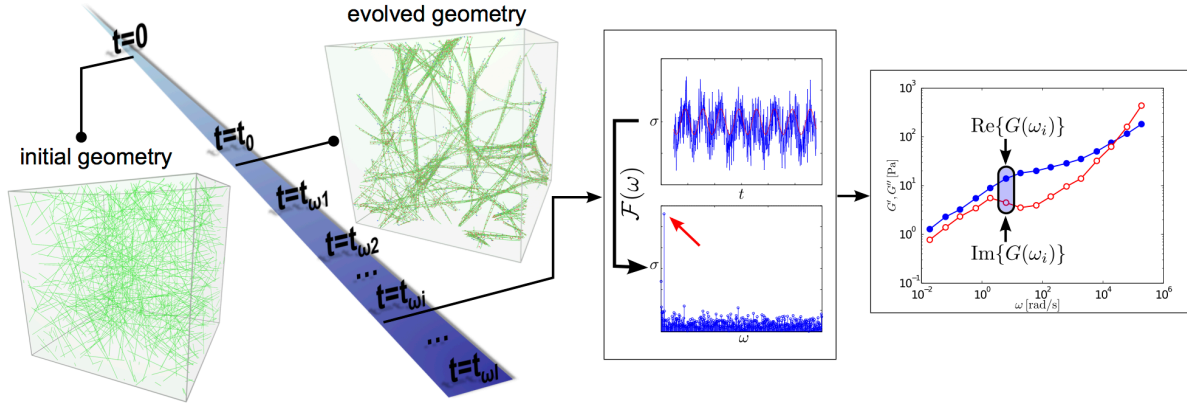
with  $\Delta G$  being the binding energy of the chemical bond and the definition of the local association rate  $k_{\text{on}}$  according to Equation (2.45) in Section 2.6.3. In order to evaluate the influence of force-induced unbinding of crosslinks, Bell's model is used [10] (cf. Equation (4.3)). The characteristic distance parameter  $\Delta x$  is chosen from the interval [1 nm; 4 nm] but did not show any significant effect on the mechanical response of the network, at least not for small deformations in the linear regime. At large strains, however, force-induced unbinding is believed to lead to cooperative unbinding [74], setting loose avalanches of unbinding events that result in sudden stress relaxation (cf. Section 6.4). In contrast to the study presented in Chapter 5, mechanical contact between filaments and contact between filaments and linkers is not modeled as mechanical interaction between filaments is almost exclusively attributed to linkers in the case of the simulated bundle networks.

Figure 6.1 depicts an exemplary bundle network with 360 filaments, which corresponds to a  $c_f = 4 \mu\text{M}$  F-actin concentration. Linker molecules can be found in three states: doubly bound (red), singly bound (blue), and unbound (not visualized). In general, a major fraction of the linkers is bound to two separate filaments within bundles. Only few linkers establish bundle-bundle crosslinks. A comprehensive list of simulation parameters is given by Tables D.1 and D.9.

## 6.2.2 Sample preparation and application of shear strain

**General remarks** In order to conduct rheological simulations efficiently, e.g., in the case of sweeping a broad frequency band, a network sample needs to be created by following the simulation procedure described in Chapter 5. The entire work flow of rheological simulations is illustrated in Figure 6.2. Usually, the sample preparation time is set to  $t_0 \approx 1500 \text{ s}$  of simulated time at a large time step size  $\Delta t$  of 0.005 s to 0.01 s. The network, that evolves during that time, has an average bundle thickness of approximately 150 nm, where the average bundle incorporates about seven to eight filaments. In vitro bundles in purely bundled actin/fascin networks feature comparable numbers of filaments in hexagonal bundles, but with smaller bundle diameters (8 - 10 nm at  $R \approx 0.01$ , [23]) for  $R$  values close to simulations'  $\bar{R}$ . The difference in diameter results from different linker sizes (simulation: 100 nm, experiment: 5 nm), the resulting bundle diameter is approximately  $1.5R_l - 2R_l$ . In simulations using the standard linker model from Chapter 2, the linker has to be made larger in order to enable self-assembly.

When the network has evolved into a state, which is purely bundled, the preparation of the sample is terminated. Subsequently, a time-dependent shear pattern of choice can be applied for a time span  $\tilde{t}$  starting from time  $t = t_0$ . Depending on the problem, different problem-dependent shear patterns can be applied, e.g., a sinusoidal shear strain with a small amplitude  $\hat{\gamma} = 0.01$  in the case of linear rheology.



**Figure 6.2** Work flow for rheological simulations. *From left to right*: first, a rheological sample is *prepared*. The result is a unique evolved network geometry at  $t = t_0$ . Then, a frequency sweep is conducted using this sample for each loading frequency over a time span of ten full periods at a strain amplitude of  $\hat{\gamma} = 0.01$ . Finally, the stress contribution of the loading frequency is extracted from the stress signal and the frequency-dependent dynamic modulus is calculated.

The centerpiece of this chapter is the investigation of the linear rheology, where a broad frequency interval  $[0.006\pi; 200000\pi]$  rad/s is probed. Instead of sweeping the frequencies sequentially, a branched simulation design is chosen which allows for a parallel computation of all frequencies. This procedure has two main advantages. On the one hand, a parallelization of the frequency sweep helps reducing the overall simulation significantly. On the other hand, it is guaranteed that all simulations have the same initial conditions: initial time and initial network geometry. Steps sizes for the different loading frequencies are summarized in Table D.10.

**Shear imposition by means of Dirichlet boundary conditions** Rheological experiments with macroscopic plate rheometers apply shear strains to samples located between the two rheometer plates. While the lower plate is held fixed, the upper plate is displaced (more precisely, rotated) with one of various temporal patterns. In this section, three such displacement patterns will be translated into corresponding Dirichlet boundary conditions. In order to probe the linear rheology of a sample, sinusoidal strains with small shear amplitudes are applied. By contrast, if the stress relaxation behavior of a network is studied, a practically instantaneous application of a fixed displacement, i.e., an approximation of a *Heaviside* step, is chosen. Finally, if nonlinear rheological phenomena are studied, e.g., the effect of force-induced crosslink unbinding at high strains, a linear shear displacement ramp is applied.

The corresponding experimental procedures can be reproduced in silico by an adequately formulated *Dirichlet* boundary value problem, which results in a displacement-driven application of what is referred to as *simple shear* in solid mechanics. Dirichlet values are prescribed at – or at least close to – both faces of the simulation box in  $e_z$ -direction, i.e. at  $z=0$  and  $z=H$ . In the finite element context, these boundary conditions are applied to sets of boundary nodes. Let  $\Omega_n = \{n_{k=1}, n_2, \dots, n_N\}$  comprise all  $N$  finite element nodes in the discretization. Furthermore, let  $\Omega_0 \subset \Omega_n$  and  $\Omega_H \subset \Omega_n$  with  $\Omega_0 \neq \Omega_H$  be subsets of Dirichlet boundary nodes close to the lower and the upper face in  $e_z$ -direction, respectively. The node set  $\Omega_d$  holds all nodes of finite elements that are discontinued by periodic boundary conditions in  $e_z$ -direction. The assignment of

nodes  $n_k$  to one of the subsets is handled by the criterion

$$n_k \begin{cases} \in \Omega_0 & , \text{if } n_k \in \Omega_d \cap z_k < L_e \\ \in \Omega_H & , \text{if } n_k \in \Omega_d \cap H - z_k \leq L_e . \\ \notin \Omega_0 \cup \Omega_H & , \text{else} \end{cases} \quad (6.2)$$

The above conditions are only sensible as long as the element adheres to the condition  $L_e \leq H/2$ . In all simulations, however, the element length is chosen to be  $L_e \ll H/2$ . Following the introductory remarks of this section,  $\Omega_0$  and  $\Omega_H$  are time-variant such that

$$\{\Omega_0, \Omega_H\} \begin{cases} = \{\emptyset\} & , \text{if } t < t_0 \\ \neq \{\emptyset\} & , \text{if } t \geq t_0 . \end{cases} \quad (6.3)$$

Nodal displacement boundary values for each Dirichlet node set can be written as

$$\hat{\mathbf{u}}_{\Omega_0} = \mathbf{u}_{t=t_0}|_{\Omega_0}, \quad \hat{\mathbf{u}}_{\Omega_H} = \mathbf{u}_{t=t_0}|_{\Omega_H} + \hat{\mathbf{u}}_s(t)|_{\Omega_H}, \quad (6.4)$$

$$\hat{\mathbf{u}}_s(t) = (\{\hat{u}_{k=1}(t), 0, 0\}, \{\hat{u}_2(t), 0, 0\}, \dots, \{\hat{u}_N(t), 0, 0\})^T \quad (6.5)$$

with  $\hat{u}_k(t)$  representing node-specific temporal displacement patterns. The displacement  $\mathbf{u}_s(t)$  represents the time-variant displacement pattern. As stated before, three such patterns are of particular interest for three different applications as given below:

$$\hat{u}_k = \begin{cases} \tilde{u}_k \sin(\omega(t - t_0)) & \text{for } t \geq t_0 & , \text{linear viscoelasticity} \\ \begin{cases} 2 \tilde{u}_k (1 - \cos(\tilde{\omega}(t - t_0))) \\ 2 \tilde{u}_k \end{cases} & \text{for } t_0 \leq t < t_1 & , \text{stress relaxation} \\ \tilde{u}_n(t - t_0)/(\tilde{t} - t_0) & \text{for } t \geq t_0 & , \text{nonlinear viscoelasticity} \end{cases} \quad (6.6)$$

where  $\omega, \tilde{\omega}$  denote angular frequencies and  $\tilde{u}_k = \hat{\gamma} z_k$  is the node-specific amplitude, which depends on the node's spatial coordinate  $z_k$ . The first expression of Equation (6.6) corresponds to an imposed bulk shear strain of the form

$$\gamma(t) = \hat{\gamma} \sin(\omega(t - t_0)). \quad (6.7)$$

In contrast to linear and nonlinear rheological simulations, i.e. the first and the third expression of Equation (6.6), the second expression applies to all nodes except for the ones fixed at  $z = 0$ . This displacement pattern, commonly referred to as *step strain*, imposes an affine shear deformation on the entire network.

### 6.3 Linear rheology of semiflexible bundle networks

Having presented the means to apply deformation to networks, the question remains how to interpret the gained mechanical information. A characteristic measure of elasticity for viscoelastic materials like the polymer networks studied in this thesis is the complex modulus

$$G^*(\omega) = G'(\omega) + i G''(\omega). \quad (6.8)$$

$G' = \text{Re}\{G^*\}$  denotes the elastic contribution, while  $G'' = \text{Im}\{G^*\}$  represents the dissipative contribution. In practice, sampling the viscoelastic response of the network over a broad range of loading frequencies leads to the determination of the rheological spectrum.

### 6.3.1 Temporal stress reponse and its Fourier transform

The strain-induced force response  $F_{\Omega_H}(t)$  of the network is readily available and can be directly measured by means of the internal forces of the filaments at the upper face of the simulation box ( $z = H$ ). As a result, the time-dependent stress response can be written as

$$\sigma(t) = \sigma_{\Omega_H}(t) + \sigma_f(t) = F_{\Omega_H}(t)/H^2 + \eta \hat{\gamma} \omega \cos(\omega(t - t_0)), \quad (6.9)$$

where the first summand  $\sigma_{\Omega_H}$  represents the simulated stress. The second summand  $\sigma_f$  accounts for the contribution of the fluid drag, which is added a posteriori due to the fact that the surrounding Newtonian fluid with dynamic viscosity  $\eta$  (e.g., cytoplasm) is not explicitly simulated. In order to quantify frequency-dependent contributions to  $\sigma(t)$ , the Fourier transform of (6.9)

$$\sigma(\omega) = \frac{1}{\sqrt{2\pi}} \int_{-\infty}^{\infty} \sigma(t) e^{-i\omega t} dt \quad (6.10)$$

is calculated. It is necessary to ensure a consistently scaled transform, which means that the multiplicative prefactor (*here*:  $1/\sqrt{2\pi}$ ) of the transform needs to be taken into account (e.g., when using different numerical algorithms). To this end, *Parseval's theorem* is of fundamental importance as it enforces energy conservation for the transition from the time to the frequency domain. [88, Appendix 4.3] provides more information on the theorem and how to treat Fourier spectra to make them physically meaningful. Subsequently, the contribution of the loading frequency  $\omega_l$  is extracted from (6.10) such that the moduli

$$G'(\omega_l) = \frac{\text{Re}\{\sigma(\omega_l)\}}{\hat{\gamma}}, \quad G''(\omega_l) = \frac{\text{Im}\{\sigma(\omega_l)\}}{\hat{\gamma}} \quad (6.11)$$

can be calculated. Eventually, one obtains a rheological spectrum, of which representative show-cases are depicted in Figure 6.3.

### 6.3.2 The frequency regimes of linear bundle network rheology

The spectrum displays *three* well distinguishable regimes. At very high frequencies, the dynamics of single bundles dominate the rheological behavior. In other words, bundles – not single filaments – are the base unit of the network. Interestingly, the encountered power law regime does not match expectations of  $\{G', G''\} \sim \omega^{3/4}$ . Unbinding events are mechanically negligible due to  $\omega_l/k_{\text{off}} \gg 1$ , i.e., that crosslinks between filaments may be considered permanent. At intermediate frequencies, unbinding events of linkers begin to affect rheology, which manifests in a peak in the dissipative contribution  $G''(\omega)$  similar to a simple Maxwell-type viscoelasticity [127]. Furthermore, significant sample-to-sample variation are encountered, which reveals the non self-averaging nature of the network. This regime depends on the reaction-kinetics of the linker-filament bond and is thus non-universal. Finally, at low frequencies, the spectrum again displays a power law behavior, where  $\{G', G''\} \sim \omega^{1/2}$ . Here, the turnover of binding and unbinding linkers is very high thus leading to a state, where bundles begin to fall apart and to reform elsewhere.

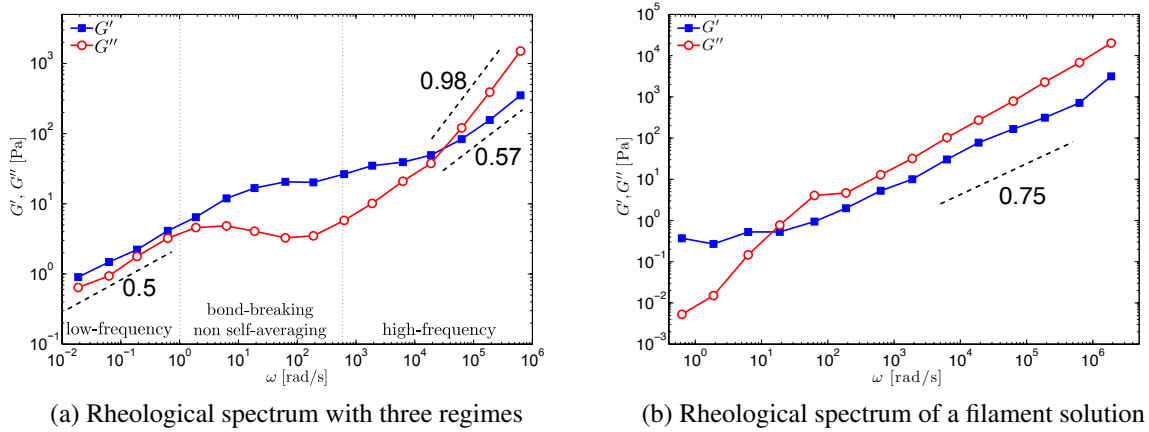


**Figure 6.3** (a) The three distinct rheological regimes of bundle networks. Basic chosen parameters include: filament concentration  $c_f = 4 \mu\text{M}$ , relative linker concentration  $n_l \approx 0.75$  ( $\bar{R} \approx 0.018$ ), association rate constant  $k_{\text{on}} = 90 \text{ s}^{-1}$ , and dissociation rate constant  $k_{\text{off}} = 3 \text{ s}^{-1}$ . At high frequencies ( $\omega > \omega_1$ ), one observes a scaling behavior with  $G' \sim \omega^{0.98}$  and  $G'' \sim \omega^{0.57}$ . At intermediate frequencies ( $\omega_2 < \omega < \omega_1$ ), there is a local maximum in  $G''$ . Finally, in the low-frequency regime, there is a power-law viscoelasticity with  $\{G', G''\} \sim \omega^{1/2}$ . (b)  $G'(\omega)$  and  $G''(\omega)$  of the same system are shown without any linkers. Here the expected  $G'(\omega), G''(\omega) \sim \omega^{3/4}$  scaling behavior is observed as predicted by [59] and experimentally validated by [58].

**High-frequency regime** At finite temperature, a semiflexible filament undergoes thermal fluctuations and, on average, is found in a contorted geometrical configuration. In networks with a mesh size  $\xi$  consisting of *single filaments* rather than bundles, the complex modulus at high frequencies according to [59] can be calculated as

$$G^*(\omega) = \frac{1}{15} \rho \xi \alpha(\omega)^{-1} - i\omega\eta, \quad (6.12)$$

where  $\rho \sim \xi^2$  represents the filament length density. The function  $\alpha(\omega)$  is the compliance to tension of a transversely fluctuating segment with bending stiffness  $\kappa = E_f l_x$  at finite temperature. Summing up contributions from all modes  $n$ , the compliance reads

$$\alpha(\omega) = \frac{1}{T q_1^4 L_p^2} \sum_{n=1}^{\infty} \frac{1}{n^4 - \frac{i\omega}{2\omega_1}}. \quad (6.13)$$

The frequency  $\omega_1 = (\kappa \pi^4) / (\gamma_{\perp} \xi^4)$  denotes the relaxation rate of the slowest transverse mode  $q_1 = \pi / \xi$  with  $\gamma_{\perp}$  being the friction coefficient per unit filament length. Forcing filaments back to a straight configuration by pulling at two separate points along the filament means that work has to be done against entropic elasticity. As a consequence, transverse modes are quenched gradually leading to the power law scaling  $G', G'' \sim \omega^{3/4}$  reported in [59, 160].

In the case of bundles consisting of multiple crosslinked filaments, this argument does not hold entirely. It is incorrect to assume that a bundle can be understood as a thicker filament with a larger (effective) persistence length  $L_p(\mathcal{N})$  due to the  $\mathcal{N}$  filaments it incorporates. Rather it has been shown that a bundle, crosslinked by harmonic springs, exhibits a scale dependence [78, 171]. According to [78], a crosslinked bundle has a mode-number-dependent bending stiffness

$$\kappa_n = \frac{\mathcal{N}^2 \kappa}{1 + (q_n \mathcal{D})^2 \frac{\delta E_f}{12 k_x}} \quad (6.14)$$

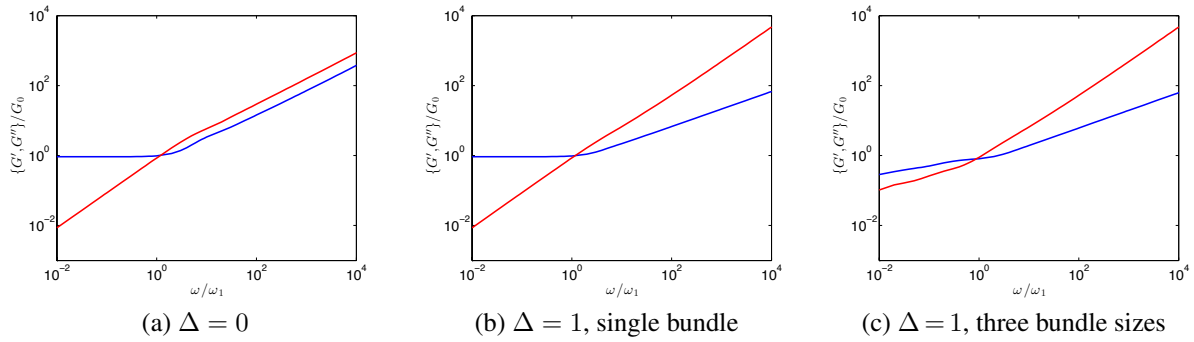


**Figure 6.4** Scaled complex moduli  $G^*(\omega)/G_0$  of semiflexible networks for bundling parameters  $\Delta = 0$ , single-filament limit (left) and  $\Delta \gg 1$ , bundle limit (right): (a) For small  $\Delta$ ,  $G^*$  approaches single filament behavior, where both  $G'$  and  $G''$  exhibit an  $\omega^{3/4}$  scaling. (b) For large  $\Delta$ , however, the moduli stray from their common scaling exponent. (c) The consideration of bundles of different lengths smears the plateau (cf. Figure 6.3). For all three graphs,  $\omega_1 = 1.0$  and  $90\alpha(0)/\pi^4 = 1.0$ .

with  $q_n = n\pi/\xi$ , denoting the wave number,  $\mathcal{D} = b\sqrt{\mathcal{N}}$  the bundle diameter,  $\delta$  the distance between crosslinks, and  $k_\times = E_l A_l/R_l$  the spring constant of the linker. The symbol  $b$  denotes the spacing between the centerlines of the bundle filaments [78]. In dense bundles,  $b$  approaches the filament diameter, in the simulated networks, the value is rather given by  $b \rightarrow R_l$ . If Equation (6.14) is inserted into Equation (6.13), an enhanced expression is yielded, which contains the characteristic (cross-over) frequency  $\omega_1$ . The striking consequence is that a new scaling behavior is found, which accounts for the effect of bundling within semiflexible networks. Based on the compliance  $\alpha(\omega)$  of single bundles, it is now possible to calculate complex modulus  $G^*(\omega)$  of a network consisting of equally sized bundles connected to each other.

When a bundle is stretched in axial direction, transverse bending fluctuations are diminished and the compliance – in slight variation of Equation (6.13) – can again be written as a sum over modes [59, 78]

$$\alpha(\omega)/\alpha(0) = \frac{90}{\pi^4} \sum_{n=1}^{\infty} \frac{1}{n^4 - \frac{i\omega}{2\bar{\omega}(n)}}, \quad (6.15)$$

with  $\alpha(0) = \xi^4/(90k_B T L_p (\mathcal{N})^4)$  as the zero-frequency compliance of a bundle with effective persistence length  $L_p(\mathcal{N}) = \mathcal{N}^2 L_p$  and  $\bar{\omega}(n)$  being the relaxation rate of the  $n^{\text{th}}$  mode. This relaxation rate  $\bar{\omega}(n)$  may vary depending on the mechanical model used for the composite bundle. However, in the limit of large  $\mathcal{N}$  and a fixed diameter  $\mathcal{D}$ , it approaches the *Timoshenko limit* for beam bending [57]:

$$\bar{\omega}(n)/\omega_1 = \frac{\mathcal{N}^2}{1 + \Delta n^2}. \quad (6.16)$$

In Equation (6.16), the dimensionless constant  $\Delta = \mathcal{N}(\pi^2/12)(E_f b^2/\delta k_\times)(\delta/\xi)^2$  is introduced, which determines the rheology of the network at high frequencies. For  $\Delta = 0$ , single filament scaling is recovered, i.e.,  $\{G', G''\} \propto \omega^{3/4}$  as depicted in Figure 6.4a. Towards the bundle limit  $\Delta \gg 1$ , different frequency-dependent scaling behaviors arise for  $G'$  and  $G''$  as demonstrated in Figure 6.4b:  $G' \simeq \omega^{1/2}$  and  $G'' \simeq \omega$ . In between the extremes, the scaling exponents vary smoothly. Upon further study of Figure 6.3, one cannot help but notice the difference in the slope of  $G'$  around  $\omega_1$  as compared to theoretical considerations visualized in Figure 6.4b. Whereas Equation (6.15) predicts a plateau modulus  $G_0$ , the observation made in Figure 6.3

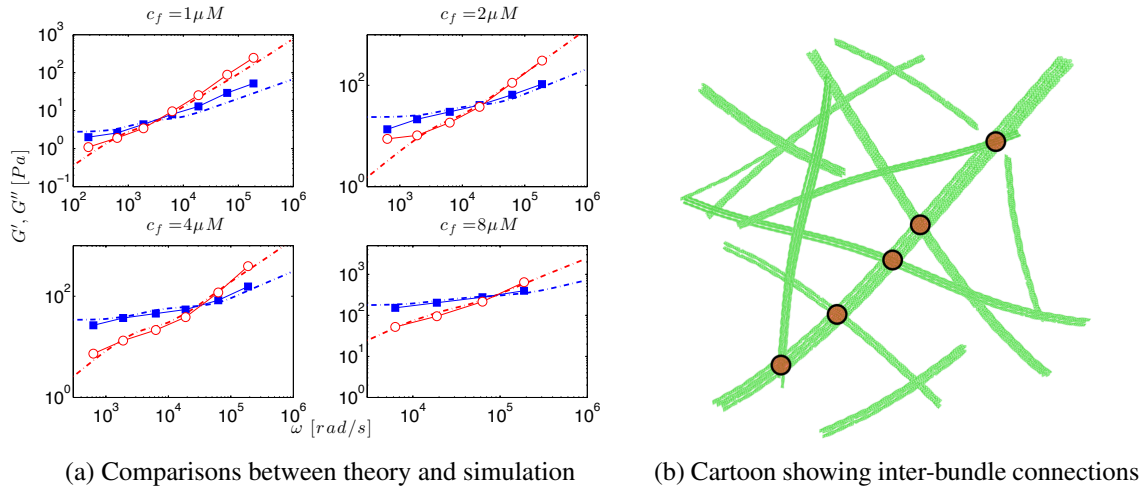


**Figure 6.5** (a) Theoretical predictions ( $\cdots$ ,  $\cdots$ ) of the high-frequency rheology of bundle networks at concentrations  $c_f = \{1, 2, 4, 8\} \mu\text{M}$  fitted to simulation results ( $\blacksquare$ ,  $\circ$ ). Storage moduli  $G'$  are depicted in blue, loss moduli  $G''$  in red color. The plateau  $\bar{G}$  is smeared due to the presence of bundle segments of different lengths. This influence of different bundle lengths is demonstrated using fits with three different bundle lengths with cross-over frequencies  $\tilde{\omega}_1 = \{1.0, 0.1, 0.01\} \text{rad/s}$ . Three different lengths do not reflect the complexity of actual bundle networks, yet already such coarse fits capture the moduli's slope well left and right of the cross-over. (b) Cartoon of a bundle network with inter-bundle connections by linkers. The red marks along the filament emphasize the idea of bundle segments in a serial circuit.

differs from the prediction by [59], where  $G'$  rises continuously towards  $\omega_1$ . This observation can be explained by considering geometrical arguments. A network consisting of bundles, that are connected among another, features an unknown distribution of free bundle lengths. The non-horizontal  $G'$  mentioned above may be understood as these bundle lengths weighing into  $G^*$  differently. As a result, the plateau  $G_0$  is smeared. In the following, a simple proof of concept will be discussed involving a primitive fit with three different bundle lengths. Choosing characteristic frequency scales  $\tilde{\omega}_1 = \{1.0, 0.1, 0.01\} \text{rad/s}$  and weights  $w_{\tilde{\omega}} = \{0.89, 0.09, 0.01\}$  leads to an inclined shape of the storage modulus  $G'$  as depicted in Figure 6.4c. The absence of a  $G'$ -plateau may be understood as a consequence of the heterogeneity in diameter and length of bundle segments in the network. In Figure 6.5, four theoretical fits to data gained from simulations are shown. Decent fits are already achieved assuming only three different bundle lengths. These fits may be improved by adding more bundle lengths. Of course, more sophisticated fitting procedures can be easily designed. At this point, it is not necessary since the inclusion of only three bundle lengths already demonstrates the consistency of theory and the phenomenology found in simulations.

Gaining *experimental* insight into the high-frequency behavior beyond the cross-over frequency  $\omega_1$  is impossible in the case of bundle networks since  $\omega_1$  is too large for any currently used experimental technique. This renders simulation the only means to examine the high-frequency regime phenomenologically. To the author's knowledge, macroscopic rheometers, that measure the bulk rheology of networks, are unable to reliably assess the high-frequency regime due to inertial effects. These kind of rheometers are limited to frequencies usually far below  $\omega_1$  of bundle networks. Microrheological set-ups such as the one used in [144] reach frequencies up to  $\omega \approx 10^3 \text{rad/s}$ . The cross-over frequency of entangled F-actin solutions are lower than this value but the  $\omega_1$  of bundle networks is not. An increase in bundle thickness en-

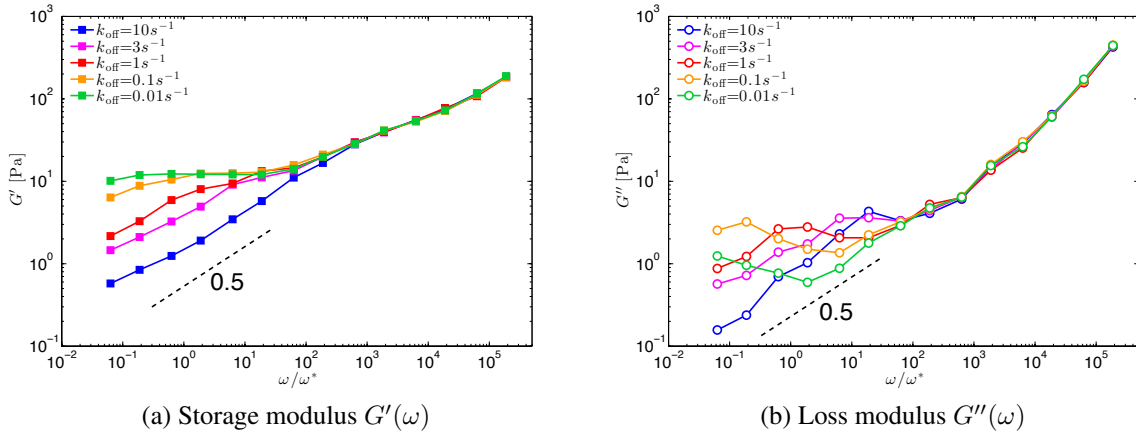


**Figure 6.6** Starting off from *one* initial network geometry, the off-rate  $k_{\text{off}}$  is varied on the range  $[0.01; 10] \text{ s}^{-1}$ . (a) Storage moduli  $G'$ . (b) Loss moduli  $G''$ . Note the  $G', G'' \sim \omega^{1/2}$  scaling for low frequencies as well as the growing gap between  $G'$  and  $G''$  with decreasing  $k_{\text{off}}$  at intermediate frequencies. The high-frequency regime is, as expected, independent of  $k_{\text{off}}$ . Linkers can be considered permanent on such short time scales.

tails an increase in  $\omega_1$ . Even for thin bundles that consist of only a few filaments, the cross-over of  $G'$  and  $G''$  is pushed to frequencies even beyond the reach of microrheology. For example, the cross-over of the simulated network in Figure 6.3a is located at about  $2 \times 10^4 \text{ rad/s}$ .

A considerable number of over 120 networks has been probed to support the claims on the universal nature of the high-frequency regime. The high-frequency regime of bundle networks has been proven unsusceptible to reaction kinetics on a physically and physiologically sensible off-rate interval  $k_{\text{off}} \in [0.01; 10] \text{ s}^{-1}$  as shown in Figure 6.6, where the same initial network geometry was simulated multiple times with varying  $k_{\text{off}}$ . Furthermore, it has been demonstrated that the rheology is in principle independent of the sample (cf. the high frequencies of Figure 6.8a).

**Intermediate-frequency regime** Towards lower frequencies  $\omega < \omega_1$ , a frequency-independent, constant-valued storage modulus is predicted by (6.15), while, on the other hand, a monotonous decrease characterizes the loss modulus (cf. Figure 6.3b and Figure 6.4a). The expected behavior for sparsely crosslinked networks is

$$G' \simeq \frac{\rho \xi}{15\alpha(0)}, \quad G'' \propto \omega. \quad (6.17)$$

Instead, the moduli in Figure 6.3a reveals a distinct behavior. Neither  $G'$  nor  $G''$  approach the predictions by Equation (6.17). This deviation can be understood by analyzing the linkers' ability to establish crosslinks in the presence of oscillatory shear strain. In order to acquire this information, the positions of both binding sites involved in a double bond at time  $t = t_0$  are tracked. Their positional drift can easily be monitored in simulations, whereas it is nearly impossible to observe this drift in vitro. Studying Figure 6.7, one notices that the distribution of binding site distances broadens even at frequencies of about  $20\pi \text{ rad/s}$ , which are well above  $k_{\text{off}}$ . On average, binding site distances remain close to the linker size  $R_l$ , which implies that the network geometry does not vary significantly over the course of the simulation. At very low frequencies, bundles even start peeling apart, which is a characteristic of the low-frequency regime discussed later on. The most intriguing observation, however, is concerned with the reduction

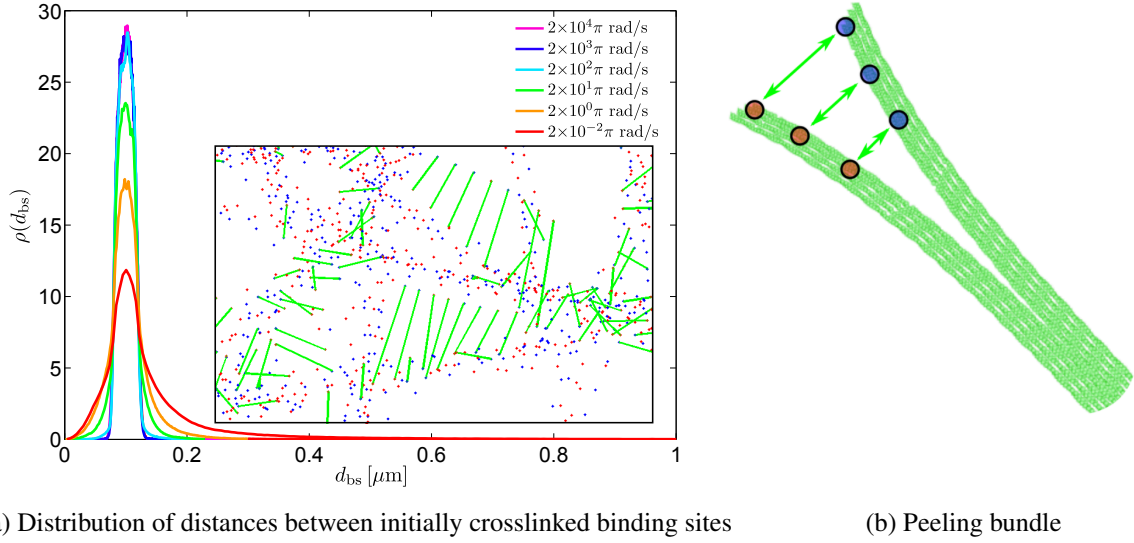


**Figure 6.7** (a) Distribution of distances between pairs of initially crosslinked inter-filament binding sites observed during oscillatory shear at different shear frequencies, showing that the network becomes more sparsely crosslinked at low frequencies due to bundle dissolution. Inset: Initially crosslinked binding site pairs (red/blue) with highlighted large distances (green) between ruptured crosslinks for the  $\omega = 0.02\pi$  rad/s case proving the dissolution of bundles. (b) Cartoon that illustrates bundle dissolution using the same color scheme as in the inset.<sup>1</sup>

of the actual number of crosslinks due to the application of shear strain. A simplified model helps understanding why such a decrease in the number of crosslinks is observed. Consider two parallel filaments connected to each other by linkers similar to the setup described in [14]. Linkers act as spacers keeping the filaments separated at an initial distance  $d_{bs} = 100$  nm. Under oscillatory shear strain with an amplitude  $\gamma \sim 0.01$ , the distance between the binding sites grows. The lateral displacement  $A = \gamma d_{bs}$  becomes larger than the molecular capture radius  $a$  ( $R_l$  for the linker model), which determines the size of its reaction volume. Now, if a stretched bond is disconnected, the current binding site distance becomes too large for an immediate reattachment. A disconnected linker stays singly bound for at least a time interval of half the period length of the oscillation  $\pi/\omega$ . The probability of a reattachment event per periodic cycle is given by

$$p_r \simeq 1 - e^{-\frac{k_{on}a}{A\omega}}. \quad (6.18)$$

At very high frequencies,  $A\omega$  approaches infinity, which leads to a reattachment probability  $p_r \ll 1$ . Summing over the number of oscillations, one arrives at a frequency-independent reduced on-rate

$$k_{eff} \simeq k_{on}(a/A) < k_{on}. \quad (6.19)$$

The high-frequency rheology remains unaffected as it is dominated by the thermal fluctuation of single bundles. At lower frequencies, however, the quotient is characterized by  $k_{on}a/(A\omega) \gg 1$  such that the reattachment probability is  $p_r \simeq 1$  and the effective on-rate reads  $k_{eff} \simeq \omega$ . The off-rate is shear-invariant, which leads to a frequency-dependent Boltzmann factor  $k_{eff}/k_{off}$ . With decreasing  $\omega$ , the effective linker density also decreases. The frequency scale  $k_{on}a/A$  for

<sup>1</sup>Figure taken and modified from [164], ©2014, American Physical Society

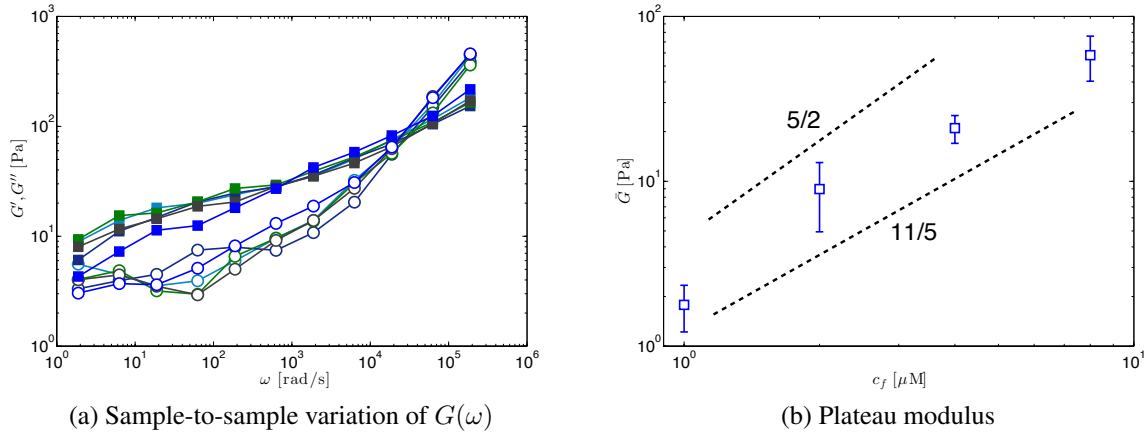


**Figure 6.8** (a) On the interval of  $\omega \in [1; 1000]$  rad/s, the rheological moduli of bundle networks display pronounced sample-to-sample variations. At frequencies  $\omega > 1000$  rad/s, sample deviation is small. The intermediate-frequency regime, however, shows deviations on a broad interval. The storage moduli  $G'$  of the different samples are indicated by closed squares, the corresponding loss moduli  $G''$  by open circles of the same color. (b) Nonlinear dependance of the plateau modulus  $\bar{G}$  on filament concentration  $c_f$ . The scaling lies in between the theoretical predictions for a solution of entangled filaments  $\bar{G} \sim c_f^{11/5}$  and a densely crosslinked network  $\bar{G} \sim c_f^{5/2}$  [149] (dashed lines).  $\bar{G}$  is computed as the arithmetic mean of frequencies 1 - 100 Hz at  $k_{\text{on}} = 90 \text{ s}^{-1}$  and  $k_{\text{off}} = 3 \text{ s}^{-1}$ .

pronounced shear-induced bond breaking effects (in Figure 6.3a:  $20\pi - 200\pi$  rad/s) and  $k_{\text{off}}$  determines the upper and lower bounds of the intermediate-frequency regime. A most interesting property of the intermediate-frequency regime is the sample-to-sample variation as depicted in Figure 6.8a. Although the different samples were prepared using identical simulation parameters, the different emerging network geometries lead to significantly differing complex moduli  $G(\omega)$ . The strong  $\sim \xi^3$  dependence of the plateau modulus  $\bar{G}$  on the mesh size explains how moderate changes in the mesh size drastically affect the modulus scale. An examination of the scaling behavior of the plateau modulus with respect to filament concentration, however, on average exhibits a well-known scaling relation. The scaling of the plateau modulus for an entangled solution of semiflexible filaments is given as  $\bar{G} \sim c_f^{11/5}$ , the scaling for a densely crosslinked network reads  $\bar{G} \sim c_f^{5/2}$  [149]. In Figure 6.8b,  $\bar{G}$  at four different filament concentrations ( $c_f = \{1, 2, 4, 8\} \mu\text{M}$ ) is depicted. The dashed lines represent the theoretical predictions the respective cases of entangled and sparsely crosslinked networks. It is shown that the concentration-dependent plateau modulus scales within familiar bounds for semiflexible bundle networks.

The intermediate-frequency regime crucially depends on the off-rate  $k_{\text{off}}$ . The influence of  $k_{\text{off}}$  becomes apparent, when  $k_{\text{off}}$  is varied as illustrated in Figure 6.6. The high-frequency regime has been found invariant to  $k_{\text{off}}$  due to its time scales lying three to five orders of magnitude below the characteristic unbinding time of a linker  $1/k_{\text{off}}$ . By contrast, the extent of what is called the intermediate-frequency regime, depends on  $k_{\text{off}}$  as is clearly demonstrated. The plateau in  $G'$  expands over an increasingly large range of frequencies with decreasing  $k_{\text{off}}$  (Figure 6.6a).  $G''$  is shown in Figure 6.6b. It is pushed to smaller values for decreasing  $k_{\text{off}}$ , which can be understood in terms of the diminishing effect of linker unbinding on stress release and thus dissipation.

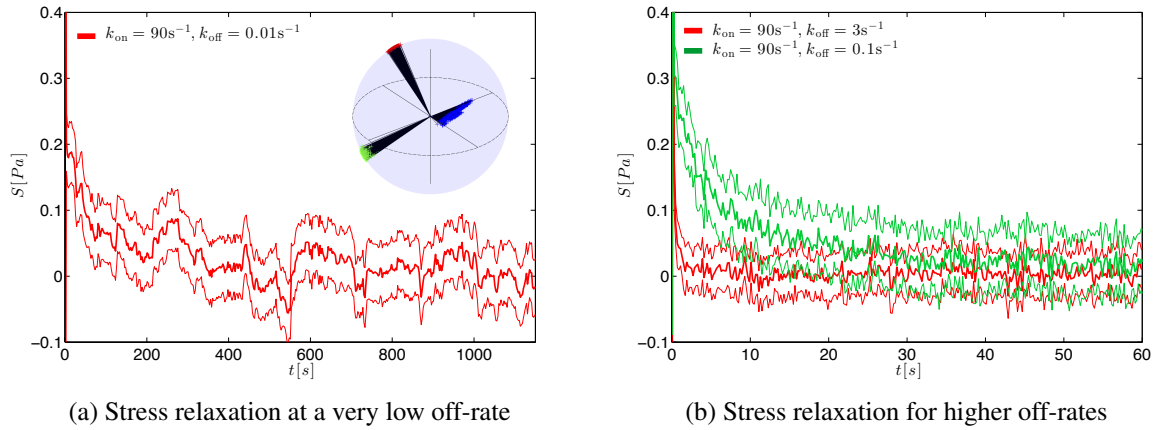


**Figure 6.9** Stress relaxation following an affine step strain deformation at  $t = t_0$  (set to zero for clarity). (a) The  $G' \sim G'' \sim \omega^{1/2}$  scaling relation predicts a  $1/t^{1/2}$  stress decay. For  $t > 200$  s spontaneous fluctuations of large amplitude overwhelm the mean stress. The stress fluctuations are accompanied by subdiffusion of the principle axes of the moment of inertia tensor (inset). (b) Two networks with different  $k_{\text{off}}$  for which the measured stresses due to the imposed strain decay completely. Thick centerlines represent the mean of the respective curves, the thinner lines represent the errors of binned subsets of the stress signal.<sup>2</sup>

**Low-Frequency regime** As Figure 6.3 shows, there exists a third characteristic frequency regime towards frequencies  $\omega \ll k_{\text{off}}$ , where the complex modulus scales with  $G' \sim G'' \sim \omega^{1/2}$ . This behavior has been previously observed in simulation [14] and experiment [220, 221]. It is connected to transient crosslinking [75] and is invariant to filament concentration. This scaling relation implies the existence of a power-law stress decay  $1/t^{1/2}$  after applying a step strain (in the present case  $\Delta\gamma = 0.04$ ). When looking at Figure 6.9a, however, the temporal stress relaxation  $S(t)$  computed from simulated data exhibits large, *spontaneous* stress fluctuations even after several hundreds of simulated seconds, making it difficult to identify the expected scaling behavior. This peculiarity becomes even more obvious upon comparison with analogous step strain simulations at different  $k_{\text{off}}$  shown in Figure 6.9b, where – apart from an individual, off-rate dependent initial decay – stresses level off to values around zero. The question arises, whether this observation might just be a numerical artifact leading to a violation of energy conservation. However, this is unlikely since in Chapter 5, the strain energy of entire networks was monitored for several thousands of simulated seconds without displaying this kind of fluctuation. Rather, the strain energy remained constant (cf. Figure 5.15) once the system had reached a *stationary state* characteristic for close-to-equilibrium structures. In order to ascertain the origin of these unexpected stress fluctuations, the principal axes of the moment of inertia tensor of the entire network are computed and visualized in the inset of Figure 6.9a. It can be clearly seen that the principal axes tumble slightly. Each of the inertia tensor’s base vector orientations as a function of time  $\phi(t)$  can be utilized to describe the diffusive properties of the present system statistically. Given that the studied system exhibits the diffusive behavior of a fluid, the inertia tensor would perform rotational Brownian motion, where

$$|\phi(\omega)|^2 \propto \omega^{-2} \quad (6.20)$$

<sup>2</sup>Figure 6.9a taken and modified from [164], ©2014, American Physical Society

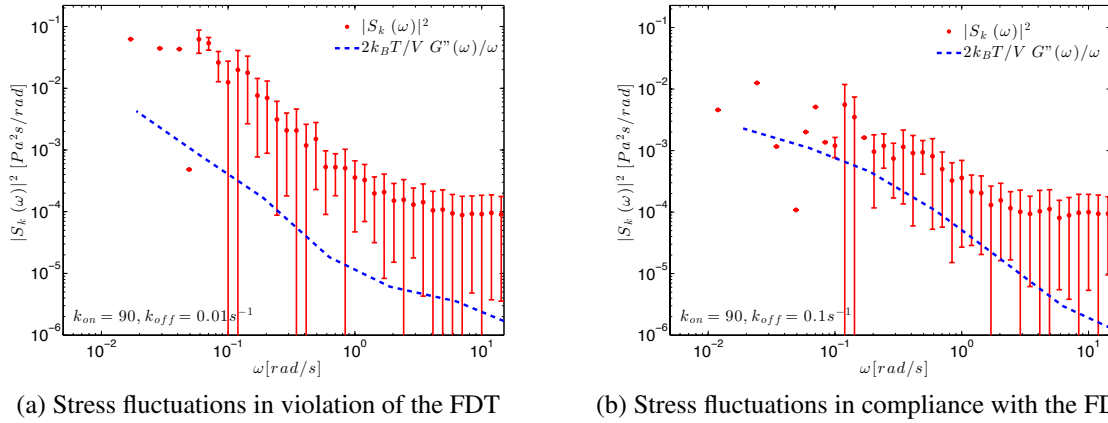


**Figure 6.10** Frequency-dependent mean square amplitude of the stress fluctuations in the low-frequency regime stemming from *in silico* measurements ( $\circ$ ); prediction by the fluctuation-dissipation theorem as calculated according to equation 6.23 (-). (a) For  $k_{\text{off}} = 0.1 \text{ s}^{-1}$ , the measured and the predicted spectrum still overlap, i.e. the assumption of thermodynamic equilibrium is still valid. The fluctuation-dissipation theorem is applicable. (b) However, with  $k_{\text{off}} = 0.01 \text{ s}^{-1}$ , the measured values exceed the prediction. The network is in a non-equilibrium state leading to increased stress amplitudes as compared to a thermally equilibrated structure.<sup>1</sup>

holds with a constant diffusion coefficient  $\mathfrak{D}$ . Alternatively, in case of an elastic network, the system can be thought of as a Lorentzian oscillator with the relation

$$|\phi(\omega)|^2 \propto \frac{\gamma_L}{(\omega - \omega_0)^2 + \gamma_L^2}. \quad (6.21)$$

The parameter  $\gamma_L$  quantifies the width of the Lorentz distribution and  $\omega_0$  denotes the location of the peak. Neither of the above predictions is observed. Rather, the best fit can be achieved by

$$|\phi(\omega)|^2 \propto \omega^{-1}, \quad (6.22)$$

which implies subdiffusive behavior. These slow orientational fluctuations of the moment of inertia tensor imply that large-scale thermal fluctuations play a key role in the low-frequency regime.

Transiently crosslinked bundle networks are non-equilibrium structures. As such, the stress fluctuations are enhanced by *aging* effects due to a slow network evolution, which has a non-equilibrium nature. In order to further investigate this idea, the fluctuation-dissipation theorem (FDT) is evaluated, which describes the relation between the average mean square amplitude of the stress fluctuations  $\langle |S(\omega)|^2 \rangle$  and the loss modulus  $G''(\omega)$ . It reads

$$\langle |S(\omega)|^2 \rangle = \frac{2k_B T}{\omega} G''(\omega). \quad (6.23)$$

Figure 6.10 depicts two stress spectra corresponding to off-rates  $k_{\text{off}} = 0.01 \text{ s}^{-1}$  (Figure 6.10a) and  $k_{\text{off}} = 0.1 \text{ s}^{-1}$  (Figure 6.10b). In case of the lower off-rate, the stress fluctuation amplitude exceeds the value predicted by the FDT at lower frequencies; we detect non-equilibrium, large-scale network reorientations that are associated with its structural aging. This observation is incompatible with equilibrium motion. As expected, a speed-up of the network's structural relaxation by increasing the linker off-rate from  $0.01 \text{ s}^{-1}$  (used in Figure 6.9a) to  $0.1 \text{ s}^{-1}$  leads to

a reduction of the observed stress fluctuations (Figure 6.9b), which pushes the network back into the bounds predicted by the FDT (Figure 6.10b). The overall structure of all of these networks, however, have not yet equilibrated, which is consistent with experimental observations [138].

### 6.3.3 Comparison of simulation and experiments

As a conclusion to the study of the linear rheology of semiflexible bundle networks, numerical results will be compared to experimental results found in literature.

**Bundling linkers** A large variety of biologically relevant linker molecules is able to form bundles of actin filaments. Each one is specific concerning binding domains on actin filaments, size, and reaction rate constants. There are linkers that exclusively create purely bundled networks such as fascin or espin. Both create – superficially seen – similar network but their effect on network mechanics is distinct from one another [134, 141]. Both linkers have been examined with respect to their linear, non-universal, intermediate-frequency rheology and their nonlinear elastic response. Their linear rheology already exhibits noticeable differences, which grow even stronger in the nonlinear regime. Other linkers like filamin create bundled networks as well, however, bundle structure and arrangement differ from actin/fascin and actin/espin networks [186], which is probably connected to filamin being a large and flexible linker ( $\sim 100$  nm) compared to fascin or espin ( $\sim 5$  nm). Linkers of the  $\alpha$ -actinin family exhibit a structural polymorphism, where one of the occurring phases consists of bundles [140]. Despite their individual properties, however, there are linker-independent rheological properties. The transient nature of crosslinks is essential for the mechanical behavior of a network and common to all experimentally studied linkers. The degree of transience is characterized by the dissociation rate constant  $k_{\text{off}}$ . This rate constant is particularly influential since it determines the experimentally accessible part of a rheological spectrum, which, according to this chapter's findings, describes a general rheology of semiflexible bundle networks. The *in vivo* off-rate of fascin is reported as  $k_{\text{off}} = 0.07 \text{ s}^{-1}$  [134], which makes it virtually impossible to access the low-frequency regime of the actin/fascin spectrum. There are other linker molecules, e.g., different species of  $\alpha$ -actinin, which have a significantly higher off-rate than fascin and, apart from a composite phase, do form bundle networks at certain concentrations.

In this subsection, the linear rheology of an actin/ $\alpha$ -actinin 4 network with  $R = 0.02$  reported by [14] is compared to the low-frequency regime predicted by simulation. In the intermediate frequency range, the linear rheology of an actin/fascin network with  $R = 0.1$  by [134] is set up against an *in silico* example featuring the *in vivo* off-rate. There is no experimental data available for the high-frequency regime beyond cross-over frequency  $\omega_1$  in case of bundle networks. Here, simulation is the sole means to access this frequency range and therefore predicts a mechanical behavior, which might or might not become measurable in the future.

**Discussion** The low-frequency experimental data and the data drawn from finite element simulations are normalized with respect to both loading frequency  $\omega$  and complex modulus  $G$ . The basic idea is that, despite the differences in filament and linker concentrations between simulations and experiments, the spectra should be superimposable if scaled consistently. In that sense, the normalization only removes sample-specific information. A good agreement between

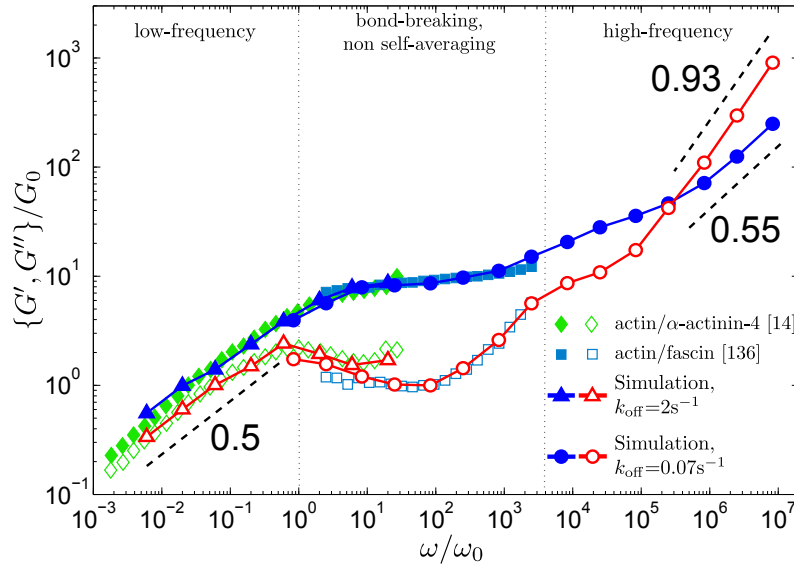


**Figure 6.11** Normalized rheological spectra of simulation and experiments. *Experimental data at low frequencies* ( $\diamond, \diamond$ ) stems from an actin/ $\alpha$ -actinin-4 network with  $R=0.02$  reported by [14]. It is compared to a simulation with  $k_{\text{on}} = 60 \text{ s}^{-1}$ ,  $k_{\text{off}} = 2 \text{ s}^{-1}$  ( $\blacktriangle, \triangle$ ). *Experimental data for the intermediate-frequency regime* ( $\blacksquare, \square$ ) stems from [136]. It is compared to a separate simulation with  $k_{\text{on}} = 90 \text{ s}^{-1}$ ,  $k_{\text{off}} = 0.07 \text{ s}^{-1}$  ( $\bullet, \circ$ ). The curves were normalized with respect to  $\omega_0$  at the local peak in  $G''$ , as well as  $G_0 = G''(\omega_0)$ , which is the corresponding value of the loss modulus. At high frequencies, experimental data is unavailable. The slopes indicated by the dashed black lines imply a bundling parameter of  $\Delta \approx 2.1$

simulation and experiment would support the claim on the universality of certain rheological properties of bundle networks. The well-defined off-rate dependent local peak in  $G''$  is chosen for the normalization of the curves, i.e., normalization factors  $\omega_0$  and  $G_0 = G''(\omega_0)$  are applied. The linker  $\alpha$ -actinin 4 used in [14] has an assumed off-rate of approximately  $k_{\text{off}} = 0.4 \text{ s}^{-1}$  (with reported values of  $0.1 - 1 \text{ s}^{-1}$ ) as compared to an in silico off-rate  $k_{\text{off}} = 2 \text{ s}^{-1}$ , which necessitates two separate normalization factors for the experimental and the numerical data set. In absolute values, normalization of the experimental data is carried out using  $\omega_{0,exp} = 2.63\pi \text{ rad/s}$  and  $G_{0,exp} = 11.71 \text{ Pa}$ . The corresponding values for the simulated data set are  $\omega_{0,sim} = \pi \text{ rad/s}$  and  $G_{0,sim} = 2.30 \text{ Pa}$ . With these values, Figure 6.11 illustrates, what can be described as an excellent match of the two compared rheological spectra. Having normalized both curve pairs by their respective factors, their shapes are nearly congruent, which impressively demonstrates that the finite element model accurately captures fundamental phenomena observed in experiments. The intermediate-frequency regime predicted by simulation is also in very good agreement with experimental values. As experimental data does not cover the local peak in  $G''$ , an approximate pair of normalization factors  $\omega_{exp}^*$  and  $G^*(\omega^*)$  is assumed. While the in vitro off-rate is not explicitly known, there exist in vivo measurements as stated above. Hence, the in silico off-rate was set to the in vivo value  $k_{\text{off}} = 0.07 \text{ s}^{-1}$  as it substantially influences the loss factor  $\delta_l = G''/G'$  in this regime. Compared to the experimental curve, one notices the steeper rise of  $G''$  towards its local peak, which can be explained by the larger size of the simulated linkers ( $R_l = 100 \text{ nm}$  vs. the size of fascin,  $\approx 5 \text{ nm}$ ). The beam elements, that represent linkers, presumably have a lower bending stiffness than fascin, thus giving rise to a more pronounced intra-bundle dissipation due to less strongly coupled bundle filaments. The absolute values of the experimental and numerical

normalization factors read  $\omega_{0,exp} = 0.008\pi$  rad/s and  $G_{0,exp} = 1.0$  Pa and  $\omega_{0,sim} = 0.024\pi$  rad/s and  $G_{0,sim} = 1.48$  Pa.

The high-frequency regime of Figure 6.11 cannot be compared to experimental data due to a lack thereof. However, it can be consistently explained by what has been considered in Section 6.3.2. Below the normalized cross-over frequency at  $\omega_1/\omega_0 \approx 2 \times 10^5$ ,  $G'$  and  $G''$  are nearly parallel down to  $\omega/\omega_0 = 10^4$ . As illustrated in Figure 6.4c, this rheological behavior is predicted by the theoretical model and is owed to the joint effect of bundle segments of different *lengths* and *diameters*. The distribution of these two parameters as well as the connectivity between separate bundles determine the individual shape of the high-frequency regime.

An estimation for the bundling parameter  $\Delta$  from Equation (6.16) can be given as well. The high-frequency regime from Figure 6.11 is characterized by  $\Delta \approx 2$ . The calculation leading to this specific value for  $\Delta$  can be found in the appendix C.

## 6.4 Aspects of nonlinear viscoelasticity of semiflexible bundle networks

Bundle networks display a remarkable dependency of their mechanical response on the strain rate  $\dot{\gamma} = d\gamma/dt$ , which has been amply demonstrated and discussed for the case of small deformations in the preceding sections of this chapter. Their rheological properties in the linear deformation regime have been shown to change drastically depending on the loading frequency. Following up on linear rheology, the nonlinear elastic response of the simulated bundle networks is probed. Mechanical nonlinearities arise from various sources such as the network structure with its local anisotropies, reaction kinetics, or the interplay of linker and filament stiffness. Here, the nonlinear elasticity of bundle networks is examined with respect to two of several possible system parameters, which upon variation yield the same effect: a continuous transition from strain-hardening to strain-softening behavior [133].

Bundle networks exhibit a strain-rate dependent transition from strain-hardening to strain-softening [134]. First, it will be shown that the computational approach is capable of capturing all effects leading to the observed behavior. In a second step, the identical behavior will be reproduced by means of a modulation of the off-rate  $k_{off}$ , which may vary, e.g., as a consequence of linker mutation.

The strength of the computational approach is not limited to a mere reproduction of experimental results, but rather lies in readily available information on the causes of a specific mechanical behavior. Therefore, the third and final part of this section is devoted to micromechanical phenomena which strongly affect the network's response to nonlinear shear deformations.

### 6.4.1 Generic description of the nonlinear elastic response

According to [133], the nonlinear elastic behavior of biopolymer networks is most conveniently studied using a time-invariant shear rate  $\dot{\gamma} = \text{const}$ . Both experiments and simulations record a discrete data set of stress values, create a smoothed stress signal  $\sigma(\gamma)$  as a function of shear  $\gamma$ , which enables the calculation of the differential modulus  $K = \partial\sigma/\partial\gamma$ , a strain-dependent material property. Following the path of deformation with increasing  $\gamma$  then reveals three distinct regimes (cf. Figure 4.14, [133]). For small strains,  $K$  remains constant. Beyond a certain strain

threshold  $\gamma_c$ , a bifurcation admits one of two possible alternatives. If the network exhibits strain-hardening, the differential modulus starts increasing with a power law relation  $K \sim \gamma^\alpha$  with a (linker-dependent) exponent  $\alpha$  until it peaks at  $\gamma_m$ , which marks the transition from elastic to plastic deformation. Beyond the peak value,  $K$  decreases rapidly due to the onset of plastic deformation and the impending destruction of the network. If the network is weakened by strain, the differential modulus decreases beyond  $\gamma_c$ .

### 6.4.2 Linker-specific nonlinear elastic response

The nonlinear elastic response differs with linker species. Actin/fascin networks are known to exhibit a continuous transition from strain-hardening to strain-softening at high linker concentrations, where the network has already switched from single filaments to a purely bundled phase [134]. As already stated, this transition can either be caused by time-dependent, non-constitutive variables such as the shear rate  $\dot{\gamma}$  or by inherent network parameters such as molar ratio  $R$  or the reaction kinetics of the filament/linker bond. The nonlinear response of bundle networks depend more strongly on the specificities of the linker molecule than the response to linear deformations. Espin, which also constitutes pure bundle networks, displays a nonlinear response distinct from that of fascin linked networks [141]. While an increase in fascin concentration elevates network stiffness but maintains the strain-hardening behavior, a similar increase in espin concentration results in strain-weakening. Filamin seems to induce strain-hardening independent of its concentration [186].

The computational approach reproduces the nonlinear response of actin/fascin networks very well as will be demonstrated in the following. Most probably, adjustments to the linker model have to be made in order to capture differing linker behavior as well.

### 6.4.3 Simulation of nonlinear network viscoelasticity

All core parameters are chosen according to specifications given in Section 6.2.1. However, a few of those parameters deviate from the general setup. The shear amplitude is set to  $\hat{\gamma} = 30\%$  in case of the sweep through different shear rates at a fixed off-rate  $k_{\text{off}} = 3 \text{ s}^{-1}$ , which represents the first of two numerical studies conducted in this section. Here, four different shear rates  $\dot{\gamma} = d\gamma/dt \in \{0.125, 1.25, 6.25, 12.5\} \text{ \%}/\text{s}$  corresponding to an experiment in [134] are used. For two further parameter studies, the shear rate is fixed to the respective shear rates  $\dot{\gamma} = 6.25 \text{ \%}/\text{s}$  and  $\dot{\gamma} = 0.625 \text{ \%}/\text{s}$ , while the off-rate is varied on the interval  $k_{\text{off}} \in [0.01 ; 10] \text{ s}^{-1}$ . Due to the low values of  $k_{\text{off}}$ , the shear amplitude is increased to  $\hat{\gamma} = 35\%$  in order to capture large strain effects at lower off-rates as well. For all simulations, the same initial network geometry is used to ensure comparability. The network evolves until  $t_0 = 1500 \text{ s}$  and is then sheared according to the Dirichlet displacement pattern introduced in Section 6.2.2. The strain rates imply times  $\tilde{t} \in [2 ; 200] \text{ s}$ , during which prescribed nodal Dirichlet values impose the shear deformation. Further information on the parametrization of the simulation are provided in appendix C.

In [133], the effect of forces acting on linker molecules is pointed out. They are expected to play an important role in experiments involving large strains as they influence chemical association and dissociation processes. Bell's equation (4.3) is deemed an adequate model for force-dependent reaction kinetics. The corresponding characteristic distance of the reaction

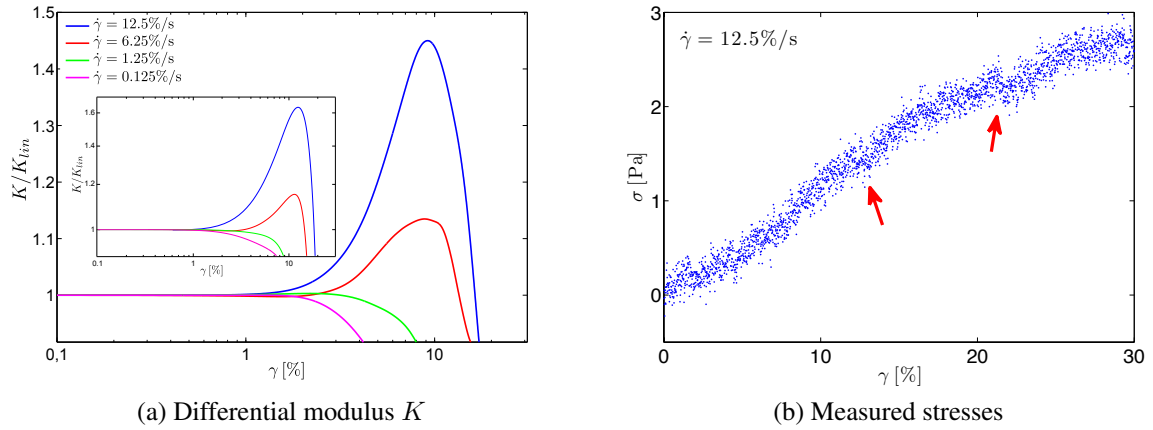


**Figure 6.12** Nonlinear shear experiment at four different strain rates  $\dot{\gamma}$ . (a) Differential modulus  $K = \partial\sigma/\partial\gamma$  over strain  $\gamma$ . At low  $\dot{\gamma}$ , the network has time for restructuring and stress release. Transient crosslinks lead to a reduction of  $K$  at high  $\gamma$ . At high  $\dot{\gamma}$ , the decrease of  $K$  at high  $\gamma$  stems from bond rupture. The inset shows analogous experimental results for an actin/fascin network at a molar ratio  $R = 0.1$  [134]. Matching curve colors represent data at the same  $\dot{\gamma}$ . The nonlinear rheology of actin/fascin bundle networks is captured well by the numerical model. (b) Measured stresses at  $\dot{\gamma} = 12.5\%/s$  showing stress drops at  $\gamma \approx 12\%$  and  $\gamma \approx 22\%$  due to ripping of linkers (red arrows).

variable is set to  $\Delta x = 10$  nm to account for the higher likelihood of disruption of a strained chemical bond as compared to an unstrained one.

The shear deformation is applied by means of a linear displacement profile mapped onto Dirichlet nodes at  $z = H$  with peak value  $\hat{u} = \hat{\gamma}H$  (cf. Equation (6.6)). The resulting stresses are treated according to Equation (6.9). A list containing the most important values for nonlinear viscoelastic simulations is provided by Table D.11.

#### 6.4.4 Effect of strain rate variation

The results of nonlinear shear experiments in computer simulations and in vitro are compared and remarkable similarities are found (compare Figure 6.12 and its inset). The onset of nonlinear mechanical behavior can be pinned to a critical strain  $\gamma_c = 1.5 - 2\%$ . For the two higher strain rates, hardening of the network is detected up to strains around  $10\%$  increasing modulus  $K$  by up to  $\sim 45\%$  for  $\dot{\gamma} = 12.5\%/s$  for the simulated case and  $\sim 60\%$  in the experiment. The two lower strain rates by contrast exhibit strain-weakening with their differential moduli decreasing beyond  $\gamma_c$ . When compared to in vitro experiments from [134], the strain-rate dependent transition from strain-hardening to strain-softening is analogous, which means that the mechanism causing this transition is captured by the numerical model. Figure 6.12b shows the development of measured stresses for shear displacements up to  $\hat{\gamma} = 30\%$  at the highest strain rate  $\dot{\gamma} = 12.5\%/s$ . Clearly, an inflection point can be seen at strains around  $10\%$ , beyond which the stress signal begins to flatten. At  $\gamma \approx 12\%$  and  $\gamma \approx 22\%$ , significant drops in the stress signal are detected, which stem from linker unbinding events. The first incident occurs at strains close to the peak stiffness of the network and contributes to the rapid decline after  $\gamma_m \approx 10\%$ . In order to investigate further, the distances of initially linked binding site pairs are evaluated (Figure 6.13). In Figure 6.13a, four characteristic developments for the distance between initially crosslinked binding sites are shown. The majority of crosslinks remains intact during the entire

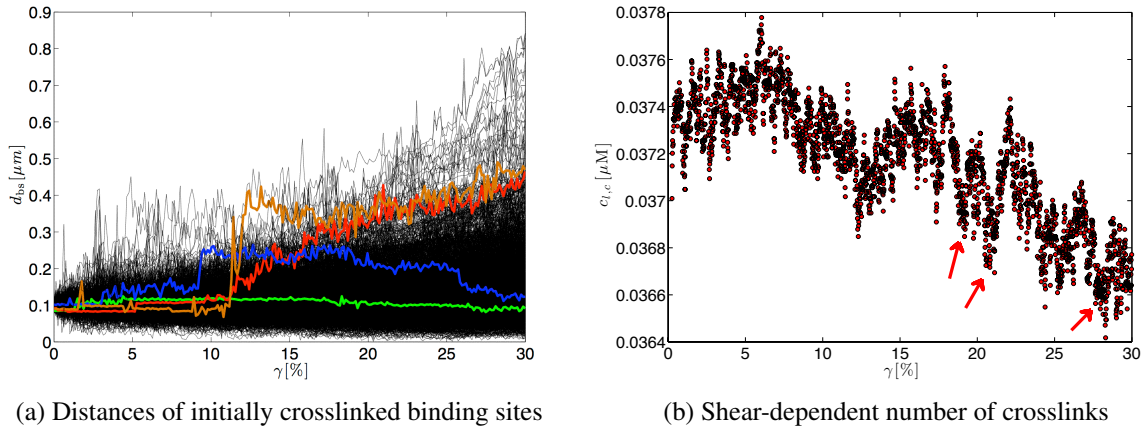


**Figure 6.13** (a) Distances of binding site pairs that were initially crosslinked at the beginning of shear displacement at  $\dot{\gamma} = 12.5\%/s$ . The initial value of  $0.1 \mu\text{m}$  represents the mean linker size  $R_l$ . Colored paths mark binding site pairs that remain close (i.e. linked) (green), that are ripped apart spontaneously at  $\gamma \approx 8\%$  (blue) and  $\gamma \approx 11\%$  (brown), as well as a binding site pair that is moved apart after having been unlinked without large ripping forces. (b) Crosslink concentration  $c_{l,c}$  plotted over shear  $\gamma$ . Overall, shearing reduces the total number of doubly bound linkers. Red arrows mark places, where larger numbers of crosslinks fail in short succession. Some of those crosslinks are partly recovered.

course of the experiment, which is represented by the green curve, that stays close to the linker size  $R_l$ . Then there are linkers, that rip under the influence of large forces acting on them. Such cases are shown by the blue and the orange curve. The corresponding pairs of binding sites remain close to each other until the force-dependent dissociation rate constant  $k_{\text{bell}}$  increases such that the bond eventually rips. Tension is built up in the corresponding filaments, which is released instantaneously upon ripping. The distance between the two binding sites increases immediately to about four times the linker size. Bond rupture events such as this one characterize the mechanical behavior of networks at large strains. Finally, there are *uninvolved* linkers, that unbind simply due to the equilibrium off-rate  $k_{\text{off}}$ . The distance over strain of one pair of binding sites, that was initially crosslinked by such a linker, is highlighted in red (Figure 6.13a). The reason for the continuous growth of distance between these two binding sites is that at least one of them lies on a filament sheared by imposed Dirichlet displacements.

The total number of detached crosslinks is small compared to the total number of crosslinks between filaments. The net loss of crosslinks until reaching the terminal value  $\hat{\gamma}$  amounts to only  $\sim 2\%$  ( $\sim 100$  linkers). However, there are sudden drops of more than 50 linkers within very small strain intervals. Such collective rupture events in bundles have been predicted recently using a simplified model [74]. In Figure 6.13b, three such events can be seen at  $\gamma \approx 17\%$ ,  $22\%$ , and  $26\%$ , where  $\sim 80$  linkers each fail successively (marked by red arrows). This observation supports the hypothesis of an initial bond failure that is followed by multiple consecutive bond failures due to a distribution of the same mechanical load to a decreasing number of linkers. Each sudden decrease in crosslinks is followed by a phase of recovery. The number of crosslinks rises again without reaching the numbers prior to rupture. After ripping, the network structure finds a new temporary state of mechanical equilibrium. The ruptured links remain singly bound in the computational model and seek to rebind, which leads to an increased probability of crosslink formation in the area of rupture. At  $\sim 22\%$  shear, an especially pronounced stress release event is recorded (Figure 6.12b).

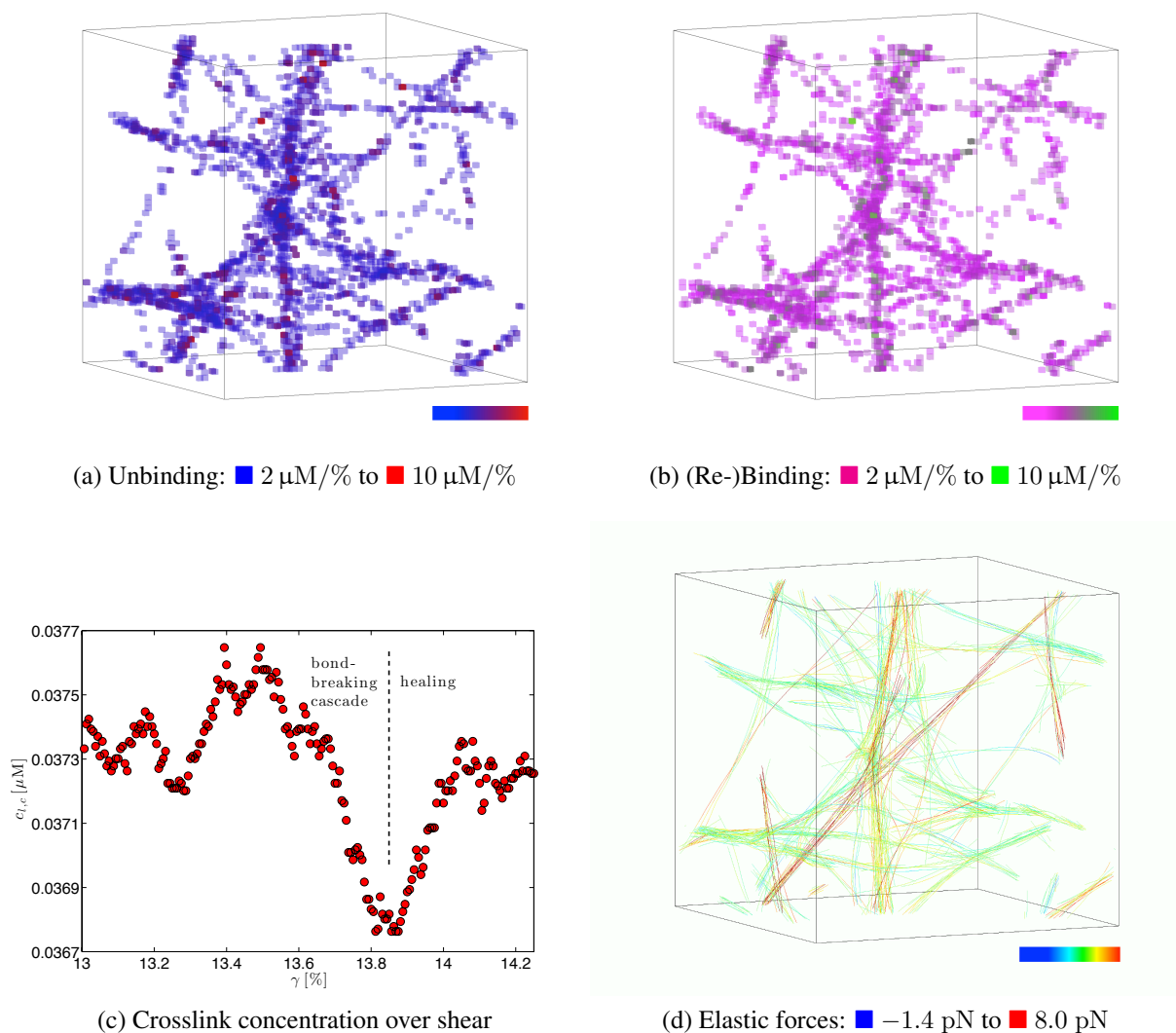


**Figure 6.14** Spatial maps of unbinding events (a), (re)binding events (b), as well as the development of crosslink concentration  $c_{l,c}$  as a function of the imposed shear (c). The strain rate for this sample is  $\dot{\gamma} = 12.5\%/s$ . The time scale of both the bond-breaking cascade and the healing process is approximately 0.03 s. The data shows that there are hotspots of unlinking events within bundles. After breaking, there are healing hotspots at the corresponding positions in the network. In (d), the elastic force magnitudes are depicted, pointing out locations of compressive forces ( $F < 0$ ) and tensile forces ( $F > 0$ ). The color scale

The question remains, in what way the crosslinks fail at large strains. Experimental data on single unbinding events is difficult, if not impossible, to obtain. Drawing such kind of information from simulations, however, is easy. One simply has to record all binding and unbinding events occurring over the course of the entire shear ramp and map these events to their respective location within the volume. An excerpt of the acquired data is shown in Figure 6.14. In a shear interval of 1.25%, unbinding and binding events are mapped to their spatial positions. Counting the number of occurring unbinding and binding events allows for the calculation of a local event intensity. At large shear deformations, linkers are increasingly strained, which influences their off-rate in accordance to Bell's model. The unbinding intensity according to Figure 6.14a is more or less uniformly distributed, meaning that a major part of the crosslinks does not experi-

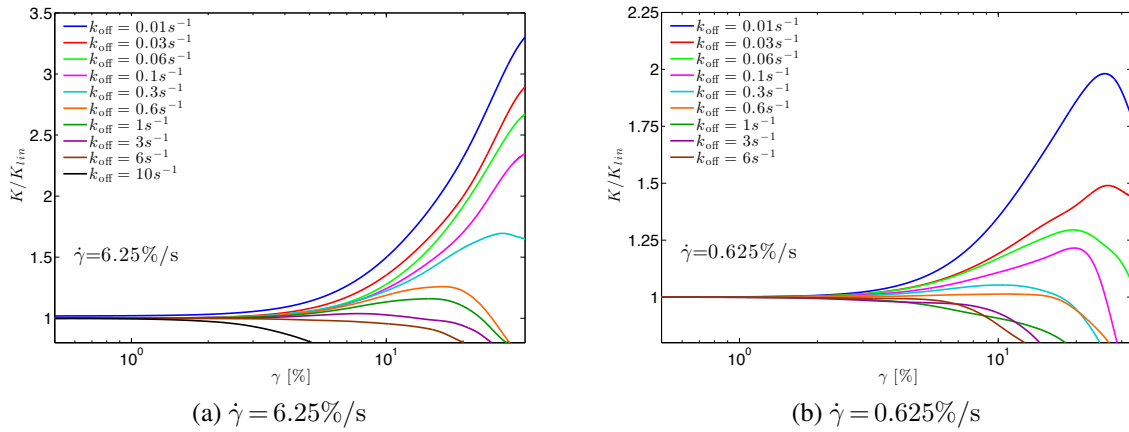


**Figure 6.15** Tuning the chemical affinity of the linker-filament bond by means of the dissociation rate constant  $k_{off}$  affects the nonlinear response. With increasing off-rate, the nonlinear response of the bundle network can be tuned from strain-hardening to strain-softening behavior. (a) For  $\dot{\gamma} = 6.25\%/s$ , the transition from hardening to weakening is located at  $k_{off} \approx 6s^{-1}$  (between the purple and brown curve). (b) Keeping all parameters (and the geometry), the same transition is shifted to a lower  $k_{off} \approx 0.6\%/s$  for  $\dot{\gamma} = 0.625\%/s$  (orange curve)

ence an increased off-rate due to strain. However, there are a few hotspots of linker unbinding as the illustration clearly shows, where the unbinding intensity is about five times higher than elsewhere. These places happen to be heavily strained locations judging by the magnitudes of the elastic forces in Figure 6.14d. When the first crosslink ruptures, the load that was carried by this crosslink until then, is distributed to neighboring linkers, which increases their individual rupture probability. As a result, linkers surrounding the initial rupture site begin to detach as well, which initiates a cascade of unbinding events as predicted by [74]. These cascades occur predominantly within bundles.

At some point, a new transient state of mechanical equilibrium of the network is found and the unbinding cascade terminates. The linkers, that have been previously detached by force, have returned to being potential crosslinks. The preceding avalanche of linker unbinding events has led to a local excess of singly bound linkers, that now seek to rebind. Unbinding hotspots become rebinding or healing hotspots (Figure 6.14b). The loss of crosslinks is replenished by the very same linkers, that were detached earlier (Figure 6.14c). However, no total recovery is observed, which can be understood in terms of the considerations presented with respect to the bond-breaking frequency regime of linear bundle rheology (cf. Section 6.3.2).

### 6.4.5 Effect of the dissociation rate constant

It is postulated, that variation of the chemical affinity of the filament-linker bond has a similar effect on the nonlinear response as the variation of strain rate since both quantities are time-dependent. In other words, it should be possible to find different pairings  $k_{off}/\dot{\gamma}$  that lead to the same stiffening or softening behavior.

The examination of the differential modulus and its development for different  $k_{off}$  is shown in Figure 6.15. A seamless transition from strain-hardening at low  $k_{off}$  to strain-softening at high  $k_{off}$  is observed by gradually tuning the off-rate from  $k_{off} = 0.01 s^{-1}$  to  $10 s^{-1}$ . Results at two different different shear rates  $k_{off} = 6.25\%/s$  and  $k_{off} = 0.625\%/s$  are shown. Whether

a transiently linked network structure stiffens or softens depends in a nontrivial way on the ratio  $k_{\text{off}}/\dot{\gamma}$ . Above  $k_{\text{off}} = 6 \text{ s}^{-1}$ , the network softens when strained with  $\dot{\gamma} = 6.25\%/s$  (Figure 6.15a). Below this value, first a stiffening response is recorded marked by the ascent of the differential modulus for growing strains beyond  $\gamma_c \approx 1 - 2\%$ . After reaching a maximal value at strains between 10 - 25% depending on the respective off-rate,  $K$  decreases again hinting at an ongoing “material failure” due to force-induced bond breaking events. For off-rates  $k_{\text{off}} < 0.1 \text{ s}^{-1}$ , the descending part of  $K$  is not reached. An identical sweep is conducted using the same values for  $k_{\text{off}}$  as before, but at a lower strain rate  $\dot{\gamma} = 0.625\%/s$ . Its results are summarized in Figure 6.15b. The descending part of the differential modulus is now visible for all off-rates. The amount of stiffening is reduced for the lower off-rates up to  $k_{\text{off}} = 0.6 \text{ s}^{-1}$ , resulting in lower peaks in the differential modulus. At off-rates  $k_{\text{off}} \geq 0.6 \text{ s}^{-1}$ , the peak values  $K_m$  are approximately halved compared to the higher shear rate for this particular network geometry. Interestingly, the hardening-to-weakening transition occurs at  $k_{\text{off}} \approx 0.6 \text{ s}^{-1}$ , which translates to approximately the same ratio  $k_{\text{off}}/\dot{\gamma}$  as for the higher strain rate. Additional investigation could lead to a better understanding of the connection between loading velocity represented by  $\dot{\gamma}$  and chemical kinetics represented by  $k_{\text{off}}$ .

#### 6.4.6 Remark on computational aspects in the nonlinear deformation regime

A remarkable number of publications deals with phenomena in the regime of nonlinear deformation by means of computational analysis ([7, 21, 94, 123] and others). Several reasons come to mind why this might be the case. First and foremost, the nonlinear deformation regime is a research topic worth studying. However, there are secondary reasons of computational nature as well. Oftentimes, linker unbinding dynamics are omitted [218, 232] such that the time scales become almost irrelevant, basically leading to a free choice of the time step size. Consequently, results can be obtained rather quickly, especially, when network evolution is omitted as well (as in above references). Furthermore, there is evidence that the stretching out of the filaments’ bending modes, which increasingly occurs at high (bulk) strains, makes the problem good-natured in the numerical sense. The attempted argument is not quantitative in nature, but is rather based on qualitative but reproducible observations during simulation. Consider a beam with a statically defined support. The application of a lateral force causes the beam to bend; the movable support yields. As the axial stiffness of structures with a high slenderness ratio exceeds the bending stiffness by far, a numerical scheme has to resolve mechanical phenomena spread over a broad range of time scales in the dynamic case, which leads to a stiff problem. If, however, the beam has fixed supports on both ends, the beam’s axial stiffness dominates the reaction to the lateral force. The tendency towards rapidly varying solutions (e.g., due to buckling) is weakened. In the context of network simulations, this means that the more stretched out a network sample is, the more it is dominated by the axial reaction of single filaments (cf. [167]). Tension tends to stabilize the problem numerically, and, as a consequence, iterative schemes exhibit an improved convergence behavior. Larger load/time steps can be made. In a sense, this is one of the few cases, where a nonlinear problem is actually *easier* to solve and technically less demanding than the corresponding linear problem, e.g., in the form of the presented linear rheology simulations.

## 6.5 Conclusions

**Linear rheology of semiflexible bundle networks** The focus of this chapter lay on a theoretical and computational analysis of crosslinked, bundled semiflexible networks. The investigations have lead to a more general understanding of the rheology of such networks and have elucidated the origins of the mechanical behavior of bundle networks, which are distinct from networks consisting of single semiflexible filaments. Semiflexible bundle networks play an exposed role in cellular mechanics [184], where they enable cell migration by forming stress fibers, support cell division and play an important role in sensory organs.

The linear rheology of semiflexible bundle networks was found to be divided into three distinct frequency regimes, each regime being dominated by one or several characteristic phenomena. The postulates at the beginning of this chapter may now be considered proven.

- (I) The high-frequency response is determined by the dynamics of single bundles. Their effective bending moduli depend on geometric properties such as the length of the bundle as well as the number of single filaments which make up the bundle. Eventually, these influences explain the newly discovered universal scaling behavior.
- (II) At intermediate frequencies, three effects can be seen as main contributors to a non-universal network rheology. There is a newly discovered dissipative process caused by a shear-induced reduction of the total number of crosslinks. Furthermore, it could be shown that the rheology at intermediate frequencies is strongly depends on the individual sample geometry. Finally, the reaction kinetics of the linker/filament bond determine the frequency range and the ratio between viscous and elastic effects.
- (III) For low frequencies, another, yet equally universal scaling behavior has been confirmed. The rheology is determined by the dissolution of bundles and large-scale rearrangements driven by equilibrium fluctuations at higher linker off-rates and non-equilibrium network evolution at lower off-rates.

**Nonlinear viscoelasticity** In the second part, the nonlinear viscoelastic response of bundle networks has been investigated. In the nonlinear regime, the generalization of the mechanical influence of linkers becomes more difficult as the specificities of different linkers become more pronounced. The *in silico* model of the linker exhibits a behavior similar to that of the linker fascin. Upon imposition of large shear deformation, force-induced unbinding of linkers is observed. Stress drops are directly linked to multiple consecutive bond breaking events. The failure of a few linkers leads to additional loading of surrounding linkers, which as a consequence tend to fail as well. *Weak spots* in the network structure are located within bundles as the above investigations imply. Collective cascades of unbinding events are generally followed immediately by a partial recovery of the structure in terms of the number of mechanical connections between its filaments. This *healing* procedure is rapid and occurs on time scales comparable to the rupture event. Recovery in parts and an overall decreasing number of crosslinks in the network structure lead to a deterioration of its mechanical properties, which is represented by the eventual decline of the differential modulus  $K$ .

**Potential engineering applications** In the thriving field of biomedical engineering, predictive simulations promote the understanding of biological materials, estimate the mechanical behavior of organs, or support medical therapy. Many applications share the need for information on the reaction of soft tissue to mechanical loading, which is mostly provided by constitutive laws based on a strain energy formulation (cf. [84] for a comprehensive library of strain energy formulations). Among currently proposed material laws, there are some that already account for cytoskeletal fiber orientation in a rather generic way [83, 170, 212], all of which suffer from a lack of information on the *actual* network architecture. Using micromechanical simulations such as the ones presented here, one could generate a mechanical sample of a network through self-assembly and determine its mechanical behavior. Figure 6.12b already hints at the general capability of providing mechanical data (shear stresses in this case) similar to [212, Figure 8], where experimental results and continuum model predictions are compared. In principle, one could establish a library of constitutive laws reflecting the distinct mechanical features of different network architectures, thus enabling more detailed models of, e.g., cellular growth or cell migration on the basis of a homogenized continuum approach [170, 211]. A more costly, but also more flexible, alternative would be the design of a multi-scale approach including Brownian dynamics simulations at the bottom level in order to provide material parameters for constitutive laws on higher levels, i.e., larger length scales. With present day hardware, however, the feasibility of such an approach is questionable in view of the fact that the simulation of network self-assembly alone already requires several days of computation time.

Leaving the immediate neighborhood of cellular mechanics, novel synthetic materials such as composites made of carbon nano-tube bundles [117] or the development of molecular machines [171] might substantially profit from the new insights.

# 7 Conclusions and outlook

## 7.1 Conclusions

This summary comprises the methodic and the scientific progress, which have been achieved in the course of this thesis. Two superior goals have been formulated at the beginning of this doctoral project. The first goal was the development of a computational framework that enables the simulation of semiflexible biopolymer networks on time and length scales relevant to cytoskeletal dynamics. Systems with a spatial expansion of up to  $10^3 \mu\text{m}^3$  have been simulated on time intervals of several hundreds up to several thousands of seconds. The second goal was the application of the newly developed approach to biophysical problems. Both goals have been achieved but, as always, more is to come than what lies behind. In two separate sections, the individual achievements will be named and briefly summarized.

### 7.1.1 Methods

At the starting point of this thesis, the fully functional BD/FE single-filament model of [36–38] was available. First steps towards the simulation of networks had already been undertaken.

The parallelization of the serial code has marked a preliminary, yet necessary first step towards the computational framework in its present state. As a consequence, the simulation of networks has become computationally affordable. In Chapter 2, the explicit simulation of the second species, the linker, and its Brownian dynamics has been introduced to the computational model, without which none of the self-assembly phenomena could have been observed. This rather inconspicuous detail has been pivotal for all subsequent steps. The increased computational effort of matching potential binding partners is counteracted by efficient search algorithms such as octree data structures and geometrical binning strategies. The chemical interaction between filaments and linkers has been designed to replicate the reaction kinetics of well-known chemical bonds between filaments and various linkers (cf. [133, 152] for reaction rate constants). Furthermore, the introduction of a confined volume by means of periodic boundary conditions has enabled the examination of network evolution and rheological simulations.

Chapter 3 has introduced two model extensions, one for filaments and one for linkers, which decouple the chemical from the mechanical resolution, enabling tightly stacked binding site topologies. These modeling steps were motivated by the following shortcomings of the original model. While the coarse-graining of filaments increases the computational efficiency of single filament simulations without noticeable drawbacks to filament dynamics, it abandons information on the microstructure of the filament. Linkers, which exclusively establish node-to-node connections, mask the model's true potential in the following way. Even if a coarser filament discretization is viable from the mechanical point of view, the consequent reduction of chemical binding opportunities affects reaction kinetics, which is unacceptable. Conversely, the refinement of the chemical resolution to monomer level leads to an insensible mechanical resolution.

Therefore, the extended filament model offers interpolated binding site positions along its centerline. In addition, the reaction volumes were further parametrized in order to account for binding site orientations according to the orientation of the filament subunits. In case of F-actin, binding sites are helically oriented. Having included this modeling feature, it is now possible to account for mechanical effects that originate from the chiral structure of the filaments. The linker model has been capacitated to establish connections at arbitrary positions between two finite element nodes of a filament. This modeling step has been accomplished by tying the positions and cross section orientations of a BFE with two *virtual* nodes to the interpolated positions and cross section orientations of two filament elements. In contrast to other mesh tying methods, no additional DOFs have been introduced. Rather, the contribution of the two virtual nodes is distributed to the four *real* nodes of the filament elements. To this end, one exploits the mathematical instruments for a consistent treatment of finite rotations in  $\mathbb{R}^3$  of the nonlinear, geometrically exact beam formulation by [103] as well as conventional linear finite element interpolation schemes. The extended models for filaments and linkers are complementary and develop their full potential only in conjunction with each other. The proposed extensions have been implemented and validated. Apart from being able to examine the self-limiting nature of bundles, one may now create previously unobservable network morphologies, namely a homogeneous isotropic network at very high linker concentrations. This network is reminiscent of actin/HMM networks. By allowing for the occupation of two binding sites on a filament by one and the same linker, the effect of decoration of filaments by HMM is mimicked. First rheological results show good qualitative agreement between simulation and experiment. Although being of only minor biological relevance, passive actin/HMM networks (i.e., HMM does not act as a motor) have posed as a model system in order to examine the effect of transient crosslinking on network mechanics [137].

Chapter 4 has introduced a simplified model of a non-processive motor based on the developments of the preceding Chapters 2 and 3. The motor model has been parametrized to resemble the activity of a single myosin head. The enzymatic cycle of myosin II has been translated into modeling requirements and has been realized by means of a contractile beam, which acts according to the mechanically relevant states of ATP hydrolysis. The modeling equivalent to the myosin power stroke is achieved by a contraction and a superimposed rotation of the motor beam element about its mechanical joint. Both the contraction and the rotation are achieved by concerted changes of the motor's mechanical reference configuration. As a result, a contractile force and a restoring moment are induced upon alteration of the reference state. Kinematically, the proposed motor model is similar to the swinging cross-bridge model (cf. [195]). The motor model has been validated with the help of *in silico* motility assays. Having used a sensible set of motor parameters, the observations made in *in vitro* motility assays have been reproduced for the quasi-1D and the two-dimensional case.

### 7.1.2 Biophysical applications

Chapter 5 documents the first major application of the computational approach to a biophysical problem: an equilibrium phase diagram of semiflexible polymer has been established. This phase diagram incorporates the fundamental thermally equilibrated morphologies of cross-linked, semiflexible biopolymer networks. Depending on the linker concentration and the linker species, the emerging network architecture can be predicted. Furthermore, the driving influence

behind network formation has been found. Filament entropy and linker entropy have been determined as the main factor for filament aggregation. A linker seeks to maximize the number of potential crosslinking sites in its vicinity. A thermally excited filament seeks to fluctuate as freely as possible. The maximization of the one leads to the minimization of the other. A maximal number of crosslinking possibilities is achieved when filaments are maximally ordered and vice versa. In addition, the cluster has been determined as an equilibrium structure rather than a kinetically trapped intermediate state for a linker with orthogonal angle preference. This finding does not contradict the claim of actin/ $\alpha$ -actinin and actin/filamin clusters to be kinetically trapped structures. Furthermore, all phase transitions of the model system are of first order with the exception of the transition from the hexagonal cluster to the hexatic lamella.

In the final chapter (Chapter 6), comprehensive studies have led to the postulation of a bundle-specific rheology with universal properties. Universal scaling behaviors have been found at very high and very low frequencies. At high frequencies, the dynamics of single bundles dominate rheology. In between, there is a non-universal regime, which reflects the network geometry and the reaction kinetics of the filament/linker bond. At low frequencies, large-scale collective motion, bundle dissolution and non-equilibrium aging phenomena dominate. Experimental data at low frequencies exists as well as measurements in the non-universal, intermediate-frequency regime. The experimentally accessible frequency range for most biological linkers lies in the intermediate-frequency regime, where their specificities are more pronounced. Excellent agreement with experimental data is found for the low-frequency regime, where the  $\omega^{1/2}$  scaling has been recovered. The intermediate-frequency regime of the simulated linker appears to be similar to that of the physiological linker fascin. There is no experimental data available on the high-frequency regime such that the novel scaling behavior found there serves as a prediction and requires experimental validation. Preliminary simulations of the nonlinear viscoelasticity of bundle networks have been performed. They demonstrate that, depending on the shear rate, i.e., an external influence, strain-hardening or strain-weakening occurs. The same behavior can also result from a variation of intrinsic parameters like the affinity of the filament/linker bond. It is speculated that the ratio of shear rate and dissociation rate constant  $\dot{\gamma}/k_{\text{off}}$  could be an interesting parameter in order to pin down the boundary between hardening and weakening.

## 7.2 Outlook

In analogy to the conclusions, the outlook is best divided into two main parts: a methodic outlook and an outlook for future biophysical applications. By contrast, possible engineering applications are discussed as well.

### 7.2.1 Methods

The most pressing matter is the development of an efficient and, more importantly, robust beam contact formulation. The evaluation of beam contact is a highly nontrivial problem as the extremely high slenderness ratios of biopolymer filaments ( $L_f/(2\sqrt{A_f/\pi}) > 800$ ) lead to stiff problems. The deterioration of the convergence of the Newton scheme attributed to a multitude of simultaneous contact pairs is in dear need of a remedy. Furthermore, randomly contacting pairs of beams inevitably entail off-diagonal entries in the global stiffness matrix, leading to a de-

terioration of the matrix' condition number. This exacerbates the numerical performance. In general, a transition from Penalty and Augmented-Lagrange methods to a Lagrange-multiplier-based contact formulation would be of advantage. On the one hand, the use of a Lagrange multiplier approach enables the exact enforcement of contact constraints. On the other hand, such an approach alleviates the unsatisfactory reliance of Penalty and Augmented-Lagrange approaches on heuristic parameters. Potential applications with an improved beam contact formulation will be given in the next section.

The second large topical complex deals with the replacement of the currently used Reissner beam element formulation by a more suitable Kirchhoff beam formulation. As elaborated in Chapter 3, the Kirchhoff beam offers several numerical advantages of secondary nature. The most striking improvement, however, is the  $C^1$ -continuous description of the beams centerline by means of higher-order Hermite polynomials. This feature improves the geometric approximation of the beam geometry compared to Reissner beam elements. In conjunction with the extended linker model from Chapter 3, the Kirchhoff beam formulation represents a powerful tool for the simulation of biopolymer networks. In fact, this joint approach has the potential of becoming the referential computational model for this kind of problem. The better geometrical approximation as compared to a Reissner beam element can be exploited by choosing a coarser discretization. Due to the capability of the linker element to bind at arbitrary positions along the filament, the reduction of global DOFs does not result in a loss of chemical detail. In analogy to the contact problem, the optimization of the linear solution procedure emerges as a secondary problem. Finally, in view of a potential refinement of the chemical resolution to the level of single monomers, efficiently parallelized search algorithms are required to handle the additional complexity due to a significantly higher number of potential binding partners.

The model of the molecular motor can be enhanced in order to reproduce the activity of more complex motor units such as the myosin thick filament. The introduction of a distinction between active motors and passive linkers for the observation of the cooperative behavior of linkers and motors can be realized without major problems. On a methodic level, one can consider switching to a Lagrange-multiplier-based constraint enforcement. Lagrange multipliers entail a higher computational effort due to the introduction of additional unknowns. However, this measure allows for a more flexible formulation of constraints, which could be useful for the modeling of more complex (processive) motor activity.

A further enhancement of the filament model can be achieved by the incorporation of interaction potentials between a pair of filaments or between filaments and other particles, e.g., linkers or other microscopic objects. Various types of intermolecular interactions are known (cf. [101]) and can be approximated by interaction models such as the Lennard-Jones potential or Coulomb's law.

Finally, untapped computational potential undoubtedly lies with a more elaborate parallelization by means of an adequate load-balancing. A periodic re-evaluation of processor-specific subdomains of the global problem can improve the computational performance of the method.

### 7.2.2 Biophysical applications

A multitude of possible paths for continued and expanded research activities exist.

The most immediate avenue of future research is the nonlinear viscoelastic behavior of biopolymer networks. First efforts on this topic have been made in Chapter 6 for the special case of

bundle networks. These efforts demonstrate the potential of the available method and should thus be put to use in future biophysical studies.

The nonlinear, geometrically exact beam formulation, that is the mechanical foundation of the approach, is not limited to modeling semiflexible filaments. Future studies can thus involve microtubule networks, networks of intermediate filaments, or, as a matter of fact, any type of fiber network that comes to mind. Staying in the biological context but leaving the cell, connective tissue made of collagen fibers could be a possible future topic of research.

In view of the progress made in Chapters 2 to 4, another area of research in the future are so-called *active networks*, in which molecular motors massively influence the mechanical properties. If a passive linker species is added on top, the network stiffens by over two orders of magnitude due to the joint effect of motors and linkers [119, 157]. By contrast, motors have also been found to fluidize networks under certain conditions [95]. Considerable theoretical work is being done on active gels (cf. [104]) such that simulations could in principle serve the same purpose as in Chapter 6, where a fruitful interplay of theory and simulation has resulted in new physical insights. Apolar assemblies of actively contracting bundles [132, 205] represent a related, but more specific topic, where the BD/FE simulations may promote a better physical understanding.

The methods developed in Chapter 3 enable the simulation of self-limiting bundle networks, which are constituted by small linkers like fascin [23]. Theory on this type of bundle system suggests that bundles do not grow beyond a certain diameter because of the competing influences of bundle twist and single-filament bending [80]. Novel insights into the self-assembly and the intrinsic mechanical properties of such hexagonally packed bundles may be gained. However, due to the tight packing of filaments, excluded volume effects are likely to matter. Therefore, as stated in Section 7.2.1, improved computational approaches to modeling the mechanical contact of slender continua are mandatory.

Another benefit of a robust beam contact formulation is the ability to study collective motion phenomena. The high-density motility assays of [183] could be reproduced as a first step, and then lead to extended analyses.

Given the incorporation of intermolecular interactions into the filament model, the effect of electrostatic charges on the diffusive behavior of molecules could be studied.

Finally, on a remote but equally interesting topic, the existence of a fundamental, but previously unknown type of *Casimir interactions* due to thermal fluctuations can be examined and quantified [106].

### 7.2.3 Engineering applications

The computational model proposed in this thesis can be used to generate information on network architectures and their respective mechanical properties in analogy to the procedures in Chapters 5 and 6. With this information at hand, the development of tailor-made continuum approaches modeling biological materials on the tissue level could be supported. Distinct network morphologies entail distinct mechanical properties as has been demonstrated in Chapter 6. Therefore, one could account for the cytoskeletal morphology by means of suitable, microstructurally informed constitutive laws. A library of material models, that offers such constitutive laws, would most likely be of advantage when modeling certain application-specific properties of the highly dynamic and versatile *material* that is the cell [108].

The proposed methods have already proven their potential to predict material properties, albeit within a limited scope. There is no reason why the method itself should not be applicable to other fibrous materials as well. Changing the filaments' and linkers' material properties in accordance to the a priori knowledge of the network constituents can enable the simulation-based design of a broad spectrum of materials, that rely on interconnected fibers.

# A Linearized stiffness matrix of the extended linker element

In Chapter 3, a method has been introduced, that ties two-noded beam elements to an arbitrary position along the interpolated geometry of other beams. The formulation of all involved beams is based on the work of [103]. Here, the linearized contributions to the tangential stiffness matrix of the tied beam element are summarized. These terms eventually find their way into equation (3.30) and enter the modified linearized residual as stated by equation (3.32).

**Elastic contributions** The assembly of the stiffness matrix is done best by starting at a node-wise description owing to the node-based interpolation of rotations. The submatrix of the element stiffness matrix for nodes  $j = 1, 2$  and  $k = 1, 2$  reads

$$\begin{aligned} \mathcal{K}_v^{[jk]} &= \int_0^L \begin{bmatrix} \mathbf{l}_t^{[j]'} \mathbf{l}_t^{[k]'} \mathbf{C}_f & \mathbf{l}_t^{[j]'} (\mathbf{C}_f \dot{\mathbf{x}}' - \dot{\mathbf{n}}) \mathbf{l}_r^{[k]} \\ \mathbf{l}_t^{[k]'} \mathbf{l}_t^{[j]'} (\dot{\mathbf{n}} - \dot{\mathbf{x}}' \mathbf{C}_f) & \mathbf{l}_t^{[j]'} \mathbf{C}_m \mathbf{l}_r^{[k]} - \mathbf{l}_t^{[j]'} \dot{\mathbf{m}} \mathbf{l}_r^{[k]} + \mathbf{l}_t^{[j]'} \dot{\mathbf{x}}' (\mathbf{n} - \mathbf{C}_m \dot{\mathbf{x}}') \mathbf{l}_r^{[k]} \end{bmatrix} ds \quad (\text{A.1}) \\ &= \begin{bmatrix} \mathcal{K}_v^{uu} & \mathcal{K}_v^{u\vartheta} \\ \mathcal{K}_v^{\vartheta u} & \mathcal{K}_v^{\vartheta\vartheta} \end{bmatrix}^{[jk]} \in \mathbb{R}^{6 \times 6} \end{aligned}$$

with the stresses  $\dot{\mathbf{n}} = \mathbf{\Lambda} \mathbf{C}_f \boldsymbol{\gamma}$  and  $\dot{\mathbf{m}} = \mathbf{\Lambda} \mathbf{C}_m \boldsymbol{\kappa}$ . The interpolation function  $\mathbf{l}_r^{[k]}$  is given by equation (3.24). Its derivative is

$$\begin{aligned} \mathbf{l}_r^{[k]'}(s) &= \mathbf{\Lambda}_R \left[ - \left( (\mathbf{T}^{-1}(\boldsymbol{\psi}_1(s)))' \mathbf{l}_t^{[k]}(s) \mathbf{T}(\boldsymbol{\psi}_1^{[k]}) + \mathbf{T}^{-1}(\boldsymbol{\psi}_1(s)) \mathbf{l}_t^{[k]'}(s) \mathbf{T}(\boldsymbol{\psi}_1^{[k]}) \right) \mathbf{v}^{[k]} + \right. \\ &\quad \left. + \left( (\mathbf{T}^{-1}(\boldsymbol{\psi}_1(s)))' \mathbf{l}_t^{[k]}(s) + \mathbf{T}^{-1}(\boldsymbol{\psi}_1(s)) \mathbf{l}_t^{[k]'}(s) \right) \mathbf{T}(\boldsymbol{\psi}_1^{[k]}) \right] \mathbf{\Lambda}_R^T. \quad (\text{A.2}) \end{aligned}$$

The matrices  $\mathbf{T}(\boldsymbol{\psi}_1)$  and  $\mathbf{T}^{-1}(\boldsymbol{\psi}_1)$  are given by equations (3.25) and (3.27), respectively. The linearized residual for the elastic part is given as

$$\text{Lin } \delta \Pi_{v,el}^{[jk]} = \delta \mathbf{d}_v^{[jk]T} \mathcal{K}_v \Delta \mathbf{d}_v^{[jk]} \quad (\text{A.3})$$

with the variation of the displacements  $\delta \mathbf{d}_v^{[j]} = (\delta \mathbf{u}_v^{[j]T} \quad \delta \boldsymbol{\vartheta}_v^{[j]T})^T$  of node  $j$  and the linearized displacements  $\Delta \mathbf{d}_v^{[k]} = (\Delta \mathbf{u}_v^{[k]T} \quad \Delta \boldsymbol{\vartheta}_v^{[k]T})^T$  of node  $k$ . Assembling the submatrices from equation (A.1) in to the element stiffness matrix  $\tilde{\mathcal{K}}_v$  for an element with two nodes, the stiffness matrix can be written as

$$\tilde{\mathcal{K}}_v = \begin{bmatrix} \mathcal{K}_v^{[11]} & \mathcal{K}_v^{[12]} \\ \mathcal{K}_v^{[21]} & \mathcal{K}_v^{[22]} \end{bmatrix} = \begin{bmatrix} \begin{bmatrix} \mathcal{K}_v^{uu} & \mathcal{K}_v^{u\vartheta} \\ \mathcal{K}_v^{\vartheta u} & \mathcal{K}_v^{\vartheta\vartheta} \end{bmatrix}^{[11]} & \begin{bmatrix} \mathcal{K}_v^{uu} & \mathcal{K}_v^{u\vartheta} \\ \mathcal{K}_v^{\vartheta u} & \mathcal{K}_v^{\vartheta\vartheta} \end{bmatrix}^{[21]} \\ \begin{bmatrix} \mathcal{K}_v^{uu} & \mathcal{K}_v^{u\vartheta} \\ \mathcal{K}_v^{\vartheta u} & \mathcal{K}_v^{\vartheta\vartheta} \end{bmatrix}^{[21]} & \begin{bmatrix} \mathcal{K}_v^{uu} & \mathcal{K}_v^{u\vartheta} \\ \mathcal{K}_v^{\vartheta u} & \mathcal{K}_v^{\vartheta\vartheta} \end{bmatrix}^{[22]} \end{bmatrix} \in \mathbb{R}^{12 \times 12}. \quad (\text{A.4})$$

This notation is inconvenient with respect to the displacement vector definition in equation (3.8), which groups translational and rotational rather than nodal submatrices. This inconvenience is readily overcome by reordering equation (A.4) such that

$$\mathcal{K}_v = \begin{bmatrix} \mathcal{K}_v^{uu} & \mathcal{K}_v^{u\vartheta} \\ \mathcal{K}_v^{\vartheta u} & \mathcal{K}_v^{\vartheta\vartheta} \end{bmatrix} = \begin{bmatrix} \begin{bmatrix} \mathcal{K}_v^{[11]} & \mathcal{K}_v^{[12]} \\ \mathcal{K}_v^{[21]} & \mathcal{K}_v^{[22]} \end{bmatrix}^{uu} & \begin{bmatrix} \mathcal{K}_v^{[11]} & \mathcal{K}_v^{[12]} \\ \mathcal{K}_v^{[21]} & \mathcal{K}_v^{[22]} \end{bmatrix}^{u\vartheta} \\ \begin{bmatrix} \mathcal{K}_v^{[11]} & \mathcal{K}_v^{[12]} \\ \mathcal{K}_v^{[21]} & \mathcal{K}_v^{[22]} \end{bmatrix}^{\vartheta u} & \begin{bmatrix} \mathcal{K}_v^{[11]} & \mathcal{K}_v^{[12]} \\ \mathcal{K}_v^{[21]} & \mathcal{K}_v^{[22]} \end{bmatrix}^{\vartheta\vartheta} \end{bmatrix} \in \mathbb{R}^{12 \times 12}. \quad (\text{A.5})$$

The following expressions for the viscous and stochastic contributions to the tangential stiffness matrix stem from [33, Appendix A.5], from which they've been adopted in a slightly varied notation in order to fit the conventions of this work.

**Viscous contributions** The translational viscous contribution to the tangential stiffness matrix is given by

$$\mathcal{D}_{v,t} = \int_0^L \mathbf{I}_t^T \left\{ (\gamma_{\parallel} - \gamma_{\perp}) [(\mathbf{x}'^T \dot{\mathbf{x}}) + \mathbf{x}'^T \dot{\mathbf{x}}_{\text{rel}}] \mathbf{I}'_t + \mathbf{D}_t \left[ \frac{\mathbf{1}}{\Delta t} - \frac{\partial \mathbf{v}}{\partial \mathbf{x}} \right] \mathbf{I}_t \right\} ds \in \mathbb{R}^{6 \times 6}. \quad (\text{A.6})$$

The rotational part is accounted for on the one hand by

$$\mathcal{D}_{v,r} = \int_0^L \mathbf{I}_t^T \left[ -(\mathbf{D}_r \dot{\boldsymbol{\theta}}) + \mathbf{D}_r \dot{\boldsymbol{\theta}} + \frac{1}{\Delta t} \mathbf{D}_m \mathbf{T}(\Delta \boldsymbol{\theta}) \right] \mathbf{I}_r ds \in \mathbb{R}^{6 \times 6}. \quad (\text{A.7})$$

The assembled matrix can be denoted as

$$\mathcal{D}_v = \begin{bmatrix} \mathcal{D}_{v,t} & \mathbf{0} \\ \mathbf{0} & \mathcal{D}_{v,r} \end{bmatrix} \in \mathbb{R}^{12 \times 12} \quad (\text{A.8})$$

**Stochastic contributions** Finally, stochastic contributions for the translational part

$$\mathcal{S}_{v,t} = \sum_{\text{IP}} \left[ \mathbf{I}_t \sqrt{\frac{2k_B T w_{\text{IP}} (\gamma_{\parallel} - \gamma_{\perp})}{\Delta t}} (\mathbf{x}'^T \mathcal{Z}_{\text{IP}}(0, 1) + \mathbf{x}' \mathcal{Z}_{\text{GP}}(0, 1)) \mathbf{I}'_t \right]_{\text{SIP}} \in \mathbb{R}^{6 \times 6} \quad (\text{A.9})$$

and the rotational part

$$\mathcal{S}_{v,r} = \sum_{\text{IP}} \left[ -\mathbf{I}_t \sqrt{\frac{2k_B T \gamma_a w_{\text{IP}}}{\Delta t}} \dot{\mathcal{Z}}_{\Lambda} \mathbf{I}_r \right]_{\text{SIP}} \in \mathbb{R}^{6 \times 6} \quad (\text{A.10})$$

with  $\mathcal{Z}_{\Lambda} = \boldsymbol{\Lambda} \mathcal{Z}_{\text{IP}}(0, 1)$ . The assembled matrix of the stochastic contributions has the form

$$\mathcal{S}_v = \begin{bmatrix} \mathcal{S}_{v,t} & \mathbf{0} \\ \mathbf{0} & \mathcal{S}_{v,r} \end{bmatrix} \in \mathbb{R}^{12 \times 12}. \quad (\text{A.11})$$

---

Eventually, the tangential stiffness matrix of the linearized problem reads

$$\mathbf{K}_v = \begin{bmatrix} \mathbf{K}_v^{uu} & \mathbf{K}_v^{u\vartheta} \\ \mathbf{K}_v^{\vartheta u} & \mathbf{K}_v^{\vartheta\vartheta} \end{bmatrix} = \begin{bmatrix} \mathcal{K}_v^{uu} + \mathcal{D}_{v,t} + \mathcal{S}_{v,t} & \mathcal{K}_v^{u\vartheta} \\ \mathcal{K}_v^{\vartheta u} & \mathcal{K}_v^{\vartheta\vartheta} + \mathcal{D}_{v,r} + \mathcal{S}_{v,r} \end{bmatrix} \in \mathbb{R}^{12 \times 12} \quad (\text{A.12})$$

and can be directly inserted into equation (3.30).



# B Methods

## B.1 Mechanical contact of beams

In Chapter 5, an Augmented-Lagrange regularization for frictionless normal contact has been applied to ensure minimal mutual overlap of filaments. Here, the most important aspects of this method will be briefly outlined. For a more thorough reading on the modeling of mechanical contact in simulations, the reader is referred to [129, 228].

**General description of contact and its weak form** The distance between the centerlines  $\mathbf{x}_1(s_1)$  and  $\mathbf{x}_2(s_2)$  of two beams with circular cross sections is minimal for exactly one pair of positions  $\{\tilde{s}_1, \tilde{s}_2\}$  if the centerlines are skew. The closest distance between two points along the centerlines is can be calculated as

$$d_{12}(s_1, s_2) = \min \|\mathbf{x}_1(s_1) - \mathbf{x}_2(s_2)\| = \|\mathbf{x}(\tilde{s}_1) - \mathbf{x}(\tilde{s}_2)\|. \quad (\text{B.1})$$

Having determined positions  $\tilde{s}_1$  and  $\tilde{s}_2$  by exploiting that the vector  $\|\mathbf{x}(\tilde{s}_1) - \mathbf{x}(\tilde{s}_2)\|$  is perpendicular to both  $\mathbf{x}'_1(\tilde{s}_1)$  and  $\mathbf{x}'_2(\tilde{s}_2)$ , the normal vector

$$\mathbf{n}_{12} = \frac{\mathbf{x}(\tilde{s}_1) - \mathbf{x}(\tilde{s}_2)}{\|\mathbf{x}(\tilde{s}_1) - \mathbf{x}(\tilde{s}_2)\|} \quad (\text{B.2})$$

can be determined. Furthermore, a distance function measuring the *gap* between the centerlines

$$g = \|\mathbf{x}(\tilde{s}_1) - \mathbf{x}(\tilde{s}_2)\| - r_1 - r_2 \quad (\text{B.3})$$

with beam radii  $r_1$  and  $r_2$  can be defined, which allows for the definition of the so-called *Karush-Kuhn-Tucker* (KKT) conditions of non-penetration

$$g \geq 0, \quad \lambda \geq 0, \quad g\lambda = 0 \quad (\text{B.4})$$

Skipping several steps, the variation of the contact potential required for a finite element discretization reads

$$\delta\Pi_\lambda = \sum_{n=1}^{N_c} \lambda_n \tilde{\mathbf{n}}_n^\top \underbrace{(\delta\mathbf{u}_{1,n} - \delta\mathbf{u}_{2,n})}_{\delta g_n} \quad (\text{B.5})$$

**Augmented-Lagrange regularization** The Augmented-Lagrange regularization is set between the simpler Penalty method and the exact enforcement of contact constraints by means of Lagrange multipliers. It reduces penetration by an iterative scheme, that adds up Penalty-like contact forces to the limit of an exact satisfaction of the non-penetration condition. This iterative

procedure is referred to as *Uzawa algorithm* (cf. [129, Chapter 6]) and updates the contact force of Uzawa step  $u+1$  by

$$\lambda^{\{u+1\}} = \langle \lambda^{\{u\}} - \epsilon^{\{u\}} g^{\{u\}} \rangle, \quad (\text{B.6})$$

where  $\langle . \rangle$  governs whether or not the update is applicable by distinguishing

$$\langle \lambda^{\{u\}} - \epsilon^{\{u\}} g^{\{u\}} \rangle = \begin{cases} \lambda^{\{u\}} - \epsilon^{\{u\}} g^{\{u\}} & , \text{ if } \lambda^{\{u\}} - \epsilon^{\{u\}} g^{\{u\}} > 0 \\ 0 & , \text{ else} \end{cases}, \text{ with } \lambda^{\{0\}} = 0. \quad (\text{B.7})$$

The variation of the Augmented-Lagrange contact potential is given by

$$\delta \Pi_{\lambda, \text{AL}} = \sum_{n=1}^{N_c} \langle \lambda^{\{u\}} - \epsilon^{\{u\}} g^{\{u\}} \rangle_n \tilde{\mathbf{n}}_n^T (\delta \mathbf{u}_{1,n} - \delta \mathbf{u}_{2,n}). \quad (\text{B.8})$$

The symbol  $\epsilon$  denotes the so-called *penalty parameter*, which represents the spring constant of the repulsive potential. If convergence is deemed slow, this parameter can be updated, i.e., increased, from one to the next iterative step. The subsequent steps of discretization and linearization of the weak form enable the use of this model for beam contact in a FE setting.

**Limitations** The Augmented-Lagrange approach to modeling the contact of beams has a few specific drawbacks but suffers from other, more general deficiencies as well. Apart from an increase of computational cost due to the introduction of an additional iterative loop, the choice of the initial penalty parameter  $\epsilon_0$  as well as possible update procedures  $\epsilon_{i+1}$  are heuristic and thus problem-specific. The approach does not solve the general problem of undetected crossovers between iterative steps when dealing with highly slender beams. Applied to problems with a large number of contact pairs, the Uzawa algorithm is often caught in intermediate states at unsatisfying residual penetrations causing non-convergence. Lastly, the approach in its current form is unable to account for the special case of contact between parallel beams. Although this scenario is unlikely to occur, it is of advantage to model parallel contact as well in view of the possible application of beam contact to bundles made of parallel filaments, which are ubiquitous in biological materials.

## B.2 Search Algorithms

The numerically efficient modeling of contact problems includes an efficient contact detection. In this thesis, two such methods have been implemented: an octree-based search and a search adopting a geometrical binning strategy.

**Octree** The octree data structure is a common tool for applications such as *nearest neighbor search* or *spatial indexing*. It has a time complexity of  $\mathcal{O}(n \log(n))$ . A volumetric octree consists of a *parent cell* (in this case, the entire cuboid (not necessarily cubic) simulation box), which is subdivided into *eight* daughter cells, hence the name. Each of these daughter cells may be refined further depending on the need to do so. This need is evaluated by means of the number of objects in each cell. In the case of beam contact problems, each element is such an object. The octree is refined until only a certain, a priori defined number of  $\leq N_{\text{stop}}$  elements

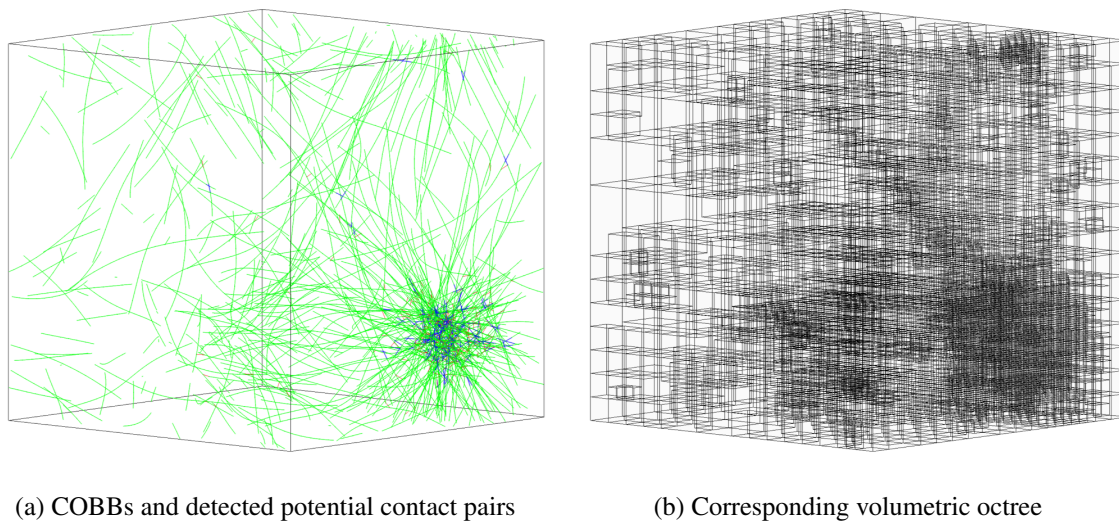


**Figure B.1** A cluster structure simulated with contact/excluded volume effects. (a) The visualization shows the COBBs of filament elements (●), crosslinker elements (●), and COBBs of potential contact pairs (●). (b) Volumetric discretization by means of the octree.

is located within each daughter cell. Each element is enveloped by a paraxial *cylindrical oriented bounding box* (COBB) with a certain radius  $r_{\text{cobb}}$ . There exist other bounding box types but the COBB has emerged the preferable option. The radius  $r_{\text{cobb}}$  commonly exceeds the actual beam radius by a safety factor  $c_{\text{cobb}}$  in order to detect potential contact pairs in advance. Having reached maximum octree refinement, a brute force search for potential contact pairs is conducted. Each COBB is evaluated with respect to all other COBBs in the daughter cell. The use of an octree shifts the bottleneck in computational efficiency from contact search back to the nonlinear solution procedure. Figure B.1 shows a cluster, whose elements have been wrapped in COBBs (Figure B.1a). The octree is built according to the COBBs and is shown in Figure B.1b. A drawback of octree data structures is the intricate parallelization of the octree setup.

**Geometric binning** *Geometric binning* is another popular volume partitioning and search strategy. In principle, this method creates a histogram of the spatial occurrences of objects, i.e., elements or *free* linkers, is created assigning each object within the volume to a certain bin. A *bin* is a cuboid subvolume, which, in contrast to the octree data structure, results simply from the equipartitioning of each dimension of the volume into  $N_{\text{bin}}$  segments. Geometric binning offers linear access times once the volume and the object contained in it have been indexed. Both the volumetric octree as well as geometric binning is used for finding pairs of linkers and binding sites that are considered for chemical bond. Depending on the network architecture, either the octree or the binning strategy is more efficient. In case of cumulated structures, the octree is superior in most cases since the brute force portion of the search can be controlled more flexibly than with the static bin size of the binning strategy. In more dilute phases, the binning strategy is more efficient due to the faster indexing. An advantage of binning strategies is that they are easily parallelized.

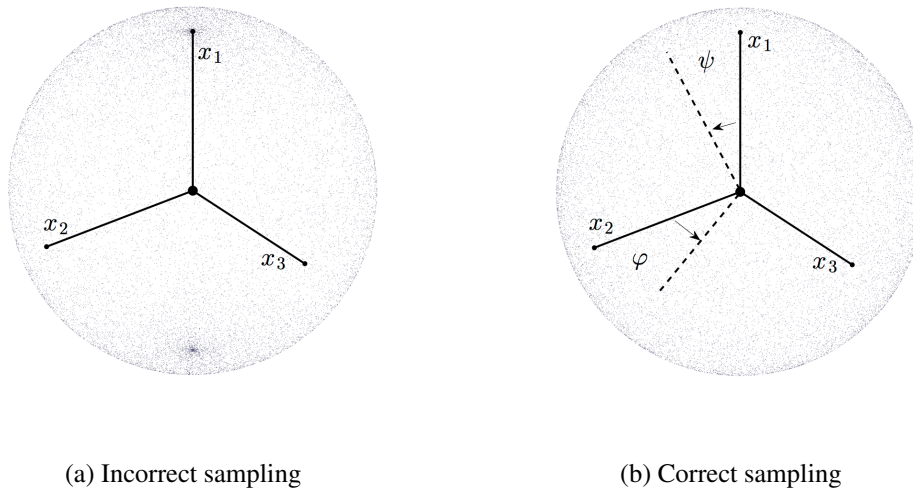


**Figure B.2** Sampling of surface  $\mathcal{S}(\varphi(x), \psi(y))$  of a unit sphere by means of angle functions  $\varphi(x)$  and  $\psi(y)$  with uniformly distributed random variables  $x$  and  $y$  on the interval  $[0; 1]$ . (a) Incorrect distribution of polar angles  $\psi(y) = \pi y$ , which leads to a higher density at the poles. (b) Correctly weighted polar angle with  $\psi(y) = 2 \arcsin(y)$ .

### B.3 Sampling of a uniform distribution of spherical coordinates

The creation of initial network geometries using a meshing tool as well as the analyses involving filament orientations rely on a description by means of spherical coordinates. While the interpretation of the azimuth angle is unproblematic, the polar angle needs to be interpreted with care (see Chapter 5). The uniform distributions of azimuth angles  $\varphi \in [0; 2\pi[$  and polar angles  $\psi \in [0; \pi]$  are given as

$$\rho(\varphi) = \frac{1}{2\pi}, \quad \rho(\psi) = \frac{1}{2} \sin \psi. \quad (\text{B.9})$$

The distribution  $\rho(\psi)$  takes on the given form because of the Jacobian involved in mapping  $(\varphi, \psi)$  to positions in Cartesian space. Results of an incorrect mapping (Figure B.2a) and the correct procedure (Figure B.2b) are shown, where the surface of a unit sphere has been sampled. The incorrect mapping leads to a higher density of samples at the poles, resulting in geometrical anisotropy when generating samples or the misinterpretation of results.

## C High-frequency bundle rheology

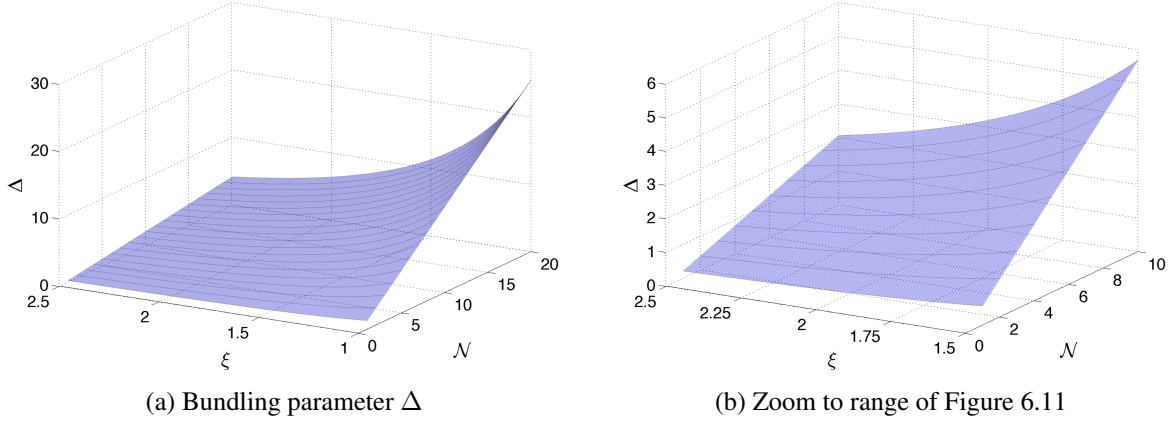


**Figure C.1** (a) The bundling parameter  $\Delta$  is plotted over the number of bundle filament  $\mathcal{N}$  and the mesh size  $\xi$ . (b) The same plot is shown again but zoomed to the relevant  $\Delta$ -range.

The following can be found in a slightly more detailed manner in [164]. It is based on theoretical work done by ALEX J. LEVINE (University of California, Los Angeles).

**Calculation of the bundling parameter  $\Delta$**  In Chapter 6, a high-frequency bundle rheology has been found distinct from that of networks of single filaments. The characteristic measure determining the degree of bundling in a system  $\Delta$  has been introduced in equation (6.16). For Figure 6.11, a parameter  $\Delta \approx 2$  was determined reflecting  $G''(\omega) \sim \omega^{0.93}$  and  $G'(\omega) \sim \omega^{0.55}$ . The scaling exponents of  $G'$  and  $G''$  in this figure imply that the network is currently in an intermediate state between the asymptotic cases of a network purely consisting of single filaments and a purely bundled one. For larger values of  $\Delta$ , one finds only the scaling consistent with the  $\Delta \gg 1$  limit discussed above. In the following, an exemplary calculation of  $\Delta$  is performed using values from simulations.

The dimensionless parameter  $\Delta$  is given by

$$\Delta = \left( \frac{\mathcal{N}\pi}{3} \right) \left( \frac{L_p k_B T}{b^2 \delta k_\times} \right) \left( \frac{\delta}{\xi} \right)^2 \quad (\text{C.1})$$

as written in Equation (6.16) except that the Young's modulus of the filaments has been replaced by their persistence length  $L_p$ . The bending modulus  $\kappa$  depends on the filament's diameter  $b$  and Young's modulus  $E_f$  and reads

$$\kappa = \frac{E_f \pi}{64} b^4. \quad (\text{C.2})$$

$\Delta$  is written as the product of three terms. The first term accounts for the size of the bundle by the number of filaments within a bundle. The second term gathers the elastic properties of filaments

and linkers. The last term reflects the network structure. The filament diameter is  $b \sim 5$  nm, the average crosslink distance  $\delta \sim 100$  nm, and the linkers' spring constant is  $k_x = 0.122$  pN/nm. Inserting these values into equation C.1 results in

$$\Delta \approx 127N \left( \frac{\delta}{\xi} \right)^2. \quad (\text{C.3})$$

From examination of the network structure, the average number of filaments per bundle has been determined as  $\mathcal{N} = 5$ . The mesh size ranges at  $1.5 \mu\text{m} \leq \xi \leq 2.5 \mu\text{m}$ . Consequently,  $\Delta$  is within the range

$$1.0 < \Delta < 2.8. \quad (\text{C.4})$$

Estimations with respect to Figure 6.11 yield  $\Delta \approx 2$  with uncertainties concerning the actual distribution of bundle thickness and the mesh size. Figure C.1 demonstrates that a deviation from the well-known  $\omega^{3/4}$  scaling occurs for any parameter  $\Delta > 0$ . As a consequence, as soon as there is only as much as the onset of bundling, the  $\omega^{3/4}$  scaling will be violated.

# D Simulation parameters

## Basic parameters

notation	description	value	unit
$k_b T$	thermal energy	$4.043 \times 10^{-3}$	aJ
$\eta$	viscosity of the background fluid	$10^{-3}$	Pa s
$E_f$	filament Young's modulus	$1.3 \times 10^9, 2.3 \times 10^9$ , [130]	pN/ $\mu\text{m}^2$
$A_f$	filament cross section	$1.9 \times 10^{-7}, 1.9 \times 10^{-5}$ , [88]	$\mu\text{m}^2$
$I_2, I_3$	moment of inertia of area	$2.85 \times 10^{-11}$	$\mu\text{m}^4$
$J$	polar moment of inertia of area	$5.7 \times 10^{-11}$	$\mu\text{m}^4$
$A_l$	linker cross section	$4.75 \times 10^{-6}$ [202]	$\mu\text{m}^2$
$E_l$	linker Young's modulus	$2.56 \times 10^6$ [166]	pN/ $(\mu\text{m})^2$
$I_l$	linker moment of inertia	$4.49 \times 10^{-11}$ [202]	$\mu\text{m}^2$
$J_l$	linker polar moment of inertia	$8.98 \times 10^{-11}$ [202]	$\mu\text{m}^2$
$\nu$	filament Poisson ratio	[0.3; 0.5]	-

**Table D.1** Basic parameters for filament model, linkers, and system variables, if not explicitly stated otherwise

## Parameters of the performance comparison in chapter 3

notation	description	value	unit
$N_f$	number of filaments	208	-
$N_e$	number of filaments	8, 16, 24, 32	-
$L_f$	filament length	4	$\mu\text{m}$
$A_f$	filament cross section	$1.9 \times 10^{-5}$	$\mu\text{m}^2$
$d_b$	distance between adjacent binding sites	0.125	$\mu\text{m}$
$N_l$	number of linkers	400, 950, 1400	$\mu\text{m}$
$2R_l$	linker size	0.1	$\mu\text{m}$
$2\Delta R_l$	linker size tolerance	0.02	$\mu\text{m}$
$k_{\text{on}}$	chemical association rate constant	90	$\text{s}^{-1}$
$k_{\text{off}}$	chemical dissociation rate constant	3	$\text{s}^{-1}$
$H$	edge length of the simulation box	5	$\mu\text{m}$

**Table D.2** Parameters of the filament and the linker model, of their interaction, and system parameters

beam model	$N_e[-]$	homogeneous	bundle	cluster	lamellar	time scale
<i>Reissner</i> , 2 nodes	32	2.461	3.980	3.276	3.714	$\times 10^5 \text{s}$
<i>Reissner</i> , interpol.	32	3.006	5.205	3.844	5.060	$\times 10^5 \text{s}$
<i>Reissner</i> , interpol.	24	2.239	4.206	2.836	3.359	$\times 10^5 \text{s}$
<i>Reissner</i> , interpol.	16	1.311	3.551	1.689	2.673	$\times 10^5 \text{s}$
<i>Reissner</i> , interpol.	8	0.805	3.433	1.216	2.352	$\times 10^5 \text{s}$

**Table D.3** Computation times of network morphologies for *standard* and *interpolated* two-noded beam element linkers.  $N_e$  is the filament discretization,  $L_f = 4 \mu\text{m}$  is the filament length, and  $T_{\text{sim}} = 300 \text{s}$  is the simulated time.

**Parameters of simulations of molecular motors in Chapter 4**

notation	description	value	unit
$L_m$	motor size	0.02	$\mu\text{m}$
$\Delta L_m$	motor size tolerance	0.01	$\mu\text{m}$
$E_m$	Young's modulus of the motor	$3 \times 10^6$	$\text{pN}/\mu\text{m}^2$
$\delta_{+,0}$	unloaded stroke distance	0.01	$\mu\text{m}$
$\delta_p$	path distance	0.036	$\mu\text{m}$
$k_{\text{on}}$	chemical association rate constant	180	$\text{s}^{-1}$
$k_{\text{off}}$	chemical dissociation rate constant	0.09	$\text{s}^{-1}$
$k_{\text{ts}}$	power stroke rate constant	800	$\text{s}^{-1}$
$\tau_c$	cycle time of the motor	0.04	s
$r$	duty ratio of the motor	0.05	—

**Table D.4** Basic motor parameters of Chapter 4

notation	description	value	unit
$T_{\text{sim}}$	simulated time	100	s
$\Delta t$	time step size	$5 \times 10^{-4}$	s
$k_B T$	thermal energy	$4.185 \times 10^{-3}$	aJ
$\eta$	viscosity of the background fluid	0.05	$\text{Pa s}$
$N_e$	discretization (elements) of the filament	10	-
$L_f$	filament length	2	$\mu\text{m}$
$N_m$	number of motors	[55; 550]	-
$L_s$	substrate length	10	$\mu\text{m}$
$N_{e,s}$	discretization of the substrate filament	20	-

**Table D.5** Parameters of the one-dimensional motility assay

notation	description	value	unit
$T_{\text{sim}}$	simulated time	20	s
$\Delta t$	time step size	$5 \times 10^{-4}$	s
$L_f$	filament length	4	$\mu\text{m}$
$N_f$	number of filaments	100	-
$N_e$	discretization of the filament	16	-
$d_b$	distance between adjacent binding sites	0.036	$\mu\text{m}$
$N_m$	number of motors	27777	-
$L_s$	substrate filament length	6	$\mu\text{m}$
$N_s$	number of substrate filaments	167	-
$N_{e,s}$	discretization of the substrate filament	20	-
$d_s$	distance between adjacent substrate filaments	0.036	$\mu\text{m}$

**Table D.6** Parameters of the two-dimensional motility assay

## Parameters of equilibrium simulations of Chapter 5

notation	description	value	unit
$\Delta t$	time step size	$2.5 \times 10^{-3}, 5 \times 10^{-3}, \underline{0.01}$	s
H	edge length, simulation box	2, <u>5</u>	$\mu\text{m}$
$L_f$	filament length	1, 2, <u>4</u>	$\mu\text{m}$
$N_f$	total number of filaments	52, <u>104</u> , <u>208</u> , 416	-
$N_e$	finite elements per filament, $L_f = 4 \mu\text{m}$	8, 16, <u>32</u>	-
$L_p$	filament persistence length	0.92, <u>9.2</u> , 92	$\mu\text{m}$
$N_l$	total number of linkers	$\geq 100$	-
$2R_l$	linker size	0.04, <u>0.1</u> , 0.2, 0.4	$\mu\text{m}$
$2\Delta R_l$	linker size tolerance	0.02	$\mu\text{m}$
$\phi$	binding angle	$[\pi/16; 7\pi/16]$	rad
$\Delta\phi$	binding angle tolerance	$\pi/16$	rad
$k_{\text{on}}$	chemical association rate	90	$\text{s}^{-1}$
$k_{\text{off}}$	chemical dissociation rate	3	$\text{s}^{-1}$
$\lambda_p$	contact penalty parameter	25	$\text{pN}/\mu\text{m}$
$\text{tol}_{\text{AL}}$	Aug.-Lag. Uzawa constraint tolerance	$4.9 \times 10^{-4}$	$\mu\text{m}$

**Table D.7** Parameters for equilibrium simulations. Underlined quantities represent values that correspond to the results presented in Chapter 5.

notation	description	value	unit
H	edge length, simulation box	10	$\mu\text{m}$
$N_f$	total number of filaments	1664	-
$L_f$	filament length	4	$\mu\text{m}$
$N_e$	finite elements per filament, $L_f = 4 \mu\text{m}$	8	-
$N_l$	total number of linkers	7200	-
$\phi$	binding angle	$7\pi/16$	rad
$\Delta\phi$	binding angle tolerance	$\pi/16$	rad
$k_{\text{on}}$	chemical association rate	90	$\text{s}^{-1}$
$k_{\text{off}}$	chemical dissociation rate	3	$\text{s}^{-1}$

**Table D.8** Parameters of the simulation with an increased system volume of  $V = 1000 \mu\text{m}^3$ .

**Remark** Some quantities like the filament length  $L_f$  have been varied over a certain range in order to test the bounds of validity of the main claim of Chapter 5, that the discovered network morphologies are universal and therefore, within sensible physical bounds, are independent of parameters like the linker stiffness, the filament length, or the persistence length of the filament in the bounds of semiflexibility.

## Rheological simulations, Chapter 6

notation	description	value	unit
H	edge length, simulation box	6	$\mu\text{m}$
$\Delta t_0$	initial time step size (before shear application)	0.01	s
$N_f$	total number of filaments	360	-
$L_f$	filament length	4	$\mu\text{m}$
$N_e$	finite elements per filament	32	-
$N_l$	total number of linkers	9000	-
$2R_l$	linker size	0.1	$\mu\text{m}$
$2\Delta R_l$	linker size tolerance	0.02	$\mu\text{m}$
$\Delta x$	Bell parameter	1, 2, 4	nm
$\phi$	binding angle	-	rad
$\Delta\phi$	tolerance of binding angle	-	rad
$k_{\text{on}}$	association rate constant	30, 60, 90, 180	$\text{s}^{-1}$
$k_{\text{off}}$	dissociation rate constant	0.01, 0.07, 0.1, 0.3, 1, 3, 6, 10	$\text{s}^{-1}$
$n_p$	number of full measured periods	10	-
$\hat{\gamma}$	shear amplitude	0.01	-

**Table D.9** General parameter set for simulations of the linear rheology of bundle networks.

$f$ [Hz]	$\Delta t$ [s]	$f$	$\Delta t$	$f$	$\Delta t$	$f$	$\Delta t$
$10^5$	$5 \times 10^{-8}$	1000	$5 \times 10^{-6}$	10	$10^{-4}$	0.1	0.0025
$3 \times 10^4$	$1.6 \times 10^{-7}$	300	$1.6 \times 10^{-5}$	3	$3.3 \times 10^{-4}$	0.03	0.003
$10^4$	$5 \times 10^{-7}$	100	$2.5 \times 10^{-5}$	1	$5 \times 10^{-4}$	0	0.005
3000	$1.6 \times 10^{-6}$	30	$8.3 \times 10^{-5}$	0.3	$8.3 \times 10^{-4}$	0.003	0.0016

**Table D.10** Frequency-dependent time step sizes used in linear rheology simulations.

notation	description	value	unit
$\Delta t_0$	initial time step size (before shear application)	0.01	s
$\Delta t$	time step size corresponding to shear rate	0.01, 0.0025, 0.0013, $5 \times 10^{-4}$ , 0.0013, 0.005	s
$\Delta x$	Bell parameter	0.01	$\mu\text{m}$
$\dot{\gamma}$	macroscopic shear rate	0.125, 1.25, 6.25, 12.5, 0.625, 6.25	%/s
$\hat{\gamma}$	shear amplitude	30, 35	%
$k_{\text{on}}$	association rate constant	90	$\text{s}^{-1}$
$k_{\text{off}}$	dissociation rate constant	3, 0.01, 0.03, 0.06, 1, 3, 6, 10	$\text{s}^{-1}$

**Table D.11** Parameters for simulations of the nonlinear viscoelasticity in Chapter 6. Slanted values correspond to simulations where  $k_{\text{off}}$  is varied.

# Curriculum Vitae

## *Kei Wieland Müller*

geboren am 10. Juni 1985 in Heidelberg als Sohn von Yoshiko Abé-Müller, M.A. und Prof. Dr. Günter Müller

born on June 10<sup>th</sup>, 1985 in Heidelberg, Germany; son of Yoshiko Abé-Müller, M.A. and Prof. Dr. Günter Müller

## Schule

Elementary & secondary education

<i>1991-1995</i>	Sepp-Herberger-Grundschule, Hohensachsen Elementary school
<i>1995-2004</i>	Werner-Heisenberg-Gymnasium, Weinheim Secondary school
<i>Juni 2004</i>	Abitur

## Studium

Higher education

<i>2004-2009</i>	Maschinenbaustudium, Technische Universität München Mechanical engineering, TUM
<i>2005-2009</i>	Stipendiat der Studienstiftung des Deutschen Volkes Scholarship holder of the German National Academic Foundation
<i>November 2009</i>	Studienabschluss, Diplom-Ingenieur (TUM) Graduation, Diplom-Ingenieur (TUM)

## Promotion

PhD

<i>2010-2014</i>	Stipendiat der International Graduate School of Science and Engineering (IGSSE) und Wissenschaftlicher Mitarbeiter am Lehrstuhl für Numerische Mechanik, TUM PhD scholarship holder of the <i>International Graduate School of Science and Engineering (IGSSE)</i> , research associate at the <i>Institute for Computational Mechanics</i> , TUM
------------------	--



# Reports of the Institute for Computational Mechanics at the Technische Universität München

- 20 (2014) Kei Müller:**  
Simulation of self-assembly and mechanics of transiently crosslinked, semiflexible biopolymer networks.
- 19 (2014) Mahmoud Ismail:**  
Reduced dimensional modeling of the entire human lung.
- 18 (2013) Florian Henke:**  
An extended finite element method for turbulent premixed combustion.
- 17 (2012) Markus Gitterle:**  
A dual mortar formulation for finite deformation frictional contact problems including wear and thermal coupling.
- 16 (2012) Andreas Maier:**  
Computational modeling of rupture risk in abdominal aortic aneurysms.
- 15 (2012) Georg Bauer:**  
A coupled finite element approach for electrochemical systems.
- 14 (2012) Alexander Popp:**  
Mortar methods for computational contact mechanics and general interface problems.
- 13 (2012) Thomas Klöppel:**  
A finite element model for the human red blood cell.
- 12 (2012) Sophie Rausch:**  
Computational and experimental modeling of lung parenchyma.
- 11 (2011) Christian Cyron:**  
Micromechanical continuum approach for the analysis of biopolymer networks.
- 10 (2011) Lena Wiechert:**  
Computational modeling of multi-field and multi-scale phenomena in respiratory mechanics.
- 9 (2010) Peter Gamnitzer:**  
Residual-based variational multiscale methods for turbulent flows and fluid-structure interaction.
- 8 (2010) Axel Gerstenberger:**  
An XFEM based fixed grid approach to fluid-structure interaction.
- 7 (2009) Ulrich Küttler:**  
Effiziente Lösungsverfahren für Fluid-Struktur-Interaktions-Probleme.

- 6 (2009) Moritz Frenzel:**  
Advanced structural finite element modeling of arterial walls for patient-specific geometries.
- 5 (2007)\* Christiane Förster:**  
Robust methods for fluid-structure interaction with stabilised finite elements.
- 4 (2004)\* Tobias Erhart:**  
Strategien zur Numerischen Modellierung transienter Impaktvorgänge bei nicht-linearem Materialverhalten.
- 3 (2004)\* Michael Gee:**  
Effiziente Lösungsstrategien in der nichtlinearen Schalenmechanik.
- 2 (2003)\* Volker Gravemeier:**  
The variational multiscale method for laminar and turbulent incompressible flow.
- 1 (2001)\* Daniel Mok:**  
Partitionierte Lösungsverfahren in der Strukturmechanik und der Fluid-Struktur-Interaktion.

---

\* This dissertation was supervised by Prof. Dr.-Ing. Wolfgang A. Wall at the Institute for Structural Mechanics at the University of Stuttgart and has been published in the respective report series.

# Bibliography

- [1] Experimental image provided by M. Vinzenz and J. V. Small, Institute for Molecular Biotechnology of the Austrian Academy of Sciences, Vienna, Austria.
- [2] Experimental images provided by K. M. Schmoller and A. R. Bausch, Lehrstuhl für Zellbiophysik E27, Technische Universität München.
- [3] Image by G. von Dassow *et al.*, <http://celldynamics.org/celldynamics/research/cytokinesis/>.
- [4] B. Alberts, A. Johnson, J. Lewis, M. Raff, K. Roberts, and P. Walter. *Molecular Biology of the Cell*. Garland Science, 5. edition, 2008.
- [5] F. Amblard, A. Maggs, B. Yurke, A. N. Pargellis, and S. Leibler. Subdiffusion and anomalous local viscoelasticity in actin networks. *Phys. Rev. Lett.*, 77(21):4470–4473, 1996.
- [6] S. S. Andrews and D. Bray. Stochastic simulation of chemical reactions with spatial resolution and single molecule detail. *Physical Biology*, 1(3):137–151, 2004.
- [7] J. A. Astroem, P. B. S. Kumar, I. Vattulainen, and M. Karttunen. Strain hardening, avalanches, and strain softening in dense cross-linked actin networks. *Phys. Rev. E*, 77(5):051913, 2008.
- [8] G. Bao and S. Suresh. Cell and molecular mechanics of biological materials. *Nat. Mater.*, 2:715–725, 2003.
- [9] C. Batters, C. P. Arthur, A. Lin, J. Porter, M. A. Geeves, R. A. Milligan, J. E. Molloy, and L. M. Coluccio. Myo1c is designed for the adaptation response in the inner ear. *The EMBO Journal*, 23(7):1433–1440, 2004.
- [10] G. I. Bell. Models for the specific adhesion of cells to cells. *Science*, 200(4342):618–627, 1978.
- [11] J. Berger, M. Reist, J. M. Mayer, O. Felt, N. A. Peppas, and R. Gurny. Structure and interactions in covalently and ionically crosslinked chitosan hydrogels for biomedical applications. *Eur. J. Pharm. Biopharm.*, 57(1):19–34, 2004.
- [12] J. R. Blundell and E. M. Terentjev. The influence of disorder on deformations in semiflexible networks. *Proc. R. Soc. A*, 467(2132):2330–2349, 2011.
- [13] I. Borukhov, R. F. Bruinsma, W. M. Gelbart, and A. J. Liu. Structural polymorphism of the cytoskeleton: A model of linker-assisted filament aggregation. *Proc. Natl. Acad. Sci.*, 102(10):3673–3678, 2005.
- [14] C. Broedersz, M. Depken, N. Y. Yao, M. R. Pollak, D. A. Weitz, and F. C. MacKintosh. Cross-link-governed dynamics of biopolymer networks. *Phys. Rev. Lett.*, 105(23):238101, 2010.
- [15] S. A. Burgess, S. Yu, M. L. Walker, R. J. Hawkins, J. M. Chalovich, and P. J. Knight. Structures of smooth muscle myosin and heavy meromyosin in the folded, shutdown state. *J. Mol. Biol.*, 372(5):1165–1178, 2007.
- [16] T. Butt, T. Mufti, A. Humayun, P. B. Rosenthal, S. Khan, S. Khan, and J. E. Molloy. Myosin motors drive long range alignment of actin filaments. *J. Biol. Chem.*, 285(7):4964–4974, 2010.
- [17] A. Cardona and M. Geradin. A beam finite element non-linear theory with finite rotations. *International Journal for Numerical Methods in Engineering*, 26(11):2403–2438, 1988.
- [18] P. M. Chaikin and T. C. Lubensky. *Principles of condensed matter physics*. Cambridge University Press, 2010.
- [19] P. L. Chandran and M. R. K. Mofrad. Rods-on-string idealization captures semiflexible filament dynamics. *Phys. Rev. E*, 79(1):011906, 2009.
- [20] P. L. Chandran and M. R. K. Mofrad. Averaged implicit hydrodynamic model of semiflexible filaments. *Phys. Rev. E*, 81(3):031920, 2010.

- [21] P. Chen and V. B. Shenoy. Strain stiffening induced by molecular motors in active crosslinked biopolymer networks. *Soft Matter*, 7(2):355–358, 2011.
- [22] M. M. A. E. Claessens, M. Bathe, E. Frey, and A. R. Bausch. Actin-binding proteins sensitively mediate f-actin bundle stiffness. *Nat. Mater.*, 5(9):748–753, 2006.
- [23] M. M. A. E. Claessens, C. Semmrich, L. Ramos, and A. R. Bausch. Helical twist controls the thickness of f-actin bundles. *Proc. Natl. Acad. Sci.*, 105(26):8819–8822, 2008.
- [24] G. M. Cooper. *The Cell: a Molecular Approach*. Sinauer Associates, Inc., 2. edition, 2000.
- [25] N. J. Cordova, B. Ermentrout, and G. F. Oster. Dynamics of single-motor molecules: The thermal ratchet model. *Proc. Natl. Acad. Sci. USA*, 89:339–343, 1992.
- [26] D. S. Courson and R. S. Rock. Actin crosslink assembly and disassembly mechanics for alpha-actinin and fascin. *Journal of Biological Chemistry*, 285(34):26350—26357, 2010.
- [27] R. Craig and J. L. Woodhead. Structure and function of myosin filaments. *Curr. Opin. Struct. Biol.*, 16(2):204–212, 2006.
- [28] M. A. Crisfield. A consistent co-rotational formulation for non-linear, three-dimensional, beam-elements. *Comput. Method. Appl. M.*, 81(2):131–150, 1990.
- [29] M. A. Crisfield. *Non-linear Finite Element Analysis of Solids and Structures, Volume 2: Advanced Topics*. Wiley, Chichester, 2003.
- [30] M. A. Crisfield and G. Jelenic. Objectivity of strain measures in the geometrically exact three-dimensional beam theory and its finite-element implementation. *Proceedings of the Royal Society of London. Series A: Mathematical, Physical and Engineering Sciences*, 455(1983):1125–1147, 1999.
- [31] C. Cruz, F. Chinesta, and G. Régnier. Review on the brownian dynamics simulation of bead-rod-spring models encountered in computational rheology. *Arch. Comput. Methods Eng.*, 19:227–259, 2012.
- [32] E. Cuthill and J. McKee. Reducing the bandwidth of sparse symmetric matrices. In *Proceedings of the 1969 24th National Conference*, ACM '69, pages 157–172, New York, NY, USA, 1969. ACM.
- [33] C. J. Cyron. *Micromechanical Continuum Approach for the Analysis of Biopolymer Networks*. PhD thesis, Technische Universität München, 2011.
- [34] C. J. Cyron, K. W. Müller, A. R. Bausch, and W. A. Wall. Micromechanical simulations of biopolymer networks with finite elements. *Journal of Computational Physics*, 244:263–251, 2013.
- [35] C. J. Cyron, K. W. Müller, K. M. Schmolzer, A. R. Bausch, W. A. Wall, and R. F. Bruinsma. Equilibrium phase diagram of semi-flexible polymer networks with linkers. *Europhys. Lett.*, 102:38003, 2013.
- [36] C. J. Cyron and W. A. Wall. Finite-element approach to brownian dynamics of polymers. *Phys. Rev. E*, 80(6):066704, 2009.
- [37] C. J. Cyron and W. A. Wall. Consistent finite-element approach to brownian polymer dynamics with anisotropic friction. *Phys. Rev. E*, 82:066705, 2010.
- [38] C. J. Cyron and W. A. Wall. Numerical method for the simulation of the brownian dynamics of rod-like microstructures with three-dimensional nonlinear beam elements. *Int. J. Numer. Meth. Engng*, 90:955–987, 2012.
- [39] P.-G. de Gennes. *Scaling Concepts in Polymer Physics*. Cornell University Press, 1979.
- [40] M. Doi and S. F. Edwards. *The theory of polymer dynamics*. Clarendon Press, Oxford, 1994.
- [41] D. Durville. Simulation of the mechanical behaviour of woven fabrics at the scale of fibers. *International Journal of Material Forming*, 3(2):1241–1251, 2010.
- [42] D. Durville. Contact-friction modeling with elastic beam assemblies: an application to knot tightening. *Computational Mechanics*, 49(6):687–707, 2012.

- 
- [43] S. Ebashi and F. Ebashi.  $\alpha$ -actinin, a new structural protein from striated muscle: I. preparation and action on actomyosin-atp interaction. *J. Biochem.*, 58:7–12, 1965.
- [44] M. Edidin. Lipids on the frontier: a century of cell-membrane bilayers. *Nat. Rev. Mol. Cell Biol.*, 4(5):414–418, 2003.
- [45] A. Einstein. Über die von der molekularkinetischen Theorie der Wärme geforderte Bewegung von in ruhenden Flüssigkeiten suspendierten Teilchen. *Annalen der Physik*, 322(8):549–560, 1905.
- [46] E. L. Elson. Cellular mechanics as an indicator of cytoskeletal structure and function. *Annu. Rev. Biophys. Biophys. Chem.*, 17:397–430, 1988.
- [47] D. L. Ermak and J. A. McCammon. Brownian dynamics with hydrodynamic interactions. *J. Chem. Phys.*, 69(4):1352–1360, 1978.
- [48] T. T. Falzone, M. Lenz, D. R. Kovar, and M. L. Gardel. Assembly kinetics determine the architecture of  $\alpha$ -actinin crosslinked f-actin networks. *Nat. Comm.*, 3:861, 2012.
- [49] W. O. Fenn. A quantitative comparison between the energy liberated and the work performed by the isolated sartorius muscle of the frog. *J. Physiol.*, 58:175, 1923.
- [50] J. M. Ferrer, H. Lee, J. Chen, B. Pelz, F. Nakamura, R. D. Kamm, and M. J. Lang. Measuring molecular rupture forces between single actin filaments and actin-binding proteins. *Proc. Natl. Acad. Sci.*, 105(27):9221–9226, 2008.
- [51] R. P. Feynman. Forces in molecules. *Phys. Rev.*, 56(4):340–343, 1939.
- [52] J. T. Finer, R. M. Simmons, and J. A. Spudis. Single myosin molecule mechanics: piconewton forces and nanometre steps. *Nature*, 368(6467):113–119, 1994.
- [53] E. Frey, K. Kroy, J. Wilhelm, and E. Sackmann. Statistical mechanics of semiflexible polymers: Theory and experiment. Technical Report cond-mat/9707021, 1997.
- [54] M. Gardel, J. Shin, F. MacKintosh, L. Mahadevan, P. Matsudaira, and D. Weitz. Scaling of f-actin network rheology to probe single filament elasticity and dynamics. *Phys. Rev. Lett.*, 93(18):188102, 2004.
- [55] M. L. Gardel, M. T. Valentine, J. C. Crocker, A. R. Bausch, and D. A. Weitz. Microrheology of entangled f-actin solutions. *Phys. Rev. Lett.*, 91(15):158302, 2003.
- [56] M. W. Gee, C. T. Kelley, and R. B. Lehoucq. Pseudo-transient continuation for nonlinear transient elasticity. *International Journal for Numerical Methods in Engineering*, 78(10):1209–1219, 2009.
- [57] J. M. Gere and S. P. Timoshenko. *Mechanics of Materials*. Nelson Thornes Ltd., Cheltenham, 5. edition, 2002.
- [58] T. Gisler and D. A. Weitz. Scaling of the microrheology of semidilute f-actin solutions. *Phys. Rev. Lett.*, 82(7):1606, 1999.
- [59] F. Gittes and F. C. MacKintosh. Dynamic shear modulus of a semiflexible polymer network. *Phys. Rev. E*, 58(2):R1241–R1244, 1998.
- [60] F. Gittes, B. Mickey, J. Nettleton, and J. Howard. Flexural rigidity of microtubules and actin filaments measured from thermal fluctuations in shape. *J. Cell Biol.*, 120(4):923–934, 1993.
- [61] D. S. Goodsell. Molecule of the month: Myosin. *RCSB PDB*, 2001.
- [62] D. S. Goodsell. Molecule of the month: Kinesin. *RCSB PDB*, 2005.
- [63] G. Grason. Braided bundles and compact coils: The structure and thermodynamics of hexagonally packed chiral filament assemblies. *Phys. Rev. E*, 79:041919, 2009.
- [64] G. Grason and R. Bruinsma. Chirality and equilibrium biopolymer bundles. *Phys. Rev. Lett.*, 99:098101, 2007.
- [65] M. J. Greenberg, C.-L. A. Wang, W. Lehman, and J. R. Moore. Modulation of actin mechanics by caldesmon and tropomyosin. *Cell Motil. Cytoskeleton*, 65(2):156–164, 2008.

- [66] T. Guérin, J. Prost, and J.-F. Joanny. Dynamic instabilities in assemblies of molecular motors with finite stiffness. *Phys. Rev. Lett.*, 104(24):248102, 2010.
- [67] T. Guérin, J. Prost, and J.-F. Joanny. Dynamical behavior of molecular motor assemblies in the rigid and crossbridge models. *Eur. Phys. J. E Soft Matter*, 34(6):60, 2011.
- [68] B. Guo and W. H. Guilford. Mechanics of actomyosin bonds in different nucleotide states are tuned to muscle contraction. *Proc. Natl. Acad. Sci.*, 103(26):9844–9849, 2006.
- [69] O. Hallatschek, E. Frey, and K. Kroy. Tension dynamics in semiflexible polymers. i. coarse-grained equations of motion. *Phys. Rev. E*, 75(3):031905, 2007.
- [70] E. H. Hauge and A. Martin-Loef. Fluctuating hydrodynamics and brownian motion. *J. Stat. Phys.*, 7(3):259–281, 1973-03-01.
- [71] D. A. Head, A. J. Levine, and F. C. MacKintosh. Deformation of cross-linked semiflexible polymer networks. *Phys. Rev. Lett.*, 91(10):108102, 2003.
- [72] C. A. Heckman and H. K. Plummer. Filopodia as sensors. *Cell. Signal.*, 25(11):2298–2311, 2013.
- [73] H. G. A. Hellmann. *Einführung in die Quantenchemie*. Franz Deuticke, 1937.
- [74] C. Heussinger. Cooperative crosslink (un)binding in slowly driven bundles of semiflexible filaments. *Phys. Rev. E*, 83(5):050902, 2011.
- [75] C. Heussinger. Stress relaxation through crosslink unbinding in cytoskeletal networks. *New. J. Phys.*, 14(9):095029, 2012.
- [76] C. Heussinger, M. Bathe, and E. Frey. Statistical mechanics of semiflexible bundles of wormlike polymer chains. *Phys. Rev. Lett.*, 99(4):048101, 2007.
- [77] C. Heussinger and E. Frey. Floppy modes and nonaffine deformations in random fiber networks. *Phys. Rev. Lett.*, 97(10):105501, 2006.
- [78] C. Heussinger and E. Frey. Force distributions and force chains in random stiff fiber networks. *Eur. Phys. J. E Soft*, 24(1):47–53, 2007.
- [79] C. Heussinger and E. Frey. The role of architecture in the elastic response of semiflexible polymer and fiber networks. *Phys. Rev. E*, 75(1):011917–14, 2007.
- [80] C. Heussinger and G. Grason. Theory of crosslinked bundles of helical filaments: Intrinsic torques in self-limiting biopolymer assemblies. *Journal of Chemical Physics*, 135:035104, 2011.
- [81] B. Hinner, M. Tempel, E. Sackmann, K. Kroy, and E. Frey. Entanglement, elasticity, and viscous relaxation of actin solutions. *Phys. Rev. Lett.*, 81(12):2614–2617, 1998.
- [82] K. C. Holmes. The swinging lever-arm hypothesis of muscle contraction. *Curr. Biol.*, 7:R112–R118, 1997.
- [83] G. Holzapfel and R. Ogden. On the bending and stretching elasticity of biopolymer filaments. *J. Elasticity*, 104:319–342, 2011. 10.1007/s10659-010-9277-2.
- [84] G. A. Holzapfel. *Nonlinear solid mechanics: a continuum approach for engineering*. Wiley, 2000.
- [85] S. Homin and G. Grason. Structural reorganization of parallel actin bundles by crosslinking proteins: Incommensurate states of twist. *Phys. Rev. E*, 82:051919, 2010.
- [86] A. Houdusse and H. L. Sweeney. Myosin motors: missing structures and hidden springs. *Curr. Opin. Struct. Biol.*, 11(2):182–194, 2001.
- [87] J. Howard. Molecular motors: structural adaptations to cellular functions. *Nature*, 389(6651):561–567, 1997.
- [88] J. Howard. *Mechanics of motor proteins and the cytoskeleton*. Sinauer Associates, Inc., 2001.
- [89] J. Howard and J. A. Spudich. Is the lever arm of myosin a molecular elastic element? *Proc. Natl. Acad. Sci. USA*, 93:4463–4464, 1996.

- [90] K. B. Howell. *Principles of Fourier Analysis*. Chapman&Hall/CRC, 2001.
- [91] C.-C. Hsieh, S. Jain, and R. G. Larson. Brownian dynamics simulations with stiff finitely extensible nonlinear elastic-fraenkel springs as approximations to rods in bead-rod models. *J. Chem. Phys.*, 124(4):044911, 2006.
- [92] H.-J. Hsu, C.-F. Lee, A. Locke, S. Q. Vanderzyl, and R. Kaunas. Stretch-induced stress fiber remodeling and the activations of jnk and erk depend on mechanical strain rate, but not fak. *PLoS ONE*, 5(8):e12470, 2010.
- [93] E. M. Huisman, C. Storm, and G. T. Barkema. Frequency-dependent stiffening of semiflexible networks: A dynamical nonaffine to affine transition. *Phys. Rev. E*, 82(6):061902–, 2010.
- [94] E. M. Huisman, T. van Dillen, P. R. Onck, and E. Van der Giessen. Three-dimensional cross-linked f-actin networks: Relation between network architecture and mechanical behavior. *Phys. Rev. Lett.*, 99(20):208103, 2007.
- [95] D. Humphrey, C. Duggan, D. Saha, D. Smith, and J. Käs. Active fluidization of polymer networks through molecular motors. *Nature*, 416(6879):413–416, 2002.
- [96] A. F. Huxley. Muscle structure and theories of contraction. *Prog. Biophys. Biophys. Chem.*, 7:255–318, 1957.
- [97] A. F. Huxley and R. Niedergerke. Structural changes in muscle during contraction: Interference microscopy of living muscle fibres. *Nature*, 173(4412):971–973, 1954.
- [98] H. E. Huxley and J. Hanson. Changes in the cross-striations of muscle during contraction and stretch and their structural interpretation. *Nature*, 173(4412):973–976, 1954.
- [99] A. Ibrahimbegovic. On finite element implementation of geometrically nonlinear reissner’s beam theory: three-dimensional curved beam elements. *Comput. Method. Appl. M.*, 122(1-2):11–26, 1995.
- [100] H. Isambert, P. Venier, A. C. Maggs, A. Fattoum, R. Kassab, D. Pantaloni, and M. F. Carlier. Flexibility of actin filaments derived from thermal fluctuations. Effect of bound nucleotide, phalloidin, and muscle regulatory proteins. *J. Biol. Chem.*, 270(19):11437–11444, 1995.
- [101] J. N. Israelachvili. *Intermolecular and Surface Forces*. Elsevier, 3. edition, 2011.
- [102] P. A. Janmey, S. Hvidt, J. Lamb, and T. P. Stossel. Resemblance of actin-binding protein/actin gels to covalently crosslinked networks. *Nature*, 345(6270):89–92, 1990.
- [103] G. Jelenic and M. A. Crisfield. Geometrically exact 3d beam theory: implementation of a strain-invariant finite element for statics and dynamics. *Comput. Method. Appl. M.*, 171(1-2):141–171, 1999.
- [104] J. F. Joanny and J. Prost. Active gels as a description of the actin-myosin cytoskeleton. *HFSP Journal*, 3(2):94–104, 2009.
- [105] F. Jülicher and J. Prost. Cooperative molecular motors. *Phys. Rev. Lett.*, 75:2618–2621, 1995.
- [106] D. Kachan, R. F. Bruinsma, K. W. Müller, W. A. Wall, and A. J. Levine. Casimir interactions stabilize bundling in semi-flexible polymers. to be submitted.
- [107] J. Käs, H. Strey, J. X. Tang, D. Finger, R. Ezzell, E. Sackmann, and P. A. Janmey.
- [108] K. E. Kasza, A. C. Rowat, J. Liu, T. E. Angelini, C. P. Brangwynne, G. H. Koenderink, and D. A. Weitz. The cell as a material. *Curr. Opin. Cell Biol.*, 19:101–107, 2007.
- [109] Y.-S. Kee and D. N. Robinson. Motor proteins: Myosin mechanosensors. *Curr. Biol.*, 18:R860–R861, 2008.
- [110] M. Kiemes, P. Benetatos, and A. Zippelius. Orientational order and glassy states in networks of semiflexible polymers. *Phys. Rev. E*, 83(2):021905, 2011.
- [111] J. M. Kim and P. S. Doyle. A brownian dynamics-finite element method for simulating dna electrophoresis in nonhomogeneous electric fields. *J. Chem. Phys.*, 125(7):074906, 2006.

- [112] J. M. Kim and P. S. Doyle. Design and numerical simulation of a dna electrophoretic stretching device. *Lab Chip*, 7(2):213–225, 2007.
- [113] T. Kim, W. Hwang, and R. Kamm. Computational analysis of a cross-linked actin-like network. *Exp. Mech.*, 49(1):91–104, 2009.
- [114] T. Kim, W. Hwang, and R. D. Kamm. Dynamic role of cross-linking proteins in actin rheology. *Biophys. J.*, 101:1597–1603, 2011.
- [115] T. Kim, W. Hwang, and R. D. Kamm. Dynamic role of cross-linking proteins in actin rheology. *Biophys. J.*, 101(7):1597–1603, 2011.
- [116] T. Kim, W. Hwang, H. Lee, and R. D. Kamm. Computational analysis of viscoelastic properties of crosslinked actin networks. *PLoS Comput. Biol.*, 5(7):e1000439, 2009.
- [117] A. Kis, G. Csanyi, J.-P. Salvetat, T.-N. Lee, E. Couteau, A. J. Kulik, W. Benoit, J. Brugger, and L. Forro. Reinforcement of single-walled carbon nanotube bundles by intertube bridging. *Nat. Mat.*, 3(3):153–157, 2004.
- [118] G. H. Koenderink, M. Atakhorrami, F. C. MacKintosh, and C. F. Schmidt. High-frequency stress relaxation in semiflexible polymer solutions and networks. *Phys. Rev. Lett.*, 96:138307, 2006.
- [119] G. H. Koenderink, Z. Dogic, F. Nakamura, P. M. Bendix, F. C. MacKintosh, J. H. Hartwig, T. P. Stossel, and D. A. Weitz. An active biopolymer network controlled by molecular motors. *Proc. Natl. Acad. Sci.*, 106(36):15192–15197, 2009.
- [120] T. Kon, T. Oyama, R. Shimo-Kon, K. Imamula, T. Shima, K. Sutoh, and G. Kurisu. The 2.8Å crystal structure of the dynein motor domain. *Nature*, 484(7394):345–350, 2012.
- [121] S. J. Kron and J. A. Spudich. Fluorescent actin filaments move on myosin fixed to a glass surface. *Proc. Natl. Acad. Sci.*, 83(17):6272–6276, 1986.
- [122] K. Kruse and F. Jülicher. Actively contracting bundles of polar filaments. *Phys. Rev. Lett.*, 85(8):1178–1181, 2000.
- [123] N. Kurniawan, S. Enemark, and R. Rajagopalan. The role of structure in the nonlinear mechanics of cross-linked semiflexible polymer networks. *J. Chem. Phys.*, 136:065101, 2012.
- [124] R. Y. Kwon, A. J. Lew, and C. R. Jacobs. A microstructurally informed model for the mechanical response of three-dimensional actin networks. *Comput. Methods Biomech. Biomed. Engin.*, 11(4):407–418, 2008.
- [125] R. S. Lakes. *Viscoelastic Solids*. CRC Press, 1. edition, 1998.
- [126] L. D. Landau and E. M. Lifshitz. *Statistical Physics*. Pergamon Press, 1980.
- [127] L. D. Landau and E. M. Lifshitz. *Theory of Elasticity*. Elsevier Butterworth-Heinemann, 3. edition, 2005.
- [128] D. Laporte, N. Ojkic, D. Vavylonis, and J.-Q. Wu.  $\alpha$ -actinin and fimbrin cooperate with myosin ii to organize actomyosin bundles during contractile-ring assembly. *Mol. Biol. Cell*, 23(16):3094–3110, 2012.
- [129] T. A. Laursen. *Formulation and Treatment of Frictional Contact Problems Using Finite Elements*. PhD thesis, Department of Mechanical Engineering, Stanford University, 1992.
- [130] L. Le Goff, O. Hallatschek, E. Frey, and F. Amblard. Tracer studies on f-actin fluctuations. *Phys. Rev. Lett.*, 89(25):258101, 2002.
- [131] M. Lenz, M. L. Gardel, and A. R. Dinner. Requirements for contractility in disordered cytoskeletal bundles. *New. J. Phys.*, 14(3):033037, 2012.
- [132] M. Lenz, T. Thoresen, M. L. Gardel, and A. R. Dinner. Contractile units in disordered actomyosin bundles arise from f-actin buckling. *Phys. Rev. Lett.*, 108:238107, 2012.
- [133] O. Lieleg. *Model Systems of the Actin Cortex*. PhD thesis, Technische Universität München, 2007.
- [134] O. Lieleg and A. R. Bausch. Cross-linker unbinding and self-similarity in bundled cytoskeletal networks. *Phys. Rev. Lett.*, 99(15):158105, 2007.

- 
- [135] O. Lieleg, M. M. A. E. Claessens, and A. R. Bausch. Structure and dynamics of cross-linked actin networks. *Soft Matter*, 6(2):218–225, 2010.
- [136] O. Lieleg, M. M. A. E. Claessens, C. Heussinger, E. Frey, and A. R. Bausch. Mechanics of bundled semi-flexible polymer networks. *Phys. Rev. Lett.*, 99(8):088102, 2007.
- [137] O. Lieleg, M. M. A. E. Claessens, Y. Luan, and A. R. Bausch. Transient binding and dissipation in cross-linked actin networks. *Phys. Rev. Lett.*, 101(10):108101, 2008.
- [138] O. Lieleg, J. Kayser, G. Brambilla, L. Cipelletti, and A. R. Bausch. Slow dynamics and internal stress relaxation in bundled cytoskeletal networks. *Nat. Mater.*, 10:236–242, 2011.
- [139] O. Lieleg, K. M. Schmoller, M. M. A. E. Claessens, and A. R. Bausch. Cytoskeletal polymer networks: Viscoelastic properties are determined by the microscopic interaction potential of cross-links. *Biophys. J.*, 96(11):4725–4732, 2009.
- [140] O. Lieleg, K. M. Schmoller, C. J. Cyron, Y. Luan, W. A. Wall, and A. R. Bausch. Structural polymorphism in heterogeneous cytoskeletal networks. *Soft Matter*, 5(9):1796–1803, 2009.
- [141] O. Lieleg, K. M. Schmoller, K. R. Purdy Drew, M. M. A. E. Claessens, C. Semmrich, L. Zheng, J. R. Bartles, and A. R. Bausch. Structural and viscoelastic properties of actin networks formed by espin or pathologically relevant espin mutants. *ChemPhysChem*, 10(16):2813–2817, 2009.
- [142] Y. Lin, X. Wei, K. Y. Sze, and V. B. Shenoy. A combined finite element-langevin dynamics (fem-ld) approach for analyzing the mechanical response of bio-polymer networks. *J. Mech. Phys. Solids*, 2013.
- [143] J. Lin-Jones, L. Sohlberg, A. Dosé, J. Breckler, D. W. Hillman, and B. Burnside. Identification and localization of myosin superfamily members in fish retina and retinal pigmented epithelium. *J. Comp. Neurol.*, 513(2):209–223, 2009.
- [144] J. Liu, M. L. Gardel, K. Kroy, E. Frey, B. D. Hoffman, J. C. Crocker, A. R. Bausch, and D. A. Weitz. Microrheology probes length scale dependent rheology. *Phys. Rev. Lett.*, 96(11):118104, 2006.
- [145] H. Lodish, A. Berk, P. Matsudaira, C. A. Kaiser, M. Krieger, M. P. Scott, S. L. Zipursky, and J. Darnell. *Molecular Cell Biology*. W. H. Freeman & Co., New York, 5. edition, 2004.
- [146] D. G. Luenberger and Y. Ye. *Linear and nonlinear Programming*. Springer, 3. edition, 2008.
- [147] R. J. Lye, M. E. Porter, J. M. Scholey, and J. R. McIntosh. Identification of a microtubule-based cytoplasmic motor in the nematode *c. elegans*. *Cell*, 51(2):309–318, 1987.
- [148] R. W. Lymn and E. W. Taylor. Mechanism of adenosine triphosphate hydrolysis by actomyosin. *Biochemistry*, 10(25):4617–4624, 1971.
- [149] F. C. MacKintosh, J. Käs, and P. A. Janmey. Elasticity of semiflexible biopolymer networks. *Phys. Rev. Lett.*, 75(24):4425, 1995.
- [150] M. Magnasco. Forced thermal ratchets. *Phys. Rev. Lett.*, 71(10):1477–1481, 1993.
- [151] A. Maloney, L. J. Herskowitz, and S. J. Koch. Effects of surface passivation on gliding motility assays. *PLOS One*, 6(6):e19522, 2011.
- [152] S. B. Marston. The rates of formation and dissociation of actin-myosin complexes. effects of solvent, temperature, nucleotide binding and head-head interactions. *Biochem. J.*, 203(2):453–460, 1982.
- [153] K. Maruyama and S. Ebashi.  $\alpha$ -actinin, a new structural protein from striated muscle: Ii. action on actin. *J. Biol. Chem.*, 58(1):13–19, 1965.
- [154] P. K. Mattila and P. Lappalainen. Filopodia: molecular architecture and cellular functions. *Nat. Rev. Mol. Cell Biol.*, 9:464–454, 2008.
- [155] C. Meier, P. A., and W. A. Wall. A locking-free finite element formulation and reduced models for geometrically exact kirchhoff rods. 2014. submitted.

- [156] C. Meier, A. Popp, and W. A. Wall. An objective 3D large deformation finite element formulation for geometrically exact curved Kirchhoff rods. *Comput. Method. Appl. M.*, 278:445–478, 2014.
- [157] D. Mizuno, C. Tardin, C. F. Schmidt, and F. C. MacKintosh. Nonequilibrium mechanics of active cytoskeletal networks. *Science*, 315(5810):370–373, 2007.
- [158] J. E. Molloy, J. E. Burns, J. Kendrick-Jones, R. T. Tregear, and D. C. S. White. Movement and force produced by a single myosin head. *Nature*, 378(6553):209–212, 1995.
- [159] A. Montesi, D. C. Morse, and M. Pasquali. Brownian dynamics algorithm for bead-rod semiflexible chain with anisotropic friction. *J. Chem. Phys.*, 122(8):084903, 2005.
- [160] D. C. Morse. Viscoelasticity of concentrated isotropic solutions of semiflexible polymers. 1. model and stress tensor. *Macromolecules*, 31(20):7030–7043, 1998.
- [161] Y. K. Mouchery, J. Kučerík, D. Diehl, and G. E. Schaumann. Cation-mediated cross-linking in natural organic matter: a review. *Rev. Environ. Sci. Biotechnol.*, 11:41–54, 2012.
- [162] N. Mücke, L. Kreplak, R. Kirmse, T. Wedig, H. Herrmann, U. Aebi, and J. Langowski. Assessing the flexibility of intermediate filaments by atomic force microscopy. *J. Mol. Biol.*, 335(5):1241–1250, 2004.
- [163] K. W. Mueller, C. J. Cyron, and W. A. Wall. Computational analysis of phases and phase transitions in semi-flexible biopolymer networks. 2014. to be submitted.
- [164] K. W. Mueller, O. Lieleg, A. R. Bausch, R. F. Bruinsma, W. A. Wall, and A. J. Levine. Rheology of semi-flexible bundle networks with transient linkers. *Phys. Rev. Lett.*, 112:238102, 2014.
- [165] J. W. Murray and A. W. Wolkoff. Roles of the cytoskeleton and motor proteins in endocytic sorting. *Advanced Drug Delivery Reviews*, 55(11):1385–1403, 2003.
- [166] T. Nishizaka, R. Seo, H. Tadakuma, K. Kinoshita, and S. Ishiwata. *Biophys. J.*
- [167] P. R. Onck, T. Koeman, T. van Dillen, and E. van der Giessen. Alternative explanation of stiffening in cross-linked semiflexible networks. *Phys. Rev. Lett.*, 95(17):178102, 2005.
- [168] A. Ortega and J. G. de la Torre. Hydrodynamic properties of rodlike and disklike particles in dilute solution. *J. Chem. Phys.*, 119(18):9914–9919, 2003.
- [169] A. Ott, M. Magnasco, A. Simon, and A. Libchaber. Measurement of the persistence length of polymerized actin using fluorescence microscopy. *Phys. Rev. E*, 48(3):R1642–R1645, 1993.
- [170] J. S. Palmer and M. C. Boyce. Constitutive modeling of the stress-strain behavior of f-actin filament networks. *Acta Biomater.*, 4(3):597–612, 2008.
- [171] F. Pampaloni, G. Lattanzi, A. Jonáš, T. Surrey, E. Frey, and E.-L. Florin. Thermal fluctuations of grafted microtubules provide evidence of a length-dependent persistence length. *Proc. Natl. Acad. Sci.*, 103(27):10248–10253, 2006.
- [172] S. Panyukov and Y. Rabin. Statistical physics of polymer gels. *Phys. Rep.*, 269(1,Ä2):1–131, 1996.
- [173] Y. V. Pereverzev, O. V. Prezhdov, M. Forero, E. V. Sokurenko, and W. E. Thomas. The two-pathway model for the catch-slip transition in biological adhesion. *Biophys. J.*, 89(3):1446–1454, 2005.
- [174] M. E. Porter and W. S. Sale. The 9 + 2 axoneme anchors multiple inner arm dyneins and a network of kinases and phosphatases that control motility. *J. Cell Biol.*, 151(5):F37–F42, 2000.
- [175] E. M. Purcell. Life at low reynolds numbers. *Am. J. Phys.*, 45(1):3–11, 1977.
- [176] S. Ramanathan and D. C. Morse. Simulations of dynamics and viscoelasticity in highly entangled solutions of semiflexible rods. *Phys. Rev. E*, 76(1):010501, 2007.
- [177] S. L. Reck-Peterson, A. Yildiz, A. P. Carter, A. Gennerich, N. Zhang, and R. D. Vale. Single-molecule analysis of dynein processivity and stepping behavior. *Cell*, 126:335–348, 2006.
- [178] P. Reimann. Brownian motors: noisy transport far from equilibrium. *Physical Reports*, 361:57–265, 2002.

- [179] I. Romero. The interpolation of rotations and its application to finite element models of geometrically exact rods. *Comput. Mech.*, 34(2):121–133, 2004.
- [180] S. Ross. *A first course in probability*. Pearson Education, Inc., 8. edition, 2010.
- [181] J. Rotne and S. Prager. Variational treatment of hydrodynamic interaction in polymers. *J. Chem. Phys.*, 50(11):4831–4837, 1969.
- [182] S. A. Sandersius and T. J. Newman. Modeling cell rheology with the subcellular element model. *Physical Biology*, 5(1):015002, 2008.
- [183] V. Schaller, C. Weber, C. Semmrich, E. Frey, and A. R. Bausch. Polar patterns of driven filaments. *Nature*, 467(7311):73–77, 2010.
- [184] A. Schmidt and M. N. Hall. Signaling to the actin cytoskeleton. *Annu. Rev. Cell Dev. Biol.*, 14(1):305–338, 1998.
- [185] K. M. Schmoller, O. Lieleg, and A. R. Bausch. Internal stress in kinetically trapped actin bundle networks. *Soft Matter*, 4(12):2365–2367, 2008.
- [186] K. M. Schmoller, O. Lieleg, and A. R. Bausch. Structural and viscoelastic properties of actin/filamin networks: Cross-linked versus bundled networks. *Biophys. J.*, 97:83–89, 2009.
- [187] B. J. Schnapp and T. S. Reese. Dynein is the motor for retrograde axonal transport of organelles. *Proc. Natl. Acad. Sci. USA*, 86:1546–1552, 1989.
- [188] M. J. Schnitzer and S. M. Block. Kinesin hydrolyses one atp per 8-nm step. *Nature*, 388(6640):386–390, 1997.
- [189] M. P. Sheetz, R. Chasan, and J. A. Spudich. Atp-dependent movement of myosin in vitro: characterization of a quantitative assay. *J. Cell. Biol.*, 99:1867–1871, 1984.
- [190] H. Shin, K. R. P. Drew, J. R. Bartles, G. C. L. Wong, and G. M. Grason. Cooperativity and frustration in protein-mediated parallel actin bundles. *Phys. Rev. Lett.*, 103(23):238102, 2009.
- [191] J. H. Shin, M. L. Gardel, L. Mahadevan, P. Matsudaira, and W. D. A. Relating microstructure to rheology of a bundled and cross-linked f-actin network in vitro. *Proc. Natl. Acad. Sci.*, 101(26):9636–9641, 2004.
- [192] J. Simo and L. Vu Quoc. A three dimensional finite strain rod model part ii: Computational aspects. *Comput. Method. Appl. M.*, 58:79–116, 1986.
- [193] J. C. Simo and L. Vu-Quoc. On the dynamics in space of rods undergoing large motions – a geometrically exact approach. *Comput. Method. Appl. M.*, 66(2):125–161, 1988.
- [194] J. A. Spudich. How molecular motors work. *Nature*, 372(6506):515–518, 1994.
- [195] J. A. Spudich. The myosin swinging cross-bridge model. *Nat. Rev. Mol. Cell Biol.*, 2(5):387–392, 2001.
- [196] J. Squire. *The Structural Basis of Muscular Contraction*. Springer, 1981.
- [197] J. Stricker, T. Falzone, and M. L. Gardel. Mechanics of the f-actin cytoskeleton. *J. Biomech.*, 43(1):9–14, 2010.
- [198] H. Sugi, H. Minoda, Y. Inayoshi, F. Yumoto, T. Miyakawa, Y. Miyauchi, M. Tanokura, T. Akimoto, T. Kobayashi, S. Chaen, and S. Sugiura. Direct demonstration of the cross-bridge recovery stroke in muscle thick filaments in aqueous solution by using the hydration chamber. *Proc. Natl. Acad. Sci.*, 105(45):17396–17401, 2008.
- [199] T. Surrey, F. Nédélec, S. Leibler, and E. Karsenti. Physical properties determining self-organization of motors and microtubules. *Science*, 292(5519):1167–1171, 2001.
- [200] Y. Takagi, E. E. Homsher, Y. E. Goldman, and H. Shuman. Force generation in single conventional actomyosin complexes under high dynamic load. *Biophys. J.*, 90(4):1295–1307, 2006.
- [201] M. Tempel, G. Isenberg, and E. Sackmann. Temperature-induced sol-gel transition and microgel formation in  $\alpha$ -actinin cross-linked actin networks: A rheological study. *Phys. Rev. E*, 54(2):1802–1810, 1996.

- [202] R. Tharmann. *Mechanical Properties of Complex Cytoskeleton Networks*. PhD thesis, Technische Universität München, 2007.
- [203] R. Tharmann, M. M. A. E. Claessens, and A. R. Bausch. Viscoelasticity of isotropically cross-linked actin networks. *Phys. Rev. Lett.*, 98(8):088103, 2007.
- [204] W. Thomson 1<sup>st</sup> Baron Kelvin. from *greek*:  $\chi\epsilon\iota\rho$  hand. “I call any geometrical figure, or group of points, “chiral”, and say that it has chirality if its image in a plane mirror, ideally realized, cannot be brought to coincide with itself.”.
- [205] T. Thoresen, M. Lenz, and M. Gardel. Reconstitution of contractile actomyosin bundles. *Biophys. J.*, 100(11):2698–2705, 2011.
- [206] S. Tojkander, G. Gateva, and P. Lappalainen. Actin stress fibers – assembly, dynamics and biological roles. *J. Cell Sci.*, 125(8):1855–1864, 2012.
- [207] Y. Y. Toyoshima, S. J. Kron, E. M. McNally, K. R. Niebling, C. Toyoshima, and J. A. Spudich. Myosin subfragment-1 is sufficient to move actin filaments in vitro. *Nature*, 328(6130):536–539, 1987.
- [208] L. R. G. Treloar. *The Physics of Rubber Elasticity*. Oxford University Press, 2005.
- [209] Y. Tsuda, H. Yasutake, A. Ishijima, and T. Yanagida. Torsional rigidity of single actin filaments and actin-actin bond breaking force under torsion measured directly by in vitro micromanipulation. *Proc. Natl. Acad. Sci.*, 93(23):12937–12942, 1996.
- [210] J. Uhde, M. Keller, E. Sackmann, A. Parmeggiani, and E. Frey. Internal motility in stiffening actin-myosin networks. *Phys. Rev. Lett.*, 93(26):268101, 2004.
- [211] G. U. Unnikrishnan, J. N. Reddy, and V. U. Unnikrishnan. Constitutive material modeling of cell: A micromechanics approach. *J. Biomech. Eng.*, 129(3):315–323, 2006.
- [212] M. J. Unterberger, K. M. Schmoller, A. R. Bausch, and G. A. Holzapfel. A new approach to model cross-linked actin networks: Multi-scale continuum formulation and computational analysis. *J. Mech. Behav. Biomed. Mater.*, 22:95–114, 2013.
- [213] E. Urban, S. Jacob, M. Nemethova, G. P. Resch, and J. V. Small. Electron tomography reveals unbranched networks of actin filaments in lamellipodia. *Nat. Cell Biol.*, 12(5):429–436, 2010.
- [214] T. P. Q. Uyeda, S. J. Kron, and J. A. Spudich. Myosin step size: estimation from slow sliding movement of actin over low densities of heavy meromyosin. *J. Mol. Biol.*, 214:699–710, 1990.
- [215] R. D. Vale and R. A. Milligan. The way things move: Looking under the hood of molecular motor proteins. *Science*, 288(5463):88–95, 2000.
- [216] R. D. Vale, T. S. Reese, and M. P. Sheetz. Identification of a novel force-generating protein, kinesin, involved in microtubule-based motility. *Cell*, 42(1):39–50, 1985.
- [217] E. Van der Giessen, T. Koeman, T. Van Dillen, and P. R. Onck. On the origin of stiffening in biopolymers. *Mater. Res. Soc. Symp. Proc.*, 874, 2005.
- [218] T. Van Dillen, P. R. Onck, and E. Van der Giessen. Stiffening of semiflexible biopolymers and cross-linked networks. *ArXiv Physics e-prints*, 2006.
- [219] C. Veigel, M. L. Bartoo, D. C. S. White, J. C. Sparrow, and J. E. Molloy. The stiffness of rabbit skeletal actomyosin cross-bridges determined with an optical tweezers transducer. *Biophys. J.*, 75(3):1424–1438, 1998.
- [220] S. M. Volkmer Ward, A. Weins, M. R. Pollak, and D. A. Weitz. Dynamic viscoelasticity of actin cross-linked with wild-type and disease-causing mutant  $\alpha$ -actinin-4. *Biophys. J.*, 95(10):4915–4923, 2008.
- [221] D. H. Wachsstock, W. H. Schwarz, and T. D. Pollard. Cross-linker dynamics determine the mechanical properties of actin gels. *Biophys. J.*, 66(0006-3495 (Linking)):801–809, 1994.
- [222] S. Walcott. The load dependence of rate constants. *J. Chem. Phys.*, 128(21):215101, 2008.

- 
- [223] S. Walcott and S. X. Sun. A mechanical model of actin stress fiber formation and substrate elasticity sensing in adherent cells. *Proc. Natl. Acad. Sci.*, 2010.
- [224] K. Wang, J. F. Ash, and S. J. Singer. Filamin, a new high-molecular-weight protein found in smooth muscle and non-muscle cells. *Proc. Natl. Acad. Sci.*, 72(11):4483–4486, 1975.
- [225] M. Wang, H. Yin, R. Landick, J. Gelles, and S. Block. Stretching dna with optical tweezers. *Biophys. J.*, 72(3):1335–1346, 1997.
- [226] D. M. Warshaw, W. H. Guilford, Y. Freyzon, E. Kremntsova, K. A. Palmiter, M. J. Tyska, J. E. Baker, and K. M. Trybus. The light chain binding domain of expressed smooth muscle heavy meromyosin acts as a mechanical lever. *J. Biol. Chem.*, 275(47):37167–37172, 2000.
- [227] G. C. L. Wong, A. Lin, J. X. Tang, Y. Li, P. A. Janmey, and C. R. Safinya. Lamellar phase of stacked two-dimensional rafts of actin filaments. *Phys. Rev. Lett.*, 91(1):018103, 2003.
- [228] P. Wriggers. *Computational Contact Mechanics*. Wiley, New York, 2002.
- [229] C. Yang, L. Czech, S. Gerboth, S.-i. Kojima, G. Scita, and T. Svitkina. Novel roles of formin mdia2 in lamellipodia and filopodia formation in motile cells. *PLoS Biol.*, 5(11):2624–2645, 2007.
- [230] Y. Yang, M. Bai, W. S. Klug, A. J. Levine, and M. T. Valentine. Microrheology of highly crosslinked microtubule networks is dominated by force-induced crosslinker unbinding. *Soft Matter*, 9(2):383–393, 2013.
- [231] A. Yildiz, M. Tomishige, E. D. Vale, and P. R. Selvin. Kinesin walks hand-over-hand. *Science*, 303(5658):676–678, 2004.
- [232] G. Zagar, P. Onck, and E. Van der Giessen. Elasticity of rigidly cross-linked networks of athermal filaments. *Macromolecules*, 44:7026–7033, 2011.
- [233] C. Zhu and R. Dixit. Single molecule analysis of the arabidopsis fra1 kinesin shows that it is a functional motor protein with unusually high processivity. *Mol. Plant*, pages 1–7, 2011.
- [234] O. C. Zienkiewicz, R. L. Taylor, and D. D. Fox. *The Finite Element Method for Solid and Structural Mechanics*. Butterworth-Heinemann, 7. edition, 2014.
- [235] O. C. Zienkiewicz, R. L. Taylor, and J. C. Zhu. *The Finite Element Method. Its Basis and Fundamentals*. Elsevier Butterworth-Heinemann, 6. edition, 2005.
- [236] M. C. Zwier and L. T. Chong. Reaching biological timescales with all-atom molecular dynamics simulations. *Curr. Opin. Pharmacol.*, 10(6):745–752, 2010.